



energies

Numerical Investigations of Combustion

Edited by
Alexandre M. Afonso, Pedro Resende and Mohsen Ayoobi

Printed Edition of the Special Issue Published in *Energies*

Numerical Investigations of Combustion

Numerical Investigations of Combustion

Editors

Alexandre M. Afonso

Pedro Resende

Mohsen Ayoobi

MDPI • Basel • Beijing • Wuhan • Barcelona • Belgrade • Manchester • Tokyo • Cluj • Tianjin



Editors

Alexandre M. Afonso
Faculdade de Engenharia
da Universidade do Porto
Portugal

Pedro Resende
Polytechnic Institute of Viana
do Castelo (IPVC)
Portugal

Mohsen Ayoobi
Wayne State University
USA

Editorial Office

MDPI
St. Alban-Anlage 66
4052 Basel, Switzerland

This is a reprint of articles from the Special Issue published online in the open access journal *Energies* (ISSN 1996-1073) (available at: https://www.mdpi.com/journal/energies/special_issues/numerical_investigations_combustion).

For citation purposes, cite each article independently as indicated on the article page online and as indicated below:

LastName, A.A.; LastName, B.B.; LastName, C.C. Article Title. *Journal Name* **Year**, *Volume Number*, Page Range.

ISBN 978-3-0365-4683-4 (Hbk)

ISBN 978-3-0365-4684-1 (PDF)

© 2022 by the authors. Articles in this book are Open Access and distributed under the Creative Commons Attribution (CC BY) license, which allows users to download, copy and build upon published articles, as long as the author and publisher are properly credited, which ensures maximum dissemination and a wider impact of our publications.

The book as a whole is distributed by MDPI under the terms and conditions of the Creative Commons license CC BY-NC-ND.

Contents

Mohsen Ayoobi, Pedro R. Resende and Alexandre M. Afonso Numerical Investigations of Combustion—An Overview Reprinted from: <i>Energies</i> 2022 , <i>15</i> , 2975, doi:10.3390/en15092975	1
Pedro R. Resende, Leandro C. Morais, Carlos Pinho, Alexandre M. Afonso Combustion Characteristics of Premixed Hydrogen/Air in an Undulate Microchannel Reprinted from: <i>Energies</i> 2022 , <i>15</i> , 626, doi:10.3390/en15020626	7
Maria Mitu, Domnina Razus and Volkmar Schroeder Laminar Burning Velocities of Hydrogen-Blended Methane–Air and Natural Gas–Air Mixtures, Calculated from the Early Stage of $p(t)$ Records in a Spherical Vessel Reprinted from: <i>Energies</i> 2021 , <i>14</i> , 7556, doi:10.3390/en14227556	23
Ju-Hwan Seol, Van Chien Pham and Won-Ju Lee Effects of the Multiple Injection Strategy on Combustion and Emission Characteristics of a Two-Stroke Marine Engine Reprinted from: <i>Energies</i> 2021 , <i>14</i> , 6821, doi:10.3390/en14206821	39
Tomasz Białecki, Wojciech Dziegielewski, Mirosław Kowalski and Andrzej Kulczycki Reactivity Model as a Tool to Compare the Combustion Process in Aviation Turbine Engines Powered by Synthetic Fuels Reprinted from: <i>Energies</i> 2021 , <i>14</i> , 6302, doi:10.3390/en14196302	55
Raul Payri, Pedro Marti-Aldaravi, Rami Abboud and Abian Bautista Numerical Analysis of GDI Flash Boiling Sprays Using Different Fuels Reprinted from: <i>Energies</i> 2021 , <i>14</i> , 5925, doi:10.3390/en14185925	71
Maria Mitu, Codina Movileanu and Venera Giurcan Deflagration Characteristics of N_2 -Diluted CH_4 - N_2O Mixtures in the Course of the Incipient Stage of Flame Propagation Reprinted from: <i>Energies</i> 2021 , <i>14</i> , 5918, doi:10.3390/en14185918	95
Sunita Pokharel, Mohsen Ayoobi and V'yacheslav Akkerman Computational Analysis of Premixed Syngas/Air Combustion in Micro-channels: Impacts of Flow Rate and Fuel Composition Reprinted from: <i>Energies</i> 2021 , <i>14</i> , 4190, doi:10.3390/en14144190	111
Felix Grimm, Timo Lingstädt, Peter Kutne and Manfred Aigner Numerical and Experimental Study of a Jet-and-Recirculation Stabilized Low Calorific Combustor for a Hybrid Power Plant Reprinted from: <i>Energies</i> 2021 , <i>14</i> , 537, doi:10.3390/en14030537	131
Filipe M. Quintino and Edgar C. Fernandes Numerical Investigation of the Impact of H_2 Enrichment on Lean Biogas/Air Flames: An Analytical Modelling Approach Reprinted from: <i>Energies</i> 2021 , <i>14</i> , 369, doi:10.3390/en14020369	151
Mehdi Jadidi, Stevan Kostic, Leonardo Zimmer and Seth B. Dworkin An Artificial Neural Network for the Low-Cost Prediction of Soot Emissions Reprinted from: <i>Energies</i> 2020 , <i>13</i> , 4787, doi:10.3390/en13184787	169
Abdulafeez Adebisi, Olatunde Abidakun and V'yacheslav Akkerman Acceleration of Premixed Flames in Obstructed Pipes with Both Extremes Open Reprinted from: <i>Energies</i> 2020 , <i>13</i> , 4094, doi:10.3390/en13164094	197

Xiaoqin Hu, Arjen Kraaijeveld and Torgrim Log

Numerical Investigation of the Required Quantity of Inert Gas Agents in Fire Suppression Systems

Reprinted from: *Energies* **2020**, *13*, 2536, doi:10.3390/en13102536 **217**

Numerical Investigations of Combustion—An Overview

Mohsen Ayoobi ¹, Pedro R. Resende ^{2,3} and Alexandre M. Afonso ^{3,*}

¹ Division of Engineering Technology, Wayne State University, Detroit, MI 48201, USA; mohsen.ayoobi@wayne.edu

² proMetheus, School of Technology and Management (ESTG), Polytechnic Institute of Viana do Castelo (IPVC), Praça Gen. Barbosa 44, 4900-347 Viana do Castelo, Portugal; pedroresende@estg.ipv.pt

³ Centro de Estudos de Fenómenos de Transporte, Departamento de Engenharia Mecânica, Faculdade de Engenharia da Universidade do Porto, Rua Dr. Roberto Frias s/n, 4200-465 Porto, Portugal

* Correspondence: aafonso@fe.up.pt

With the recent advancements in computational capacities and the widespread applications of machine learning in engineering problems, the role of numerical methods has been becoming more and more important to improve existing models or develop new models that can help researchers to better understand the underlying physics of combustion, their interaction with other physical phenomena such as turbulence, and their impacts on the performance of the related applications at both fundamental and practical levels. This Special Issue aims to highlight the most recent advances in the development and application of such numerical methods. This editorial presents an overview of the articles published under this Special Issue is presented.

Resende et al. [1] conducted a numerical investigation to analyze the combustion characteristics of a H₂ and air mixture in a complex geometry of an undulate microchannel. The findings from this article help to understand and verify whether the flammability at microscales can be improved by designing non-straight microchannels as an alternative to the burner with recirculation of reaction products. In particular, the authors of this article evaluate the effect of the geometry on the combustion characteristics over a range of different inlet velocities while keeping other boundary conditions, including the equivalence ratio and external heat flux losses, the same.

Using both experimentally and numerically obtained data, Mitu et al. [2] examined the influence of hydrogen on the laminar burning velocity for different methane/hydrogen and natural gas/hydrogen mixtures with air at ambient initial conditions. In particular, this paper reports laminar burning velocities (LBV) of hydrogen-blended methane–air and natural gas–air mixtures, using mixtures at ambient initial pressure and temperature ($p_0 = 0.97\text{--}1.04$ bar, $T_0 = 22\text{--}25$ °C). The mixtures of interest in this work consist of single fuel–air (CH₄–air) and multifuel–air mixtures, where the multifuel was CH₄ blended with H₂, or natural gas blended with H₂, both under various amounts of added hydrogen, in the range of 0 to 50 mol% (with respect to the initial fuel amount). With this study, they showed that hydrogen addition increased LBV for all the examined binary flammable mixtures. The fraction of added hydrogen affects LBV linearly at moderate hydrogen fractions. However, this impact becomes stronger at higher hydrogen fractions. This study shows that hydrogen addition can significantly change the thermal diffusivity of flammable CH₄–air or natural gas/air mixtures, the rate of heat release, and the concentration of active radical species in the flame front, thus contributing to LBV variation. The findings from this work contribute to the existing data pool for flame propagation in hydrogen-blended CH₄/air and natural gas/air mixtures.

Considering the fact that the multiple-injection strategy could potentially be the solution to reduce engine exhaust gas emissions, Seol et al. [3] investigated the combustion process and emission characteristics inside the cylinder of a two-stroke marine main engine equipped on a university's training ship. In this work, the authors used the simulation

Citation: Ayoobi, M.; Resende, P.R.; Afonso, A.M. Numerical Investigations of Combustion—An Overview. *Energies* **2022**, *15*, 2975. <https://doi.org/10.3390/en15092975>

Received: 8 April 2022

Accepted: 13 April 2022

Published: 19 April 2022

Publisher's Note: MDPI stays neutral with regard to jurisdictional claims in published maps and institutional affiliations.



Copyright: © 2022 by the authors. Licensee MDPI, Basel, Switzerland. This article is an open access article distributed under the terms and conditions of the Creative Commons Attribution (CC BY) license (<https://creativecommons.org/licenses/by/4.0/>).

software ANSYS Fluent 2019R2 to perform 3D simulations and capture the combustion process and emission formation inside the engine cylinder. In these simulations, they considered two operating modes of the engine—single-injection mode and double-injection mode—and analyzed the in-cylinder pressure, temperature, and emission characteristics. The results from this work showed that using double-injection mode reduces the in-cylinder pressure and temperature peaks by 6.42% and 12.76%. NO and soot emissions were also reduced up to 24.16% and 68%, respectively, in the double-injection mode in comparison with the single-injection mode. However, CO₂ emission and ISFOC were increased by 7.58% and 23.55%, respectively, in the double-injection mode. Both positive and negative effects of the double-injection strategy on the engine should be taken into consideration by the operators.

Bialecki et al. [4] verified a reactivity model to compare the combustion process of different alternative fuels in turbine engines. For this research, they used synthetic blending components from alcohol to jet and hydro-processed esters and fatty-acid technologies and their blends with conventional jet fuel. Using laboratory tests (bench tests were carried out on a test rig with a miniature turbojet engine) to understand the differences between the properties of the tested fuels and record the carbon oxide concentrations in the exhaust gas, they were able to form empirical power functions and describe the relations between carbon oxide concentration and fuel mass flow rate. These formulations suggested that the combustion mechanism of the fuel with the blend of Jet A-1 and hydro-processed esters and fatty acids is different from that of the fuel that contains an alcohol or jet synthetic component.

Payri et al. [5] conducted research towards modeling the fuel injection process to characterize the in-cylinder mixture formation and subsequent combustion process in modern direct-injection gasoline engines. In particular, these modeling efforts are important to understand flash boiling, which usually occurs when the fuel is injected into an ambient pressure below the saturation pressure of the liquid and is characterized by fast breakup and evaporation rates. Flash boiling could potentially lead to undesired behaviors such as spray collapse and affect the mixture preparation negatively. In particular, the work by Payri et al. developed a comprehensive spray model that was validated for the Spray G baseline condition (G1) and extended to cold flash-boiling conditions. First, this model was implemented for iso-octane and then extended to n-hexane, n-heptane, and n-pentane. The extension of the model to different fuels was a novel approach and enabled the assessment of fuel properties on spray morphology under flash-boiling conditions.

Mitu et al. [6] conducted rigorous experimental measurements in a spherical combustion bomb to investigate the combustion characteristics of N₂-diluted CH₄-N₂O mixtures with a stoichiometric equivalence ratio at several initial pressures (0.5–1.75 bar) and initial ambient temperatures. The methodology employed in this study is based on the cubic law of the pressure rise during the early (incipient) period of flame propagation. Their results include the burnt mass fractions and flame radii at various moments of flame propagation in the course of the incipient stage, while reporting the cubic law coefficients and corresponding laminar burning velocities of the selected time interval. The findings from this work contribute to safety enhancement in industrial facilities that handle and store nitrous oxide while expanding the combustion database for fuel-N₂O flames. Furthermore, such investigations of hydrocarbon–nitrous oxide combustion can provide valuable information on the fundamental chemical kinetics relevant to complex oxidation systems involving nitrogen and help address prediction-, prevention-, and protection-related concerns.

To address the increasing demand for clean and green energy, researchers have been investigating potential fuels with low emissions, such as synthetic gas (syngas), especially at microscales. Combustion in microscale systems presents even more complexity, and it is important to describe syngas combustion and comprehend its properties at such scales. In this direction, Pokharel et al. [7] studied premixed syngas combustion in a two-dimensional channel, with a length of 20 mm and a half-width of 1 mm, using computational approaches. They used a fixed temperature gradient at the upper wall to account for the conjugate

heat transfer through the walls. Using the San Diego mechanism involving 46 species and 235 reactions, stoichiometric premixed syngas combustion with various compositions of carbon monoxide, methane, and hydrogen, over a range of inlet velocities was simulated. Simulation results were used to define different metrics and analyze various combustion phenomena, such as ignition, flame stabilization, and flames with repeated extinction and ignition. The flame stability and ignition time were found to correlate with the inlet velocity for a given syngas mixture composition. Similarly, for a given inlet velocity, the correlation of the flame properties with respect to the syngas composition was further scrutinized. Since syngas is generated from a variety of different sources and methodologies, it can consist of different species of a wide range of concentrations. Therefore, the findings of this work are critically important in selecting the appropriate composition of syngas depending on the application.

Grimm et al. [8] investigated an atmospheric prototype burner, designed for operation in a hybrid power plant, both numerically and experimentally, to examine its capabilities. With the help of a solid oxide fuel cell (SOFC) mounted upstream of the burner in the gas turbine system, a potentially large operational flexibility and efficiency can be achieved. Operating the burner with the SOFC off-gas, heat-loss mechanisms are in the order of magnitude of the thermal power output. Therefore, the combustor requires careful design considerations, which can be addressed using the multiple computational fluid dynamics (CFD) modeling strategies utilized in this study. The findings from this work show that the presented combustor system enables low-calorific combustion over a large range of operation conditions, despite major heat-loss effects, and results in low NO_x emissions.

Quintino et al. [9] conducted one-dimensional numerical simulations for three base biogas blends (BG100, BG90, and BG80) with different equivalence ratios (0.8 to 1.0) and hydrogen contents in the fuel mixture (up to 50% in volume). The results from these simulations were used to study the impact of H₂ enrichment on the laminar flame speed (SL) of lean biogas/air flames and develop an analytical correlation to model SL to extend the application range of the existing equations in the literature. Analyzing the impacts of thermal diffusive, dilution, and chemical effects of CO₂ and H₂ on SL at ambient pressure and temperature, they proposed a correlation that was in good agreement with the data from the literature and simulations. By isolating the contributions of CO₂ and H₂ in independent variables, the proposed equation in this work can be directly used to estimate SL without the need for a priori adaptations of fit parameters.

Jadidi et al. [10] proposed a novel approach to predict soot emissions at low computational costs using artificial neural networks (ANN). While soot formation in combustion systems is a major concern due to its adverse environmental and health effects, most industrial device simulations still neglect or simply approximate soot formation to avoid the complexity of this phenomenon and/or reduce computational costs (processing hardware and time). It is therefore essential to develop accurate, easy-to-use, and computationally inexpensive methodologies to accurately estimate soot concentrations. The authors of this article built and trained an ANN using data from the CoFlame code [11]. This ANN can work as a post-processing tool to estimate the soot volume fraction numerically with a low computational cost at various conditions, while it only needs properties from the gas-phase conservation equations (mass, momentum, energy, and species mass fractions) as inputs. It is noted that the authors have addressed the issues of dimensionality that were observed previously in the library-based soot-estimator models, which can potentially extend the concept of the soot estimator to transient and turbulent flames. The accuracy of the proposed methodology can be improved by using more accurate CFD simulations to generate more quality data and better train the network and minimize the error propagation effect. This work is one of the first attempts (if not the first) to train artificial neural networks based on detailed modeling of soot formation.

The article published by Adebisi et al. [12] revolves around the flame behavior and its propagation regimes. Specifically, they quantified the morphology and dynamics of a premixed flame propagating through a comb-shaped array of obstacles in open channels of

various blockage ratios with fuel mixtures of various thermal-expansion ratios. This work was conducted using computational simulations of the reacting flow described by transport properties, a fully compressible hydrodynamics, and Arrhenius chemical kinetics. They observed that in relatively wider channels, it is more likely for the flame to experience more than one propagation regime. Post-processing the simulation results, the authors identified three main stages of flame propagation in a fully open obstructed pipe, namely: (i) quasi-steady propagation, (ii) exponential flame acceleration, and (iii) saturation of the burning velocity. The accelerating phase was found to be exponential in nature and consistent of the theoretical prediction from the literature. The quasi-steady propagation stage fits the regime of flame oscillations for the low-Reynolds-number flames. In the stage of saturation burning velocity, the growing flame velocity saturates when approaching the speed of sound. The authors determined that the blockage ratio is the main parameter that influences the final saturated flame tip velocity. The authors also employed machine learning with the logistic regression algorithm to characterize and differentiate the parametric domains of accelerating and non-accelerating flames.

Hu et al. [13] conducted a numerical investigation to help determine the required quality of inert gas agents in fire suppression systems. This work is significantly important regarding health and safety concerns associated with active chemicals because inert gas agents have the potential to be widely used in fire suppression systems. In this study, the authors developed the general expressions between oxygen concentration, the discharge rate of inert gas agents, and the ventilation rate of the air–agent mixture. These expressions can help to minimize the hypoxic effects in an occupied area when accurately controlling the discharge quantity of inert gas agents to dilute the oxygen concentration. They then used the Fire Dynamic Simulator to model the dilution and fire-extinguishing efficiencies of inert gas agents when discharging inert gas agents into an enclosure was modeled. Using simulation results, they showed that the average oxygen mass fraction approximately reaches the design level at the end of the discharge period. The findings from this work indicate that the ventilation systems not only play an important role in mitigating the risk of over-pressurizing the released inert gas agents but also help to reduce the required quantity of inert gas agents.

Author Contributions: Conceptualization, M.A., P.R.R. and A.M.A.; methodology, M.A., P.R.R. and A.M.A.; investigation, M.A., P.R.R. and A.M.A.; writing—original draft preparation, M.A.; writing—review and editing, M.A., P.R.R. and A.M.A.; funding acquisition, M.A., P.R.R. and A.M.A. All authors have read and agreed to the published version of the manuscript.

Funding: This research received no external funding.

Conflicts of Interest: The authors declare no conflict of interest.

References

1. Resende, P.R.; Morais, L.C.; Pinho, C.; Afonso, A.M. Combustion Characteristics of Premixed Hydrogen/Air in an Undulate Microchannel. *Energies* **2022**, *15*, 626. [[CrossRef](#)]
2. Mitu, M.; Razus, D.; Schroeder, V. Laminar Burning Velocities of Hydrogen-Blended Methane–Air and Natural Gas–Air Mixtures, Calculated from the Early Stage of $p(t)$ Records in a Spherical Vessel. *Energies* **2021**, *14*, 7556. [[CrossRef](#)]
3. Seol, J.-H.; Pham, V.C.; Lee, W.-J. Effects of the Multiple Injection Strategy on Combustion and Emission Characteristics of a Two-Stroke Marine Engine. *Energies* **2021**, *14*, 6821. [[CrossRef](#)]
4. Białecki, T.; Dziegielewski, W.; Kowalski, M.; Kulczycki, A. Reactivity Model as a Tool to Compare the Combustion Process in Aviation Turbine Engines Powered by Synthetic Fuels. *Energies* **2021**, *14*, 6302. [[CrossRef](#)]
5. Payri, R.; Marti-Aldaravi, P.; Abboud, R.; Bautista, A. Numerical Analysis of GDI Flash Boiling Sprays Using Different Fuels. *Energies* **2021**, *14*, 5925. [[CrossRef](#)]
6. Mitu, M.; Movileanu, C.; Giurcan, V. Deflagration Characteristics of N_2 -Diluted CH_4 - N_2O Mixtures in the Course of the Incipient Stage of Flame Propagation. *Energies* **2021**, *14*, 5918. [[CrossRef](#)]
7. Pokharel, S.; Ayoobi, M.; Akkerman, V. Computational Analysis of Premixed Syngas/Air Combustion in Micro-channels: Impacts of Flow Rate and Fuel Composition. *Energies* **2021**, *14*, 4190. [[CrossRef](#)]
8. Grimm, F.; Lingstädt, T.; Kutne, P.; Aigner, M. Numerical and Experimental Study of a Jet-and-Recirculation Stabilized Low Calorific Combustor for a Hybrid Power Plant. *Energies* **2021**, *14*, 537. [[CrossRef](#)]

9. Quintino, F.M.; Fernandes, E.C. Numerical Investigation of the Impact of H₂ Enrichment on Lean Biogas/Air Flames: An Analytical Modelling Approach. *Energies* **2021**, *14*, 369. [[CrossRef](#)]
10. Jadidi, M.; Kostic, S.; Zimmer, L.; Dworkin, S.B. An Artificial Neural Network for the Low-Cost Prediction of Soot Emissions. *Energies* **2020**, *13*, 4787. [[CrossRef](#)]
11. Mueller, M.E.; Pitsch, H. Large eddy simulation of soot evolution in an aircraft combustor. *Phys. Fluids* **2013**, *25*, 110812. [[CrossRef](#)]
12. Adebisi, A.; Abidakun, O.; Akkerman, V. Acceleration of Premixed Flames in Obstructed Pipes with Both Extremes Open. *Energies* **2020**, *13*, 4094. [[CrossRef](#)]
13. Hu, X.; Kraaijeveld, A.; Log, T. Numerical Investigation of the Required Quantity of Inert Gas Agents in Fire Suppression Systems. *Energies* **2020**, *13*, 2536. [[CrossRef](#)]

Article

Combustion Characteristics of Premixed Hydrogen/Air in an Undulate Microchannel

Pedro R. Resende ^{1,2}, Leandro C. Morais ³, Carlos Pinho ² and Alexandre M. Afonso ^{2,*}

¹ proMetheus, Escola Superior de Tecnologia e Gestão, Instituto Politécnico de Viana do Castelo, 4900-347 Viana do Castelo, Portugal; pedroresende@estg.ipv.pt

² CEFT, Department of Mechanical Engineering, University of Porto, 4200-465 Porto, Portugal; ctp@fe.up.pt

³ Institute of Science and Technology, São Paulo State University (Unesp), Sorocaba 18087-180, Brazil; leandro.cardoso@unesp.br

* Correspondence: aafonso@fe.up.pt

Abstract: This work reports a numerical investigation of microcombustion in an undulate microchannel, using premixed hydrogen and air to understand the effect of the burner design on the flame in order to obtain stability of the flame. The simulations were performed for a fixed equivalence ratio and a hyperbolic temperature profile imposed at the microchannel walls in order to mimic the heat external losses occurred in experimental setups. Due to the complexity of the flow dynamics combined with the combustion behavior, the present study focuses on understanding the effect of the fuel inlet rate on the flame characteristics, keeping other parameters constant. The results presented stable flame structure regardless of the inlet velocity for this type of design, meaning that a significant reduction in the heat flux losses through the walls occurred, allowing the design of new simpler systems. The increase in inlet velocity increased the flame extension, with the flame being stretched along the microchannel. For higher velocities, flame separation was observed, with two detected different combustion zones, and the temperature profiles along the burner centerline presented a non-monotonic decrease due to the dynamics of the vortices observed in the convex regions of the undulated geometry walls. The geometry effects on the flame structure, flow field, thermal evolution and species distribution for different inlet velocities are reported and discussed.

Keywords: numerical study; microcombustion; hydrogen; complex geometry

Citation: Resende, P.R.; Morais, L.C.; Pinho, C.; Afonso, A.M. Combustion Characteristics of Premixed Hydrogen/Air in an Undulate Microchannel. *Energies* **2022**, *15*, 626. <https://doi.org/10.3390/en15020626>

Academic Editors: Alexandre M. Afonso, Pedro Resende, Mohsen Ayoobi and Dimitrios Katsaprakakis

Received: 14 October 2021
Accepted: 1 January 2022
Published: 17 January 2022

Publisher's Note: MDPI stays neutral with regard to jurisdictional claims in published maps and institutional affiliations.



Copyright: © 2022 by the authors. Licensee MDPI, Basel, Switzerland. This article is an open access article distributed under the terms and conditions of the Creative Commons Attribution (CC BY) license (<https://creativecommons.org/licenses/by/4.0/>).

1. Introduction

The technology advances in the last years allowed the development of integrated system devices at microscale, including both electro and mechanical components designated by MEMS (Micro Electro-Mechanical Systems) [1]. This type of system needs external power supply and, given the typical battery limitations, efforts have been made to develop alternatives based on microcombustion in order to take advantage of the high-density energy of the hydrocarbon and hydrogen fuels. Nevertheless, early experimental studies involving microcombustion presented some difficulties to obtain a stable flame caused mainly by two phenomena: the low residence time inside of the microcombustor to complete combustion and the higher heat losses from the combustion chamber walls [2,3].

In order to better understand the microcombustion dynamics and overcome some of the referred limitations, several numeric studies were carried out to obtain more detailed information. Raimondeau et al. [4] presented a numerical study on flammability limitations that relied on simple models to analyze the radical and thermal effects in the flame quenching using a methane/air mixture. They established that both effects were caused by the wall, the thermal quenching resulted from the high heat losses through the combustor walls, leading to a situation where the auto-sustainable combustion is no longer possible, and the radical quenching was due to a deficit homogeneous chemistry caused by the radicals absorption at the wall and their subsequent recombination. This establishes the importance of a good choice of the wall properties to achieve a stable flame. For this

reason, Norton and Vlachos [5] performed a numerical study to analyze the impact of different combinations of the wall thermal conductivity and thickness in the external heat losses, also changing the dimensions of the combustion chamber and operation conditions. Their study allowed to define the optimal values of terms of wall thermal conductivity, dimensions and flow velocity to obtain an auto-sustainable methane/air mixture flame.

In sequence, Norton and Vlachos [6] performed a similar study using a propane and air mixture, obtaining similar conclusions for the scale reduction to micro. However, the range of thermal conductivity to be used for a stable combustion is higher due to lower ignition temperature of the propane. In an attempt to improve the thermal efficiency, Federici and Vlachos [7] simulated a propane and air mixture combustion inside of a simple channel reactor with and without recirculation to analyze the flame stability. They reported that the flame is more susceptible to extinction at the limits of highly conductive inner walls or lower fuel inlet velocities, obtaining the same stability effect in both situations. In addition, in the case of low-conductivity walls or high inlet velocities, the system became more stable with the presence of the recirculation due to the heat transferred to the cool reactants provided by the recirculation gases through the outer wall, causing ignition and flame stabilization. Federici et al. [8] continued their work by experimentally and numerically studying the flame stabilization on catalytic microburners with and without recirculation using the same fuel. At the limits of highly conductive walls, they achieved the same stabilization effect in both geometries, but for low conductivity walls, the microburner with recirculation became more effective when compared with the single channel due to the lower capacity to preheat the cool reactants.

To further understand the external heat losses impact in the combustion due to material properties of the combustor chamber walls, Li et al. [9,10] numerically studied the effect of different physical and boundary conditions on the flame temperature for H_2 and CH_4 microscale mixture combustion using stainless steel walls. They simulated both gas and solid phases and highlighted the importance of the reactants preheating through the axial heat conduction of the chamber walls to obtain a stable flame, suggesting the use of geometries with recirculation. These types of studies consisted essentially of 2D geometries, so to analyze the 3D effect, Pizza et al. [11] simulated a premixed hydrogen/air flame in a 3D microtube with different diameters and velocities, and they were able to observe three axisymmetric combustion modes by varying the inlet velocity: steady mild combustion, oscillatory ignition/extinction, typically known as FREI (flame with repetitive extinction-ignition), and steady flames. The FREI phenomenon was also reported in their previous work [12]. For higher diameter, the combustion dynamics became more complex, presenting a steady non-axisymmetric flame and a spinning flame which rotated azimuthally. They reported the existence of a critical tube diameter for the transition combustion modes. Later, Aikun et al. [13] simulated the combustion in a 3D rectangular microchannel using a hydrogen/air mixture and analyzed the impact on the flame in terms of flame temperature and length for different wall material, channel height and the inlet velocity. The temperature field showed three distinct regions, the preheating, the combustion and the cooling region, with the flame anchoring near the entrance in a cone-shaped structure. For the tested velocity range, the flame remained stable even in the limited cases, without extinction. In addition, in relation to wall materials, they reported that, in case of lower heat conductivity, the wall temperature becomes more intense, which could lead to thermal stress fracture. However, on the opposite side, with higher heat conductivity, the external heat losses increase, leading to a decrease in the reaction and probably to the extinction of the flame.

In order to improve the combustion efficiency, Pan et al. [14] studied a hydrogen/oxygen premixed combustion in microporous media combustor to achieve higher conversion efficiency of a micro thermophotovoltaic system and concluded that it is possible to obtain a more intense combustion with porous media materials with low specific heat and high thermal conductivity. By using a different fuel, Yan et al. [15] analyzed the geometrical parameters on CH_4 /air premixed combustion in a 3D heat recirculation micro-combustor with baffles. Recently, Peng et al. [16] investigated the combustion and thermal performance enhancement of a nozzle inlet microtube using hydrogen/air. Moreover,

Resende et al. [17,18] studied the impacts of N_2 dilution on a premixed H_2 /air combustion in terms of flame structure and pollutant emissions, NO_x , for a large range of equivalence ratios and dilution amounts. More recently, other numerical studies were performed to understand the geometrical effects on the microcombustion phenomenon. Li et al. [19] numerically investigated the behavior of a H_2 /air blend in a microcombustion chamber with cavities and found that these cavities can also expand the working range of the inlet velocity. Abbaspour and Alipoor [20] investigated the combustion characteristics of hydrogen/air premixed mixture in 1 mm converging–diverging microtubes with heated walls. Chabane et al. [21] performed a numerical study of catalytic combustion in a meso-scale channel with non-planar walls by exploring four different wall configurations and combining either obstacles or cavities and a continuous or segmented Pt-coating. Zuo et al. [22] developed a ribbed micro-cylindrical combustor, and performed a study with micro-cylindrical reduced wall thickness [23,24] and an elliptical cross-section microcombustor [25].

The present work numerically investigates the combustion characteristics in a complex geometry of one undulate microchannel using a H_2 and air mixture. The objective is to verify if the flammability at microscales can be improved by designing non-straight microchannels as an alternative to the burner with recirculation of reaction products. The effect of the geometry on the combustion characteristics is analyzed by varying the inlet velocity but keeping the same boundary conditions, equivalence ratio and external heat flux losses. In the methodology section, the fundamental governing equations that describe the physics of this work are presented, followed by the computational domain section, which provides detailed information regarding the specific problem addressed in this study. In the results section, the main findings of this study are presented and discussed in detail and, finally, the paper is concluded by summarizing the main achievements of this work.

2. Methodology

The governing equations used in the simulations to describe the microcombustion phenomenon are the conservation equations of total mass, momentum, species mass fractions and energy, for a compressible, continuous, multi-component and thermally perfect gas mixture, considered as Newtonian fluid, in a laminar flow, and can be expressed as :

$$\frac{\partial \rho}{\partial t} + \nabla(\rho \mathbf{u}) = 0 \quad (1)$$

$$\rho \left[\frac{\partial \mathbf{u}}{\partial t} + \nabla \cdot \mathbf{u} \mathbf{u} \right] = -\nabla p + \nabla \tau + \rho \mathbf{g} \quad (2)$$

$$\frac{\partial}{\partial t}(\rho Y_k) + \nabla(\rho Y_k \mathbf{u}) = -\nabla(\rho Y_k \mathbf{V}_k) + \dot{R}_k \quad k = 1, \dots, N_C \quad (3)$$

$$\rho C_p \frac{\partial T}{\partial t} + \rho C_p \mathbf{u} \nabla T = -\nabla \mathbf{q} - \rho \sum_{k=1}^{N_C} C_{p,k} Y_k \mathbf{V}_k - \sum_{k=1}^{N_C} h_k \dot{\Omega}_k \quad (4)$$

Here, \mathbf{u} , ρ , t , p , \mathbf{g} and $\boldsymbol{\sigma}$ represent the mixture velocity vector, the mixture density, time, the pressure, the acceleration vector due to gravity and the fluid stress tensor, respectively. N_C is the total number of species, T is the temperature, and $\dot{\Omega}_k$, \dot{R}_k , h_k , Y_k and \mathbf{V}_k are the net production rate of the k^{th} species, the formation rate, the enthalpy, the mass fraction and the diffusion velocity, respectively. \mathbf{q} the heat flux vector and C_p represents the specific heat coefficients. The gas mixture is assumed to be an ideal gas and its density is calculated through the equation of state.

The diffusion velocities of species k are calculated from Fick's law and the thermal diffusion effect:

$$\mathbf{V}_k = -\frac{D_k}{Y_k} \nabla Y_k - \frac{D_k \Theta_k}{X_k} \frac{1}{T} \nabla T \quad (5)$$

where X_k , D_k and Θ_k are the mole fraction, the mixture-averaged diffusion coefficient of species k and the thermal diffusion.

The heat flux vector, \mathbf{q} , is defined as:

$$\mathbf{q} = -\lambda \nabla T + \mathbf{q}_{rad} \quad (6)$$

where \mathbf{q}_{rad} is the radiative heat transfer and λ is the mixture thermal conductivity. However, some studies demonstrated that the radiative heat transfer could be neglected due to the smaller impact at microscale.

The radiative heat transfer can be modeled by assuming the optically thin radiation hypothesis in which self-absorption of radiation is neglected. The radiative heat transfer contribution in the energy equation is described as:

$$\nabla \mathbf{q}_{rad} = -4\sigma a_p (T^4 - T_{env}^4) \quad (7)$$

where σ is the Stefan–Boltzmann constant, T_{env} is the environment temperature and a_p is the Planck mean absorption coefficient.

The equations described above were implemented in the laminarSMOKE code by Cuoci et al. [26], according to the numerical procedure presented in Figure 1. A detailed kinetic mechanism consisted of 32 species and 173 reactions are used in this work to take the chemical reaction pathways of premixed hydrogen combustion into account [27]. This mechanism was developed and validated by CRECK Modelling Group in Polytechnic University of Milan, and more details can be found in [27]. The mathematical and physical models implemented in the laminarSMOKE were validated at microscale in previous studies of [17,18,28], and the results were able to capture the reaction pathways with good accuracy.

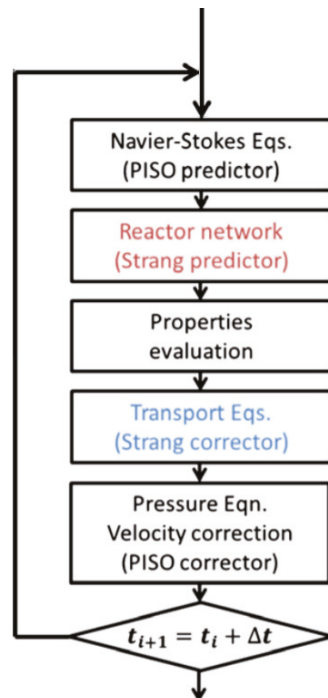


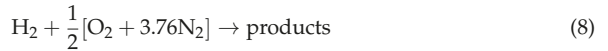
Figure 1. Numerical algorithm, adapted from Cuoci et al. [26].

3. Problem Description and Computational Domain

As reported previously, in order to verify if the flammability at microscales can be improved by designing non-straight microchannels, here we proposed an undulate symmetric microchannel burner, as represented in Figure 2a. The undulated microchannel

presents 10 mm length and minimum/maximum height of 0.30/1.28 mm in the center of the chamber, where the inlet and outlet keep the same height of 0.8 mm for 2 mm length.

For all simulations, the equivalence ratio and inlet temperature are the same, $\phi = 1.0$ and $T_{in} = 300$ K, respectively, at atmospheric pressure. The reaction composition of the H₂/air mixture for $\phi = 1.0$ is given by Equation (8). The remaining boundary conditions are represented in the schematic illustration of the case setup (Figure 2a).



In all simulations, the temperature profile at the wall remained constant during each simulation. A hyperbolic temperature profile was imposed at the burner walls in which the wall temperature increases from 300 K at the inlet to 1300 K at 2/10 of the channel length, remaining constant at 1300 K afterward. This temperature distribution profile is extensively used to mimic the experimental profiles and was used in several works [12,28–30].

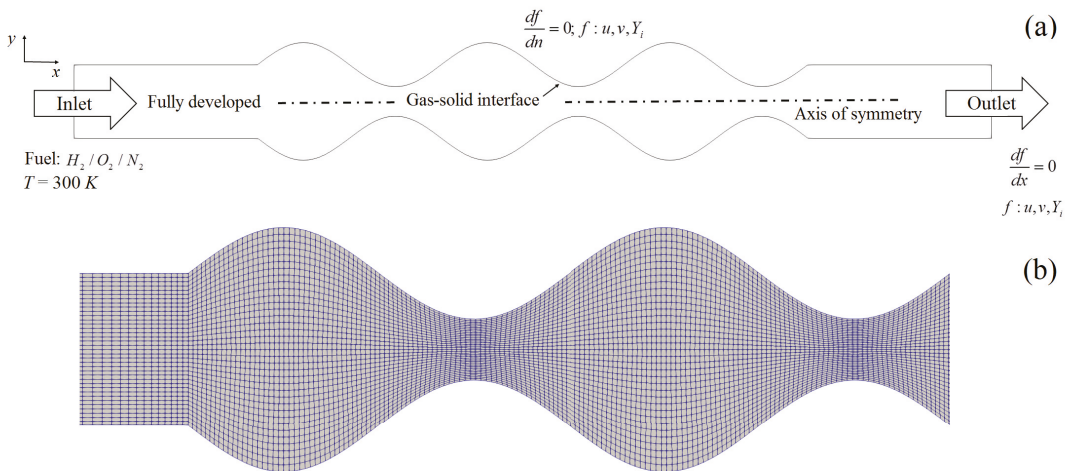


Figure 2. Schematic illustration of the (a) undulated geometry and (b) mesh resolution.

In order to verify the effect of the inlet velocity, U_{in} , on the flame structure, combustion dynamics and emissions, we performed a set of simulations for different inlet velocities, ranging from 4 to 22 m/s, as described in detail in Table 1.

Table 1. Summary of the simulated cases in this study.

Description	U_{in} (m/s)
C1	4
C2	8
C3	10
C4	14
C5	18
C6	22

Two distinct mesh resolutions were used in order to verify the independence of the results. The smaller computational domain comprises 10,836 total volume cells, with equidistant space cell in the center, resulting in a refinement of the smaller width zones (Figure 2b). The refined mesh has 21,672 total volume cells, similar to the mesh resolution

used in previous works while studying the effect of N_2 dilution on a H_2 and air combustion in a microchannel by Resende et al. [17,18]. Figure 3 presents the temperature profiles obtained with both computational domains using the conditions of case C1, Table 1, and it can be observed that the results presented a good agreement for both mesh resolutions.

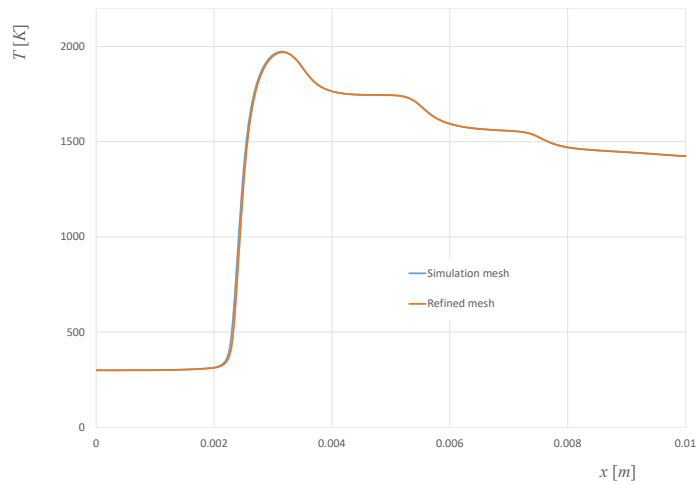


Figure 3. Temperature profile obtained in the mesh independence study using the conditions of case C1.

4. Results

In this section, the results for the flame dynamics, NO_x emissions, temperatures and heat release rates are discussed in detail for different inlet velocities. The dynamics of the flame structure are analyzed by comparing with other cases carried out in previous works. The comparison with experimental data is not possible due to the difficulty in measuring the combustion characteristics at this scale and because, to the authors' best knowledge, there are no experimental results for these and similar geometries.

The impact of the inlet velocity on the flame structure for the stable cases can be observed in Figure 4, presenting the contour maps of the heat release rate distribution Q and the streamlines of the flow field. Regardless of the inlet velocity, the flame becomes stable with the location of the maximum values of Q distribution, shifting downstream up to case C3, for $U_{in} = 10$ m/s. For higher inlet velocities, the heat release rate is divided into two different regions that are further stretched for higher inlet velocities. Another interesting observation is the effect of the vortices on the Q distribution for higher inlet velocities due to geometry of the burner that narrows the heat release into the middle of the burner, even in the convex zones.

Figure 5 presents the contour maps of the elevated temperature T^* which represents the temperature difference between the gas temperature (T) and the maximum wall temperature, defined here as $T^* = T - \max(T_{wall})$ (if $T < T_{wall,max}$, $T^* = 0$), allowing a better comprehension of the results by eliminating the wall temperature effects. The elevated temperature is higher for lower inlet velocity, for C1 case, located at the first contraction of the burner. As the inlet velocity increases, the flame is stretched downstream and the maximum T^* values decrease. For inlet velocities between 10 and 14 m/s, C3 and C4, the flame splits into the two first cavity regions at the burner entrance. For velocities above 18 m/s, cases C5 and C6, the flame is divided into the three cavity regions of the undulated microchannel.

Due to the detailed kinetic mechanism used in the simulations, it is possible to study the different species of the combustion reaction. Figure 6 presents the contour maps

of OH species. Here, the OH is used to identify the front of the flame. The OH mass fraction distribution shows the flame structure becoming more stretched as the inlet velocity increases with the maximum OH concentrations located more further downstream in the microcombustion chamber. For higher inlet velocities, above 14 m/s, case C4, there are two distinct OH concentrations regions, one at the entrance and the other downstream of the microchannel, with a reduction in the maximum OH value and the maximum flame temperature as the energy release becomes more dispersed. However, the energy dispersion, consequence of the Q stretching downstream (Figure 7), allows to maintain a higher flame temperature along the burner centerline, as observed in Figure 8.

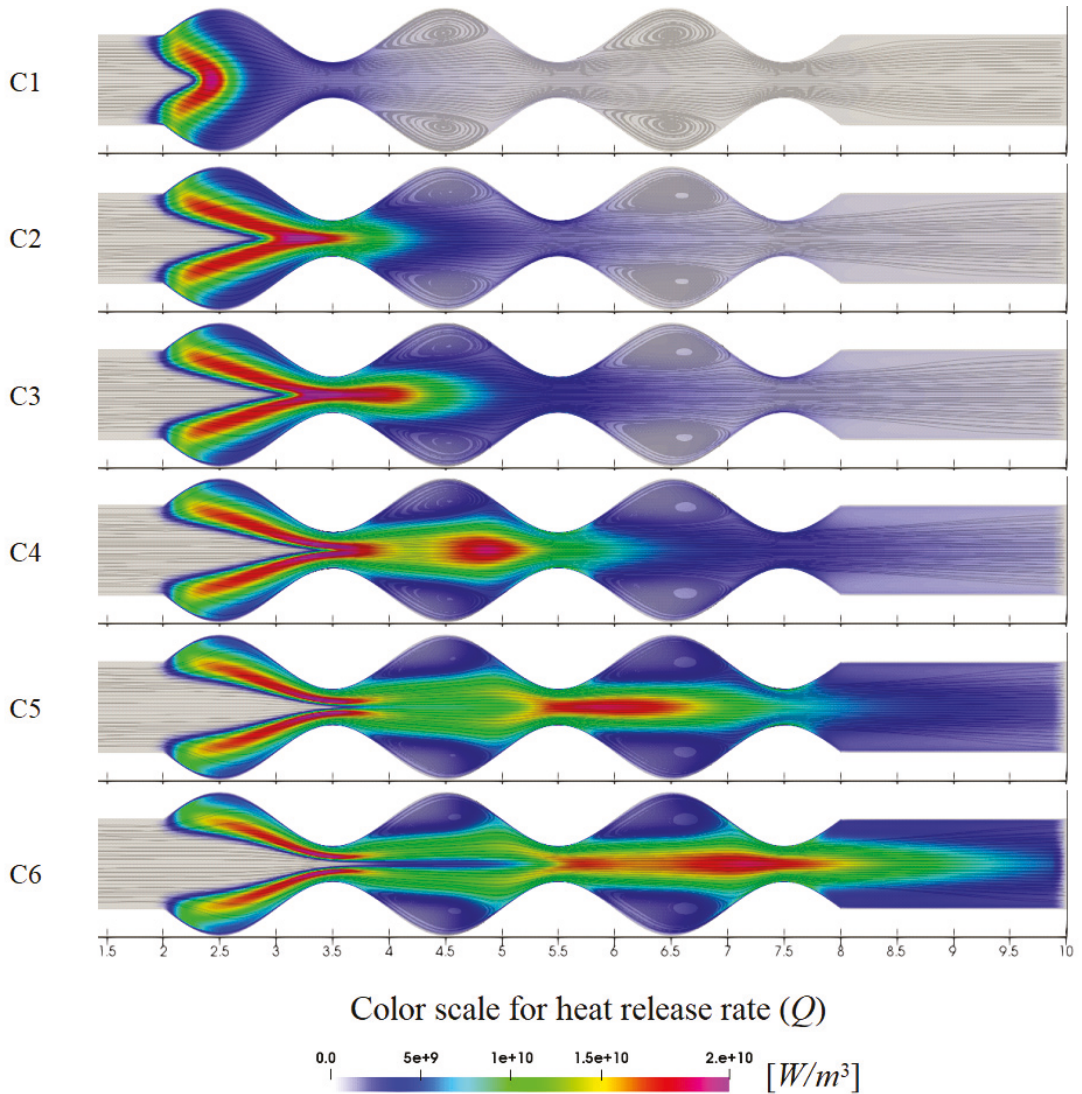


Figure 4. Contour maps for the streamlines superimposed on heat release rate distribution for different cases.

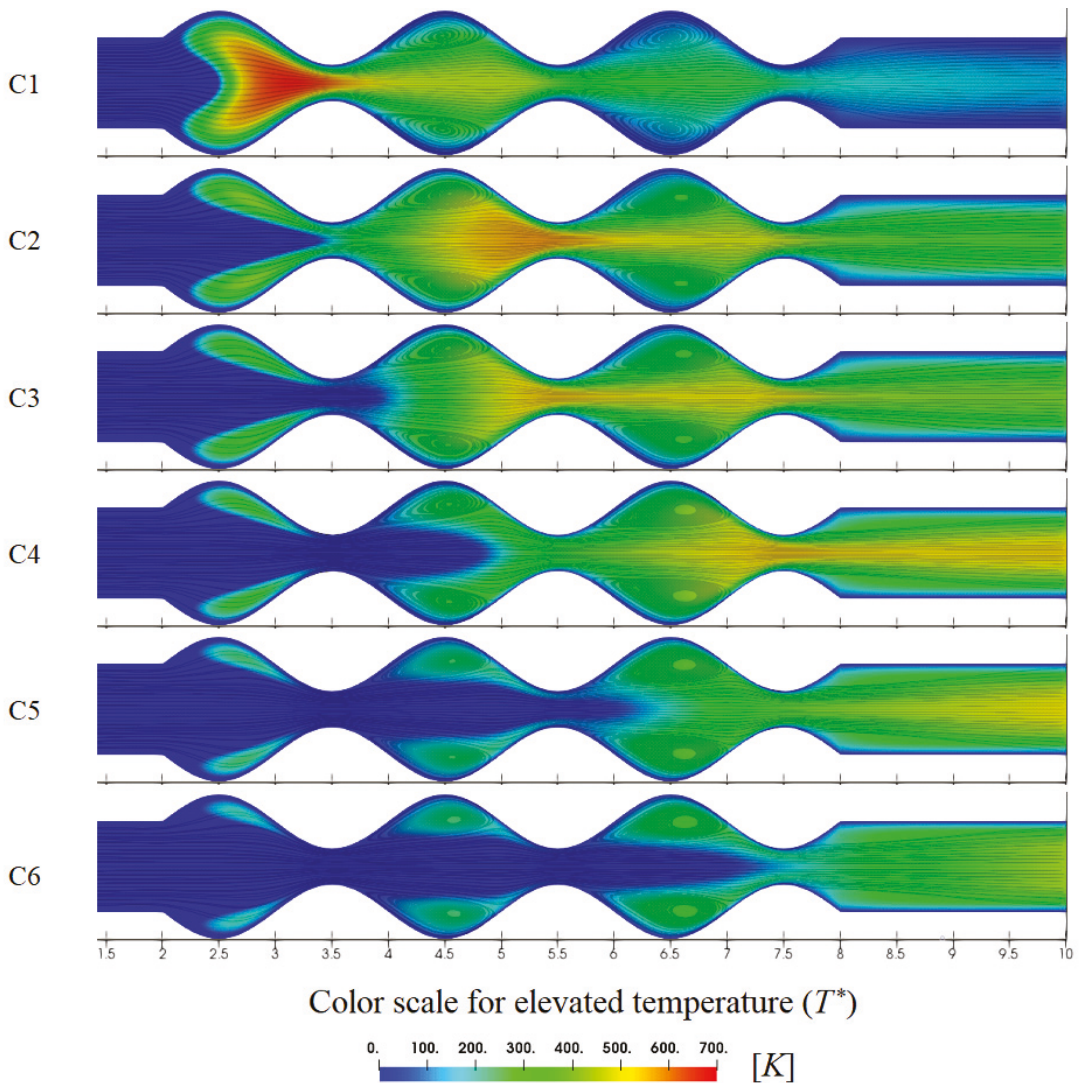


Figure 5. Contour maps for the streamlines superimposed on elevated temperature distribution for different cases.

Figure 7 presents heat release rate profiles along the centerline axis for different inlet velocities. For lower inlet velocity, cases C1 and C2, one can observe the typical profile observed in microchannel combustion with the heat release rate peak near the flame location, while the energy peak shifting downstream with the increase in the inlet velocity. Increasing the inlet flow rate for C3, the heat release profile presents a maximum value of Q , higher than the other cases, and non-monotonic decay is observed after the heat release peak. For the remaining cases, the Q profiles become broader due to the convective effect of the inlet velocity, and the non-monotonic behavior is more pronounced while the magnitude of the maximum values of Q remains similar to C1.

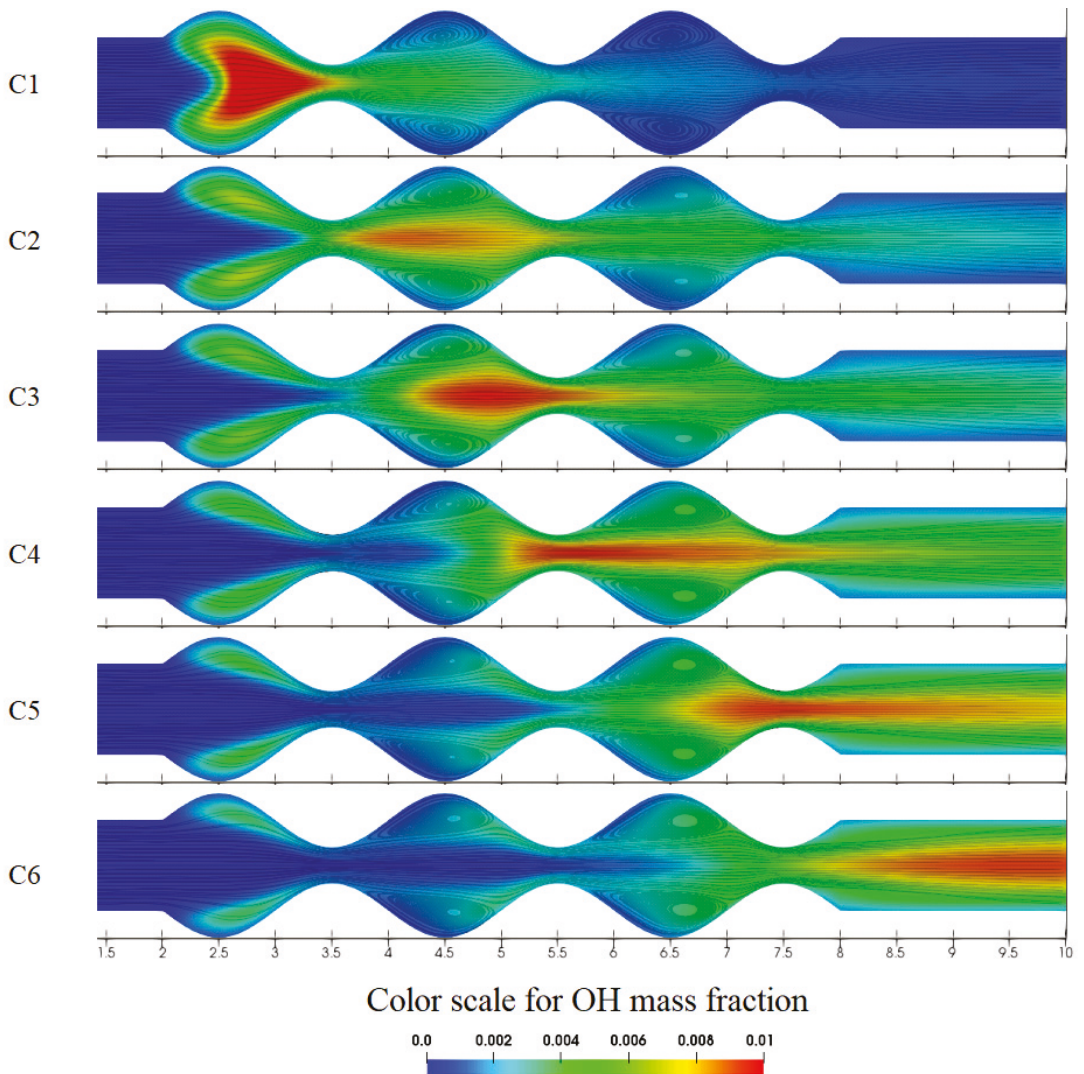


Figure 6. Contour maps for the streamlines superimposed on OH mass fraction distribution for different cases.

It should be noted that the increase in the maximum values of Q are not sufficient to increase the flame temperature, as can be observed in Figure 8, presenting the temperature profiles along the centerline axis for different inlet velocities. Figure 8 also presents the hyperbolic temperature profile imposed at the microburner walls. It can be observed that, as the inlet velocity increases, the loci of the maximum value for the temperature at the centerline shifts downstream in the microchannel. For the lower inlet velocity, case C1, it can be observed that the undulated walls of the microchannel impacts the temperature profile at the centerline, reflected in a stepping temperature profile along the microchannel.

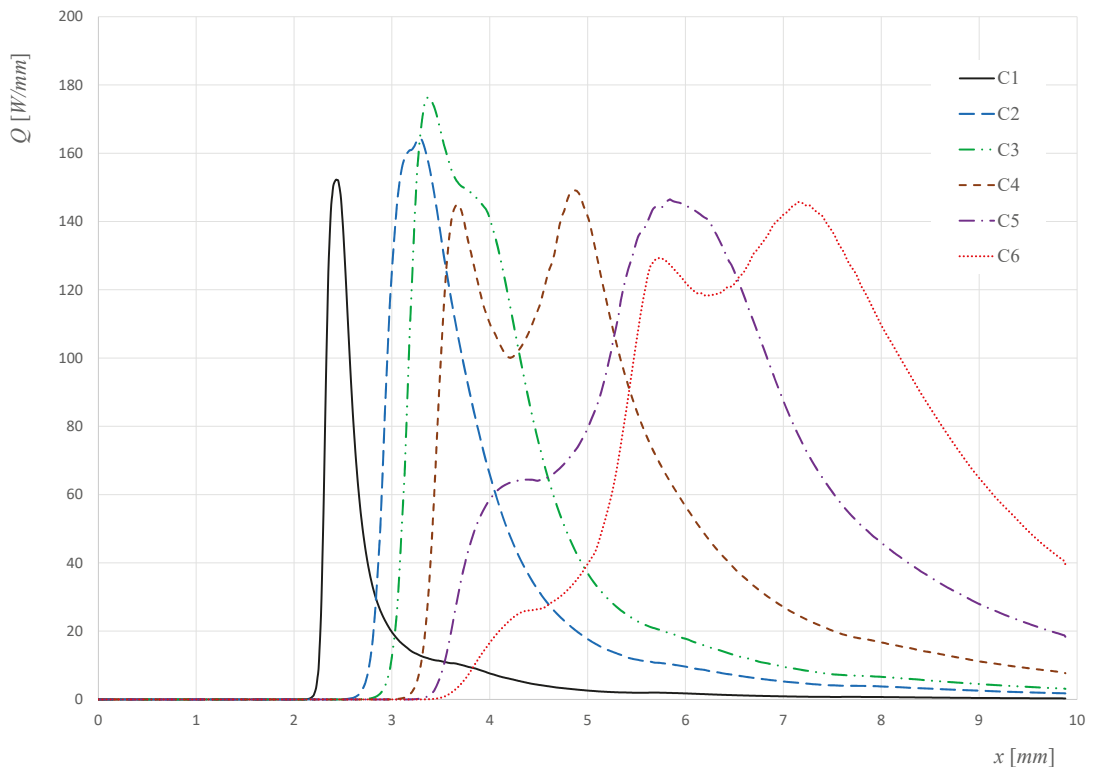


Figure 7. Heat release rate profiles along the centerline axis for different inlet velocities.

In order to better understand the effect of the geometric non-uniform microchannel walls, a new case was included, referred to as R1 in Figure 8, presenting the predictions of a premixed H_2 /air combustion in a uniform axisymmetric channel burner performed by Resende et al. [17], for the same boundary conditions of equivalence ratio, $\phi = 1.0$, and inlet velocity, 4 m/s, (equivalent to the case C1). Note that, in order to facilitate the comparison, the loci of the flame/temperature sharp increase for the uniform wall case, R1, was shifted to the respective loci of undulate microchannel, case C1, as can be verified in Figure 8.

Typically, in channel burners, the temperature reduction evolution along the centerline, after reaching the maximum value, is accomplished by a smooth variation, case R1, but here is made by steps caused by the heat losses through the walls. As the distance from the wall increases, there is a reduction in heat losses, consequence of the mass gas mixture/reaction products present between the flame and the wall, which acts as resistance to the heat flux and the temperature stabilizes. This effect can be visualized by the presence of the vortices for the case C1 at $x = 4.5$ and 6.5 mm, in Figure 5, and as the vortex becomes larger, the resistance to the heat flux increases and consequently causes the temperature stabilization. In other cases, the recirculation effect leads to a small reduction in temperature in the centerline after reaching the maximum flame temperature as, for example, cases C2 and C3. Comparing both cases at $x = 6.5$ mm, it is possible to visualize that the temperature reduction is smaller in case C3 when compared to C2. In the first, the temperature reduces to 1790 K and, in the second, to 1756 K, consequence of the vortex size at that location, where the vortex of C3 is higher than the C2 due to the higher inlet velocity of C3.

In addition, another phenomenon occurs before the flame, specially for highest inlet velocities, which could be considered as a pre-combustion effect caused by the stretching of the flame combined with the vortices size and the burner geometry, as mentioned before,

when referring to the presence of different structures of the heat release rate. This can be seen in Figure 8, through the linear temperature evolution along the chamber where, as the inlet velocity increases, the temperature increases more slowly and the maximum value is reached downstream of the channel.

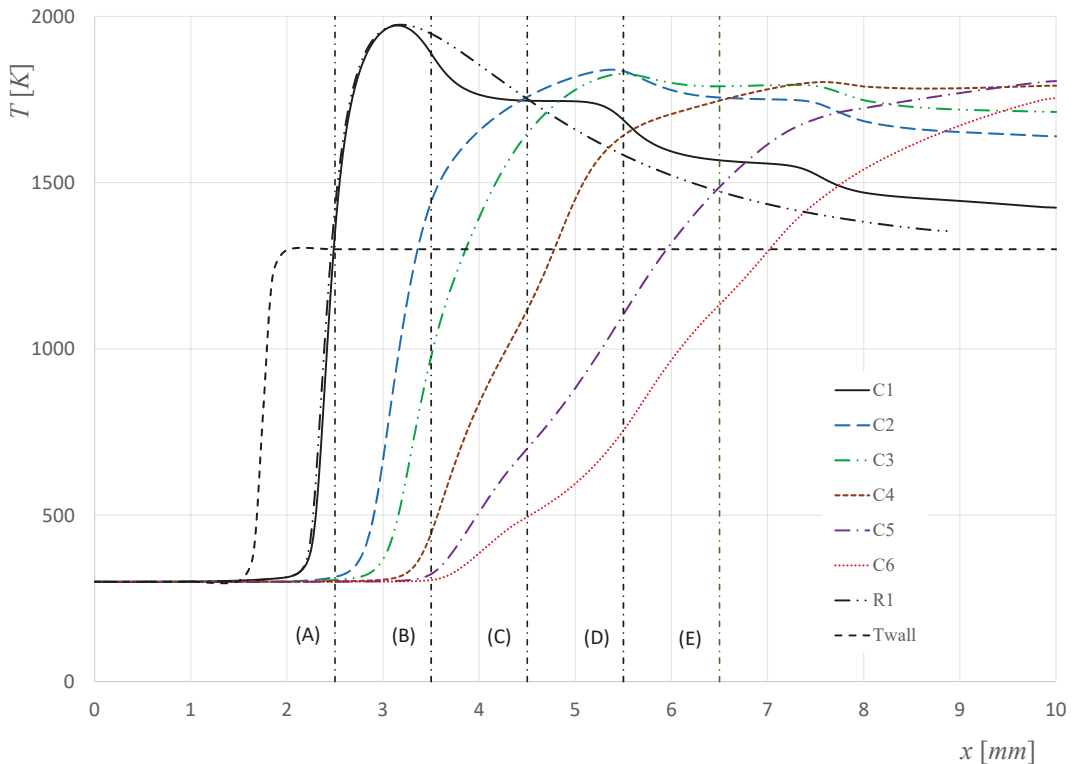


Figure 8. Temperature profiles along the centerline axis for different inlet velocities.

Figure 9 shows temperature profiles along the cross-sectional direction of the burner at several channel locations, $x = 2.5, 3.5, 4.5, 5.5$ and 6.5 mm, referred to in Figure 8 through the letters (A) to (E). These locations correspond to the consecutive middle of the convex and the contraction zones of the burner. Note that temperatures above the wall temperature represent a combustion reaction zone; therefore, it is possible to identify the extension of a single or separated flame.

For the case C1, for all locations across the burner, the temperatures are above T_{wall} , which means that the flame is continuous, starting with a V shape at the entrance of the burner and, after reaching the maximum temperature value at $x = 3.15$ mm, it decreases with the maximum values across the burner, occurring always in the center.

As the inlet velocity increases, the flames becomes weaker in the first convex zone (Figure 9A), while presenting a decrease in temperature. In all cases, the maximum flame temperature occurs at the center of the burner.

The mass fraction distribution of the main species for the C1 and R1 cases, along the centerline of the burner, can be visualized in Figure 10. To compare both cases, the referred location adjustment was performed, keeping the same flame front location for both cases. In the C1 case, the hydrogen and the oxygen are completely consumed, but in the R1 case, the H_2 fraction reduces in front of the flame and then increases. As a consequence, the N_2 and OH species are lower when compared with the C1 case. The mass fraction of water, H_2O

stabilizes at 0.25 for both cases; however, in the C1 case, it presents a shorter augmentation due to the effect of the velocity increase caused by the presence of the contraction.

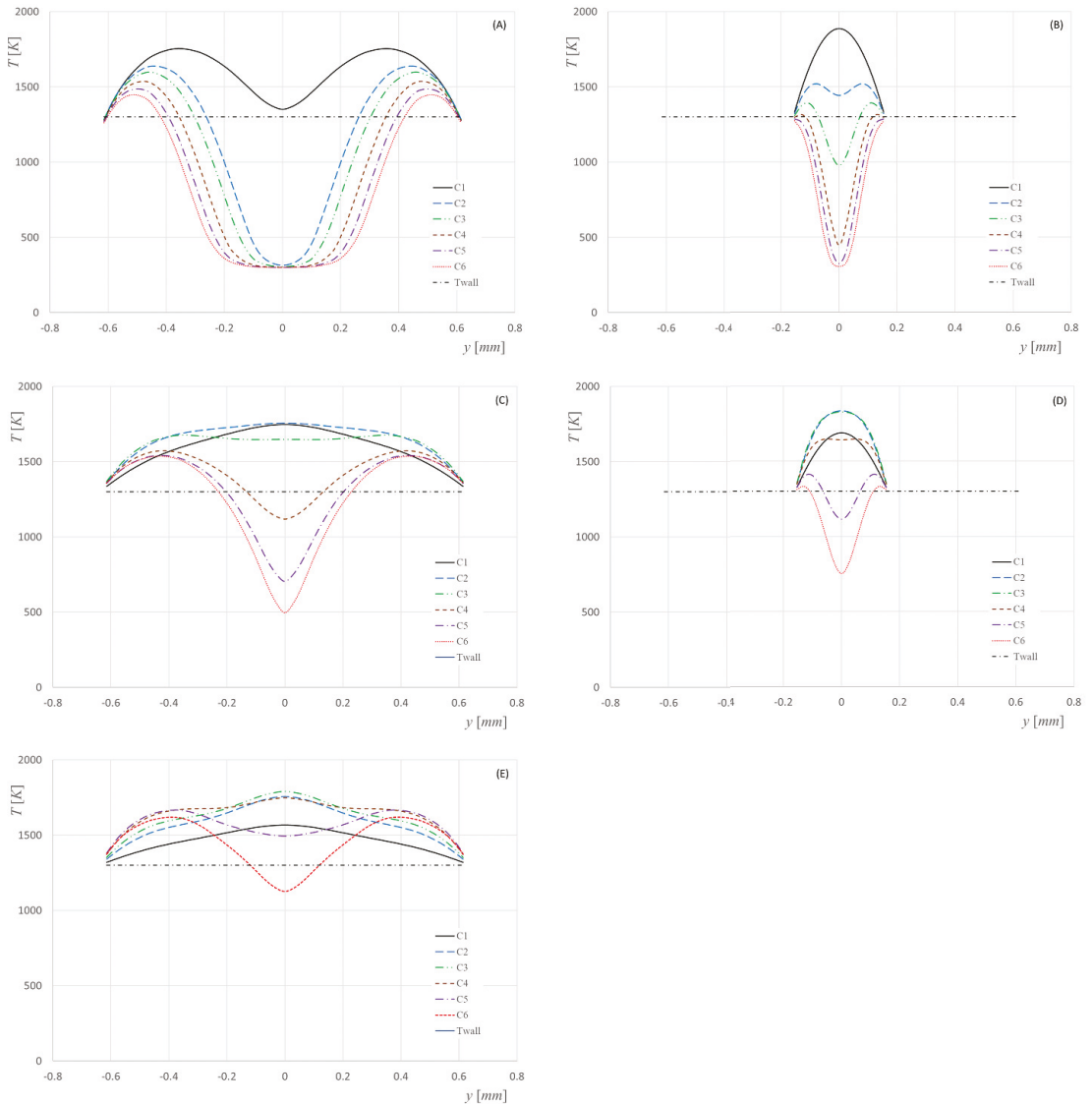


Figure 9. Temperature profiles across the burner for all cases. (A): $x = 2.5$ mm; (B): $x = 3.5$ mm; (C): $x = 4.5$ mm; (D): $x = 5.5$ mm; (E): $x = 6.5$ mm.

In terms of pollutant emissions, C1 presented a higher NO_x value of 4.25 ppm versus 3.32 ppm for case R1, due to the complete consumption of hydrogen in the combustion.

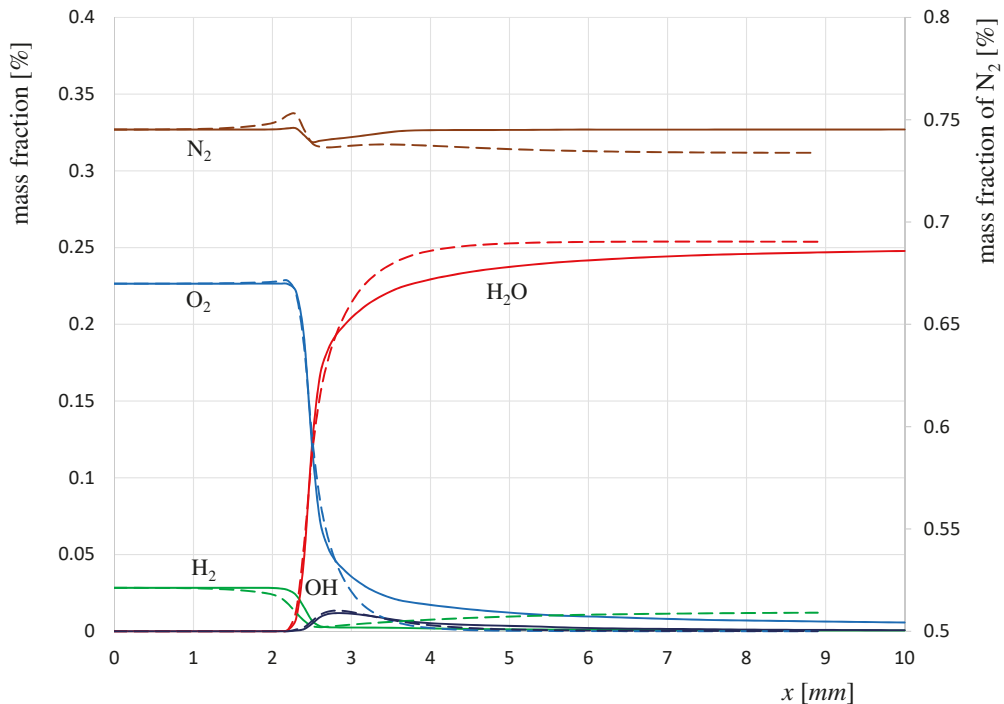


Figure 10. Comparison between the cases CH1 (continuum lines) and R1 (dashed lines) of the main species mass fractions in axial direction along the centerline.

5. Conclusions

A numerical study of a premixed H₂/air combustion in an undulated microchannel was performed to analyze the effects of geometry impact on the flame structure and dynamics using different inlet velocities, from 4 to 22 m/s, with an equivalence ratio of $\phi = 1.0$. In all the tested cases, a hyperbolic temperature profile at the wall was imposed to mimic the heat external losses occurred in experimental setups. Due to the non-linear geometry of the burner, the increase in the inlet velocity defines a flame that extends along the burner, and although the instabilities appear at velocities above 8 m/s for all cases, the flame stabilizes regardless of the inlet velocity. However, the flame is stretched and divided into two parts for velocities above 14 m/s. Here, the evolution of the temperature along the axis, after reaching the maximum value, decreases by steps, instead of a smooth variation as occurs with the typical combustion in a channel burner. This effect is caused by the mass gas of the mixture/reaction products present in the vortices located in the convex regions, which acts as a resistance to the flux of heat losses. The larger the vortex size is, the higher the resistance to the heat flux. This also imposes smaller temperature decreases along the axis, consequence of the flame stretch combined with the heat flux resistance. This reduction in heat transfer to the walls is quite important in the flame stability in microcombustion and allows the development of new geometries based on the undulate or other non-uniform shapes as an alternative to existing burners.

Author Contributions: Investigation, P.R.R.; Validation, L.C.M., C.P. and A.M.A.; Data curation, P.R.R.; Writing—original draft, P.R.R.; Writing—review and editing, L.C.M., C.P. and A.M.A.; supervision, A.M.A. All authors have read and agreed to the published version of the manuscript.

Funding: This research received external funding by FAPESP through Project No. 2015/26842-3. A.M. Afonso was supported by Project UID/EMS/00532/2019 of CEFT (Centro de Estudos de Fenómenos de Transporte) and through Project PTDC/EMS-ENE/3362/2014-funded by FEDER funds.

Data Availability Statement: The data will be made available at reasonable request from the corresponding author.

Acknowledgments: P. R. Resende acknowledges the funding by FAPESP through Project No. 2015/26842-3. A. M. Afonso acknowledges the FCT for financial support through Project UID/EMS/00532/2019 of CEFT (Centro de Estudos de Fenómenos de Transporte) and through Project PTDC/EMS-ENE/3362/2014-funded by FEDER funds through COMPETE2020-Programa Operacional Competitividade e Internacionalização (POCI) and by national funds through FCT-Fundação para a Ciência e a Tecnologia.

Conflicts of Interest: The authors declare no conflict of interest.

Nomenclature

a_p	Planck mean absorption coefficient
C_p	Specific heat coefficients
D_k	Mixture-averaged diffusion coefficient of species k
\mathbf{g}	Gravity acceleration vector
h_k	Enthalpy
N_C	Total number of species
p	Pressure
\mathbf{q}	Heat flux vector
\mathbf{q}_{rad}	Radiative heat transfer
\dot{R}_k	Formation rate
t	Time
T	Temperature
T_{env}	Environment temperature
\mathbf{u}	Mixture velocity vector
\mathbf{V}_k	Diffusion velocity
X_k	Mole fraction of species k
Y_k	Mass fraction
Θ_k	Thermal diffusion of species k
$\boldsymbol{\sigma}$	Fluid stress tensor
λ	Mixture thermal conductivity
ρ	Mixture density
σ	Stefan–Boltzmann constant
$\dot{\Omega}_k$	Net production rate of the k^{th} species

References

- Ju, Y.; Maruta, K. Microscale combustion: Technology development and fundamental research. *Prog. Energy Combust. Sci.* **2011**, *37*, 669–715. [[CrossRef](#)]
- Nakamura, Y.; Gao, J.; Matsuoka, T. Progress in small-scale combustion. *J. Therm. Sci. Technol.* **2017**, *12*, JTST0001. [[CrossRef](#)]
- Resende, P.R.; Ayooobi, M.; Afonso, A.M. Numerical Investigations of Micro-Scale Diffusion Combustion: A Brief Review. *Appl. Sci.* **2019**, *9*, 3356. [[CrossRef](#)]
- Raimondeau, S.; Norton, D.; Vlachos, D.G.; Masel, R.I. Modeling of high-temperature microburners. *Proc. Combust. Inst.* **2002**, *29*, 901–907. [[CrossRef](#)]
- Norton, D.G.; Vlachos, D.G. Combustion characteristics and flame stability at the microscale: A CFD study of premixed methane/air mixtures. *Chem. Eng. Sci.* **2003**, *58*, 4871–4882. [[CrossRef](#)]
- Norton, D.G.; Vlachos, D.G. A CFD study of propane/air microflame stability. *Combust. Flame* **2004**, *138*, 97–107. [[CrossRef](#)]
- Federici, J.A.; Vlachos, D.G. A computational fluid dynamics study of propane/air microflame stability in a heat recirculation reactor. *Combust. Flame* **2008**, *153*, 258–269. [[CrossRef](#)]
- Federici, J.A.; Wetzel, E.D.; Geil, B.R.; Vlachos, D.G. Single channel and heat recirculation catalytic microburners: An experimental and computational fluid dynamics study. *Proc. Combust. Inst.* **2009**, *32*, 3011–3018. [[CrossRef](#)]
- Li, J.; Chou, S.K.; Li, Z.W.; Yang, W.M. A comparative study of H₂-air premixed flame in micro combustors with different physical and boundary conditions. *Combust. Theory Model.* **2008**, *12*, 325–347. [[CrossRef](#)]
- Li, J.; Chou, S.K.; Yang, W.M.; Li, Z.W. A numerical study on premixed micro-combustion of CH₄-air mixture: Effects of combustor size, geometry and boundary conditions on flame temperature. *Chem. Eng. J.* **2009**, *150*, 213–222. [[CrossRef](#)]

11. Pizza, G.; Frouzakis, C.E.; Mantzaras, J.; Tomboulides, A.G.; Boulouchos, K. Three-dimensional simulations of premixed hydrogen/air flames in microtubes. *J. Fluid Mech.* **2010**, *658*, 463–491. [[CrossRef](#)]
12. Pizza, G.; Frouzakis, C.E.; Mantzaras, J.; Tomboulides, A.G.; Boulouchos, K. Dynamics of premixed hydrogen/air flames in microchannels. *Combust. Flame* **2008**, *152*, 433–450. [[CrossRef](#)]
13. Aikun, T.; Pan, J.; Xia, S.; Hong, X. Numerical simulation study of premixed Hydrogen-Oxygen combustion process in micro-scale rectangular channel. In Proceedings of the International Conference on Computer Distributed Control and Intelligent Environmental Monitoring, Changsha, China, 19–20 February 2011.
14. Pan, J.; Wu, D.; Liu, Y.; Zhang, H.; Tang, A.; Xue, H. Hydrogen/oxygen premixed combustion characteristics in micro porous media combustor. *Appl. Energy* **2015**, *160*, 802–807. [[CrossRef](#)]
15. Yan, Y.; Pan, W.; Zhang, L.; Tang, W.; Chen, Y.; Li, L. Numerical study of the geometrical parameters on CH₄/air premixed combustion in heat recirculation micro-combustor. *Fuel* **2015**, *159*, 45–51. [[CrossRef](#)]
16. Peng, Q.; Jia, E.Q.; Yang, W.; Xu, H.; Chen, J.; Meng, T.; Qiu, R. Effects analysis on combustion and thermal performance enhancement of a nozzle-inlet micro tube fueled by the premixed hydrogen/air. *Energy* **2018**, *160*, 349–360. [[CrossRef](#)]
17. Resende, P.R.; Afonso, A.; Pinho, C.; Ayoobi, M. Impacts of Dilution on Hydrogen Combustion Characteristics and NO_x Emissions. *J. Heat Transf.* **2018**, *141*, 012003. [[CrossRef](#)]
18. Resende, P.; Pinho, C.; Ayoobi, M.; Afonso, A.; Afonso, A. Numerical studies of fuel-rich micro combustion: effect of N₂ dilution on NO_x emissions. In Proceedings of the 24th ABCM International Congress of Mechanical Engineering ABCM, Brno, Czech Republic, 12–14 July 2017. [[CrossRef](#)]
19. Li, L.; Yang, W.; Fan, A. Effect of the cavity aft ramp angle on combustion efficiency of lean hydrogen/air flames in a micro cavity-combustor. *Int. J. Hydrogen Energy* **2019**, *44*, 5623–5632. [[CrossRef](#)]
20. Abbaspour, P.; Alipoor, A. Numerical study of combustion characteristics and oscillating behaviors of hydrogen–air combustion in converging–diverging microtubes. *Int. J. Heat Mass Transf.* **2020**, *159*, 120127. [[CrossRef](#)]
21. Chabane, A.M.; Truffin, K.; Angelberger, C. Direct numerical simulation of catalytic combustion in a meso-scale channel with non-planar walls. *Combust. Flame* **2020**, *222*, 85–102. [[CrossRef](#)]
22. Zuo, W.; Jia, E.Q.; Liu, H.; Peng, Q.; Zhao, X.; Zhang, Z. Numerical investigations on an improved micro-cylindrical combustor with rectangular rib for enhancing heat transfer. *Appl. Energy* **2016**, *184*, 77–87. [[CrossRef](#)]
23. Zuo, W.; Jia, E.Q.; Peng, Q.; Zhao, X.; Zhang, Z. Numerical investigations on thermal performance of a micro-cylindrical combustor with gradually reduced wall thickness. *Appl. Therm. Eng.* **2017**, *113*, 1011–1020. [[CrossRef](#)]
24. Zuo, W.; Zhang, Y.; Li, J.; Li, Q.; He, Z. A modified micro reactor fueled with hydrogen for reducing entropy generation. *Int. J. Hydrog. Energy* **2019**, *44*, 27984–27994. [[CrossRef](#)]
25. Zuo, W.; Jia, E.Q.; Hu, W.; Jin, Y.; Han, D. Numerical investigations on combustion characteristics of H₂/air premixed combustion in a micro elliptical tube combustor. *Energy* **2017**, *126*, 1–12. [[CrossRef](#)]
26. Cuoci, A.; Frassoldati, A.; Faravelli, T.; Ranzi, E. A computational tool for the detailed kinetic modeling of laminar flames: Application to C₂H₄/CH₄ coflow flames. *Combust. Flame* **2013**, *160*, 870–886. [[CrossRef](#)]
27. Ranzi, E.; Frassoldati, A.; Grana, R.; Cuoci, A.; Faravelli, T.; Kelley, A.P.; Law, C.K. Hierarchical and comparative kinetic modeling of laminar flame speeds of hydrocarbon and oxygenated fuels. *Prog. Energy Combust. Sci. Technol.* **2012**, *38*, 468–501. [[CrossRef](#)]
28. Cova, A.; Resende, P.R.; Cuoci, A.; Ayoobi, M.; Afonso, A.M.; Pinho, C.T. Numerical Studies of Premixed and Diffusion Meso/Micro-Scale Flames. *Energy Procedia* **2017**, *120*, 673–680. [[CrossRef](#)]
29. Tsuboi, Y.; Yokomori, T.; Maruta, K. Lower limit of weak flame in a heated channel. *Proc. Combust. Inst.* **2009**, *32*, 3075–3081. [[CrossRef](#)]
30. Alipoor, A.; Mazaheri, K. Combustion characteristics and flame bifurcation in repetitive extinction-ignition dynamics for premixed hydrogen-air combustion in a heated micro channel. *Energy* **2016**, *109*, 650–663. [[CrossRef](#)]

Article

Laminar Burning Velocities of Hydrogen-Blended Methane–Air and Natural Gas–Air Mixtures, Calculated from the Early Stage of $p(t)$ Records in a Spherical Vessel

Maria Mitu ^{1,*}, Domnina Razus ¹ and Volkmar Schroeder ²

¹ “Ilie Murgulescu” Institute of Physical Chemistry, Romanian Academy, 202 Spl. Independentei, 060021 Bucharest, Romania; drazus@icf.ro

² Formerly Bundesanstalt fuer Materialforschung und-Pruefung (BAM), Unter den Eichen 87, 12205 Berlin, Germany; vk.schroeder@gmx.de

* Correspondence: maria_mitu@icf.ro

Abstract: The flammable hydrogen-blended methane–air and natural gas–air mixtures raise specific safety and environmental issues in the industry and transportation; therefore, their explosion characteristics such as the explosion limits, explosion pressures, and rates of pressure rise have significant importance from a safety point of view. At the same time, the laminar burning velocities are the most useful parameters for practical applications and in basic studies for the validation of reaction mechanisms and modeling turbulent combustion. In the present study, an experimental and numerical study of the effect of hydrogen addition on the laminar burning velocity (LBV) of methane–air and natural gas–air mixtures was conducted, using mixtures with equivalence ratios within 0.90 and 1.30 and various hydrogen fractions r_H within 0.0 and 0.5. The experiments were performed in a 14 L spherical vessel with central ignition at ambient initial conditions. The LBVs were calculated from $p(t)$ data, determined in accordance with EN 15967, by using only the early stage of flame propagation. The results show that hydrogen addition determines an increase in LBV for all examined binary flammable mixtures. The LBV variation versus the fraction of added hydrogen, r_H , follows a linear trend only at moderate hydrogen fractions. The further increase in r_H results in a stronger variation in LBV, as shown by both experimental and computed LBVs. Hydrogen addition significantly changes the thermal diffusivity of flammable CH_4 –air or NG–air mixtures, the rate of heat release, and the concentration of active radical species in the flame front and contribute, thus, to LBV variation.

Keywords: hydrogen; methane; natural gas; laminar burning velocity (LBV); closed vessel combustion

Citation: Mitu, M.; Razus, D.; Schroeder, V. Laminar Burning Velocities of Hydrogen-Blended Methane–Air and Natural Gas–Air Mixtures, Calculated from the Early Stage of $p(t)$ Records in a Spherical Vessel. *Energies* **2021**, *14*, 7556. <https://doi.org/10.3390/en14227556>

Academic Editors: Adonios Karpetsis and Giancarlo Sorrentino

Received: 16 September 2021

Accepted: 8 November 2021

Published: 12 November 2021

Publisher’s Note: MDPI stays neutral with regard to jurisdictional claims in published maps and institutional affiliations.



Copyright: © 2021 by the authors. Licensee MDPI, Basel, Switzerland. This article is an open access article distributed under the terms and conditions of the Creative Commons Attribution (CC BY) license (<https://creativecommons.org/licenses/by/4.0/>).

1. Introduction

In recent years, dependence on fossil fuels as the main energy source has led to a worldwide crisis, due to fossil fuel depletion, and environmental problems due to pollutant emissions have become severe. To respond to these problems, continuous attempts have been made in the exploration of clean, renewable alternatives for sustainable development [1,2]. The research on alternative fuels is mainly focused on natural gas [3–7], hydrogen [8–15], and alcohols [16,17], able to be mixed with gasoline, diesel, or to form mutual blends.

The extended use of natural gas (NG) as fuel in internal combustion (IC) and gas turbines prompted numerous research groups to examine its combustion in air, under various initial conditions (NG/air ratio, pressure, temperature, additives) [4–6]. A common practice in NG use is its blending with hydrogen. Hydrogen has attracted the attention of researchers as a renewable clean energy source. Hydrogen is easily ignitable and its flame spreads quickly, which is essential for IC engines to order to work under an improved combustion efficiency [7–15]. Hydrogen addition to NG is a good option for

decreasing CO, CO₂, and NO_x emissions, especially for fuel-lean mixtures [18]. Other effects of H₂ addition to NG are the stabilizing effect on lean NG–air flames, along with an increased risk of flame flash-back in burners originally designed for natural gas [3,19]. Hydrogen raises numerous safety issues, especially when mixed with other flammable gases. The main cause of such effects is the higher reactivity of H₂ compared to each C₁–C₄ alkanes from NG, resulting in important variations of ignition and propagation characteristic parameters of NG–air combustion: decreases in ignition delay times of self-ignition and minimum ignition energies, increases in adiabatic flame temperature and in laminar burning velocity [9,11,20,21]. Taking into account the variable composition of NG as a result of current changes in its supplies, many studies were conducted on CH₄/H₂/air flames [8,11,13,14,19–32]. Such studies revealed the effect of H₂ enrichment: enlargement of the flammability range of CH₄–air mixtures [11,13,14], decreases in ignition delay times in jet-stirred reactors, rapid compression machines or shock tubes [21,26,30], decreases in maximum experimental safe gap (MESG) [11], and increases in flame speed and laminar burning velocity [8,22–32]. Another beneficial effect of enriching methane with hydrogen consists of the increase in flame resistance to strain-induced extinction, as highlighted by Di Sarli et al. [33,34]. Di Sarli et al. investigated a hythane lean and stoichiometric mixture with hydrogen mole fraction in the fuel, r_{H_2} , within 0–0.5 using time-resolved particle image velocimetry (PIV). The authors discussed the interactions that occur between the flame front and the observed toroidal vortex structures [33]. For the same hydrogen-enriched methane/air premixed flames, Di Sarli and Di Benedetto investigated the effects of non-equidiffusion on their unsteady propagation [34]. Numerical studies of flame ignition and propagation also outlined the increase in reactivity determined by H₂ addition and discussed the pathways of CH₄–H₂ oxidation in air, as compared to CH₄ oxidation [3,7,18,19,26,30,32,35].

Experimental and numerical studies were conducted on NG/H₂/air flames as well at various ratios [NG] to [H₂], overall equivalence ratios, and initial pressures and temperatures, using stationary flames or outwardly propagating non-stationary flames, in both unconfined and confined conditions [7,9,11,13,18,26,30–42].

Studies of closed vessel explosions delivered the characteristic parameters of flame propagation under confined conditions (the maximum explosion pressure p_{max} , the explosion delay time θ_{max} , the maximum rate of pressure rise $(dp/dt)_{max}$, and deflagration index K_G) for NG and H₂-blended NG [11,13,29,43]. Closed vessel experiments offer the necessary information for laminar burning velocity determination. This is a highly examined topic, since laminar burning velocities are key factors for validation of detailed mechanisms of fuel–air combustion. Studies of outwardly spherical flames based on transient records of flame radius and pressure [8,22,25–30,36–42] were reported for H₂-blended CH₄ and H₂-blended NG with variable initial composition (variable [H₂]/[CH₄] and [H₂]/[NG] ratios or variable equivalence ratios), initial pressure, or initial temperature. Additional information on flame structure (temperature and chemical species profiles) able to enlighten the influence of H₂ addition on hydrocarbon fuel combustion is found in studies on stationary flames [19,23,24,28,31,32,41].

The conventional combustion of either pure methane or of its blends with hydrogen raises several issues related to emissions of high pollutants such as NO_x. Such issues, associated with the dense energy input caused by preheating the flammable mixtures, can be solved by some new technologies, as suggested in recent articles describing MILD (flameless) combustion [44,45]. The flameless combustion of CH₄/H₂ in a laboratory-scaled furnace was investigated by Celtek [44], proving this is an effective way to reduce pollutant emissions despite the intense energy induced by air preheating, which causes higher flame temperatures. Even when various inlet operating conditions are used, outside canonical configurations (e.g., inside a small-scale device), the specific MILD advantage can be obtained by an adequate degree of dilution, as outlined by Cerello et al. [45].

The aim of the present work is to examine hydrogen influence on laminar burning velocity for different methane/hydrogen and natural gas/hydrogen mixtures with air at

ambient initial conditions. For this, $p(t)$ data obtained in experimental investigations were used. These measurements, performed according to European Standards EN 15967 [46], were originally conducted to determine the maximum explosion pressure p_{max} , the maximum rate of pressure rise $(dp/dt)_{max}$, and the deflagration index K_G . The paper reports LBVs of hydrogen-blended methane–air and natural gas–air mixtures, using mixtures at ambient initial pressure and temperature ($p_0 = 0.97$ – 1.04 bar, $T_0 = 22$ – 25 °C). The mixtures being studied consist of single fuel–air (CH₄–air) and multifuel–air mixtures, where the multifuel was CH₄ blended with H₂, or natural gas blended with H₂, both under various amounts of added hydrogen, within 0–50 mol% (in respect to the initial fuel amount). The studied systems had either a constant fuel (CH₄ or NG)/H₂ ratio and a variable equivalence ratio or a variable fuel (CH₄ or NG)/H₂ ratio and a constant equivalence ratio. Their laminar burning velocities were determined from the cubic law constants, evaluated from $p(t)$ records obtained in the early stage of closed vessel explosions. Thus, the LBV of H₂-blended CH₄–air and NG–air were determined from single $p(t)$ records, without the additional optical methods of investigation, and were found to describe well the behavior of these multifuel mixtures.

The present results represent a contribution to the data pool regarding the flame propagation in hydrogen-blended CH₄/air and NG/air mixtures. Earlier studies [47,48] provided data for risk assessment at gas processing facilities, especially those involving the introduction of hydrogen into existing natural gas networks under project NATURALHY financed by the EU. The unwanted consequences of such events, i.e., loss of assets, human injuries, fatalities, or severe environmental impacts, can be avoided by a proper safety analysis based on experiments, as discussed by Amin et al. [49].

2. Experimental Procedure

The experiments were conducted at BAM as part of a systematic investigation on safety-related characteristics of natural gas–hydrogen mixtures [11,43]. The pressure–time curves obtained during the determination of explosion limits, explosion pressures, and deflagration constants (K_G) could be used directly to calculate the LBVs using the method described below. The laboratory set-up was previously described in detail [11]. The set-up affords the monitoring of closed vessel explosions for gaseous mixtures of variable composition, pressure, and temperature. A 14 L spherical vessel with central ignition was used to perform experiments with quiescent gas mixtures. An exploding wire igniter (nickeline wire, diameter: 0.12 mm, distance of electrodes: 5 mm) delivered about 15 J for ignition. The ignition systems used are in accordance with EN 1839 [50].

The pressure measurements were made with piezoresistive pressure transducers, type PAA10 (Keller). For mixture preparation pressure transducers with a measuring range between 0 bar (abs) and 2 bar (abs) or between 0 bar (abs) and 5 bar (abs) were used. For measuring the explosion pressure, pressure transducers with a measuring range between 0 bar (abs) and 10 bar (abs) were used. The measuring frequency was 20,000 Hz. The digitized signals of the measuring sensors were connected to an A/D converter, type MCL-USB (16 channels, 16 Bit A/D, sampling frequency: 500 kHz, from Jet Systemtechnik GmbH) and a PC for displaying, storing, and evaluating the data.

Two types of European natural gas were tested: one representing a typical Russian natural gas composition, nearly pure methane, and one of wet type containing CH₄ and a significant amount of C₂–C₄ alkanes, similar to Northern Sea natural gas [11]. The composition of the studied natural gas is given in Table 1.

Table 1. Composition of studied wet natural gas.

Component	CH ₄	C ₂ H ₆	C ₃ H ₈	n-C ₄ H ₁₀
Fraction in NG, mol%	89.3	8.0	2.0	0.7

Using pure CH₄ and wet natural gas blended with H₂, multifuel–air mixtures of variable hydrogen content and equivalence ratio were studied at ambient initial pressure and temperature. Their composition is given in Table 2. The hydrogen content in the initial flammable mixture is expressed as the fraction r_H , defined as:

$$r_H = \frac{[H_2]}{([CH_4] + [H_2])} \text{ or } r_H = \frac{[H_2]}{([NG] + [H_2])} \quad (1)$$

The equivalence ratio, φ , of any flammable mixture is defined as:

$$\varphi = \frac{\frac{[\text{fuel}]}{[\text{oxygen}]}}{\left(\frac{[\text{fuel}]}{[\text{oxygen}]}\right)_{\text{st}}}$$

where the index “st” refers to the stoichiometric concentration of the fuel–air mixture.

Table 2. Studied systems (fraction of H₂, r_H , and equivalence ratios, φ).

Fuel	r_H	Equivalence Ratios, φ
CH ₄ –air	0	0.95–1.15
CH ₄ –H ₂ –air	0.05; 0.10; 0.25; 0.50	0.90–1.30
Natural gas (NG)–air	0	0.90–1.20
Natural gas (NG)–H ₂ –air	0.10; 0.25; 0.50	0.95–1.15

The mixtures of CH₄ or NG with different fractions of hydrogen and air were prepared in a pressure resistant stainless-steel vessel, according to the partial pressure method at total pressure of 2 bar or 5 bar, assuming an ideal gas behavior for all gaseous components.

3. Computing Program

The burning velocities of fuel–air and multifuel–air systems, at ambient initial conditions, were delivered by the kinetic modeling of their flames using COSILAB software (version 3.0.3) and Gas Research Institute (GRI) mechanism version 3.0 [51], where 53 chemical species and 325 elementary reactions are taken into account. The input data were taken from the thermodynamic and molecular databases of Sandia National Laboratories, USA, according to the international standard (format for CHEMKIN). The runs were performed for premixed 1D adiabatic laminar free flames of stoichiometric CH₄–air, NG–air, and H₂-blended mixtures at ambient initial conditions. In these runs, a steady Newton solver (25 iterations, relative tolerance 10^{−5}; absolute tolerance 10^{−8}), an unsteady Newton solver (15 iterations, relative tolerance 10^{−4}; absolute tolerance 10^{−6}), and an unsteady Euler solver were used, as mentioned earlier [52,53]. The parameters of the adaptive grid were GRAD = 0.1, CURV = 0.2, with a maximum ratio of adjacent cell size between 1.3 and 1.1.

4. Data Evaluation

The pressure rise in the early stage of closed vessel explosions, Δp , was found to increase with time from ignition, t , according to so-called “cubic law” [52,54]:

$$\text{or } r_H = \frac{[H_2]}{([NG] + [H_2])} \quad (2)$$

The equation is valid as long as the spherical propagation of the combustion wave is not disturbed. In small-scale explosions, the flame front of reactive mixtures does not develop significant cellular structures and no gas turbulence appears. Indeed, the pressure rise Δp was found proportional to t^3 in quiescent conditions of combustion (CH₄–air, at $p_0 = 1$ bar (Dobashi [55]) and aviation grade JP-4 fuel with air, at $p_0 = 135$ –275 bar (Knapton

et al. [56]) and to $t^{3.6-6.0}$ in turbulent conditions (CH₄-air, at $p_0 = 1$ bar (Dobashi [55]). In large-scale explosions (vessels with a volume between 1 and 10 m³), where the buoyancy effect determines the distortion of the flame, even in the early stage, the time exponent varied between 3.3 and 5.0 for stoichiometric CH₄-air mixtures diluted with various amounts of nitrogen (Sapko et al. [57]).

Assuming the isothermal compression of unburned gas ahead the flame front, the laminar burning velocity, S_u , was related to k , the cubic law coefficient of pressure rise by the relationship [54]:

$$S_u = R \cdot \left(\frac{k}{\Delta p_{max}} \right)^{\frac{1}{3}} \left(\frac{p_0}{p_{max}} \right)^{\frac{2}{3}} \quad (3)$$

where R is the radius of the explosion vessel, Δp_{max} is the peak pressure rise in the explosion at the initial pressure p_0 , and $p_{max} = \Delta p_{max} + p_0$. The measured values of Δp_{max} and p_{max} are used as input values for S_u calculation.

The cubic law coefficient can be determined for each experiment over a restricted pressure range ($p_0 \leq p \leq 2p_0$) using a nonlinear regression method with a relationship of the form:

$$\Delta p = a + k (t - c)^3 \quad (4)$$

where a and c are corrections for pressure and time, respectively, necessary for eliminating the signal shift of the pressure transducer and the possible delay in signal triggering [52]. Smaller residuals and a random error distribution, indicating better correlations, were obtained by using this modified Equation (4), instead of Equation (2).

The method was successfully used for determining LVBs of various hydrocarbon-oxidizer mixtures [52–54,58–61] under various initial conditions of pressure and/or temperature.

5. Results and Discussion

A set of experimental burning velocities of CH₄-H₂-air mixtures obtained from $p(t)$ measurements in a closed spherical vessel at ambient initial pressure, temperature, and constant r_H , is given in Table 3.

Table 3. Typical values of S_u for H₂-blended CH₄ mixed with air at $r_H = 0.25$.

[CH ₄]/mol%	[H ₂]/mol%	[CH ₄ + H ₂]/mol%	Equivalence Ratio, φ	S_u /(cm s ⁻¹)
8.40	2.80	11.20	0.978	58.6
8.84	2.96	11.80	1.037	61.0
9.14	3.06	12.20	1.077	60.2
9.14	3.06	12.20	1.077	60.9
9.14	3.06	12.20	1.077	61.9
9.30	3.10	12.40	1.098	61.6
9.44	3.16	12.60	1.117	58.6
9.60	3.20	12.80	1.139	58.0
10.04	3.33	13.40	1.199	51.5
10.50	3.50	14.00	1.263	45.6

The influence of the initial composition (characterized by r_H and φ) on experimental laminar burning velocities is shown in Figure 1, where data referring to CH₄-H₂-air and NG-H₂-air mixtures are given. The burning velocities of all mixtures increase by increasing the equivalence ratio and reaching their peak values, then start to decrease at higher equivalence ratios. The LVB variation due to H₂ addition is observed already at $r_H = 0.05$ for lean CH₄-air mixtures. In the range of rich CH₄-air and NG-air mixtures, the LVB changes significantly only at $r_H > 0.10$. For higher hydrogen contents ($r_H = 0.25$ and 0.50), a marked increase in LVB appears over the whole examined range of equivalence ratios.

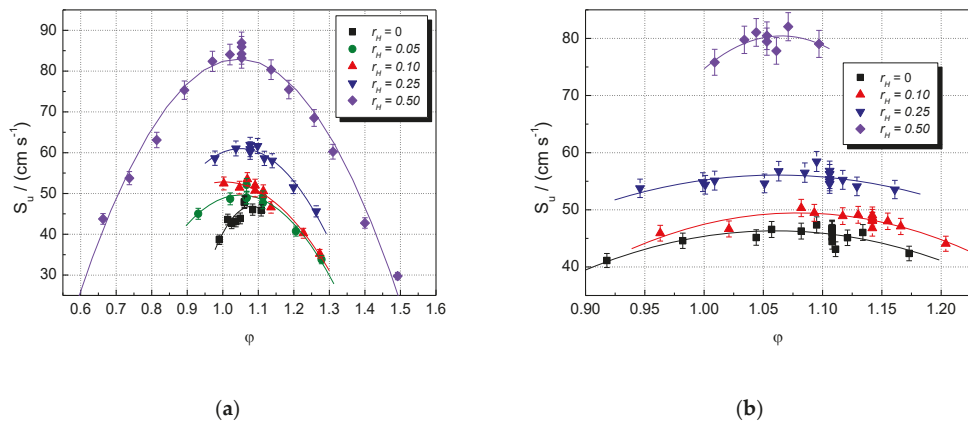


Figure 1. Experimental laminar burning velocities of single fuel–air and multifuel–air mixtures with various r_H at ambient initial pressure and temperature: (a) CH₄–H₂–air; (b) NG–H₂–air mixtures (present data).

The LBV of the stoichiometric CH₄–air mixture is $S_u = 40 \text{ cm s}^{-1}$, in good agreement with most literature data: $S_u = 41.2 \text{ cm s}^{-1}$ [62], 41.0 cm s^{-1} [6], 40 cm s^{-1} [5], and 38 cm s^{-1} [53]. For this stoichiometric CH₄–air mixture, the earlier reported LBVs vary within 35 and 41.5 cm s^{-1} [4–6,62] at ambient initial conditions, a domain where the present values range well. For the stoichiometric NG–air mixture, the LBV is $S_u = 45.7 \text{ cm s}^{-1}$, close to 44.0 cm s^{-1} , previously reported [6,37].

Hydrogen addition to CH₄ or NG results in an increase in S_u at all initial concentrations of CH₄ or NG. The blended mixtures (CH₄–H₂ or NG–H₂) with a constant [H₂] having various equivalence ratios develop the maxima of their burning velocities at slightly rich mixtures, with $\phi = 1.05 \pm 0.05$.

Both datasets were well fitted by 2nd order polynomials, plotted as well in Figure 1. The points are scattered around the best-fit lines; a possible cause is the turbulence created already in the early stage of explosion by the ignition, made by a strong initiation source (exploding wires, which delivered 15 J). This turbulence could determine deviations from the spherical propagation and errors of the model used. Other methods were also used to extract the laminar burning velocity from transient pressure measurements [63–67]. These methods require equilibrium calculations of unburned and burned gas states to determine LBV using the transient burned mass fraction. They are rigorous methods, which also deliver the temperature gradients in the burned gas and afford the evaluation of the flame stretch effect on burning velocity. In comparison with them, the actual method for determining LBVs from pressure measurements in the early stage of explosion propagation has the advantage of delivering LBVs without additional computations and without additional experimental techniques for measuring the flame radius. This aspect is an advantage when flammable mixtures of multifuels or multi-oxidizers are examined, and the thermodynamic calculations of the intermediate states are impossible or very difficult.

Examination of literature on LBV of H₂-blended CH₄–air and NG–air mixtures provides a wide database of comparison. All datasets show the same variation of burning velocities when examined as a function of the equivalence ratio (at constant r_H) or function of r_H (at constant ϕ) [3,7,19,21,23,27–30,37,38,68,69]. Differences arise among measurements performed using different techniques, involving various corrections of the recorded information.

A closer examination of present results compared with literature data can be made by examining the LBV of stoichiometric CH₄–air and NG–air mixtures blended with hydrogen at various fractions of added H₂, as shown by the plots given in Figure 2. With respect to CH₄–H₂–air mixtures (Figure 2a), the present results are found to match well with those obtained as stretch-free LBV, using the technique of counter-flow flames [23]. For the

examined range of the fraction of added hydrogen, $r_H \leq 0.5$, they seem to depend linearly on it. The same holds for the other datasets, obtained mostly with stationary flames using the heat flux technique [4,24,28,31]. However, by extending these plots to the whole range of hydrogen composition ($0 \leq r_H \leq 1.0$), one can see the fast increase in LBV at hydrogen fractions higher than 0.5. At all fractions of added H_2 , the datasets obtained using the heat flux method consist of lower LBV than the present data, which were not stretch-corrected, but their trend is the same. The H_2 -blended NG–air mixtures can be characterized by similar plots (Figure 2b); their LBV follows the same marked increase with r_H at hydrogen fractions higher than 0.3.

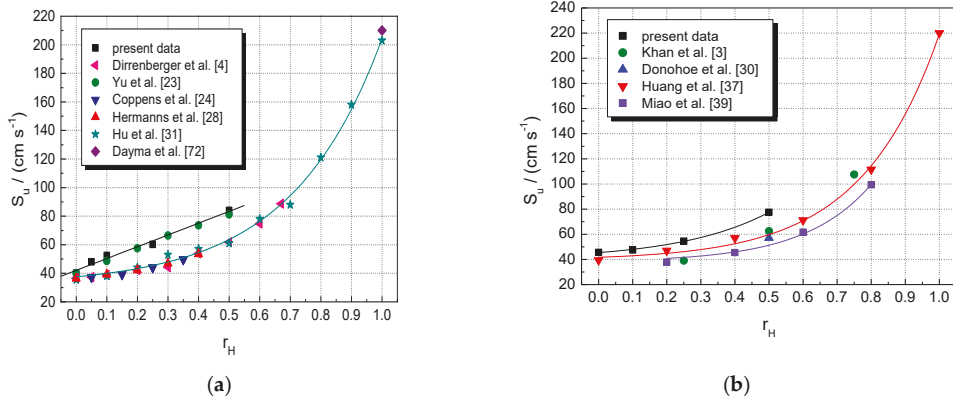


Figure 2. Laminar burning velocities of single fuel–air and multifuel–air mixtures with various r_H at ambient initial pressure and temperature: (a) CH_4 – H_2 –air; (b) NG – H_2 –air mixtures (present experimental data, in comparison with literature values).

A comparison of LBV for the stoichiometric CH_4 – H_2 –air and NG – H_2 –air mixtures, using the present data, is shown in Figure 3 (experimental LBV) and Figure 4 (computed LBV) where the dimensionless (relative) LBV_{rel} , defined as:

$$LBV_{rel} = \frac{[S_u]_{fuel+H_2}}{[S_u]_{fuel}} \quad (5)$$

is plotted against the mole fraction of hydrogen, r_H .

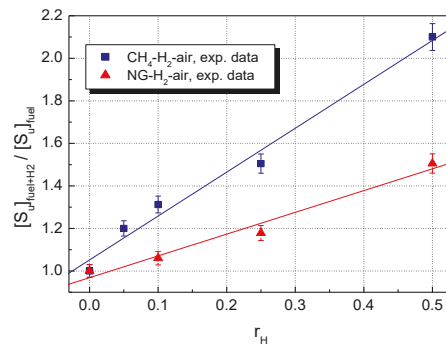


Figure 3. Experimental LBV of H_2 -blended CH_4 –air and NG –air with various hydrogen contents at ambient initial conditions.

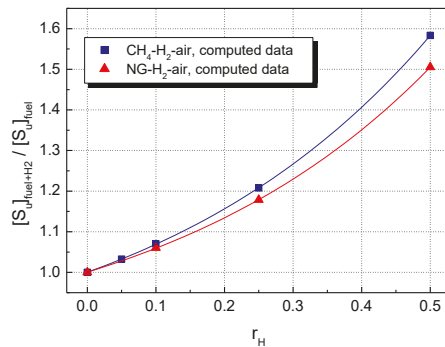


Figure 4. Computed LBV of H₂-blended CH₄-air and NG-air with various hydrogen contents at ambient initial conditions.

For both experimental and calculated datasets, H₂ addition influences to a greater extent the LBV of CH₄-air, as compared to NG-air.

For the restricted range of hydrogen fractions $0 \leq r_H \leq 0.5$, the experimental relative burning velocities $LBV_{rel} = \frac{[S_u]_{fuel+H_2}}{[S_u]_{fuel}}$ are linearly correlated with r_H . This aspect was already observed for CH₄-H₂-air and NG-H₂-air mixtures [23,36,68,69] and for other hydrogen-blended fuels as well [3,7,8,19,21,23,69,70].

At any hydrogen concentration, the burning velocities of NG-H₂-air are smaller than those of CH₄-H₂-air, as a consequence of the presence of heavier hydrocarbons in NG. Both experimental and modeling studies on the effect of hydrogen addition to the C₂, C₃, or C₄ alkanes [3,8,19–21,69,70] showed that the enhancement of LBV upon the addition of 50% H₂ was about 20–40% lower compared to when the fuel was pure methane.

The computed LBV can be compared to present experimental LBVs when plotted as functions of the equivalence ratios of H₂-blended CH₄-air and NG-air mixtures, as shown in Figure 5. The shape of the experimental (Figure 1) and computed LBVs plots is similar. The plots obtained for CH₄-H₂-air have marked maxima appearing around $\varphi = 1.10$ for all r_H . In contrast to them, the plots obtained for NG-H₂-air are rather flat; their maxima appear in the range $\varphi = 1.0$ –1.10.

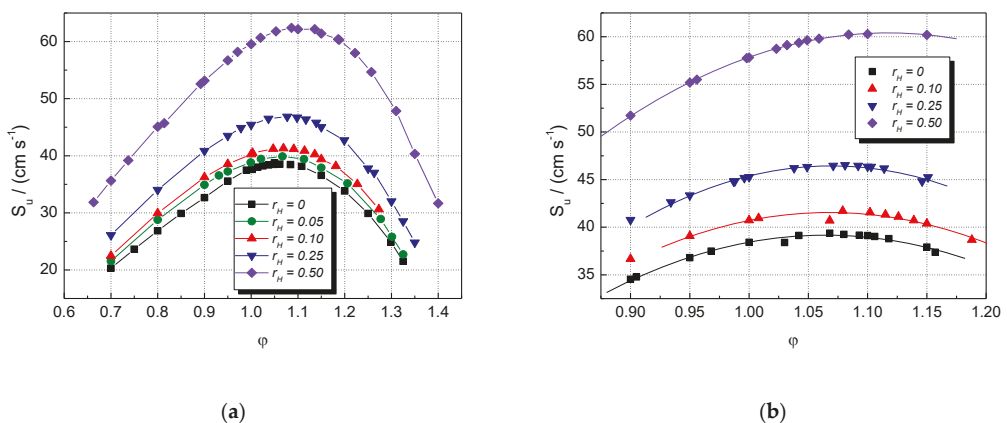


Figure 5. Computed laminar burning velocities of single fuel-air and multifuel-air mixtures with various r_H at ambient p_0 and T_0 : (a) CH₄-H₂-air (b) NG-H₂-air mixtures.

Another comparison between the experimental and the computed burning velocities is shown in Figure 6 for the stoichiometric $\text{CH}_4\text{-H}_2\text{-air}$ and $\text{NG-H}_2\text{-air}$ mixtures with various hydrogen contents.

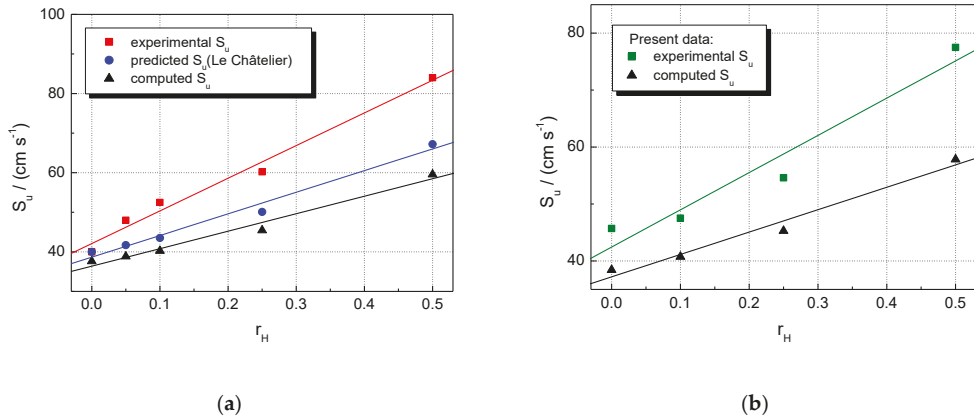


Figure 6. Laminar burning velocities of stoichiometric multifuel–air mixtures with various r_H at ambient initial pressure and temperature: (a) $\text{CH}_4\text{-H}_2\text{-air}$; (b) $\text{NG-H}_2\text{-air}$ mixtures.

For both CH_4 and NG mixtures, the computed LBV are lower than the experimental LBVs, and the differences increase in parallel with r_H . Figure 6a contains an additional plot of predicted LBVs, calculated from the experimental LBVs of pure $\text{H}_2\text{-air}$ and $\text{CH}_4\text{-air}$ mixtures and the composition of blended mixtures by using an equation proposed by Di Sarli et al. [25]:

$$S_{u,(\text{CH}_4+\text{H}_2)} = \frac{1}{\frac{r_H}{S_{u,\text{H}_2}} + \frac{1-r_H}{S_{u,\text{CH}_4}}} \quad (6)$$

The relationship is similar to Le Châtelier's rule for predicting the flammability limits of multifuel gases, using the flammability limit of each fuel from the mixture [71]. For the examined range of hydrogen concentrations, the predicted LBVs are lower than those directly obtained from experiments. However, one must consider that S_{u,H_2} used to determine the predicted LBVs were taken from the literature [71] and do not belong to the present set of experimental burning velocities.

The deviations between experimental and computed LBV can be assigned to the fact that GRI 3.0 Mech is adequate for modeling the combustion of C1–C4 alkanes (components of natural gas) but less adequate for modeling the combustion of multifuel–air mixtures with a high H_2 content. Better predictions were obtained after using improved mechanisms [19,25,28,30].

The enhancement effect of hydrogen upon flame propagation in H_2 -blended mixtures can be better understood by examining the flame structure obtained from the kinetic modeling of $\text{CH}_4\text{-air}$ and $\text{CH}_4\text{-H}_2\text{-air}$ flames. In this purpose, the stoichiometric composition of these flammable mixtures was chosen for systems at ambient initial pressure and temperature.

The influence of H_2 concentration on temperature and the volumetric rate of heat release profiles of $\text{CH}_4\text{-H}_2\text{-air}$ flames is shown in Figures 7 and 8 at $0 \leq r_H \leq 0.5$. The temperature of burned gas is not influenced by hydrogen addition; only the flame front thickness (evaluated as the half of the reaction zone) is decreased by H_2 addition. This variation was assigned by Salzano et al. [69] to the increased amount of NO_x produced by the combustion of H_2 -blended $\text{CH}_4\text{-air}$ ternary mixtures. In contrast to this trend, H_2 addition to $\text{CH}_4\text{-air}$ results in a marked change in the heat release, as shown by data from Figure 8. Similar plots were obtained for H_2 -blended NG-air ternary mixtures.

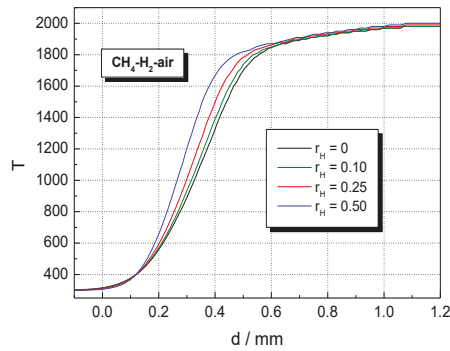


Figure 7. Computed temperature profiles in the flame front of stoichiometric CH₄-H₂-air flames with variable r_H ; ambient p_0 and T_0 .

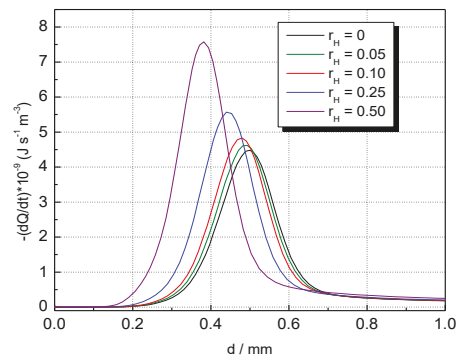


Figure 8. Volumetric rates of heat release in the flame front of CH₄-H₂-air flames with variable r_H ; ambient p_0 and T_0 .

The change in the volumetric rates of heat release with the fraction of added hydrogen is shown in Figure 9 for both CH₄-H₂-air and NG-H₂-air flames. Similar plots are obtained by examining r_H 's influence on the sum of peak mass fractions of the most abundant radical species: H, OH, O, and HO₂, shown in Figure 10. The differences between CH₄-H₂-air and NG-H₂-air flames are observed only for mixtures with a hydrogen content below 0.25.

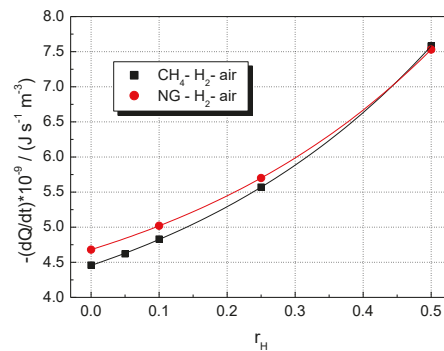


Figure 9. Influence of hydrogen fraction, r_H , on peak values of volumetric rates of heat release in the flame front of H₂-blended fuels; flames of stoichiometric mixtures at ambient p_0 and T_0 .

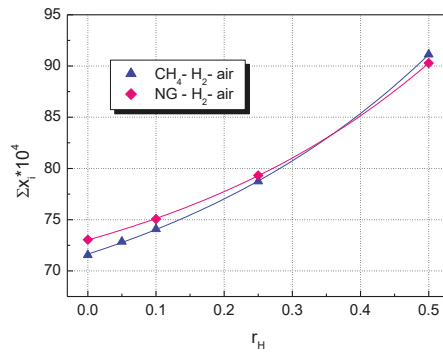


Figure 10. Influence of hydrogen fraction, r_H , on the sum of peak mass fractions from radical species, H₂-blended fuels; flames of stoichiometric mixtures at ambient p_0 and T_0 .

The modeling, thus, indicates a combined (synergetic) influence of these two factors: the rate of heat release and the abundance of reactive radical species. Their individual influence on LBVs is shown in Figures 11 and 12.

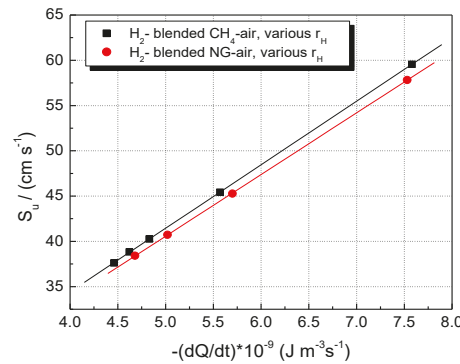


Figure 11. Experimental LBV of stoichiometric CH₄-H₂-air and NG-H₂-air mixtures in correlation with the peak values of volumetric rates of heat release; flames at ambient p_0 and T_0 .

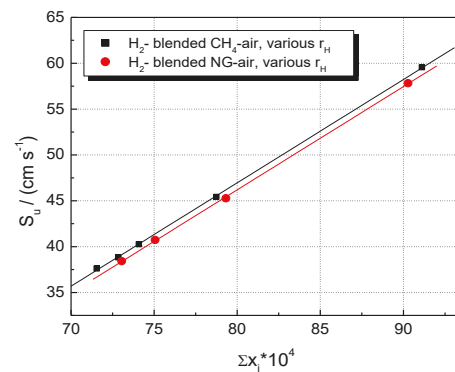


Figure 12. Experimental LBV of stoichiometric CH₄-H₂-air and NG-H₂-air mixtures in correlation with the sum of peak mass fractions of radical species; flames at ambient p_0 and T_0 .

The literature data show that H₂ blending of CH₄-air or NG-air results in the enhancement of their reactivity [3,7,8,19,21,23,36–38,69,70,72,73], determining the LBV increase even if the temperature of their burned gases is little influenced by H₂ addition. The results of the present study, thus, show good agreement with previous studies on these flammable mixtures.

A less examined factor contributing to the observed variations of LBV is the thermal diffusivity of blended mixtures, which increases many folds by hydrogen addition. In accordance with the thermal theory of flame propagation, the laminar burning velocity can be written as:

$$S_u \sim [D \cdot C_0^{1-n} \cdot \exp\left(-\frac{E_a}{RT_f}\right)]^{\frac{1}{2}} \quad (7)$$

where $D = \frac{\lambda}{\rho \cdot c_p}$ is the thermal diffusivity of the flammable mixture, C_0 is the total initial fuel concentration, T_f is the end temperature in the flame front, and n and E_a are the overall activation parameters (reaction order and activation energy) of the oxidation reaction [74]. The thermophysical properties of CH₄, H₂, O₂, and N₂ are listed in Table 4. Close values are expected for NG, when compared to pure CH₄. Indeed, the high thermal conductivity of hydrogen influences the thermal diffusivity of H₂-blended CH₄-air and NG-air mixtures, resulting in higher LBVs compared to non-blended flammable mixtures.

Table 4. Heat capacities, c_p , densities, ρ , thermal conductivities, λ , and thermal diffusivities, D , of gaseous components [75].

Additive	CH ₄	H ₂	O ₂	N ₂
c_p /(J·mol ⁻¹ ·K ⁻¹)	35.70	28.84	29.38	29.12
c_p /(J·kg ⁻¹ ·K ⁻¹)	2231	14,420	918	1040
ρ (kg m ⁻³)	0.717	0.0899	1.429	1.251
λ /(mW·m ⁻¹ ·K ⁻¹)	33.0	180.5	26.6	25.8
$D \cdot 10^6$ (m ² s ⁻¹)	20.63	129.2	20.28	19.83

6. Conclusions

The flammability characteristics of methane or natural gas enriched with hydrogen are frequently studied to ensure the safe use of these mixtures in various activity branches. Although, in practical applications, hydrogen concentration does not exceed 20%, the present study was focused on hydrogen percentages between 0 and 50% in the blended CH₄-H₂ or natural gas-H₂ mixtures.

In the study, the propagation of H₂-blended methane or natural gas-air flames in a closed spherical vessel was monitored by means of $p(t)$ variation recorded in the early stage of spherical propagation. Its novelty consists of the possibility to determine LBV from single $p(t)$ records, without additional optical methods of investigation. This simple method for evaluating data does not consider the flame stretch in this incipient stage of propagation and the flame width. However, the delivered results can be used for a preliminary characterization of the propagation stage by the LBV, extrapolated to the initial moment of experiment, i.e., at $(p_0; T_0)$. An additional reason is based on the possibility to use the present method for multifuel- or multioxidizer-flammable mixtures, where the exact calculation of thermodynamic conditions for the burned gas, under transient conditions, is difficult, even impossible.

The experimental laminar burning velocities were examined in comparison with the computed burning velocities obtained from the numerical modeling of 1D laminar flames with the GRI 3.0 mechanism.

A fair agreement between the experimental burning velocities and reference values from the literature was observed not only for CH₄-air mixtures but for H₂-blended CH₄-air mixtures as well. The same good agreement found for present LBVs of NG-air mixtures

with literature values confirmed the possibility of using the actual simple method for extracting laminar burning velocities from the measurements of transient pressure in the early stage of explosion propagation.

The addition of increasing amounts of H₂ to CH₄ or to natural gas was found to determine the increase in laminar burning velocity for all investigated compositions of the methane–air or natural gas–air mixtures. In parallel, a strong influence of added hydrogen on the rate of heat release and concentration of active radical species in the flame front was observed. The results are assigned to the higher thermal conductivity and thermal diffusivity of hydrogen, resulting in a higher reaction rate and a higher heat dissipation rate of H₂-blended mixtures.

The reported data can further help to identify the degree of danger of explosions and develop more effective measures to prevent explosions of flammable mixtures.

Author Contributions: Conceptualization, V.S., M.M., and D.R.; methodology, M.M. and V.S.; software, M.M. and D.R.; validation, M.M. and V.S.; formal analysis, D.R.; investigation, V.S.; resources, V.S.; data curation, M.M.; writing—original draft preparation, M.M. and D.R.; writing—review and editing, M.M., D.R., and V.S. All authors have read and agreed to the published version of the manuscript.

Funding: This research received no external funding.

Institutional Review Board Statement: Not applicable.

Informed Consent Statement: Not applicable.

Data Availability Statement: Not applicable.

Acknowledgments: The present study was partially financed by the Bundesanstalt fuer Materialforschung und pruefung (BAM) and by the Romanian Academy under the scientific cooperation on flammability of complex gaseous mixtures, concluded between BAM and “Ilie Murgulescu”, Institute of Physical Chemistry of the Romanian Academy.

Conflicts of Interest: The authors declare no conflict of interest.

References

- Gad, M.S.; Ismail, M.A. Effect of waste cooking oil biodiesel blending with gasoline and kerosene on diesel engine performance, emissions and combustion characteristics. *Process Saf. Environ. Prot.* **2021**, *149*, 1–10. [[CrossRef](#)]
- Gad, M.S.; El-Shafay, A.S.; Hashish, H.M. Assessment of diesel engine performance, emissions and combustion characteristics burning biodiesel blends from jatropha seeds. *Process Saf. Environ. Prot.* **2021**, *147*, 518–526. [[CrossRef](#)]
- Khan, A.R.; Ravi, M.R.; Ray, A. Experimental and chemical kinetic studies of the effect of H₂ enrichment on the laminar burning velocity and flame stability of various multicomponent natural gas blends. *Int. J. Hydrogen Energy* **2019**, *44*, 1192–1212. [[CrossRef](#)]
- Dirrenberger, P.; Le Gall, H.; Bounaceur, R.; Herbinet, O.; Glaude, P.A.; Konnov, A.; Battin-Leclerc, F. Measurements of laminar flame velocity for components of natural gas. *Energy Fuels* **2011**, *25*, 3875–3884. [[CrossRef](#)]
- Liao, S.Y.; Jiang, D.M.; Cheng, Q. Determination of laminar burning velocities for natural gas. *Fuel* **2004**, *83*, 1247–1250. [[CrossRef](#)]
- Zhang, B.; Xiu, G.; Bai, C. Explosion characteristics of argon/nitrogen diluted natural gas—Air mixtures. *Fuel* **2014**, *124*, 125–132. [[CrossRef](#)]
- Ren, F.; Chu, H.; Xiang, L.; Han, W.; Gu, M. Effect of hydrogen addition on the laminar premixed combustion characteristics the main components of natural gas. *J. Energy Inst.* **2019**, *92*, 1178–1190. [[CrossRef](#)]
- Tang, C.L.; Huang, Z.H.; Law, C.K. Determination, correlation, and mechanistic interpretation of effects of hydrogen addition on laminar flame speeds of hydrocarbon—Air mixtures. *Proc. Combust. Inst.* **2011**, *33*, 921–928. [[CrossRef](#)]
- Brower, M.; Petersen, E.L.; Metcalfe, W.; Curran, H.J.; Fueri, M.; Bourque, G.; Aluri, N.; Guethe, F. Ignition delay time and laminar flame speed calculations for natural gas/hydrogen blends at elevated pressures. *J. Eng. Gas Turbines Power* **2013**, *135*, 021504. [[CrossRef](#)]
- Ma, Q.; Zhang, Q.; Chen, J.; Huang, Y.; Shi, Y. Effects of hydrogen on combustion characteristics of methane in air. *Int. J. Hydrogen Energy* **2014**, *39*, 11291–11298. [[CrossRef](#)]
- Askar, E.; Schröder, V.; Schütz, S.; Seemann, A. Power-to-gas: Safety characteristics of hydrogen/natural-gas mixtures. *Chem. Eng. Trans.* **2016**, *48*, 397–402. [[CrossRef](#)]
- Li, T.; Hampf, F.; Lindstedt, R.P. Experimental study of turbulent explosions in hydrogen enriched syngas related fuels. *Process Saf. Environ. Prot.* **2018**, *116*, 663–676. [[CrossRef](#)]
- Molnar, M.; Schroeder, V. Hazardous properties of hydrogen and hydrogen containing fuel gases. *Process Saf. Environ. Prot.* **2019**, *130*, 1–5. [[CrossRef](#)]

14. Wang, T.; Zhou, Y.; Luo, Z.; Wen, H.; Zhao, J.; Su, B.; Cheng, F.; Deng, J. Flammability limit behavior of methane with the addition of gaseous fuel at various relative humidities. *Process Saf. Environ. Prot.* **2020**, *140*, 178–189. [[CrossRef](#)]
15. Zhen, X.; Tian, Z.; Wang, Y.; Liu, D.; Li, X. A model to determine the effects of low proportion of hydrogen and the flame kernel radius on combustion and emission performance of direct injection spark ignition engine. *Process Saf. Environ. Prot.* **2021**, *147*, 1110–1124. [[CrossRef](#)]
16. Chen, H.; He, J.J.; Chen, Z.M.; Geng, L.M. A comparative study of combustion and emission characteristics of dual-fuel engine fueled with diesel/methanol and diesel-polyoxymethylene dimethyl ether blend/methanol. *Process Saf. Environ. Prot.* **2021**, *147*, 714–722. [[CrossRef](#)]
17. Mitu, M.; Brandes, E.; Hirsch, W. Mitigation effects on the explosion safety characteristic data of ethanol/air mixtures in closed vessel. *Process Saf. Environ. Prot.* **2018**, *117*, 190–199. [[CrossRef](#)]
18. Dagaut, P.; Nicolle, A. Experimental and detailed kinetic modeling study of hydrogen-enriched natural gas blend oxidation over extended temperature and equivalence ratio ranges. *Proc. Combust. Inst.* **2005**, *30*, 631–638. [[CrossRef](#)]
19. Nilsson, E.J.; van Sprang, A.; Larfeldt, J.; Konnov, A.A. The comparative and combined effects of hydrogen addition on the laminar burning velocities of methane and its blends with ethane and propane. *Fuel* **2017**, *189*, 369–376. [[CrossRef](#)]
20. Kuppa, K.; Goldmann, A.; Schöffler, T.; Dinkelacker, F. Laminar flame properties of C1–C3 alkanes/hydrogen blends at gas engine conditions. *Fuel* **2018**, *224*, 32–46. [[CrossRef](#)]
21. Mosisa Wako, F.; Pio, G.; Salzano, E. The Effect of Hydrogen Addition on Low-Temperature Combustion of Light Hydrocarbons and Alcohols. *Energies* **2020**, *13*, 3808. [[CrossRef](#)]
22. Milton, B.E.; Keck, J.C. Laminar burning velocities in stoichiometric hydrogen and hydrogen-hydrocarbon gas mixtures. *Combust. Flame* **1984**, *58*, 13–22. [[CrossRef](#)]
23. Yu, G.; Law, C.K.; Wu, C.K. Laminar flame speeds of hydrocarbon+ air mixtures with hydrogen addition. *Combust. Flame* **1986**, *63*, 339–347. [[CrossRef](#)]
24. Coppens, F.H.V.; De Ruyck, J.; Konnov, A.A. Effects of hydrogen enrichment on adiabatic burning velocity and NO formation in methane+ air flames. *Exp. Therm. Fluid Sci.* **2007**, *31*, 437–444. [[CrossRef](#)]
25. Di Sarli, V.; Di Benedetto, A. Laminar burning velocity of hydrogen–methane/air premixed flames. *Int. J. Hydrogen Energy* **2007**, *32*, 637–646. [[CrossRef](#)]
26. Bourque, G.; Healy, D.; Curran, H.; Zinner, C.; Kalitan, D.; de Vries, J.; Aul, C.; Petersen, E. Ignition and Flame Speed Kinetics of Two Natural Gas Blends with High Levels of Heavier Hydrocarbons. *J. Eng. Gas Turbines Power* **2008**, *132*, 1051–1066, ASME Paper GT2008-51344. [[CrossRef](#)]
27. Tahtouh, T.; Halter, F.; Samson, E.; Mounaim-Rousselle, C. Effects of hydrogen addition and nitrogen dilution on the laminar flame characteristics of premixed methane–Air flames. *Int. J. Hydrogen Energy* **2009**, *34*, 8329–8338. [[CrossRef](#)]
28. Hermanns, R.T.E.; Konnov, A.A.; Bastiaans, R.J.M.; De Goeij, L.P.H.; Lucka, K.; Koehne, H. Effects of temperature and composition on the laminar burning velocity of CH₄ + H₂ + O₂ + N₂ flames. *Fuel* **2010**, *89*, 114–121. [[CrossRef](#)]
29. Salzano, E.; Cammarota, F.; Di Benedetto, A.; Di Sarli, V. Explosion behavior of hydrogen–methane/air mixtures. *J. Loss Prev. Process Ind.* **2012**, *25*, 443–447. [[CrossRef](#)]
30. Donohoe, N.; Heufer, A.; Metcalfe, W.K.; Curran, H.J.; Davis, M.L.; Mathieu, O.; Plichta, D.; Morones, A.; Petersen, E.L.; Güthe, F. Ignition delay times, laminar flame speeds, and mechanism validation for natural gas/hydrogen blends at elevated pressures. *Combust. Flame* **2014**, *161*, 1432–1443. [[CrossRef](#)]
31. Dayma, G.; Zhang, S.; Li, Q.F.; Pan, X.B.; Liao, S.Y.; Wang, H.Q.; Yang, C.; Wei, S. Experimental investigation on the effects of hydrogen addition on thermal characteristics of methane/air premixed flames. *Fuel* **2014**, *115*, 232–240. [[CrossRef](#)]
32. Jithin, E.V.; Varghese, R.J.; Velamati, R.K. Experimental and numerical investigation on the effect of hydrogen addition and N₂/CO₂ dilution on laminar burning velocity of methane/oxygen mixtures. *Int. J. Hydrogen Energy* **2020**, *45*, 16838–16850. [[CrossRef](#)]
33. Di Sarli, V.; Di Benedetto, A.; Long, E.J.; Hargrave, G.K. Time-Resolved Particle Image Velocimetry of dynamic interactions between hydrogen-enriched methane/air premixed flames and toroidal vortex structures. *Int. J. Hydrogen Energy* **2012**, *37*, 16201–16213. [[CrossRef](#)]
34. Di Sarli, V.; Di Benedetto, A. Effects of non-equidiffusion on unsteady propagation of hydrogen-enriched methane/air premixed flames. *Int. J. Hydrogen Energy* **2013**, *38*, 7510–7518. [[CrossRef](#)]
35. El-Sherif, S.A. Control of emissions by gaseous additives in methane–Air and carbon monoxide–Air flames. *Fuel* **2000**, *79*, 567–575. [[CrossRef](#)]
36. Huang, Z.; Zhang, Y.; Zeng, K.; Liu, B.; Wang, Q.; Jiang, D. Measurements of laminar burning velocity for natural gas-hydrogen-air-mixtures. *Combust. Flame* **2006**, *146*, 302–311. [[CrossRef](#)]
37. Huang, Z.; Zhang, Y.; Wang, Q.; Wang, J.; Jiang, D.; Miao, H. Study on flame propagation characteristics of natural gas–hydrogen–air mixtures. *Energy Fuels* **2006**, *20*, 2385–2390. [[CrossRef](#)]
38. Huang, Z.; Zhang, Y.; Zeng, K.; Liu, B.; Wang, Q.; Jiang, D. Natural gas-hydrogen-air premixed mixture combustion with a constant volume bomb. *Energy Fuels* **2007**, *21*, 692–698. [[CrossRef](#)]
39. Miao, H.; Jiao, Q.; Huang, Z.; Jiang, D. Measurement of laminar burning velocities and Markstein lengths of diluted hydrogen-enriched natural gas. *Int. J. Hydrogen Energy* **2009**, *34*, 507–518. [[CrossRef](#)]

40. Zheng, S.; Zhang, X.; Xu, J.; Jin, B. Effects of initial pressure and hydrogen concentration on laminar combustion characteristics of diluted natural gas–hydrogen–Air mixture. *Int. J. Hydrogen Energy* **2012**, *37*, 12852–12859. [CrossRef]
41. De Ferrières, S.; El Bakali, A.; Gasnot, L.; Montero, M.; Pauwels, J.F. Kinetic effect of hydrogen addition on natural gas premixed flames. *Fuel* **2013**, *106*, 88–97. [CrossRef]
42. Song, Z.; Zhang, X.; Hou, X.; Li, M. Effect of initial pressure, temperature and equivalence ratios on laminar combustion characteristics of hydrogen enriched natural gas. *J. Energy Inst.* **2018**, *91*, 887–893. [CrossRef]
43. Schroeder, V.; Askar, E.; Habib, A.K.; Tashqin, T. Sicherheitstechnische Eigenschaften von Erdgas-Wasserstoff-Gemischen. *Res. Rep.* **VH2539** **2016**.
44. Cellek, M.S. Flameless combustion investigation of CH₄/H₂ in the laboratory-scaled furnace. *Int. J. Hydrogen Energy* **2020**, *45*, 35208–35222. [CrossRef]
45. Ceriello, G.; Sorrentino, G.; Cavaliere, A.; Sabia, P.; de Joannon, M.; Ragucci, R. The role of dilution level and canonical configuration in the modeling of MILD combustion systems with internal recirculation. *Fuel* **2020**, *264*, 116840. [CrossRef]
46. European Standard EN 15967. *Determination of Maximum Explosion Pressure and the Maximum Rate of Pressure Rise of Gases and Vapours*; 2011.
47. Lowesmith, B.J.; Hankinson, G. Large scale high pressure jet fires involving natural gas and natural gas/hydrogen mixtures. *Process Saf. Environ. Prot.* **2012**, *90*, 108–120. [CrossRef]
48. Janès, A.; Lesage, J.; Weinberger, B.; Carson, D. Experimental determination of minimum ignition current (MIC) ratio of hydrogen/methane (H₂NG) blends up to 20 vol.% of hydrogen. *Process Saf. Environ. Prot.* **2017**, *107*, 299–308. [CrossRef]
49. Amin, M.T.; Khan, F.; Amyotte, P. A bibliometric review of process safety and risk analysis. *Process Saf. Environ. Prot.* **2019**, *126*, 366–381. [CrossRef]
50. European Standard EN 1839. *Determination of Explosion Limits of Gases and Vapours*; 2017.
51. COSILAB, Version 3.0.3; Rotexo-Softpredict-Cosilab GmbH & Co KG: Bad Zwischenhahn, Germany, 2012.
52. Giurcan, V.; Razus, D.; Mitu, M.; Oancea, D. Numerical study of the laminar flame propagation in ethane-air mixtures. *Cent. Eur. J. Chem.* **2014**, *12*, 391–402. [CrossRef]
53. Mitu, M.; Giurcan, V.; Razus, D.; Oancea, D. Inert gas influence on the laminar burning velocity of methane-air mixtures. *J. Hazard. Mater.* **2017**, *321*, 440–448. [CrossRef]
54. Razus, D.; Oancea, D.; Movileanu, C. Burning velocity evaluation from pressure evolution during the early stage of closed-vessel explosions. *J. Loss Prev. Process Ind.* **2006**, *19*, 334–342. [CrossRef]
55. Dobashi, R. Experimental study on gas explosion behavior in enclosure. *J. Loss Prev. Process Ind.* **1997**, *10*, 83–89. [CrossRef]
56. Knapton, J.; Stobie, I.; Krier, H. Burning Rate Studies of Fuel Air Mixtures at High Pressures. *Combust. Flame* **1973**, *21*, 211–220. [CrossRef]
57. Sapko, M.; Furno, A.; Kuchta, J. *Flame and Pressure Development of Large-Scale CH₄-Air-N₂ Explosions*; U.S. Bureau of Mines Report No. 8176; Bureau of Mines, US Department of the Interior: Washington, DC, USA, 1976.
58. Mitu, M.; Razus, D.; Giurcan, V.; Oancea, D. Normal burning velocity and propagation speed of ethane–Air: Pressure and temperature dependence. *Fuel* **2015**, *147*, 27–34. [CrossRef]
59. Razus, D.; Oancea, D.; Brinzea, V.; Mitu, M.; Movileanu, C. Experimental and computed burning velocities of propane–Air mixtures. *Energy Convers. Manag.* **2010**, *51*, 2979–2984. [CrossRef]
60. Giurcan, V.; Mitu, M.; Razus, D.; Oancea, D. Experimental study and kinetic modeling of laminar flame propagation in premixed stoichiometric n-butane-air mixture. *Rev. Chim. (Bucharest)* **2019**, *70*, 1125–1131. Available online: <https://revistadechimie.ro/pdf/5%20GIURCAN%204%2019.pdf> (accessed on 8 November 2021). [CrossRef]
61. Razus, D.; Mitu, M.; Giurcan, V.; Movileanu, C.; Oancea, D. Methane-unconventional oxidant flames. Laminar burning velocities of nitrogen-diluted methane–N₂O mixtures. *Process Saf. Environ. Prot.* **2018**, *114*, 240–250. [CrossRef]
62. Dahoe, A.E.; de Goey, L.P.H. On the determination of the laminar burning velocity from closed vessel gas explosions. *J. Loss Prev. Process Ind.* **2003**, *16*, 457–478. [CrossRef]
63. Metghalchi, M.A.K.J.; Keck, J.C. Laminar burning velocity of propane-air mixtures at high temperature and pressure. *Combust. Flame* **1980**, *38*, 143–154. [CrossRef]
64. Elia, M.; Ulinski, M.; Metghalchi, M. Laminar burning velocity of methane–Air–diluent mixtures. *J. Eng. Gas Turbines Power* **2001**, *123*, 190–196. [CrossRef]
65. Rahim, F.; Elia, M.; Ulinski, M.; Metghalchi, M. Burning velocity measurements of methane-oxygen-argon mixtures and an application to extend methane-air burning velocity measurements. *Int. J. Engine Res.* **2002**, *3*, 81–92. [CrossRef]
66. Razus, D.; Brinzea, V.; Mitu, M.; Movileanu, C.; Oancea, D. Burning velocity of Propane-Air Mixtures from Pressure-time Records during Explosions in a Closed Spherical Vessel. *Energy Fuels* **2012**, *26*, 901–909. [CrossRef]
67. Mitu, M.; Razus, D.; Giurcan, V.; Oancea, D. Experimental and Numerical Study of Laminar Burning Velocity of Ethane-Air Mixtures of Variable Initial Composition, Temperature and Pressure. *Energy Fuels* **2014**, *28*, 2179–2188. [CrossRef]
68. Zhang, Y.; Fu, J.; Shu, J.; Xie, M.; Liu, J. A chemical kinetic investigation of laminar premixed burning characteristics for methane-hydrogen-air mixtures at elevated pressures. *J. Taiwan Inst. Chem. Eng.* **2020**, *111*, 141–154. [CrossRef]
69. Salzano, E.; Pio, G.; Ricca, A.; Palma, V. The effect of a hydrogen addition to the premixed flame structure of light alkanes. *Fuel* **2018**, *234*, 1064–1070. [CrossRef]

70. Tang, C.; Zhang, Y.; Huang, Z. Progress in combustion investigations of hydrogen enriched hydrocarbons. *Renew. Sustain. Energy Rev.* **2010**, *30*, 195–216. [[CrossRef](#)]
71. Zabetakis, M. *Flammability Characteristics of Combustible Gases and Vapors*; No. 627; US Bureau of Mines Bull, US Department of the Interior: Washington, DC, USA, 1965.
72. Dayma, G.; Halter, F.; Dagaut, P. New insights into the peculiar behavior of laminar burning velocities of hydrogen—Air flames according to pressure and equivalence ratio. *Combust. Flame* **2014**, *161*, 2235–2241. [[CrossRef](#)]
73. Su, B.; Luo, Z.; Wang, T.; Xie, C.; Cheng, F. Chemical kinetic behaviors at the chain initiation stage of CH₄/H₂/air mixture. *J. Hazard. Mater.* **2021**, *403*, 123680. [[CrossRef](#)] [[PubMed](#)]
74. Glassman, I.; Yetter, R. *Combustion*, 4th ed.; Chapter 4; Academic Press: Burlington, MA, USA, 2008. [[CrossRef](#)]
75. Lide, D.R. CRC Handbook of Chemistry and Physics. Internet Version. 2005. Available online: <http://www.hbcpnetbase.com> (accessed on 9 October 2020).

Article

Effects of the Multiple Injection Strategy on Combustion and Emission Characteristics of a Two-Stroke Marine Engine

Ju-Hwan Seol¹, Van Chien Pham^{2,*} and Won-Ju Lee^{3,4,*}¹ South Sea Fisheries Management Service, 128 Imhang-ro, Jeju-si 63280, Korea; seoljh0721@naver.com² Graduate School, Korea Maritime and Ocean University, 727, Taejong-ro, Yeongdo-gu, Busan 49112, Korea³ Division of Marine System Engineering, Korea Maritime and Ocean University, 727, Taejong-ro, Yeongdo-gu, Busan 49112, Korea⁴ Interdisciplinary Major of Maritime AI Convergence, Korea Maritime and Ocean University, 727, Taejong-ro, Yeongdo-gu, Busan 49112, Korea

* Correspondence: phamvanchien.kmou@gmail.com (V.C.P.); skywonju@kmou.ac.kr (W.-J.L.); Tel.: +82-51-410-4262 (W.-J.L.)

Abstract: This paper presents research on the effects of the multiple injection strategies on the combustion and emission characteristics of a two-stroke heavy-duty marine engine at full load. The ANSYS FLUENT simulation software was used to conduct three-dimensional simulations of the combustion process and emission formations inside the engine cylinder in both single- and double-injection modes to analyze the in-cylinder pressure, temperature, and emission characteristics. The simulation results were then compared and showed good agreement with the measured values reported in the engine's sea-trial technical reports. The simulation results showed reductions in the in-cylinder pressure and temperature peaks by 6.42% and 12.76%, while NO and soot emissions were reduced up to 24.16% and 68%, respectively, in the double-injection mode in comparison with the single-injection mode. However, the double-injection strategy increased the CO₂ emission (7.58%) and ISFOC (23.55%) compared to the single-injection. These are negative effects of the double-injection strategy on the engine that the operators need to take into consideration. The results were in line with the literature reviews and would be good material for operators who want to reduce the engine exhaust gas emission in order to meet the stricter IMO emission regulations.

Keywords: two-stroke engine; multiple injection; combustion; emission; numerical simulation; computational fluid dynamic (CFD)

Citation: Seol, J.-H.; Pham, V.C.; Lee, W.-J. Effects of the Multiple Injection Strategy on Combustion and Emission Characteristics of a Two-Stroke Marine Engine. *Energies* **2021**, *14*, 6821. <https://doi.org/10.3390/en14206821>

Academic Editor: Talal Yusaf

Received: 17 September 2021

Accepted: 14 October 2021

Published: 19 October 2021

Publisher's Note: MDPI stays neutral with regard to jurisdictional claims in published maps and institutional affiliations.



Copyright: © 2021 by the authors. Licensee MDPI, Basel, Switzerland. This article is an open access article distributed under the terms and conditions of the Creative Commons Attribution (CC BY) license (<https://creativecommons.org/licenses/by/4.0/>).

1. Introduction

In comparison with gasoline engines, direct injection (DI) diesel engines offer better reliability and higher thermal efficiency. Therefore, they have been being widely and commonly used not only in light-duty public transport, private vehicles but also in heavy-duty marine transportation. However, because of the increasing environmental hazards of marine engine exhaust emissions, as well as the International Maritime Organization (IMO) emission regulations being more and more stringent, the exhaust gas emissions such as nitrogen oxide (NO_x), soot, and carbon dioxide (CO₂) must be reduced to meet the stricter emission standards [1].

Theoretically, engine exhaust gas emission reduction approaches are divided into three categories, including (1) pre-treatment; (2) internal treatment; and (3) post-treatment [2]. In the pre-treatment approach, fuels, the main factor that affect the engine's combustion and emission characteristics, are substituted or handled prior to supply to engines. Regarding substitute fuels, various gas fuels are currently being increasingly employed in marine engines to reduce engine exhaust gas emissions. Effects of various alternative gas fuels on reducing engine exhaust gas emissions were analyzed in detail in our previous publications [3,4].

In the internal treatment approach, the combustion of the fuel inside the engine cylinder will be modified towards the goal of achieving lower exhaust gas emissions. Using innovative fuel injection systems [5,6], lean or rich combustions [7], pre-chamber type combustion, innovative combustion bowl feature [8], etc. are examples of this method. In addition, the method of adding water to the engine combustion chamber to reduce the peak temperature in the cylinder or modifying the engine working cycle (exhaust gas recirculation–EGR for example) are also other effective ways to reduce emissions. They are also being effectively used in the marine industry today.

In the post-treatment approach, it is necessary to equip exhaust gas after-treatment devices to treat the exhaust gas after it has left the engine. Using selective catalytic reduction (SCR) systems for NO_x reduction is an example of this method [2]. These methods don't require modifications on fuels or existing engines, but exhaust gas after-treatment devices are mandatory. This results in an increase in additional costs and makes the engine room become more cramped.

Focusing on the internal treatment approach, multiple injection strategies have been proven to be effective solutions to reduce soot or even NO_x and soot simultaneously in both heavy-duty DI diesel engines [9–13] and light-duty DI diesel engines [14–23]. Nehmer and Reitz [9] showed that multiple injection helps to reduce both particle matter (PM) and NO_x emissions from controlled pressure rise. The effectiveness of multiple injection strategies for the simultaneous reduction of NO_x and PM in DI diesel engines was also reported in [10,11,13–16,18–22]. Numerical simulations were also carried out to explore the chemical mechanism of NO_x and soot reduction for multiple injection strategies by Han et al. [11]. They found that, in multiple-injection strategies, due to the subsequent injections occurred in a high-temperature environment that was produced by combustion of previous injections, the injected fuel burnt more rapidly resulting in a reduction in soot formation rates. Therefore, the net production of soot was dramatically reduced. Furthermore, soot formed in a high-temperature environment had been oxidized more effectively leading to a great reduction in engine-out soot emissions in multiple injection strategies. These previous researches have proven that multiple injection strategies have similar effects to the retarded injection strategy in the single injection method on NO_x reduction applied on conventional DI diesel engines. The reduction in soot emissions is due to the fact that the soot-producing fuel-rich regions are significantly reduced when the fuel dose is divided into several times to be injected into the combustion chamber. Zhang [14] reported that the soot emission was closely related to the pilot flame (first-dose injection flame) and could be reduced by reducing this pilot flame by using only a small amount of fuel for the first injection in multiple injection strategies. Another study on multiple injection strategies was done by Tanaka et al. [16]. They also reported that it is possible to simultaneously reduce exhaust gas emissions by decreasing the influence of the pilot flame through minimizing the fuel quantity in the pilot (first-time) injection or retarding this first-time injection timing.

Meanwhile, Choi and Reitz [17] experimentally studied the effects of single and split injections on soot formation in a DI engine. They found that the split injection reduced soot emissions without penalty on NO_x emissions compared with the single injection. Montgomery and Reitz [12] also reported the same finding when they evaluated the effects of EGR and multiple injections on PM and NO_x emissions from a DI diesel engine. Yang and Chung also reported in [23] that, when multiple injection strategies were applied, a significant reduction in soot emissions could be achieved without penalty on NO_x emissions.

Based on the literature above, it is clear that the multiple injection strategy offers an effective solution to reduce engine exhaust gas emissions. This study focuses on the combustion process and emission characteristics inside the cylinder of a two-stroke marine main engine equipped on a university's training ship.

The simulation software ANSYS Fluent with its state-of-the-art models was used to perform 3D simulations calculating the combustion process and emission formation inside

the engine cylinder. There are two operating modes of the engine that have been simulated, including the single injection mode and the double injection mode, in order to analyze the engine in-cylinder pressure, temperature, and emission characteristics. The simulation results were then validated by comparing them with the engine's sea-trial data.

2. Simulated Engine and CFD Analysis

2.1. Simulated Engine Specifications

The research object of this study is a 2-stroke diesel marine engine. The combustion process of the engine is studied and simulated to investigate the effects of the double-injection strategy on the engine's in-cylinder pressure, temperature, and emission characteristics compared to those when using the conventional single-injection strategy. Two engine operating modes were simulated: (1) single-injection mode and (2) double-injection mode. In both the two modes, apart from changes in the injection strategy, other operating parameters, and thus simulation parameters were kept unchanged in order to clearly investigate the effects of the injection strategy on the engine output and emissions.

The three-dimensional (3D) model of the engine cylinder, piston, cylinder head with exhaust valve of the simulated engine is shown in Figure 1. The engine has six cylinders with only one exhaust valve on each cylinder mounted at the cylinder head center and two fuel injectors mounted symmetrically on the cylinder head. The piston surface is a U-type shape. The engine cylinder diameter and piston stroke are 420 mm and 1360 mm, respectively. Specifications of the simulated engine are shown in Table 1.

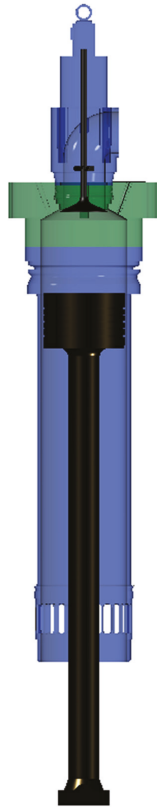


Figure 1. Structure principle schematic of the simulated engine.

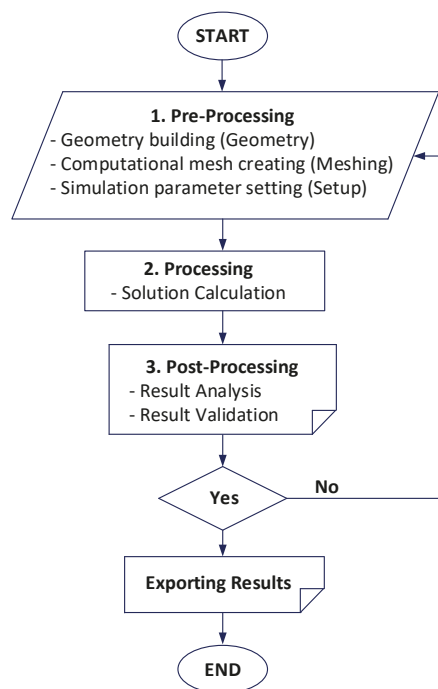
Table 1. The specifications of the simulated engine.

Parameter	Value	Unit
Type of Engine	2-Stroke Diesel Engine	
Name of Engine	6L42MC-ME	
No. of Cylinder	6	
Cylinder Bore × Stroke	420 × 1360	mm
Connecting Rod Length	1700	mm
Compression Ratio	13.5	
Rated Power @ Rated Speed	4485 @ 160	kW @ rpm
IMEP	18	bar
No. of Fuel Injector	2	
Fuel	Diesel (C ₁₀ H ₂₂)	
LCV of Diesel	42,343 *	kJ/kg

* Provided by ANSYS Fluent database.

2.2. CFD Analysis

The ANSYS Fluent 2019R2 simulation software with its state-of-the-art models was employed to simulate the combustion and emission formation inside the engine cylinder. The simulation process was performed from the exhaust valve closing (EVC) to the exhaust valve opening (EVO) and included three steps: (1) pre-processing, (2) processing, and (3) post-processing. The first step included building the computational domain (Geometry), creating movable computational meshes (Meshing), and setting up the simulation parameters (Setup). The solutions were calculated in the second step. In the third step, the simulation results were analyzed and reported. After obtaining the simulation results, the simulation results and measured results were compared for the validation of the simulation models. This process was repeated until the simulation and measured results matched. Figure 2 shows the workflow of the study.

**Figure 2.** The workflow of the study.

The $k-\epsilon$ turbulence model was selected to simulate the turbulence of the fluid flow inside the engine cylinder. This is the commonly widely used model in the simulation of the combustion of internal combustion engines (ICEs) [24]. To simulate the combustion process of the engine the Non-premixed Combustion model was used. This model allows simulating non-premixed combustion in which fuels and oxidizers are supplied to the combustion chamber separately [25]. The Discrete Phase Model (DPM) was used to simulate the fuel injection. This model offers a way to correct the injection velocities and initial droplet diameters due to cavitation. In order to simulate the breaking up of the phenomenon of fuel droplets, the Kelvin-Helmholtz Rayleigh-Taylor (KHRT) sub-model was used. The Auto-ignition model was used for simulating the self-ignition phenomenon that occurs in an auto-ignited diesel engine.

The Extended Zeldovich model was used to simulation the NO formation characteristic [25,26]. This chemical reaction mechanism consists of seven species and three reactions and is able to predict NO formation with high accuracy over a wide range of equivalence ratios. This model was presented in detail and can be found in Appendix C of our previous publication [3,4]. The Moss-Brookes model [25,27] was used to simulate the soot formation due to the combustion process. To simulate the collisions and interactions between fuel droplets and walls the Stochastic Collision sub-model, which is based on the algorithm of O'Rourke [25], was used. The non-premixed combustion model and Moss-Brookes soot models can be found in references [25,27]. Other CFD models can be found in references [25–27]. Table 2 shows a summary of the numerical models used in this study.

Table 2. The summary of the numerical models.

Model	Description	
Combustion	Non-premixed Combustion model [25]	
Emission	NO	Extended Zeldovich
	Soot	Moss-Brookes model
Atomization	Spray	Discrete Phase Model (DPM)
	Breakup	KHRT
	Ignition	Auto-ignition
Collision	Stochastic Collision model	
Turbulence	$k-\epsilon$ turbulence model	

2.3. Computational Mesh, Boundary and Initial Conditions

The combustion chamber geometry was built by using the AutoCAD software (Autodesk, California, USA) and the computational mesh was then created by the ANSYS (Autodesk, California, USA) Meshing platform. The boundary conditions (BCs), initial conditions, and simulation parameters were declared in the setup platform. The solution was then calculated in series using an 8-core processor and took approximately 72 h of CPU time. Figure 3 shows half of the 3D symmetry combustion chamber geometry while Figure 4 shows half of the 3D computational mesh of the combustion chamber at the top dead center (TDC).

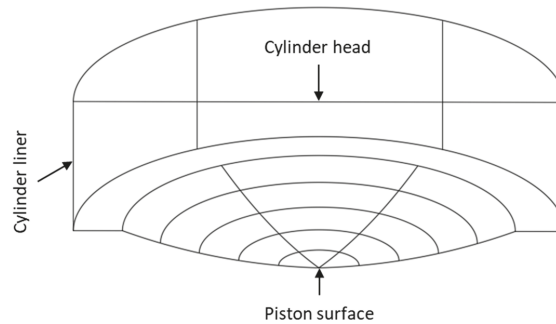


Figure 3. Half of the 3D symmetry combustion chamber geometry.

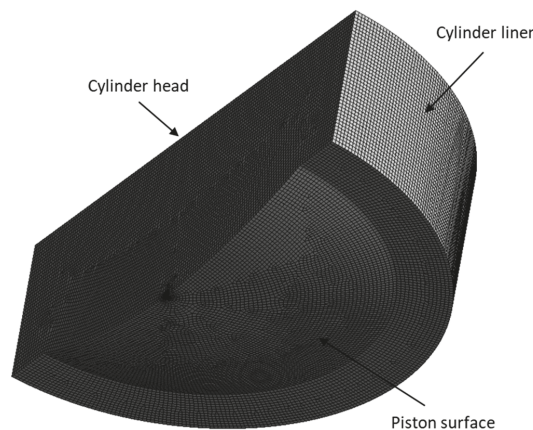


Figure 4. Half of the 3D computational mesh of the combustion chamber at the TDC.

Due to the movement of the piston, we needed to use a dynamic mesh in this study. Due to the re-meshing during calculation, the mesh quality and mesh resolution might be changed. In order to keep the mesh quality within acceptable range, we used the dynamic layering method with a collapse factor of 0.4 and a split factor of 0.4 for dynamic moving mesh modeling. The computational mesh will be re-meshed according to the movement of the piston based on the dynamic layering method. Specifically, during the piston downward movement, mesh layers will be added when the outermost layer (boundary piston surface mesh layer) height increases by more than 40% (split factor of 0.4) of the declared height when setting the meshing. In contrast, during the piston upward movement, mesh layers will be collapsed when the outermost layer height decreases by more than 40% (collapse factor of 0.4) of the declared height. This means that the number of mesh layers and thus the number of elements will be increased or decreased according to the moving down or up of the piston. In this way, the mesh quality and resolution will be kept almost unchanged during calculation.

Due to the specificity of the dynamic layering method, we have used hexahedral elements for computational mesh. This type of elements is also the most perfect for computational mesh due to its very high orthogonal quality. We had also performed a lot of simulations with different mesh resolutions (coarse, medium, and fine) until mesh-independence of the calculation results was achieved. Finally, we obtained the final mesh with parameters as shown in Table 3.

Table 3. Mesh Statistics and Quality.

Mesh Statistics and Quality	
Type of elements	Hexahedral
No. of nodes at the TDC	459,058
No. of elements at the TDC	508,650
Aspect ratio	17.05
Maximum Skewness ratio	0.76
Minimum Orthogonal quality	0.45

The BCs at the cylinder head, piston surface and cylinder liner were defined as impermeable wall BCs. The cylinder geometry was planed symmetric, so the cyclic BCs were assigned to the cutting surfaces of the computational domain. The simulation was started from the EVC of 30 CAD after the bottom dead center (ABDC) (EVC = 30 CAD ABDC) to the EVO of 30 CAD before the bottom dead center (BBDC) (EVO = 30 CAD BBDC). The schematic of the engine working cycle is shown in Figure 5 while Figure 6 shows the start of injection (SOI) and injection duration in both the single and double injection modes.

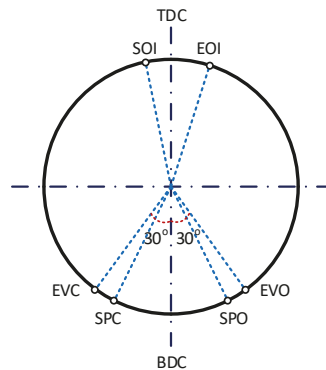


Figure 5. The schematic of the engine working cycle (TDC: Top dead center; BDC: Bottom dead center; EVO: Exhaust valve opens; EVC: Exhaust valve closes; SPO: Scavenging-air port opens; SPC: Scavenging-air port closes; SOI: Start of injection; EOI: End of injection).

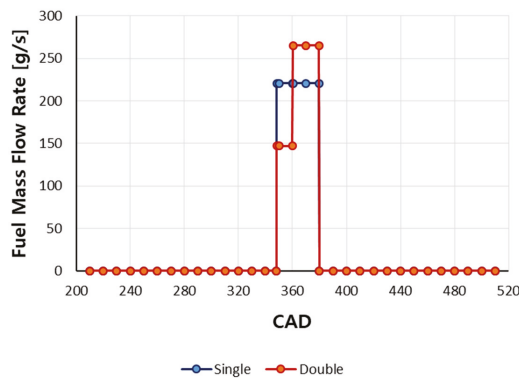


Figure 6. Injection properties in the operating modes.

The BCs and initial conditions were chosen from the sea-trial report of the actual engine provided by the operating officer. Table 4 shows the BCs and initial conditions for the numerical simulation cases.

Table 4. Boundary conditions and initial conditions for the numerically simulation cases.

Boundary Conditions	Boundary Type/Specific Condition
Cylinder head	Wall/Temp./297 °C
Piston	Mesh movement/Temp./297 °C K
Liner	Wall/Temp./197 °C
Segment cut	Cyclic
Initial conditions	Value
Scavenging air Press.	2.0 bar
Scavenging air Temp.	28 °C
EVC	30 CAD ABDC
EVO	30 CAD BBDC
SOI	12 CAD BTDC
Injection duration	32 CAD

2.4. Simulation Cases and Fuel Properties

In this study, the combustion process of the engine running in two fuel injection modes at full load was simulated, including single injection and double injection. In single injection mode, fuel was injected directly into the engine's combustion chamber in just one injection. Meanwhile, the fuel was divided into two injections to inject into the engine's combustion chamber in double injection mode. All other simulation conditions were kept unchanged. The properties of the diesel fuel are shown in Table 5.

Table 5. The diesel fuel properties [25,28,29].

Fuel	Diesel	Unit
Density	730	kg/m ³ @ 25 °C, 1 at
Chemical name/formula	Diesel/C ₁₀ H ₂₂	
Lower calorific value	42,000	kJ/kg
Molecular weight	142.284	kg/kmol
Boiling point	174	°C
Auto-Ignition temperature	223	°C
Specific heat capacity (Cp)	2090	J/kg·K @ 25 °C

The simulation results were then validated against the engine's sea-trial data provided by the engine manufacturer. The simulation results showed a good agreement with the measured results written in the engine's sea-trial technical reports and were presented in detail in Section 3—Simulation results.

3. Simulation Results

To clearly investigate the effects of the injection strategy on the combustion and emission characteristics of the engine, all of the BCs and engine's working conditions were kept unchanged, excepting the difference in the fuel injection strategy. In this section, the in-cylinder pressure, temperature and emissions characteristics of the engine will be presented and analyzed.

3.1. In-Cylinder Pressure

The simulated in-cylinder pressure diagrams in both injection modes are shown in Figure 7a while Figure 7b shows the comparison between simulated and experimental peak

pressure inside the engine cylinder obtained from the sea-trial. As can be seen in Figure 7, the peak pressures in both single and double injections are similar to those in comparison with the experimental results. The deviation between simulated and experimental results in the single injection mode was only 4.85%, while it was 8.3% in the double injection mode. These deviations are acceptable in CFD analysis. Comparing the two simulation cases, the results showed that the in-cylinder peak pressure in the double injection mode was 6.42% lower than that compared with the single injection mode (Figure 7a).

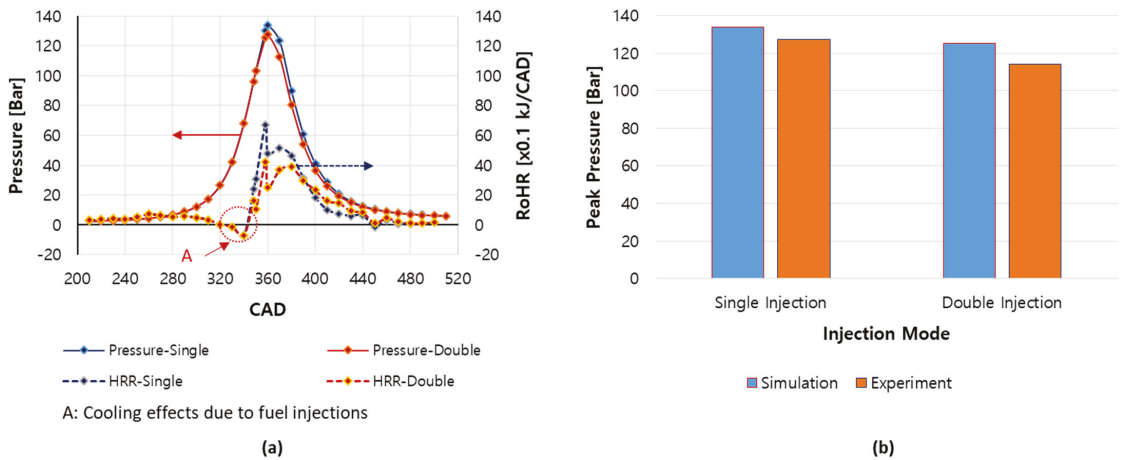


Figure 7. Simulated cylinder pressure diagrams (a) and comparison between simulated and experimental peak pressure (b).

As shown in Figure 6, in the double injection mode, since only 25% of the total fuel was injected into the engine cylinder before the TDC and 75% of the total fuel was injected from the TDC, the rate of heat release (RoHR) in the engine cylinder before the TDC in the double injection mode was lower than that in the single-injection mode. From the TDC, even though the fuel injected into the engine cylinder in the double injection mode was higher than that in the single-injection mode, but the fuel was injected after the TDC when the piston was in the downward movement. These resulted in a reduction in the in-cylinder peak pressure in the double injection mode compared with the single-injection mode, as shown in Figure 7a. The reductions in the in-cylinder peak pressure when using multiple injection strategy were also reported by Nehmer and Reitz in [9], and Qiu et al. in [22].

3.2. In-Cylinder Temperature

The in-cylinder temperature diagrams with RoHR traces in both simulation cases are shown in Figure 8. The simulation result showed that the in-cylinder peak temperature in the double-injection mode was lower than that in comparison with the single-injection mode. However, the mean in-cylinder temperature in the double-injection mode was higher than that compared with the single-injection mode during the expansion process. This resulted in a higher exhaust gas temperature in the double-injection mode compared to the single-injection mode.

As the same as in-cylinder peak pressure, the decrease in the in-cylinder peak temperature in double-injection compared with single-injection is the result of less fuel being injected before the TDC, resulting in lower RoHR inside the engine cylinder. On the other hand, more fuel was injected into the engine cylinder after the TDC in the double-injection mode resulting in a higher RoHR inside the engine cylinder and thus higher in-cylinder temperature during the expansion process as can be seen in Figure 8.

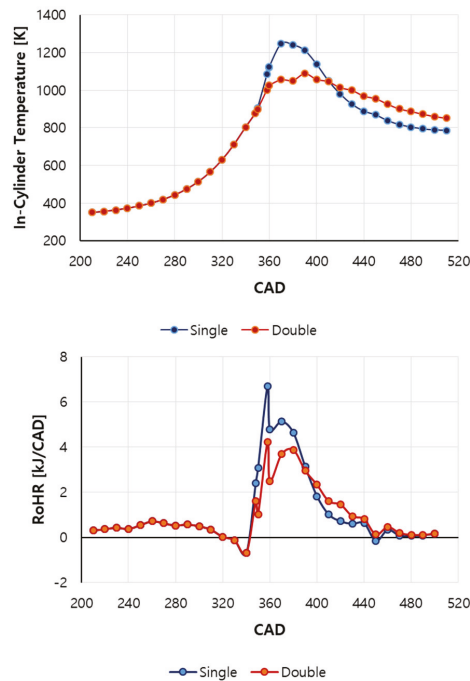


Figure 8. Simulated cylinder temperature diagrams with RoHR traces in both simulation cases.

3.3. NO Emission

The NO emissions generated in both injection modes are shown in Figure 9a, while Figure 9b shows the comparison between simulated and experimental NO emission of the engine obtained from the sea-trial. As can be seen in Figure 9a, the NO emission generated in the double injection mode was 24.16% lower than that compared with the single injection mode. Figure 9b shows a very good agreement between Simulated and experimental NO emission in both injection modes. The deviation between simulated and experimental results in the single injection mode was only 3.6%, while it also was only 3.62% in the double injection mode.

According to the extended Zelodovich NO formation mechanism, the NO formation is greatly influenced by the in-cylinder temperature peak and oxygen (O_2) concentration within the engine cylinder. NO formation occurs in regions in the cylinder where the local temperature is above 1800 K and the formation rate increase significantly with the increase of the local in-cylinder temperature [30–32]. The simulation results showed a reduction of 12.76% in the in-cylinder temperature peak in the double-injection mode compared to the single-injection mode (Figure 8). This resulted in a reduction of 24.16% in NO emission in the double-injection mode in comparison with the single-injection mode as shown in Figure 9a. Reduction effects on NOx emission as well as soot (PM) have been reported by Fang et al. in their publication on Fuel, 2008 [18] and other researchers in [9–11,13–16,19–22].

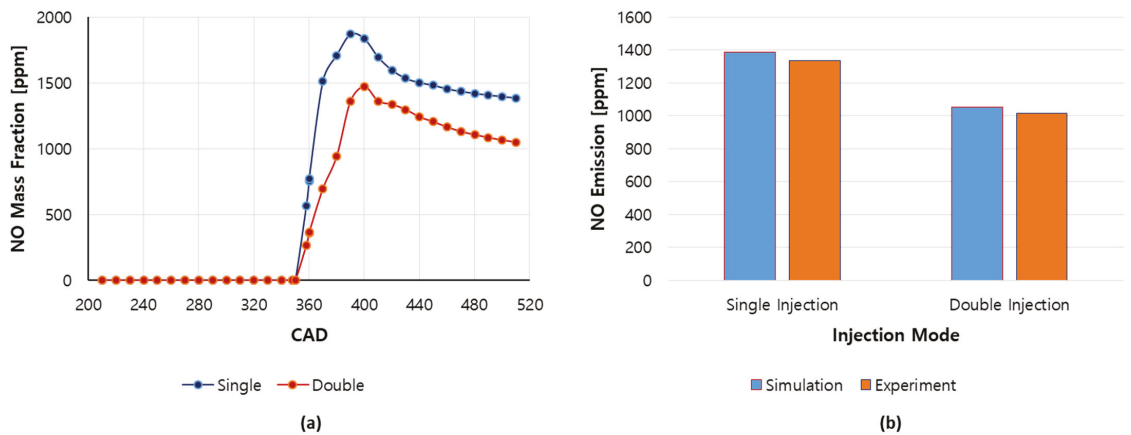
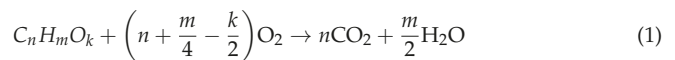


Figure 9. The mean NO mass fraction diagrams (a) and comparison between simulated and experimental NO emission (b).

3.4. Soot Formation

Soot is the main component of particulate matter (PM) emission [33–36]. Under high temperature and equivalence ratios (fuel-rich conditions), which are typically found in diesel diffusion combustions, hydrocarbon fuels have a strong tendency to form carbonaceous particles, i.e., soot. Soot particles are formed very early in the diffusion combustion process because of the dissociation of fuels under high temperature and high equivalence ratio conditions. Usually, under normal engine running conditions of diesel engines, most of the soot that formed in the early combustion stage will be depleted due to oxidation in the late stages of the combustion. This typically takes place in oxygen-rich regions of the combustion chamber in the late stage of the engine cycle (expansion process). Therefore, in diesel engines, the soot formation, and completeness of the soot oxidation process determines the particle emission characteristics of the engine [34]. The parameters that play the most important role during the soot formation inside the engine cylinder are the local equivalence fuel/air ratio (C/H -ratio and C/O -ratio), in-cylinder temperature, pressure, and residence time [34].

Under ideal reaction conditions, the products of hydrocarbon fuel combustions are only CO_2 and H_2O . The amount of oxygen required for a complete chemical reaction (the stoichiometric oxygen requirement- $O_{2, \text{stoichiometric}}$) can be calculated from the following reaction equation [25]:



In the above equation k , m , and n represent the number of oxygen, hydrogen and carbon atoms of the considered fuel, respectively.

The actual amount of oxygen available for combustion is expressed by the air access ratio λ or by its inversion, the equivalence (fuel-air) ratio ϕ :

$$\phi = \frac{1}{\lambda} = \frac{O_{2, \text{stoichiometric}}}{O_{2, \text{actual}}} \quad (2)$$

The soot formations in both injection modes are shown in Figure 10. The simulation results showed that the maximum soot emission generated in the double-injection mode was reduced up to more than 68%. In addition, the soot mass fraction plot in the double-injection mode showed two peaks as can be seen in Figure 10. This is the result of the double-injection strategy in which the fuel dose was divided into two injections to be injected into the engine cylinder.

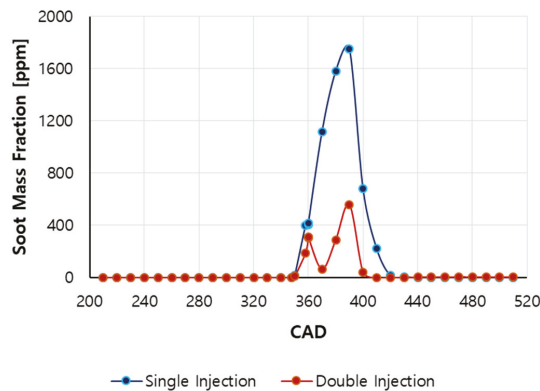


Figure 10. The mean soot mass fraction diagrams.

Reduction in soot formation is explained as the reduction effect in the fuel/air equivalence ratio ϕ . By dividing the fuel dose into two injections, the mass fraction of fuel in each injection was decreased resulting in a reduction in the fuel/air equivalence ratio, the factor that mainly and strongly affects the soot formation in ICES as widely known. Figure 10 also showed that, in the double-injection mode, the amount of soot produced inside the engine cylinder was not only reduced but they were also completely oxidized more quickly in comparison with the single-injection mode. This is because the oxidation of soot in the cylinders has been promoted by higher cylinder temperatures during the engine expansion process in the double-injection. Once again, reduction effects on soot as well as NO_x emission when using double-injection strategy is in line with the report by Fang et al. in their publication on Fuel, 2008 [18] and other researchers in [9–17,19–23].

In addition, Tree et al. mentioned in [37] that fuel pyrolysis plays an important role in soot formation in compression-ignition engines (CIEs). Pyrolysis is a process that changes the molecular structure of organic compounds, such as fuels, under high-temperature conditions without significant oxidation although O₂ species may be present. All fuels will undergo pyrolysis and produce basically the same species: polyacetylenes, polycyclic aromatic hydrocarbons (PAH), unsaturated hydrocarbons, and especially acetylene. Pyrolysis reactions are usually endothermic owing to the fact that their rates are strongly temperature-dependent [38]. Fuel pyrolysis leads to the production of some species which are precursors or building blocks for soot. Fuel pyrolysis to form soot precursor increase with temperature. Therefore, soot increases as the temperature increases. The same tendency was also reported in [39,40]. In this study, as presented in Figure 8, the in-cylinder peak temperature was reduced in the double-injection strategy. As a result, this resulted in a decrease in soot formation inside the engine cylinder, as shown in Figure 10.

3.5. Carbon Dioxide (CO₂) Emission

The CO₂ mass fraction in both injection modes is shown in Figure 11a, while Figure 11b shows the comparison between simulated and experimental CO₂ emission of the engine obtained from the sea-trial. The simulation results pointed that the CO₂ emission in the case of double-injection was 7.58% higher than that of single-injection (Figure 11a). In comparison with the experimental results, the deviation between the simulated and experimental CO₂ mass fraction was 7.36% (Figure 11b) and acceptable in CFD analysis.

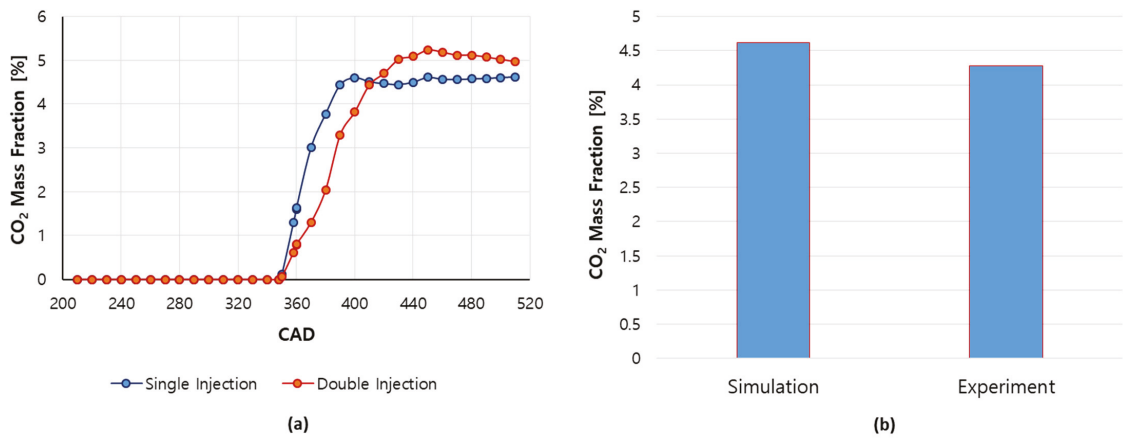


Figure 11. The mean CO₂ emission diagrams (a) and comparison between simulated and experimental CO₂ emission (b).

Regarding the reasons for the increasing CO₂ emission in the double-injection mode, as has been known, carbon dioxide is a product of the complete combustion of hydrocarbon fuels. Firstly, hydrocarbon fuels will be oxidized to CO during the combustion process, and then it is oxidized to form CO₂ sequentially if the in-cylinder temperature is high enough and there is still enough O₂ in the cylinder. Therefore, CO₂ formation strongly depends on the in-cylinder temperature and the concentration of oxygen in the engine cylinder. As can be seen in Figure 8, even though the in-cylinder peak temperature in the double-injection mode was lower than that in the single-injection mode, but the in-cylinder temperature during expansion stroke was higher because most of the fuel (75% of mass) was injected and burned after the TDC, in the late combustion phase of the double-injection mode. The higher temperature inside the engine cylinder during the late stage of the combustion in the case of double-injection mode promoted CO oxidation to produce CO₂ resulting in an increase in CO₂ emission in the double-injection mode in comparison with the single-injection mode, as shown in Figure 11a.

3.6. Specific Fuel Oil Consumption

Figure 12 shows the indicated specific fuel oil consumption (ISFOC) in both injection modes. The simulation results showed an increase in the ISFOC of the engine when operated in the double-injection mode. Specifically, the ISFOC was increased 23.55% when operating the engine in the double-injection mode compared to that in the single-injection mode. The increase in the ISFOC can be explained by a decrease in the peak pressure in the cylinder leading to a decrease in engine power when operated in the double-injection mode. This result points that using the double-injection strategy to reduce NO and soot emission not only results in an increase in CO₂ emission but also an increase in the SFOC of the engine. These are negative effects of the double-injection strategy on the engine that the operators need to take into consideration when operating the engine.

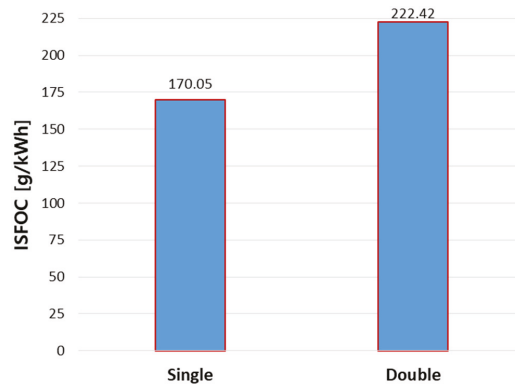


Figure 12. The ISFOC of the engine in both injection modes.

4. Conclusions

This paper numerically investigated the effects of the double-injection strategy on the combustion and emission characteristics of a two-stroke diesel marine engine. The simulation results were then compared and showed good agreement with the measured results obtained from the engine's sea-trials.

The main outcomes of the study are as follows:

- The in-cylinder peak pressure in the double-injection mode was 6.42% lower compared with the single injection mode.
- The in-cylinder peak temperature in the double-injection mode was lower in comparison with the single-injection mode resulting in a significant reduction in NO emission (24.16%).
- The maximum soot emission generated in the double-injection mode was reduced by more than 68% in comparison with the single-injection mode.
- However, the double-injection strategy increased the CO₂ emission (7.58%) and ISFOC (23.55%) compared to the single-injection. These are negative effects of the double-injection strategy on the engine that the operators need to take into consideration when operating the engine.

The results were in line with the existing literature and provides good material for operators who want to reduce engine exhaust gas emissions in order to meet the stricter IMO emission regulations.

Author Contributions: Conceptualization, V.C.P. and W.-J.L.; Methodology, V.C.P. and W.-J.L.; Software, V.C.P.; Validation, J.-H.S. and W.-J.L.; Formal analysis, J.-H.S.; Data curation, J.-H.S. and W.-J.L.; Writing—original draft preparation, V.C.P.; Writing—review and editing, V.C.P. and J.-H.S.; Project administration, W.-J.L.; Funding acquisition, W.-J.L. All authors have read and agreed to the published version of the manuscript.

Funding: This research was supported by the Ministry of Education of Republic of Korea and the National Research Foundation of Korea (NRF-2019R1G1A1005342) and by the Ministry of Science and ICT of Republic of Korea and National IT Industry Promotion Agency (S1226-21-1001).

Institutional Review Board Statement: Not applicable.

Informed Consent Statement: Not applicable.

Data Availability Statement: Not applicable.

Conflicts of Interest: The authors declare no conflict of interest.

References

- Thomson, H.; Corbett, J.J.; Winebrake, J.J. Natural gas as a marine fuel. *Energy Policy*. **2015**, *87*, 153–167. [CrossRef]
- Woodyard, D. *Pounders Marine Diesel Engines and Gas Turbines*, 9th ed.; Elsevier: Burlington, MA, USA, 2009.
- Pham, V.C.; Choi, J.H.; Rho, B.S.; Kim, J.S.; Park, K.N.; Park, S.K.; Le, V.V.; Lee, W.J. A numerical study on the combustion process and emission characteristics of a natural gas-diesel dual-fuel marine engine at full load. *Energies* **2021**, *14*, 1342. [CrossRef]
- Pham, V.C.; Rho, B.-S.; Kim, J.-S.; Lee, W.-J.; Choi, J.-H. Effects of various fuels on combustion and emission characteristics of a four-stroke dual-fuel marine engine. *J. Mar. Sci. Eng.* **2021**, *9*, 1072. [CrossRef]
- Martin, G.C.; Mueller, C.J.; Milam, D.M.; Radovanovic, M.S.; Gehrke, C.R. Early direct-injection, low-temperature combustion of diesel fuel in an optical engine utilizing a 15-hole, dual-row, narrow-included-angle nozzle. *SAE Int. J. Engines* **2008**, *1*, 1057–1082. [CrossRef]
- Polonowski, C.J.; Mueller, C.J.; Gehrke, C.R.; Bazyn, T.; Martin, C.M.; Lillo, M. An experimental investigation of low-soot and soot-free combustion strategies in a heavy-duty, single-cylinder, direct-injection, optical diesel engine. *SAE Int. J. Fuels Lubr.* **2012**, *5*, 51–77. [CrossRef]
- Dunn-Rankin, D. *Lean Combustion Technology and Control*; Elsevier Ltd.: Amsterdam, The Netherlands; Academic Press: Boston, MA, USA, 2011.
- Belgiorno, G.; Boscolo, A.; Dileo, G.; Numidi, F.; Pesce, F.C.; Vassallo, A.; Ianniello, R.; Beatrice, C.; Blasio, G.D. Experimental study of additive-manufacturing-enabled innovative diesel combustion bowl features for achieving ultra-low emissions and high efficiency. *SAE Int. J. Adv. Curr. Pract. Mobil.-V130-99E* **2021**, *3*, 672–684. [CrossRef]
- Nehmer, D.A.; Reitz, R.D. Measurement of the effect of injection rate and split injections on diesel engine soot and NOx emissions. *SAE Pap.* **1994**, 940668.
- Tow, T.C.; Pierpont, D.A.; Reitz, R.D. Reducing particulate and NOx emissions by using multiple injections in a heavy duty DI diesel engine. *SAE Pap.* **1994**, 940897.
- Han, Z.; Uludogan, A.; Hampson, G.J.; Reitz, R.D. Mechanism of soot and NOx emission reduction using multiple injection in a diesel engine. *SAE Pap.* **1996**, 960633.
- Montgomery, D.T.; Reitz, R.D. Six-mode cycle evaluation of the effect of EGR and multiple injections on particulate and NO_x emissions from a DI diesel engine. *SAE Tech. Pap.* **1996**, 960316.
- Pierpont, D.A.; Montgomery, D.T.; Reitz, R.D. Reducing particulate and NOx using multiple injections and EGR in a D.I. diesel. *J. Fuels Lubr.* **1995**, *104*, 171–183.
- Zhang, L. A study of pilot injection in a DI diesel engine. *SAE Pap.* **1999**, *1*, 3493.
- Chen, S.K. Simultaneous reduction of NOx and particulate emissions by using multiple injections in a small diesel engine. *SAE Pap.* **2000**, *1*, 3084.
- Tanaka, T.; Ando, A.; Ishizaka, K. Study on pilot injection of DI diesel engine using common rail injection system. *JSAE Rev.* **2002**, *23*, 297–302. [CrossRef]
- Choi, C.Y.; Reitz, R.D. An experimental study on the effects of oxygenated fuel blends and multiple injection strategies on DI diesel engine emissions. *Fuel* **1999**, *78*, 1303–1317. [CrossRef]
- Fang, T.; Coverdill, R.E.; Lee, C.F.; White, R.A. Effects of injection angles on combustion processes using multiple injection strategies in an HSDI diesel engine. *Fuel* **2008**, *87*, 3232–3239. [CrossRef]
- Chacko, N.; Rajkumar, S.; Thanragaja, J. Experimental and modeling analysis of multiple-injection strategies with B20 operation in a CRDI engine. *Fuel* **2021**, *293*, 120433. [CrossRef]
- Plamondon, E.; Seers, P. Parametric study of pilot–main injection strategies on the performance of a light-duty diesel engine fueled with diesel or a WCO biodiesel–diesel blend. *Fuel* **2019**, *236*, 1273–1281. [CrossRef]
- Jorques Moreno, C.; Stenlaas, O.; Tunestal, P. Influence of small pilot on main injection in a heavy-duty diesel engine. *SAE Tech. Pap.* **2017**, *1*, 708. [CrossRef]
- Qiu, L.; Cheng, X.; Liu, B.; Dong, S.; Bao, S.Z. Partially premixed combustion based on different injection strategies in a light-duty diesel engine. *Energy* **2016**, *96*, 155–165. [CrossRef]
- Yang, S.Y.; Chung, S.H. An experimental study on the effects of high-pressure and multiple injection strategies on DI diesel engine emissions. In *SAE Technical Paper Series*; SAE International: Warrendale, PA, USA, 2013.
- Durbin, P.A. Near-wall turbulence closure modeling without “damping functions”. *Theor. Comput. Fluid Dyn.* **1991**, *3*, 1–13.
- ANSYS *Fluent Theory Guide*; ANSYS, Inc.: Canonburg, PA, USA, 2013; Available online: <http://www.ansys.com> (accessed on 7 July 2021).
- Rao, V.; Honnery, D. A comparison of two NOx prediction schemes for use in diesel engine thermodynamic modelling. *Fuel* **2013**, *107*, 662–670. [CrossRef]
- Brookes, S.; Moss, J. Predictions of soot and thermal radiation properties in confined turbulent jet diffusion flames. *Combust. Flame*. **1999**, *116*, 486–503. [CrossRef]
- PubChem Compound. n-heptane–Compound Summary. National Center for Biotechnology Information. 8600 Rockville Pike, Bethesda MD, 20894 USA. 16 September 2004. Available online: <https://pubchem.ncbi.nlm.nih.gov/compound/8900> (accessed on 7 September 2020).
- Friend, D.G.; Ely, J.F. and Ingham, H. Thermophysical properties of methane. *J. Phys. Chem. Ref. Data* **1989**, *18*, 583. [CrossRef]
- Heywood, J.B. *Internal Combustion Engine Fundamentals*; McGraw-Hill Education: New York, NY, USA, 1998.

31. Wei, L.; Geng, P. A review on natural gas/diesel dual fuel combustion, emissions and performance. *Fuel Process. Technol.* **2016**, *142*, 264–278. [[CrossRef](#)]
32. Kuo, K.K. *Principles of Combustion*, 2nd ed.; John Wiley and Sons: New York, NY, USA, 2005.
33. Maricq, M.M.; Chase, R.E.; Xu, N.; Laing, P.M. The effects of the catalytic converter and fuel sulfur level on motor vehicle particulate matter emissions: Light duty diesel vehicles. *Environ. Sci. Technol.* **2002**, *36*, 283–289. [[CrossRef](#)]
34. Burnett, R.T.; Cakmak, S.; Brook, J.R.; Krewski, D. The role of particulate size and chemistry in the association between summertime ambient air pollution and hospitalization for cardiorespiratory diseases. *Environ. Health Perspect.* **1997**, *105*, 614–620. [[CrossRef](#)]
35. Kittelson, D.B.; Watts, W.F.; Johnson, J.P. On-road and laboratory evaluation of combustion aerosols -part 1: Summary of diesel engine results. *J. Aerosol Sci.* **2006**, *37*, 913–930. [[CrossRef](#)]
36. Rounce, P.; Tsolakis, A.; York, S.A.P.E. Speciation of particulate matter and hydrocarbon emissions from biodiesel combustion and its reduction by after-treatment. *Fuel* **2012**, *96*, 90–99. [[CrossRef](#)]
37. Tree, D.R.; Svensson, K.I. Soot processes in compression ignition engines. *Prog. Energy Combust. Sci.* **2007**, *33*, 272–309. [[CrossRef](#)]
38. Smith, O.I. Fundamentals of soot formation in flames with application to diesel engine particulate emissions. *Prog. Energy Combust. Sci.* **1981**, *7*, 275–291. [[CrossRef](#)]
39. Gowthaman, S.; Sathiyagnanam, A.P. Effects of charge temperature and fuel injection pressure on HCCI engine. *Alex. Eng. J.* **2016**, *55*, 119–125. [[CrossRef](#)]
40. Pan, W.; Yao, C.; Han, G.; Wei, H.; Wang, Q. The impact of intake air temperature on performance and exhaust emissions of a diesel methanol dual fuel engine. *Fuel* **2015**, *162*, 101–110. [[CrossRef](#)]

Article

Reactivity Model as a Tool to Compare the Combustion Process in Aviation Turbine Engines Powered by Synthetic Fuels

Tomasz Bialecki *, Wojciech Dzięgielewski , Mirosław Kowalski and Andrzej Kulczycki

Fuels and Lubricants Division, Air Force Institute of Technology (ITWL), 01-494 Warsaw, Poland; wojciech.dziewielewski@itwl.pl (W.D.); miroslaw.kowalski@itwl.pl (M.K.); andrzej.kulczycki@itwl.pl (A.K.)

* Correspondence: tomasz.bialecki@itwl.pl; Tel.: +48-261-851-406

Abstract: The paper aims to verify the thesis that the reactivity model, developed in earlier research, can be used to compare the fuels combustion processes in turbine engines, which is important for predicting the behavior of different alternative fuels in combustion process. Synthetic blending components from alcohol to jet and hydroprocessed esters and fatty acids technologies and their blends with conventional jet fuel were used in tests. The undertaken laboratory tests reveal the differences between the properties of the tested fuels. Bench tests were carried out on a test rig with a miniature turbojet engine, according to authorial methodology. For each blend, on selected points of rotational speed the carbon oxide concentration in the exhaust gases was recorded. The obtained results allowed the formulation of empirical power functions describing relations between carbon oxide concentration and fuel mass flow rate. Based on general assumptions, the reactivity model was adopted to compare the combustion processes of the different fuels in turbine engines. The directions of further research on the development of the proposed model were indicated.

Keywords: combustion process; reactivity model; synthetic jet fuels; turbine engines

Citation: Bialecki, T.; Dzięgielewski, W.; Kowalski, M.; Kulczycki, A. Reactivity Model as a Tool to Compare the Combustion Process in Aviation Turbine Engines Powered by Synthetic Fuels. *Energies* **2021**, *14*, 6302. <https://doi.org/10.3390/en14196302>

Academic Editors: Alexandre M. Afonso, Pedro Resende and Mohsen Ayooobi

Received: 29 July 2021

Accepted: 24 September 2021

Published: 2 October 2021

Publisher's Note: MDPI stays neutral with regard to jurisdictional claims in published maps and institutional affiliations.



Copyright: © 2021 by the authors. Licensee MDPI, Basel, Switzerland. This article is an open access article distributed under the terms and conditions of the Creative Commons Attribution (CC BY) license (<https://creativecommons.org/licenses/by/4.0/>).

1. Introduction

Intensive development of road and air transport leads to increasing air pollution from internal combustion engines. At a global scale, the most important is carbon dioxide (CO₂) emission, considered a cause of the global warming effect. At a local scale, more important is carbon oxide (CO) emission, unburned hydrocarbons, particulate matter (PM), as well as nitrogen oxides (NO_x) emissions.

The majority of countries have declared important the implementation of CO₂ emissions reduction programs and the promotion of the use of energy from renewable sources [1]. The fundamental way to achieve the goal is the implementation of biofuels into road, marine and air transport [2–4]. Alternative or synthetic fuels, unlike conventional fossil fuels, are produced from a feedstock other than crude oil. If the used feedstock is biomass, waste, animal fat, biogas, etc. then we define it as biofuels.

Biofuels have been implemented in road transport for about 20 years. The components commonly used in fuels are bioethanol as an automotive gasoline component and fatty acid methyl esters (FAME) as a diesel fuel component. The technologies used to manufacture alternative fuels for aircraft turbine engines have been under development for about 10 years [5]. As of today, the seven synthetic components are approved for aviation turbine engines [6], while it is anticipated that further fuels using alternative feedstocks [7] will be introduced to the market. Regarding the chemical composition, jet fuels containing synthesized hydrocarbons are more similar to conventional fuels than biofuels containing bioethanol and FAME. However, the hydrocarbon composition influences the combustion process, hence the engine operating parameters and composition of exhaust gases [8–10].

Research regarding new components, both for compression-ignition, and aviation turbine engines demands the development of predictive methods, and the assessment of the effect of a fuel chemical composition on the combustion process [11–14].

2. Modelling of the Combustion Process

The combustion process in the turbine engine is characterized by strong diversification of reaction chains depending on engine operating parameters and the temperature of the combustion chamber [15–21]. Fuel combustion in turbine engines is a complex process. In general, the combustion process can be treated as the linkage of the following processes: fuel atomization after injection to the combustion chamber; vaporization, together with further thermal degradation; a large number of chemical reactions as fuel oxidation occurs [22]. Where the turbine engine is not equipped with injectors but is equipped with evaporator tubes, no fuel atomization takes place.

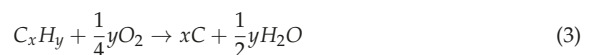
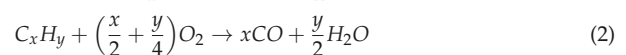
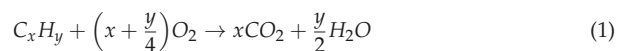
In the combustion process, there are strong interactions between elemental processes. This brings about difficulties in modelling it. In particular, it is very difficult to mathematically describe the influence of the fuel chemical composition on the combustion process. The chemical composition of the fuels is qualitatively described by the structure of the compounds present in the fuel. The only quantitative data are the concentrations of individual compounds, or more frequently, the concentrations of hydrocarbons i.e., n-paraffins, iso-paraffins, naphthenes, aromatics. The molecules of individual chemical compounds interact with each other, which affects fuels atomization, vaporization, as well as chemical reactions during the combustion process. However, the nature of molecular interactions has not been sufficiently understood. Certain authors [23], for example, describe the creation of molecular clusters by polycyclic aromatic hydrocarbons (PAH), and point to the clusters as the soot source. The molecular cluster is an ordered structure of unique properties, different from the volumetric properties of fuel treated as the liquid. This regards the energy state and ability to transfer energy. Conventional jet fuel does not contain PAH or any synthetic components. However, monoaromatics and other kinds of hydrocarbons can form similar structures that influence the chemical reactions in the combustion process.

The above-mentioned complexity of the chemical composition of fuels, as well as the complexity of individual processes taking place in the combustion chamber, makes modelling of the combustion process difficult [24,25].

Research on the dependence of the combustion process, and as a consequence, engine operating parameters, and exhaust gas composition, is being carried out at different levels, from macroscopic (engine tests) to molecular (tests in laboratory reactors). Currently available models such as SAE [26], and that based on such solvers as Ansys Fluent [27] and Chemkin [28] do not sufficiently take into account the chemical composition and properties of fuels. Indeed, the SAE model requires the assumption that fuel is a single compound consisting of C, H, N, O, S. In contrast, Ansys Fluent and Chemkin take into account thermodynamic data and selected properties of material (fuel), such as neat heat of combustion, viscosity, thermal conductivity, mass diffusivity and thermal diffusion. Moreover, Ansys Fluent provides a description of several fuel combustion mechanisms (including reactions, thermodynamic data, and transport data) that are appropriate for use in combustion simulations of:

- Methane/ethane;
- Propane;
- Hydrogen.

During the combustion process in a turbine engine, the following (chains of) reactions are possible:



Reactions (1)–(3) are a summary record of the long chains of reactions. In addition, conventional and synthetic fuels are mostly a mixture of many (even up to 1000) chemical compounds, mainly hydrocarbons. The usefulness of the SAE model and that of the solvers indicated above are limited. The reason for such situation is that in the application of statistical tools to formulate the necessary dependencies with any weaknesses of the statistics:

- The values of the constant parameters of these relationships are determined for a specific set of tested fuels, the values may be incorrect for a new fuel, e.g., synthetic fuel;
- A physical interpretation of statistically determined parameters is not possible.

The use of mathematical models for the combustion process, as currently available [28,29], give dependencies that show significant deviation from experimental data.

When considering the possibility of introducing a new, synthetic fuel, two basic questions should be answered, with regard to a comparison with conventional fuel:

- How will this new fuel change the combustion process in the engine;
- How will this new fuel change the emission of exhaust components.

Consequently, the products formed during combustion (CO_2 , CO and PM) are important components of exhaust gases. The concentration of CO_2 , CO and PM in exhaust gases is used to:

- Assess the influence of the combustion process in turbine engines on air pollution;
- Assess the influence of fuel chemical composition on the combustion process.

The impact of fuel chemical composition on the combustion process can be assessed qualitatively or quantitatively. The quantitative assessment gives a more complete description of this impact, but it needs quantitative data related to the fuel chemical composition and the chemical reactions of fuel combustion. The reactions (1–5) can be described quantitatively by kinetic equations, where the data are the volume of fuel introduced into combustion chamber ($m_f t$) and concentration of the chosen product of combustion. The kinetic equations make possible formulation of the function describing relationships between the concentration of the products of fuel combustion ($[\text{CO}]$ or $[\text{CO}_2]$) and m_f . Such relationships seem to be more useful in combustion process analysis than the analysis of separate $[\text{CO}]$ values for various m_f (as usually found in literature).

The reaction rate constants in the kinetic equations of combustion (described by the Arrhenius equation) can be related to the conditions of combustion process—temperature in combustion chamber and chemical structure of the fuel—activation energy. The activation energy has a physical meaning in relation to a single reaction, but in relation to a chain of reactions it is difficult to interpret it, physically. Consequently, it is practically impossible to relate the reaction rate constant quantitatively to the chemical structure of the fuel.

The basic problem is how to describe quantitatively the chemical composition of fuel, when such fuel consists of many compounds (mainly hydrocarbons). The way, proposed in this paper, is by using the reactivity model. The general assumption of this model is that every fuel, even that very complex, can be assigned a α_i coefficient that is the ratio of the external forcing causing the combustion process, to the energy response of the system resulting from chemical reactions. The coefficient α_i can be treated as the quantitative measure of fuels structure related to the given process. The reactivity of the tested product (fuel, lubricating oil, etc.) is understood as its ability to undergo chemical reactions caused by external mechanical (tribology) or thermal (combustion of fuel) influences that affect the course of the operational process, i.e., lubrication or engine operation.

The mathematical assumptions of the reactivity model were previously developed for reactions initiated by heat and mechanical forces that stimulated tribological processes [30].

The assumptions of the reactivity model are based on the relation of two functions: $f(z)$ and $\phi(z)$. The fundamental relationship for this model is the following:

$$\alpha_i = \frac{f(z) - f_0(z)}{\phi(z) - \phi_0(z)} \cdot \frac{d\phi(z)}{df(z)} \quad (6)$$

Here, the combustion process is described by two functions of the same variable z (chosen independent parameter characterizing the combustion process, e.g., m_f), where $f(z)$ and $\phi(z)$ are related to the tested fuel, and $f_0(z)$ and $\phi_0(z)$ are related to the reference fuel.

This general relationship should be adapted to the process that is the subject of this investigation. In case of the investigations described in this paper, the observed process is the fuel combustion in the turbine jet engine. The parameter that provides quantitative information about the influence of chemical structure of the tested fuel on the combustion process is the reactivity coefficient α_i , and:

$$f(z) = L \quad (7)$$

$$\phi(z) = A(z) \quad (8)$$

where z is the parameter chosen as the only variable and $A(z)$ is a function describing the reactions initiated by the energy supplied from environment to the system (L). Herein, $A(z)$ can be expressed as the function of constant rate of reaction or the concentration of the products of the reaction—according to the problem being solved.

Preliminary research has shown that this model can be useful for the analysis of various processes. This allows us to focus on one chosen component of a very complex blend, and describe this component influence on a complex process such as the fuel combustion in an engine [21]. The investigation of the influence of synthetic components on the combustion process in turbine engines should be conducted in a relative manner. It is assumed that the concentration of carbon monoxide in the exhaust gases is an indicator of the similarity of the combustion process of synthetic fuel to the reference conventional fuel.

During preliminary investigations on catalysis and tribocatalysis [30], it was found that instead of the kinetic equation (kinetic model), the dynamic reactivity model can be used. The reactivity model, developed by these authors for catalytic (including tribochemical) processes modelling, can be more useful than models developed up to now in modelling the influence of fuel chemical composition and properties on the combustion process.

The paper aims to verify the thesis that the reactivity model, developed in earlier research, can be used to compare fuels combustion processes in turbine engines. Taking into account the usefulness of models for predicting the influence of new components or additives added to the fuel on combustion process, and the needed analysis of the influence of new fuel components on the mechanism of the combustion process, a new model is proposed. Preliminary tests have shown that this model can be useful for describing the mechanisms of various processes analysis which allows us to focus on the one chosen compound or component in a very complex mixture, as well as to describe this chosen component influence on a complex process such as the fuel combustion in an engine. In this paper, this model was chosen to verify the possibility of its application for the description of combustion process. The assumptions of the proposed, new mathematical model of fuel combustion are based on a model developed previously for reactions initiated by heat and mechanical forces.

3. Materials and Methods

3.1. Tested Fuels

Fossil jet fuel Jet A-1 and its blends with synthetic blending components from alcohol to jet (ATJ) and hydroprocessed esters and fatty acids (HEFA), approved by ASTM D7566, were used in the tests. The synthetic components from ATJ and HEFA technologies consist of synthetic hydrocarbons. The above-mentioned tested fuels were designated in the paper as:

- Conventional jet fuel—Jet 1 and Jet 2;
- Blend of Jet 1 with 5% of synthetic component HEFA—5HEFA;
- Blend of Jet 1 with 20% of synthetic component HEFA—20HEFA;
- Blend of Jet 1 with 30% of synthetic component HEFA—30HEFA;

- Blend of Jet 2 with 50% of synthetic component ATJ—50ATJ;
- Synthetic blending component from ATJ technology—ATJ.

The properties of the tested fuels are shown in Table 1.

Table 1. Properties of tested fuels.

Property	Tested Fuels						
	Jet 1	5HEFA	20HEFA	30HEFA	Jet 2	50ATJ	ATJ
Density at 15 °C, kg/m ³	793.1	790.5	787.0	782.7	793.0	776.1	758.6
Viscosity at −20 °C, mm ² /s	3.069	3.288	3.403	3.470	3.062	3.654	4.740
Net heat of combustion, MJ/kg	43.312	43.335	43.484	43.570	43.231	43.599	44.027
Aromatics, %(V/V)	15.1	14.3	12.1	10.6	17.3	8.8	0
Distillation:							
10% Recovery, °C	166.1	170.6	169.9	169.0	166.1	170.5	175.5
50% Recovery, °C	183.4	186.8	188.3	189.3	183.4	182.1	181.2
90% Recovery, °C	208.1	214.1	220.2	224.7	208.1	209.0	210.3
End point, °C	231.2	2394	246.7	249.5	231.2	246.2	262.7

All selected laboratory properties affect the combustion process. The net heat of combustion determines the economy of the engine and its characteristics, and, along with the density, it is taken into account in flight range calculations. Viscosity affects the injection process and the fuel stream range and its atomization into the combustion chamber. Distillation affects the rate of fuel evaporation, while aromas tend to incomplete combustion.

The addition of synthetic component to conventional fuel brings about changes in several physicochemical properties. When HEFA and ATJ are added, the density decreases and the viscosity and heat of combustion increases. These changes are so significant that they can differentiate the combustion process. The differences in the composition of tested fuels are typified by the example of the content of aromas, the value of which is proportional to their blend in the tested fuel. The smallest differences occur in the course of distillation, although in this case the influence of the composition on the distillation of the blend is also noticeable, especially in end point.

3.2. Bench Test

The analysis of the combustion process was conducted using a laboratory test rig with a miniature turbojet engine—MiniJETRig (Figure 1). The test rig was constructed for the research of alternative fuels combustion processes [31–33], and it is also used in other development works [9,34,35]. MiniJETRig consists of:

- A miniature turbojet engine—single spool with a single stage radial compressor and annular combustion chamber. It works in the range of 33,000–120,000 rpm and generates a maximum thrust of 140 N;
- An exhaust analyzer with an electrochemical sensor in the range of 0–2000 (ppm) for CO measurement and an infrared sensor in the range of 0–25 (%) for CO₂ measurement. The accuracy of the device measurements is 5% of the measured value;
- Control system with data acquisition based on the measurement cards;
- During the undertaken tests, measurements were made with the following sensors:
- Optical rotational speed measurement sensor—SFH 203 FA photodiode, measuring range: 0–120,000 rpm;
- Fuel mass flow rate measurement system (thermodynamic flow measurement)—Digmes FHKSC flow meter, measuring range: 0.033–2 L/min, accuracy ± 2% of the measured value.

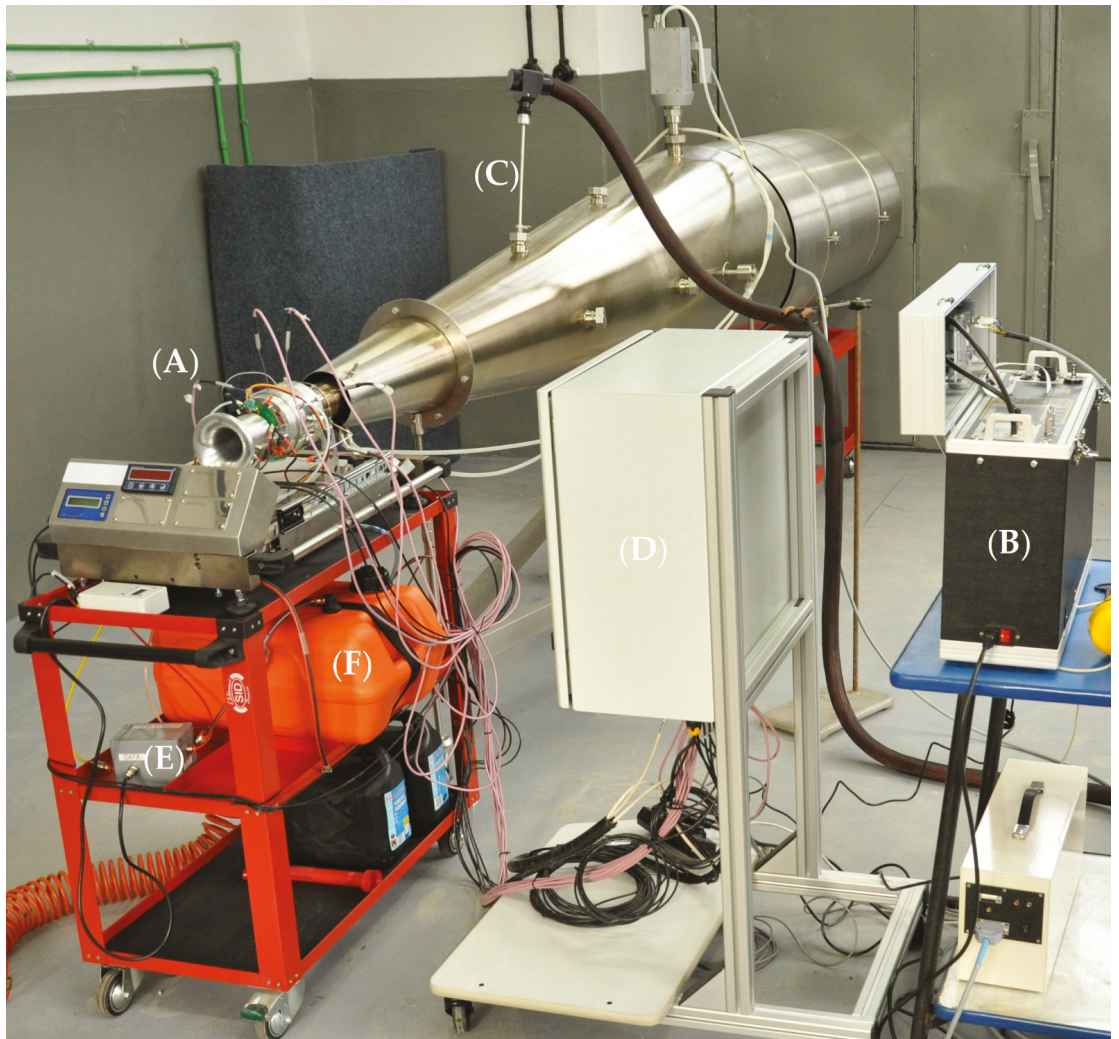


Figure 1. MiniJETRig: (A) miniature turbojet engine, (B) exhaust analyzer, (C) exhaust gas sample probe, (D) block of measurement cards, (E) flow meter, (F) fuel tank.

The tests were conducted at the range of 45,000–120,000 rpm. Due to the stabilization of the measured parameters, the results from the last 20 s of the engine run on a selected operating mode (100 individual measurements) were averaged and assumed as the measurement result. The fuel mass flow rate was regulated to obtain the expected value of engine rotational speed.

CO concentration in exhaust gases was assumed as a similarity criterion of the combustion process for different fuels. The CO formation during the combustion process in turbine engines can be the result of the low local concentration of O₂ in the combustion chamber or CO can be treated as intermediate product in hydrocarbons oxidation to CO₂. However, the results of CO and CO₂ concentration during the combustion of Jet A-1 fuel in turbine engines are similar to the change of the products concentration of follow-up reactions. This suggests that CO can play the role of being an intermediate product (Figure 1).

Figure 2 shows that at low rotational speeds (idle), the mechanism of the combustion process expressed by CO and CO₂ concentrations is different than at higher rotational speeds (cruise or take-off). For this reason, to develop the reactivity model, only bench test results from 70,000 rpm to 111,000 rpm were analyzed. In the presented graphs, the vertical error bars correspond to the combined standard uncertainty, obtained by combining the individual standard uncertainties (Type A and B).

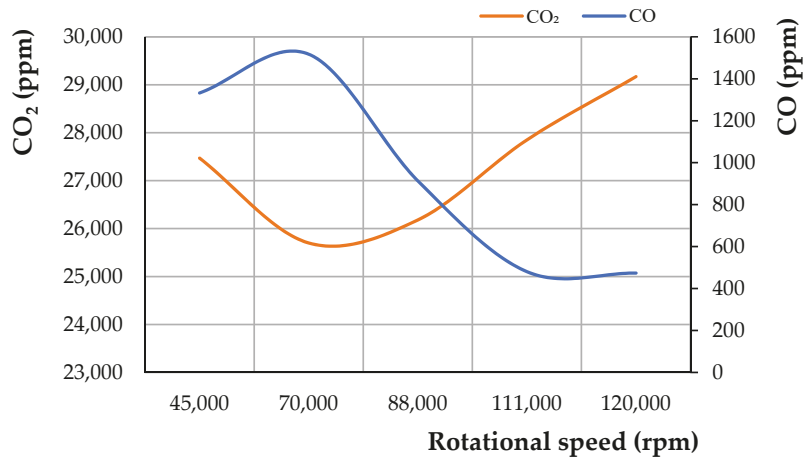


Figure 2. Relationship between CO and CO₂ concentrations in exhaust gases emitted by the miniature jet engine.

4. Results

4.1. Application of the Reactivity Model to the Assessment of the Combustion Process

The results of the engine tests of fuels containing synthetic components are shown in Figure 3 and the functions describing trend lines are shown in Table 2. The relationship between CO concentration in exhaust gases and fuel mass flow rate were discovered to be power functions.

Table 2. The power functions describing relationships between CO concentration in exhaust gases and fuel mass flow rate.

Fuel	Function (from the Trend Line) CO = am_f^n	R ² Coefficient of Determination
Jet 1	CO = 2812 m_f^{-1184}	0.90
5HEFA	CO = 2764 m_f^{-1159}	0.93
20HEFA	CO = 2761 m_f^{-1107}	0.94
30HEFA	CO = 2601 m_f^{-1056}	0.93
Jet 2	CO = 2698 m_f^{-1073}	0.92
50ATJ	CO = 2899 m_f^{-1080}	0.93
ATJ	CO = 3022 m_f^{-1036}	0.94

The above data shows that each tested fuel takes on individual values of the a and n parameters. Using one function defined for a wide range of engine operation parameters, the independent variable m_f was found to be connected with CO concentration (the selected parameter describing the combustion process). The reactivity model allows us to interpret physically/chemically, the a and n parameters. Other known models are based on statistical dependences with several consequences. However, the statistically obtained parameters cannot be interpreted physically/chemically.

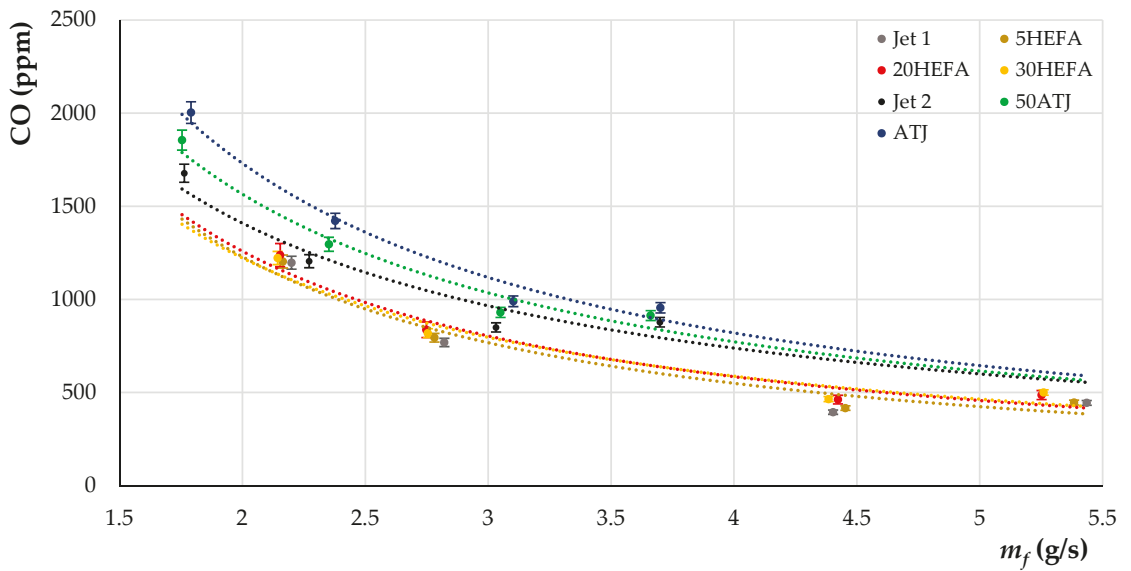


Figure 3. The relationship between CO concentration and fuel mass flow rate.

Figures 4 and 5 reveal the impact of components concentration in the blends with Jet A-1 fuel on the a and n parameters. Herein, the a and n parameters were found to change proportionally to the concentration of the synthetic component in the fuel, however, the trend of changes for the HEFA component is opposite to that observed for ATJ. Such differences in trends may be a consequence of different reaction mechanisms during combustion.

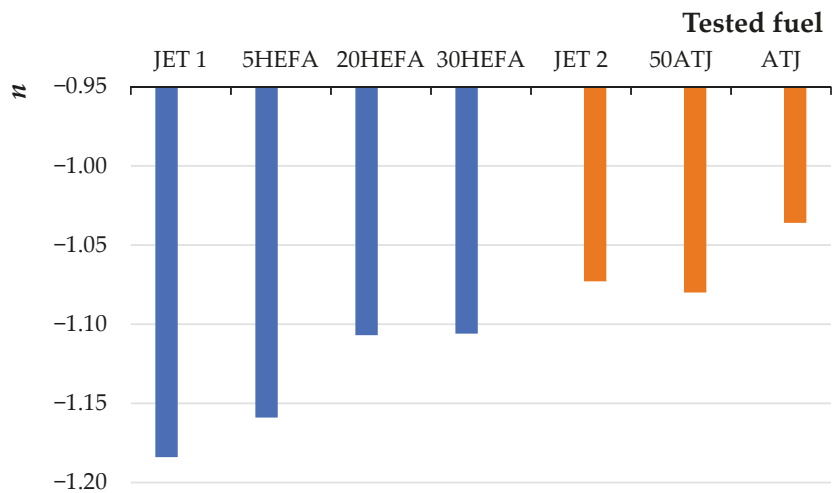


Figure 4. The influence of concentration of HEFA component in blend with Jet A-1 on the n parameter.

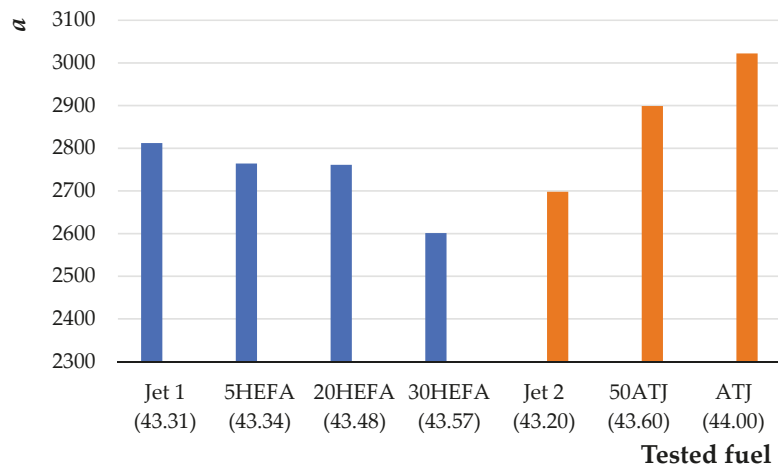


Figure 5. The influence of concentration of HEFA component in blend with Jet A-1 on the a parameter (net heat of combustion [MJ/kg] in brackets).

It should be noted that HEFA consists of a variety of paraffinic and isoparaffinic hydrocarbons, ATJ is a mixture of isoparaffins, while Jet A-1 fuels contain hundreds of paraffinic, isoparaffinic, olefinic, naphthenic and aromatic hydrocarbons.

4.2. The Use of the Reactivity Model in the Analysis of the Combustion Process—Theoretical Approach

Based on (6), the overall reactivity model was adapted to develop a combustion model. Usually, the combustion process is described by emission of products such as CO_2 , CO , unburned hydrocarbons, etc. In this study the concentration of carbon monoxide in the exhaust gases is treated as an indicator of the similarity of the combustion process of synthetic fuel to the fossil fuel. Moreover, the constant rate of fuel combustion to CO_2 in the range of subsequent reactions formation is treated as weakly dependent on the chemical composition of the fuel. For this reason, the influence of fuel chemical composition on CO_2 formation was not analyzed. Consequently, kinetic equations that describe CO creation during the combustion were applied in the reactivity model (6).

In the case wherein the reactivity model will describe only the part of energy generated by the system that is connected with Reaction (2)—oxidation of the fuel hydrocarbons to the CO and H_2O (dependence (6)), this should be expressed as:

$$(L_{\text{CO}} - L_0) = \alpha_i A[\text{CO}] \quad (9)$$

The reactivity model describes the open system as it is shown in Figure 6.

The combustion process can be treated as consisting of:

- Parallel Reactions (1) and (2);
- Follow-up Reactions (2) and (5);
- The kinetic equations were formulated for both above cases. It was assumed that:
- The fuel is introduced once into the combustion chamber in the amount of $[\text{C}_x\text{H}_y]_0 = m_f t$;
- The order of Reactions (1) and (2) in relation to the tested fuels $[\text{C}_x\text{H}_y]$ is n ;
- Reaction (5) is of the first order.

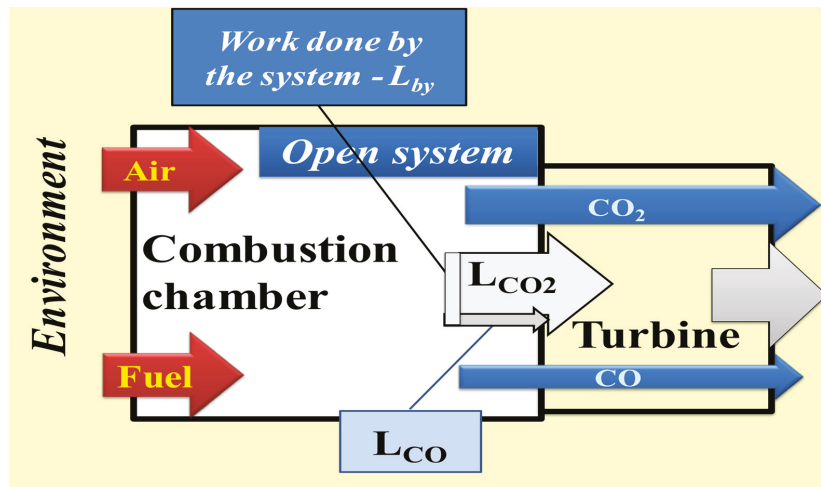


Figure 6. The application of the reactivity model in turbine engine combustion.

The following kinetic equations have been formulated:

1. In the case of the parallel Reactions (1) and (2):

$$\frac{d[C_xH_y]}{dt} = c_2k_{CO}[C_xH_y]^{n_p} + c_1k_{CO_2}[C_xH_y]^{n_p} \quad (10)$$

After integration of Equation (10):

$$[C_xH_y]^{-n_p+1} = [C_xH_y]_0^{-n_p+1} - (-n_p + 1)(c_2k_{CO} + c_1k_{CO_2})t \quad (11)$$

$$[C_xH_y] = \left\{ [C_xH_y]_0^{-n_p+1} - (-n_p + 1)(c_2k_{CO} + c_1k_{CO_2})t \right\}^{\frac{1}{-n_p+1}} \quad (12)$$

$$[C_xH_y] = \left\{ (m_f t)^{-n_p+1} - (-n_p + 1)(c_2k_{CO} + c_1k_{CO_2})t \right\}^{\frac{1}{-n_p+1}} \quad (13)$$

$$\frac{d[CO]}{dt} = c_2k_{CO}[C_xH_y]^{n_p} \quad (14)$$

$$[CO] = c_2k_{CO}[C_xH_y]^{n_p}t \quad (15)$$

$$[CO] = c_2k_{CO}t \left\{ [C_xH_y]_0^{-n_p+1} + (-n_p + 1)(c_2k_{CO} + c_1k_{CO_2})t \right\}^{\frac{n_p}{-n_p+1}} \quad (16)$$

$$[CO] = c_2k_{CO}t \left\{ (m_f t)^{-n_p+1} + (-n_p + 1)(c_2k_{CO} + c_1k_{CO_2})t \right\}^{\frac{n_p}{-n_p+1}} \quad (17)$$

Using Pascal's triangle, Equation (17) can be shown as follows:

$$[CO] = c_2k_{CO}t (m_f t)^{n_p} + A_0 - \left\{ (-n_p + 1)(c_2k_{CO} + c_1k_{CO_2})t \right\}^{\frac{n_p}{-n_p+1}} \quad (18)$$

In addition, Equation (16) can be expressed as:

$$[CO] = c_2k_{CO}(m_f t)^{n_p} \quad (19)$$

in case the $A_0 - \left\{ (-n_p + 1)(c_2k_{CO} + c_1k_{CO_2})t \right\}^{\frac{n_p}{-n_p+1}}$ is small, then $c_2k_{CO} = a$ and $n_p = n$.

2. In the case of the follow-up Reactions (2) and (5):

$$\frac{d[\text{CO}]}{dt} = c_2 k_{\text{CO}} [\text{C}_x\text{H}_y]^{n_p} - c_5 k_{\text{CO}_2} [\text{CO}] \quad (20)$$

Assuming that $[\text{C}_x\text{H}_y]$ after a relatively short, fixed time t is constant, the integration in the range from 0 to $[\text{CO}]$ leads to the following dependence:

$$\frac{[\text{CO}]}{c_2 k_{\text{CO}} [\text{C}_x\text{H}_y]^{n_p}} - c_5 k_{\text{CO}_2} [\text{CO}] = t \quad (21)$$

$$c_2 k_{\text{CO}} [\text{C}_x\text{H}_y]^{n_p} - c_5 k_{\text{CO}_2} [\text{CO}] = \frac{1}{t} [\text{CO}] \quad (22)$$

$$[\text{CO}] = \frac{c_2 k_{\text{CO}} [\text{C}_x\text{H}_y]^{n_p}}{c_5 k_{\text{CO}_2} + \frac{1}{t}} \quad (23)$$

Here, $[\text{C}_x\text{H}_y]$ was determined as follows:

$$-\frac{d[\text{C}_x\text{H}_y]}{dt} = c_2 k_{\text{CO}} [\text{C}_x\text{H}_y]^{n_p} \quad (24)$$

After integration in the range from $[\text{C}_x\text{H}_y]_0$ to $[\text{C}_x\text{H}_y]$ the following equation was obtained:

$$[\text{C}_x\text{H}_y] = \left\{ [\text{C}_x\text{H}_y]_0^{-n_p+1} - (-n_p + 1)(c_2 k_{\text{CO}} t) \right\}^{\frac{1}{-n_p+1}} \quad (25)$$

Using Pascal's triangle, $[\text{C}_x\text{H}_y]$ can be expressed as:

$$[\text{C}_x\text{H}_y] = \left\{ [\text{C}_x\text{H}_y]_0 + B_0 - (-n_p + 1)(c_2 k_{\text{CO}} t) \right\}^{\frac{1}{-n_p+1}} \quad (26)$$

By introducing Equation (26) to Equation (23) and substituting $[\text{C}_x\text{H}_y]$ by $m_f t$ the following equation was obtained:

$$[\text{CO}] = \frac{c_2 k_{\text{CO}}}{c_5 k_{\text{CO}_2} + \frac{1}{t}} [\text{C}_x\text{H}_y]_0^{n_p} + B_0 - \left\{ (-n_p + 1)(c_2 k_{\text{CO}} t) \right\}^{\frac{n_p}{-n_p+1}} \quad (27)$$

Equation (27) can thus be expressed as:

$$[\text{CO}] = \frac{c_2 k_{\text{CO}}}{c_5 k_{\text{CO}_2} + \frac{1}{t}} (m_f t)^{n_p} \quad (28)$$

in case the $B_0 - \left\{ (-n_p + 1)(c_2 k_{\text{CO}} t) \right\}^{\frac{n_p}{-n_p+1}}$ is small, than $\frac{c_2 k_{\text{CO}}}{c_5 k_{\text{CO}_2} + \frac{1}{t}} = a$ and $n_p = n$.

Both obtained Equations (19) and (28) are similar to these obtained experimentally as the trend lines.

It is difficult to determine the values of the reactions rate constant (k_{CO} and k_{CO_2}). Consequently, it is difficult to link their values with the properties of the fuel that may be a bridge to the chemical structure of the combusted product. It is proposed to use the reactivity model, represented by Equation (9), to relate the value of k_{CO} to the physicochemical properties of the tested fuels (a mixture of several hundred hydrocarbons). Assuming that L_{CO} can be expressed as a part of total energy released in the combustion process $L_{\text{CO}} = g(Q_n m_f t)$, Equation (9) can be formulated as follows:

$$z = m_f \quad (29)$$

$$f(z) = L_{\text{CO}} = g(Q_n m_f t) \quad (30)$$

$$\phi(z) = A[\text{CO}] = A c_2 k_{\text{CO}} t m_f^{-n_p+1} \quad (31)$$

$$f_1(Q_n m_{ft}) = A\alpha_i[CO] + L_0 \quad (32)$$

As a result, Equation (31) can be expressed as:

$$[CO] = \frac{\{f_1(Q_n m_{ft}) - L_0\}}{A\alpha_i} \quad (33)$$

In both assumed cases (parallel and follow-up reactions), CO concentration in exhaust gases should be linear functions of the net heat of combustion (Q_n) of the tested fuels. Hence, the a parameter: c_2k_{CO} in Equation (19) and $(\frac{c_2k_{CO}}{c_5k_{CO_2} + \frac{1}{T}})$ in Equation (28) should depend on the coefficient α_i , the values of which should be different for compositions of jet fuel and different kinds of synthetic components and be similar values for the compositions of jet fuel and the same kind of synthetic components. The a parameter is the product of parameters, the values of which are fixed for a given fuel, including α_i —coefficient of fuels reactivity related to its combustion. Moreover, in the case where the influence of m_f on $[CO]$ is assessed, the ratio of Q_n/α_i should be a constant value for different blends.

As shown in Figure 4, in the case of fuels containing HEFA synthetic component, the value of the a parameter decreases when Q_n increases. In the case of fuels containing ATJ synthetic component, the value of the a parameter increases with the Q_n increase. Both synthetic components increase the net heat of combustion proportionally to their concentration in the blend (Figure 7). As the outcome of solving Equations (19) and (28) are related to the data shown on Figures 6 and 7, this suggests that the mechanism of the influence of synthetic components on the combustion process is different in the case of blends consisting of HEFA and in the case of blends consisting of ATJ.

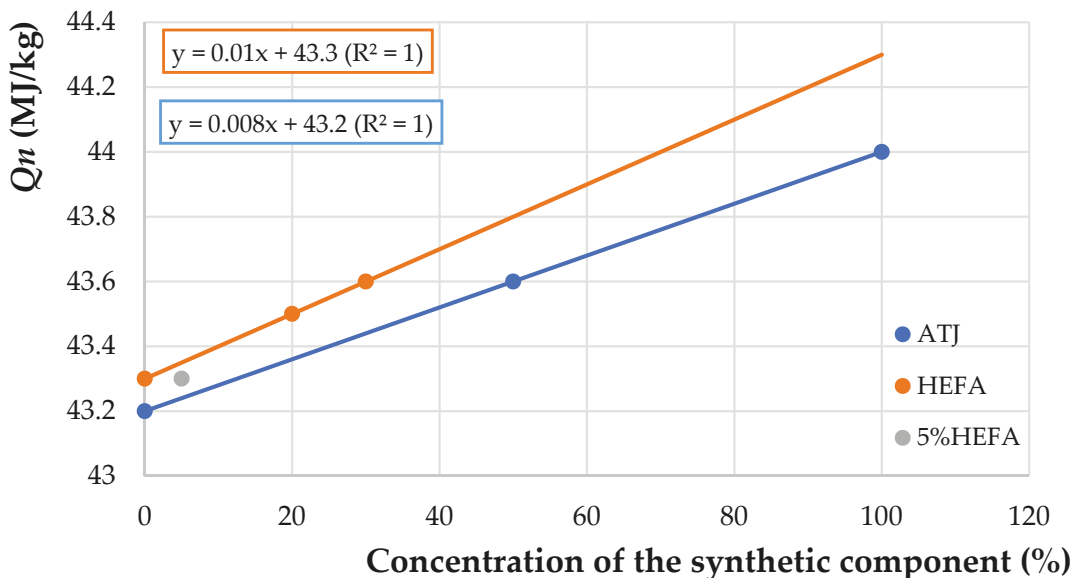


Figure 7. The relationship between calorific value Q_n of the tested blends and the concentration of a synthetic component; properties of the blend containing 5% of HEFA differ from the relationship found for blends containing HEFA in higher concentration.

Consequently, it can be concluded that the influence of synthetic components on the mechanism of the fuel combustion process is different in the case of blends containing HEFA component and blends containing ATJ. The above demonstrates the usefulness of the reac-

tivity model in researching complex processes such as fuel combustion. Using the reactivity model, each parameter of obtained relationships can be interpreted physically/chemically. In contrast, other currently applied models are based on statistical dependences with all the recognized consequences, the most important being that statistically obtained parameters cannot be interpreted physically/chemically.

5. Conclusions

In this paper, the application of the reactivity model developed in earlier research for comparing fuel combustion processes in turbine engines fueled by various synthetic blends was investigated. The analysis of the combustion process was carried out by means of a test rig with miniature turbojet engine. Conventional jet fuel and its blends with synthetic blending components derived from ATJ and HEFA technology were used in the bench tests.

The experimental data obtained allowed to develop trend lines described by power functions of the concentration of CO as dependent variable, and the fuel mass flow rate, m_f as independent variable. For each of the tested blends, a power function was obtained with a different value of parameter a and exponent n . Similar power functions can be formulated using the general reactivity model. While the parameters of the trend line cannot be physically interpreted, the quantities occurring in the relationships formulated on the basis of the reactivity model have a physical meaning. Consequently, the general reactivity model can be used to study the similarities and differences of various combustion mechanisms.

For each fuel chemical composition, a specific function was obtained, i.e., that the values of a and n parameters depend on the fuel chemical composition. Hence, it can be concluded that the a parameter can be expressed as the function of net heat of combustion of the tested fuel and that the Q_n varies linearly with the change of synthetic components concentration in the fuel.

The analysis of the relationship between a values in power functions and the net heat of combustion of the tested blends leads to conclusion that there is different mechanism of combustion in cases wherein the fuel is the blend of Jet A-1 and HEFA and wherein the fuel contains a ATJ synthetic component.

The above conclusions require confirmation by increasing of the number of tested fuels. In the authors' opinion, Equations (19) and (28) will be useful in further planned research, including:

- Connection of a and n parameters with the physicochemical properties of tested fuels;
- Connection of a and n parameters with a wider group of engines.

Author Contributions: Conceptualization, A.K.; methodology, A.K. and T.B.; formal analysis, W.D.; investigation, T.B. and W.D.; writing—original draft preparation, A.K.; writing—review and editing, T.B. and M.K.; visualization, W.D. and A.K.; supervision, M.K. and A.K. All authors have read and agreed to the published version of the manuscript.

Funding: This research was funded by the Ministry of Science and Higher Education (Poland) for the project financed within the framework of the statutory activity.

Institutional Review Board Statement: Not applicable.

Informed Consent Statement: Not applicable.

Data Availability Statement: The data presented in this study are available on request from the corresponding author.

Conflicts of Interest: The author declares no conflict of interest.

Nomenclature

a_{CO}	the part of L_{CO} in L_{by}
A	coefficient (constant) for given mechanisms of reaction of fuel combustion [J·(s/mole) ^{np-1}]
A^0	sum of chosen components in relationship resulted from the Pascal triangle (parallel reactions) α_i ; reactivity coefficient of tested fuel
B_0	sum of chosen components in relationships resulting from the Pascal triangle (follow-up reactions)
C	concentration of the synthetic component (%) c_1 coefficient determining the participation of $[O_2]^{n_p(\frac{x}{2} + \frac{y}{2})}$ in the rate of reaction (1)
c_2	coefficient determining the participation of $[O_2]^{n_p(\frac{x}{2} + \frac{y}{2})}$ in the rate of reaction (2)
c_5	coefficient determining the participation of $[O_2]^{n_p(\frac{x}{2} + \frac{y}{2})}$ in the rate of reaction (5)
[CO]	the number of carbon monoxide moles in 1 kg of exhaust gases; equivalent to the concentration in the case of a constant mass of gases in the combustion chamber being assumed (mole)
CO	the concentration of CO in exhaust gases (ppm)
[CO ₂]	the number of carbon dioxide moles in 1 kg of exhaust gases; equivalent to concentration in the case of a constant mass of gases in the combustion chamber being assumed (mole)
CO ₂	the concentration of CO ₂ in exhaust gases (ppm)
[C _x H _y]	the number of fuel moles (mole)
[C _x H _y] ₀	the number of fuel moles at the beginning of the process (mole)
ε	energy supplied to reaction zone, other than heat (RT) (J/mole)
e	Euler's number
e_0	stream of energy emitted by the solid surface (J/s)
E_a	activation energy (J/mole)
k	rate constant of reaction that stimulates the observed process
k_{CO}	rate constant of fuel combustion to CO [(mole/kg exhaust gases) ^(1-np) s ⁻¹]
k_{CO_2}	rate constant of fuel combustion to CO ₂ [(mole/kg exhaust gases) ^(1-np) s ⁻¹]
L	energy supplied from environment to the system (as tested fuel being burnt) (J)
L_0	energy supplied from environment to the system (as reference fuel being burnt) (J)
L_{CO}	portion of the energy from the fuel combustion that comes from fuel molecule oxidation to CO (J)
L_{on}	energy introduced into the system, treated as the sum of L_{CO_2} and L_{CO} (J)
L_{by}	energy generated by the system (J)
L_{CO_2}	portion of the energy from the fuel combustion that comes from fuel molecule oxidation to CO ₂ (J)
m_f	fuel mass flow rate (g/s)
n_p	chemical reaction order
Q	heat generated during the combustion process (J)
Q_n	net heat of combustion (MJ/kg)
R	gas constant
R^2	coefficient of determination
t	duration of the combustion process (s)
T	average temperature of reaction system (K)

References

1. Directive (EU) 2018/2001 of the European Parliament and of the Council of 11 December 2018 on the Promotion of the Use of Energy from Renewable Sources. Available online: <https://eur-lex.europa.eu/legal-content/EN/TXT/?uri=CELEX%3A32018L2001> (accessed on 16 December 2020).
2. Navas-Anguita, Z.; García-Gusano, D.; Iribarren, D. Long-term production technology mix of alternative fuels for road transport: A focus on Spain. *Energ. Convers. Manag.* **2020**, *226*, 113498. [CrossRef]
3. Paulauskiene, T.; Bucas, M.; Laukinaite, M. Alternative fuels for marine applications: Biomethanol-biodiesel-diesel blends. *Fuel* **2019**, *248*, 161–167. [CrossRef]
4. Kumal, R.R.; Liu, J.; Gharpure, A.; Vander Wal, R.L.; Kinsey, J.S.; Giannelli, B.; Stevens, J.; Leggett, C.; Howard, R.; Forde, M.; et al. Impact of biofuel blends on black carbon emissions from a gas turbine engine. *Energ. Fuel* **2020**, *34*, 4958–4966. [CrossRef]

5. Yang, J.; Xin, Z.; He, Q.; Corscadden, K.; Niu, H. An overview on performance characteristics of bio-jet fuels. *Fuel* **2019**, *237*, 916–936. [[CrossRef](#)]
6. ASTM International. *ASTM D7566 Standard Specification for Aviation Turbine Fuel Containing Synthesized Hydrocarbons*; ASTM International: West Conshohocken, PA, USA, 2020.
7. Zhang, B.Y.; Duan, D.; Hei, H.; Villota, E.; Ruan, R. Jet fuel production from waste plastics via catalytic pyrolysis with activated carbons. *Appl. Energy* **2019**, *251*, 113337. [[CrossRef](#)]
8. Kulczycki, A.; Kaźmierczak, U. Method of preliminary evaluation of bio components influence on the process of biofuels combustion in aviation turbine engines. *J. KONES* **2017**, *24*, 83–90.
9. Gawron, B.; Białecki, T.; Janicka, A.; Górniak, A.; Zawisłak, M. Exhaust toxicity evaluation in a gas turbine engine fueled by aviation fuel containing synthesized hydrocarbons. *Aircr. Eng. Aerosp. Tec.* **2020**, *92*, 60–66. [[CrossRef](#)]
10. Reksowardojo, I.K.; Duong, L.H.; Zain, R.; Hartono, F.; Marno, S.; Rustyawan, W.; Putri, N.; Jatiwiramurti, W.; Prabowo, B. Performance and exhaust emissions of a gas-turbine engine fueled with biojet/ Jet A-1 blends for the development of aviation biofuel in tropical regions. *Energies* **2020**, *13*, 6570. [[CrossRef](#)]
11. Iturbe-Hernández, A.; Guzmán, J.E.V.; Vicente, W.; Salinas-Vazquez, M. Microturbine characteristics and emissions using biofuel blends. *Biofuels* **2020**, *1*–9. [[CrossRef](#)]
12. Przysowa, R.; Gawron, B.; Białecki, T.; Łęgowik, A.; Merkisz, J.; Jasiński, R. Performance and emissions of a microturbine and turbofan powered by alternative fuels. *Aerospace* **2021**, *8*, 25. [[CrossRef](#)]
13. Karyeyen, S.; Ilbas, M. Experimental and numerical analysis of turbulent premixed combustion of low calorific value coal gases in a generated premixed burner. *Fuel* **2018**, *220*, 586–598. [[CrossRef](#)]
14. Pires, A.P.P.; Han, Y.; Kramlich, J.; Garcia-Perez, M. Chemical composition and fuel properties of alternative jet fuels. *BioResources* **2018**, *13*, 2632–2657. [[CrossRef](#)]
15. Białecki, T.; Dziegielewski, W.; Gawron, B.; Kaźmierczak, U.; Kulczycki, A. The role of molecularly ordered structures in energy transport enhancement during combustion process—A new conception of a reaction mechanism of fuel components oxidation. *J. KONES* **2018**, *25*, 17–24.
16. Jankowski, A.; Kowalski, M. Design of a new alloy for internal combustion engines pistons. In Proceedings of the 7th International Conference on Mechanics and Materials in Design (M2D2017), Albufeira, Portugal, 11–15 June 2017.
17. Żyluk, A.; Pietraszek, M. Investigation of an additional oxidizer charge effect on selected operational characteristics of a solid-fuelrocket engine. *J. Theor. Appl. Mech.* **2014**, *52*, 139–149.
18. Dussan, K.; Won, S.H.; Ure, A.D.; Dryer, F.L.; Dooley, S. Chemical functional group descriptor for ignition propensity of large hydrocarbon liquid fuels. *P. Combust. Inst.* **2019**, *37*, 5083–5093. [[CrossRef](#)]
19. Anderson, A.; Karthikeyan, A.; Ramesh Kumar, C.; Ramachandran, S.; Praveenkumar, T.R. Lowest emission sustainable aviation biofuels as the potential replacement for the Jet-A fuels. *Aircr. Eng. Aerosp. Tec.* **2020**, *93*, 502–507.
20. Kozakiewicz, A.; Kowalski, M. Unstable operation of the turbine aircraft engine. *J. Theor. Appl. Mech.* **2013**, *51*, 719–727.
21. Kulczycki, A. Theoretical approach to modelling the combustion process in turbine engines fuelled by alternative aviation fuels containing various components/bio components. *Combust. Engines* **2017**, *71*, 245–249. [[CrossRef](#)]
22. Lefebvre, A.H.; Ballal, D.R. *Gas Turbine Combustion: Alternative Fuels and Emissions*, 3rd ed.; CRC Press: Boca Raton, FL, USA, 2010.
23. Gatchell, M.; Zettergren, H. Knockout driven reactions in complex molecules and their clusters. *J. Phys. B At. Mol. Opt.* **2016**, *49*, 1–19. [[CrossRef](#)]
24. Vanhpve, G.; Petit, G.; Minetti, R. Experimental study of the kinetic interactions in the low-temperature autoignition of hydrocarbon binary mixtures and a surrogate fuel. *Combust. Flame* **2006**, *145*, 521–532. [[CrossRef](#)]
25. Tanaka, S.; Ayala, F.; Keck, J.C.; Heywood, J.B. Two-stage ignition in HCCI combustion and HCCI control by fuels and additives. *Combust. Flame* **2003**, *132*, 219–239. [[CrossRef](#)]
26. ARP 1533C. *Procedure for the Analysis and Evaluation of Gaseous Emission from Aircraft Engines*; SAE International: Warrendale, PA, USA, 2016.
27. Govindan, R.; Jakhar, O.; Mathur, Y. Computational analysis of Thumba biodiesel-diesel blends combustion in CI engine using Ansys-fluent. *IJCMS* **2014**, *3*, 29–39.
28. Meeks, E.; Ando, H.; Choul, C.P.; Dean, A.M.; Hodgson, D.; Koshi, M.; Lengyel, I.; Maas, U.; Naik, C.V.; Puduppakkam, K.V.; et al. New modelling approaches using detailed kinetics for advanced engines. In Proceedings of the 9th International Conference on Modelling and Diagnostics for Advanced Engine Systems (COMODIA 2008), Sapporo, Japan, 28–31 July 2008.
29. Pitz, W.J.; Cernansky, N.P.; Dryer, F.L.; Egolfopoulos, F.N.; Farrell, J.T.; Friend, D.G.; Pitsch, H. Development of an experimental database and chemical kinetic models for surrogate gasoline fuels. *SAE Tech. Pap.* **2007**. [[CrossRef](#)]
30. Kajdas, C.; Kulczycki, A.; Ozimina, D. A new concept of the mechanism of tribocatalytic reactions induced by mechanical forces. *Tribol. Int.* **2017**, *107*, 144–151. [[CrossRef](#)]
31. Gawron, B.; Białecki, T. Impact of a Jet A-1/HEFA blend on the performance and emission characteristics of a miniature turbojet engine. *Int. J. Environ. Sci. Technol.* **2018**, *15*, 1501–1508. [[CrossRef](#)]
32. Gawron, B.; Białecki, T.; Janicka, A.; Suchocki, T. Combustion and emissions characteristics of the turbine engine fueled with HEFA blends from different feedstocks. *Energies* **2020**, *13*, 1277. [[CrossRef](#)]

33. Suchocki, T.; Witanowski, Ł.; Lampart, P.; Kazimierski, P.; Januszewicz, K.; Gawron, B. Experimental investigation of performance and emission characteristics of a miniature gas turbine supplied by blends of kerosene and waste tyre pyrolysis oil. *Energy* **2021**, *215*, 119125. [[CrossRef](#)]
34. Gawron, B.; Bialecki, T.; Górniak, A.; Janicka, A.; Zawisłak, M. An Innovative method for exhaust gases toxicity evaluation in the miniature turbojet engine. *Aircr. Eng. Aerosp. Technol.* **2017**, *89*, 757–763. [[CrossRef](#)]
35. Janicka, A.; Zawisłak, M.; Zaczyńska, E.; Czarny, A.; Górniak, A.; Gawron, B.; Bialecki, T. Exhaust toxicity investigation of turbojet engine fed with conventional and biofuel, performed with aid of BAT-CELL Method. *Toxicol. Lett.* **2017**, *280*, 202. [[CrossRef](#)]

Article

Numerical Analysis of GDI Flash Boiling Sprays Using Different Fuels

Raul Payri ^{1,*}, Pedro Marti-Aldaravi ¹, Rami Abboud ¹ and Abian Bautista ²

¹ CMT—Motores Térmicos, Universitat Politècnica de València, Edificio 6D, 46022 Valencia, Spain; pedmar15@mot.upv.es (P.M.-A.); raab2@mot.upv.es (R.A.)

² MAHLE Electronics SL., Carrer de Nicolau Coprènic, 12, Paterna, 46980 Valencia, Spain; abianbr@gmail.com

* Correspondence: rpayri@mot.upv.es

Abstract: Modeling the fuel injection process in modern gasoline direct injection engines plays a principal role in characterizing the in-cylinder mixture formation and subsequent combustion process. Flash boiling, which usually occurs when the fuel is injected into an ambient pressure below the saturation pressure of the liquid, is characterized by fast breakup and evaporation rates but could lead to undesired behaviors such as spray collapse, which significantly effects the mixture preparation. Four mono-component fuels have been used in this study with the aim of achieving various flashing behaviors utilizing the Spray G injector from the Engine Combustion Network (ECN). The numerical framework was based on a Lagrangian approach and was first validated for the baseline G1 condition. The model was compared with experimental vapor and liquid penetrations, axial gas velocity, droplet sizes and spray morphology and was then extended to the flash boiling condition for iso-octane, n-heptane, n-hexane, and n-pentane. A good agreement was achieved for most of the fuels in terms of spray development and shape, although the computed spray morphology of pentane was not able to capture the spray collapse. Overall, the adopted methodology is promising and can be used for engine combustion modeling with conventional and alternative fuels.

Keywords: flash boiling; gasoline direct injection; computational fluid dynamics; Spray G; discrete droplet method; fuel surrogates

Citation: Payri, R.;

Marti-Aldaravi, P.; Abboud, R.; Bautista, A. Numerical Analysis of GDI Flash Boiling Sprays Using Different Fuels. *Energies* **2021**, *14*, 5925. <https://doi.org/10.3390/en14185925>

Academic Editors: Alexandre M. Afonso, Pedro Resende and Mohsen Ayooobi

Received: 1 August 2021

Accepted: 16 September 2021

Published: 18 September 2021

Publisher's Note: MDPI stays neutral with regard to jurisdictional claims in published maps and institutional affiliations.



Copyright: © 2021 by the authors. Licensee MDPI, Basel, Switzerland. This article is an open access article distributed under the terms and conditions of the Creative Commons Attribution (CC BY) license (<https://creativecommons.org/licenses/by/4.0/>).

1. Introduction

Gasoline direct injection (GDI) engines have penetrated the automotive market at a high rate in the past decade. Significant advantages, such as increased efficiency, lower knocking tendency, volumetric efficiency enhancement, and improved transient response have diverted the research focus from the well-known port fuel injection (PFI) towards GDI systems [1–3]. With these benefits, new challenges manifest themselves requiring further optimization strategies in order to reduce soot and particulate matter emissions that may result from phenomena such as tip wetting and wall-impingement [4,5]. Thus, spray air interaction and mixture formation in GDI engines require great care as the effect on the subsequent combustion phase significantly impacts the engine's thermal efficiency [6]. Flash boiling, when the fuel is ejected in a superheated state into the cylinder, has been characterized with an intense atomization phase and high plume-to-plume interaction in multi-hole injectors [7]. This phenomenon usually occurs at engine part load operation, where the in-cylinder pressure decreases below that of the fuel saturation pressure, leading to vapor bubble formation and liquid disintegration [8]. Thus, air-entrainment is enhanced and the fuel exits the nozzle with a wider angle which further promotes the air-fuel mixing process.

Various experimental and computational efforts have been elaborated in order to characterize the macroscopic and microscopic characteristics of gasoline spray development under various engine-like operating conditions. To this end, the Engine Combustion Network (ECN), a collaboration among research institutions and companies focusing

on engine combustion processes, have exhaustively investigated the GDI process and established a wide database of experimental and numerical data associated to a GDI injector named Spray G [9].

Computational Fluid Dynamics (CFD) is a viable tool when it comes to predicting the fuel injection process in internal combustion engines. Research work regarding this topic ranges from examining internal and near nozzle flow to external spray analysis in the far field. A collaborative investigation [10] has been done by ECN contributors where different modeling techniques and turbulence models were implemented in an effort to predict the mass flow rate and momentum of the Spray G injector. Mass flow rate profiles were accurately predicted although the fuel density in the vicinity of the nozzle was over-predicted signifying an offset in the velocity magnitude estimation. Shahangian et al. [11] aimed to couple internal nozzle flow simulations with external flow analysis described by the discrete droplet method (DDM). The DDM approach is a Eulerian–Lagrangian method where the liquid is considered as a discrete number of parcels and is injected into the domain where it evolves based on its interaction with the gas phase in the Eulerian field [12]. Their objective was to eliminate the need of performing experimental measurements of mass flow rate, which is an input for the DDM. Alternatively, they used the internal nozzle flow simulations to estimate the main variables, such as the injector hydraulic coefficients and mass flow, and fed them to the DDM model. Other authors resort to solely utilizing the DDM approach which has proved to be an accurate method in predicting the spray macroscopic and microscopic parameters [13,14]. Paredi et al. [15] simulated various operating conditions of the Spray G injector and implemented a specific flash boiling evaporation model to predict liquid evaporation under superheated conditions. They demonstrated that in order to develop a comprehensive model, liquid and vapor penetration are not sufficient to assess the spray development and fuel–air mixing, but further analysis regarding axial gas velocity, droplet diameters, and spray morphology are essential.

Flash boiling in GDI engines has been studied experimentally and numerically by various authors both in a constant volume vessel and in engines [16,17]. Experimentally, Sun et al. [18] visualized the spray development under flashing conditions in an optical engine and analyzed the subsequent influence on the combustion process. They found that flash boiling atomization results in a higher indicated mean effective pressure (IMEP) and lower particulate matter emissions due to the more vigorous vaporization process. Similarly, Dong et al. [19] showed that the cycle to cycle variation (CCV) decreases under flash boiling conditions and that the fuel distribution in the cylinder is more homogeneous. Lacey et al. [20] studied the behavior of Gasoline and LPG surrogates, namely iso-octane and propane, under a wide range of R_p values, ratio of saturation pressure of the fuel at its temperature in the rail to the ambient pressure, and deduced that the flashing behavior of the fuels are different under similar R_p values. Propane only exhibited plume interaction and collapse for very high R_p values as compared to iso-octane. Based on this observation, the authors in [20] defined a new criteria for flashing behavior and subsequent spray collapse depending on the injector geometry and thermodynamic properties of the fuel. Li et al. [21] expanded the study of Lacey et al. to a 5 hole GDI injector. They related nucleation and bubble growth processes to spray collapse concluding that suppression of those phenomena at elevated chamber pressures account for the non-occurrence of spray collapse of propane. Numerically, Nocivelli et al. [22] applied three different techniques for their simulation of subcooled and mild flash boiling injection conditions using the ECN Spray G injector. The different methods consisted of a DDM simulation with the typical blob injector method, one-way couple of Eulerian nozzle flow, and initialized Lagrangian parcel diameters with data from X-ray radiography measurements. It was shown that the blob injector coupled with the KHRT breakup model is quite capable of capturing the liquid phase penetration for both sub-cooled and flash boiling conditions although the main drawback is the extensive stripping and breakup activity that leads to small droplet diameters. In addition, the one way coupling provided promising results and proves to be

more predictive than the DDM approach since it relies on internal nozzle flow simulations for simulation initialization.

The aim of this study is to develop a comprehensive spray model validated for the Spray G baseline condition (G1) and extended to cold flash boiling conditions. The developed model was implemented first for iso-octane and then extended to n-hexane, n-heptane, and n-pentane. The extension of the model to different fuels enabled the assessment of fuel properties on spray morphology under flash boiling conditions. To the authors knowledge, the same model setup used for predicting flash boiling behavior of different fuels was not previously done. This paper is divided as follows, first, the numerical and experimental methodologies are depicted. Then, results are displayed and discussed for each fuel investigated starting with the spray validation case. The last section presents the main conclusions drawn and future outlook.

2. Materials and Methods

2.1. Numerical Methodology

The adopted numerical models are described in this section. All the simulations were performed in the LibICE framework, which is a set of libraries and solvers based on OpenFOAM developed by the ICE Research Group of Politecnico di Milano for the simulation of physical processes in Internal Combustion Engines [23–25]. More specifically, a dedicated solver for non-reacting flows based on the PIMPLE algorithm was employed. The time was discretized by the Euler scheme whereas the divergence and gradient terms were discretized by second order accurate Gauss Schemes. In addition, linear interpolation schemes were adopted. An initial time step was set to $1 \mu\text{s}$ and varied throughout the simulation while maintaining a Courant number less than 1.

For what concerns the computational grid, a structured grid of hexahedral cells was used with a base size of 1 mm grid, which was further refined down to 0.5 mm using Adaptive Mesh Refinement (AMR). These mesh characteristics were chosen after analyzing the effect of various grid base and minimum cell sizes as shown in Figure 1. The figure demonstrates that not only the minimum cell size significantly influences the result but also the base size, as can be seen with the 2 mm base size and 0.5 mm minimum cell size. Further refinement of the grid to 0.25 mm marginally varies the result and it remains within the experimental error range with respect to the chosen mesh setup but with triple increase in cost (190 min compared with 60 min on 8 cores).

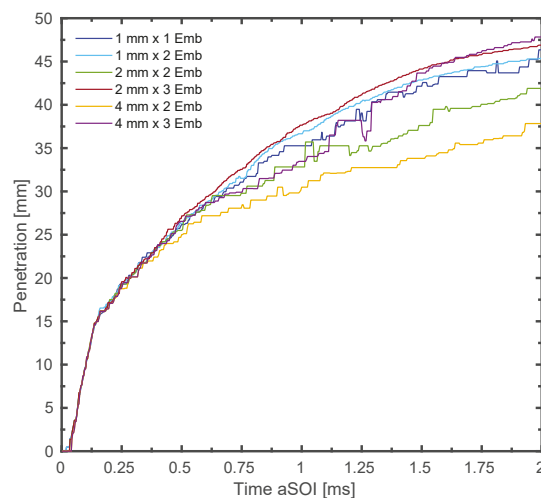


Figure 1. Effect of different mesh base and minimum cell sizes on the spray penetration.

AMR is an effective tool in reducing the computational cost by refining the grid only in the region of interest. That being said, the refinement was performed based on the total fuel mass fraction, where the lower and upper thresholds were set to 0.01 and 1, respectively. The field takes into account both liquid and vapor fuel fractions in a given cell and refines the cells according to the threshold limits. The calculations are performed in a rectangular domain of 110 mm width and 100 mm of height. The boundaries of the domain are all modeled as walls and the domain is large enough so that liquid parcels do not interact with them. The RANS approach was adopted for turbulence modeling. All simulations were carried out with the standard $k - \epsilon$ turbulence model with a turbulent dissipation constant, C_1 , of 1.55 increased from a standard value of 1.44. The model was chosen due to the improved spray morphology and gas entrainment it entails as compared with other models, such as the RNG $k - \epsilon$ model [26]. Increasing the C_1 parameter is consistent with the “round jet correction” according to Pope and improves the spray jet morphology when the standard $k - \epsilon$ is used to resolve the turbulent field [27]. The turbulent kinetic energy and dissipation rate were initialized to $1 \text{ m}^2/\text{s}^2$ and $90 \text{ m}^2/\text{s}^3$, respectively.

2.2. Spray Models

The approach utilizes the Discrete Droplet Method which signifies that suitable sub-models should be implemented to describe the introduction of parcels into the computational domain and the subsequent stages that the parcels undergo from primary atomization until liquid evaporation. The velocity profile of the Lagrangian parcels is directly proportional to the mass flow rate and inversely proportional to the area contraction coefficient C_a , both of which are user inputs. The mass flow rate profile used was that of the well known ECN Spray G injector at 200 MPa of injection pressure. The area contraction coefficient was set to 0.8 leading to an initial velocity of 150 m/s for the spray G1 baseline condition in this study. The Lagrangian field of the simulation was statistically represented by 60,000 parcels so as to have a suitable compromise between simulation run time and accuracy.

The primary breakup was modeled by the turbulence induced Huh Gosman atomization model [28]. The fuel is injected into constant volume chamber as spherical blobs with the same diameters as the orifice holes, $165 \mu\text{m}$ in this study. The model accounts for the turbulent motion at that nozzle outlet by producing an initial surface perturbation on the parcels. These perturbations grow due to the aerodynamic forces induced by the gas phase. The primary parcel diameter reduction rate is proportional to the ratio between the atomization length and time scales:

$$\frac{dD}{dt} = -C_5 \frac{L_a}{\tau_a} \quad (1)$$

where C_5 is a tuning factor (value shown in Table 1). The characteristic atomization length scale is dependent on the turbulence length scale L_t according to the relation:

$$L_a = C_1 L_t = C_2 L_w \quad (2)$$

where L_w is the wavelength of surface perturbations induced by turbulence with $C_1(2.0)$ and $C_2(0.5)$. The atomization time scale is calculated from a linear combination of turbulent time and wave growth time scales:

$$\tau_a = C_3 \tau_t + C_4 \tau_w \quad (3)$$

The wave growth rate time scale is obtained from a formulation based on Kelvin–Helmholtz (KH) instability theory. Literature values for $C_3(1.2)$ and $C_4(0.5)$ were adopted. The turbulent length and time scales are evaluated using the turbulent kinetic energy k and its dissipation rate ϵ according to:

$$L_t = C_\mu \frac{k^{1.5}}{\epsilon} \quad (4)$$

$$\tau_t = C_\mu \frac{k}{\epsilon} \quad (5)$$

C_μ in Equations (4) and (5) is the same constant used in the $k - \epsilon$ turbulence model and equal to 0.09. The stripped mass, as a result of the diameter reduction in Equation (1), is calculated according to:

$$m_s = \rho_l N_p \frac{\pi}{6} (D_{old}^3 - D_{new}^3) \quad (6)$$

where ρ_l is the liquid fuel density, N_p is the particle number, D_{old} the parent parcel diameter, and D_{new} the newly computed diameter. The Huh Gosman model also predicts the initial plume cone angle according to the atomization length and time scales where the spray is assumed to diverge radially with a velocity proportional to the ratio between the atomization length and time scale. However, previous studies have shown that these correlations underpredict the spray cone angle for Spray G applications [29]. Therefore, the plume cone angle was imposed separately and the Huh Gosman model was only responsible for the primary atomization phase.

Table 1. Spray model constants.

Constant	Model	Value
C_5	HG	1.0
We_{limit}	HG	40
B_0	KHRT	0.61
B_1	KHRT	34
C_τ	KHRT	1.0
C_{RT}	KHRT	0.16
C_{BU}	KHRT	2.5

The break up of the secondary droplets stripped from parent parcels is governed by the Kelvin–Helmholtz Rayleigh–Taylor (KHRT) breakup model. The distinction between the regions where primary atomization takes place and where the secondary break up activity takes control is defined by the so-called core length and is computed according to:

$$L_c = C_{BU} \cdot d \sqrt{\frac{\rho_l}{\rho_g}} \quad (7)$$

where C_{BU} is a parameter that takes into account flow conditions inside the injector, d is the injector orifice diameter, and ρ_l and ρ_g are the density of liquid and gas phase, respectively. Hence, the KH stripping activity is decoupled from the primary atomization process and is only applied after a certain distance from the injector tip. This was done in order to prevent excessive stripping due to the KH model in the near nozzle region that would lead to small droplet diameters which negatively influence the air entrainment and thus impacts the spray morphology. The KH stripping activity stems from the idea that each droplet has instabilities on its surface as it leaves the nozzle, similarly to what was mentioned previously in the Huh Gosman model. These instabilities grow due to the gas–liquid interaction resulting from high relative velocities. The wave growth rate is expressed by omega, ω_{KH} , and its characteristic length by lambda, λ_{KH} . The wave with the fastest growth rate will detach and create new droplets that will have a diameter proportional to λ_{KH} and B_0 , where B_0 is a model constant usually set to 0.61. As a consequence, the parent parcel will lose some mass as child droplets are continuously detaching leading to a reduction of the parent droplet diameter according to:

$$\frac{dD}{dt} = -\frac{D - D_{KH}}{\tau_{KH}} \quad (8)$$

with τ_{KH} being the characteristic KH breakup time and expressed as:

$$\tau_{KH} = 3.778B_1 \frac{D}{\omega_{KH}\lambda_{KH}} \quad (9)$$

τ_{KH} can be tuned by operating on the model constant B_1 (value shown in Table 1). When the RT breakup model is triggered, the droplets undergo a catastrophic breakup event once they have passed a certain period of time that is equal to or greater than the RT characteristic time τ_{RT} . Similarly to the KH model, the characteristic growth rate of the wave could be computed according to:

$$\lambda_{RT} = C_{RT}2\pi\sqrt{\frac{3\sigma}{a(\rho_l - \rho_g)}} \quad (10)$$

where C_{RT} is a model constant which accounts for the effects that create instabilities over the surface and requires careful calibration as it strongly effects the droplet diameter and velocity properties. σ is the surface tension and a is the acceleration that the droplet undergoes to the aerodynamic force that it is subjected to and is computed according to Equation (11):

$$a = \frac{3}{8}C_d \frac{\rho_g u_{rel}^2}{\rho_l d} \quad (11)$$

which depends on the relative velocities between the liquid and gas, their densities, and the droplet drag coefficient C_d . Once the condition for τ_{RT} is satisfied, the disintegration of the parent droplet to a number of equally size droplets is done and the new diameter is set according to:

$$d_c = \lambda_{RT} \quad (12)$$

Liquid evaporation was modeled by a mass based approach [30] whenever flash boiling conditions were non-existent and the evaporation rate is expressed as:

$$\frac{dm_d}{dt} = \pi D \beta \rho_v Sh \ln \left(\frac{1 - Y_{v,\infty}}{1 - Y_{v,s}} \right) \quad (13)$$

in which D represents the droplet diameter, β is the mass diffusion coefficient, Sh is the Sherwood number, ρ_v is the vapor fuel density, and $Y_{v,\infty}$ and $Y_{v,s}$ are the fuel vapor mass fractions evaluated at point in the far field and close to the droplet surface at saturation conditions, respectively. The term in parentheses is usually called the Spalding number and denoted by B . Equation (13) is only valid for evaporation without boiling. The reason is that if the evaporation pressure approaches the pressure of the system, B would tend to zero since the fuel vapor mass fraction at the droplet surface would tend to unity. This would lead to an unrealistic infinite evaporation rate which is not physical. Therefore, under flash boiling conditions, the Adachi Rutland flash boiling evaporation model [31,32] is implemented instead, where the heat exchange between the droplet interior and the surroundings control the phase change process rather than diffusion. The readers are advised to refer to the work of Paredi et al. [15] for a complete description of the model formulation and implementation in LibICE. The main constants for the spray sub-models are tabulated in Table 1.

2.3. Post-Processing Techniques

The post-processing fields and routines implemented throughout this paper are outlined in this section. Vapor penetration was numerically calculated based on the mixture fraction. It was defined by the distance from the nozzle tip position up to where 0.1% of mixture fraction was found. Axial liquid phase penetration were measured according to the projected liquid volume (PLV) fraction [33] which enables a direct comparison between

experimental and CFD data. The procedure is based on the relation of the liquid volume fraction to the optical thickness of the liquid along the light path according to Equation (14):

$$\tau \frac{\pi D^3}{6 C_{ext}^*} = \int_{-y_\infty}^{y_\infty} LVF dy \quad (14)$$

where D is the droplet diameter taken as $7 \mu\text{m}$ according to Phase Doppler Interferometer (PDI) measurements provided by General Motors (GM) to the ECN and C_{ext}^* is the extinction cross-section acquired from MIE theory. It was assumed that the droplet diameter and extinction coefficient are constant along the light path. C_{ext}^* can be calculated using MiePlot [34] and is a function of the droplet diameter, light wavelength, and the collection angle of the optical setup. It was calculated to be $44.6 \times 10^{-6} \text{mm}^2$ for Spray G with iso-octane. The PLV indicates how much liquid volume is present in a certain projected area and thus has the units of $\text{mm}^3(\text{liquid})/\text{mm}^2$. Two different thresholds were used and recommended by ECN in order to reduce the uncertainties of the dependence on the chosen diameter value. Hence, a high and a low threshold were used according to Equations (15) and (16), respectively,

$$\int_{-y_\infty}^{y_\infty} LVF dy = 2.0 \times 10^{-3} \text{mm}^3/\text{mm}^2 \quad (15)$$

$$\int_{-y_\infty}^{y_\infty} LVF dy = 2.0 \times 10^{-4} \text{mm}^3/\text{mm}^2 \quad (16)$$

The PLV was numerically computed by integrating the Eulerian LVF of the spray for different slices and projecting it on a two-dimensional plane. The liquid penetration was then deduced as the maximum axial position from the nozzle tip with a LVF value below either of the thresholds. The axial gas velocity was computed by a probe point placed at 15mm distance away from the injector tip location and was compared with Particle Image Velocimetry (PIV) measurements [35]. Finally, the radial Sauter Mean Diameter (SMD) distribution was computed along a line passing through one of the plumes at perpendicular plane 15mm below the injector tip according to Figure 2 and was compared with experimental PDI measurements performed by GM [36].

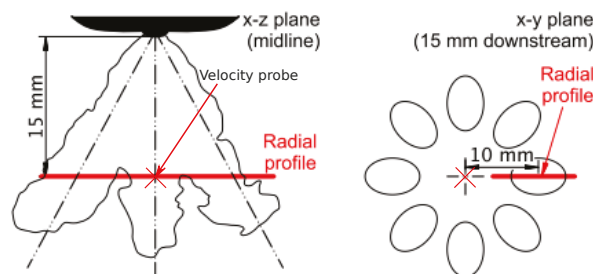


Figure 2. Location of line probe for SMD data sampling and velocity measurement point [37].

2.4. Experimental Methodology

The experimental facility used to measure the flash boiling condition for all the fuels will be briefly discussed in this section. For a more detailed explanation about the optical techniques and post-processing algorithms, the readers are advised to refer to [38].

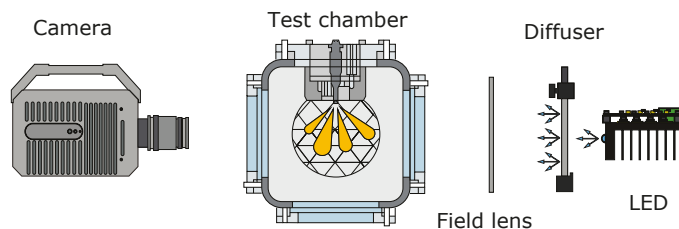
The injector used in the spray visualization measurements is the Spray G injector (serial AV67-026) used by the ECN [9]. It is a solenoid driven eight hole injector designed for Direct Injection Spark Ignition (DISI) engine configurations. The geometrical details of the injector are shown in Table 2.

Table 2. Spray G injector characteristics.

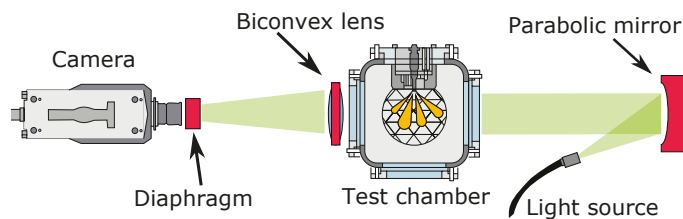
Parameter	Value
No. of holes	8
Orifice	circular
Hole	straight
Nozzle	step hole
l/d ratio	1.4
Orifice diameter	165 μm
Orifice length	160–180 μm *
Orifice drill angle	37°
Full outer angle	80°

* Lengths of inner and outer diameters.

The high pressure fuel system is similar to that used for diesel injectors and has been previously described in [39]. More importantly, the spray visualization was based on two optical techniques: single-pass schlieren was used for the vapor phase and diffused back illumination (DBI) for the liquid phase. The latter setup is shown in Figure 3, where the main optical components can be depicted. A blue light emitting diode (LED) light source was placed on one side of the test chamber where an engineered diffuser with 100 mm diameter was used leading to a uniform light transmission. A Fresnel lens characterized by a focal length of 67 mm was utilized in order to reproduce the diffused light at the optical plane of interest. The Photron S9 camera acquisition speed was set to 30 kHz and the spatial resolution was 4.25 pixel/mm with a field of view of 384×376 pixels.

**Figure 3.** DBI optical setup for liquid phase visualization.

The schlieren setup consisted of point illumination light source coming from a 1 kW Mercury–Xenon arc lamp. A parabolic mirror is used to parallelize the rays before passing through the test vessel. After passing through the chamber, the rays are converged at the focal length (450 mm) of a biconvex lens where a diaphragm, with 4 mm cutoff diameter, is placed right before the high speed camera to provide a highly contrasted image, as shown in Figure 4. The high speed Photron SA5 camera acquisition rate was set to 30 kHz and had a field of view of 512×512 pixels. The spatial resolution for the Schlieren technique was 4.4 pixel/mm. More details regarding the experimental facility and optical techniques utilized for this study could be found in [40]. The main methodology for image processing is detailed in Payri et al. [38].

**Figure 4.** Schlieren optical setup for liquid phase visualization.

2.5. Fuels and Test Conditions

The fuels used in the experimental campaign as well as in numerical simulations consist of gasoline fuel surrogates. Usually, iso-octane and n-heptane mixtures are used to simulate gasoline fuels with different octane numbers. For flash boiling conditions, fuel volatility becomes an important factor and for this reason various surrogate mono-component fuels are chosen with similar distillation curves of commercial gasoline. Table 3 displays the fuels used in this study along with the main properties. It is evident that the vapor pressure of fuels are quite different, leading to distinct behaviors under flash boiling conditions.

Table 3. Properties of the fuels investigated obtained from NIST database [41].

Properties	iso-octane	n-heptane	n-hexane	n-pentane	Units
Liquid density	688.59	677.81	652.84	618.8	kg/m ³
Vapor pressure	7.18	6.72	22.01	73.57	kPa
Surface tension	18.16	19.82	17.73	15.25	mN/m
Viscosity	0.456	0.376	0.291	0.214	mNs/m ²
Specific heat	2.04	2.24	2.26	2.34	kJ/kgK

Properties obtained at 300 K.

Table 4 shows the operating conditions considered in this study. The baseline condition G1 was used to first validate the spray model with iso-octane. Following this stage, simulations were done for Spray G2 cold condition variant and compared with experimental measurements carried out at CMT-Motores Térmicos by the techniques described in Section 2.4 for the fuels previously shown. In addition, a total of 10 injection events, 160 frames each, were acquired for every G2 cold condition.

Table 4. Operating conditions.

Parameters	G1	G2-cold	Units
Energizing time	0.68	0.68	ms
Injection Pressure	200	200	MPa
Ambient pressure	6	0.5	bar
Fuel temperature	363	363	K
Ambient temperature	573	293	K
Injected mass	10	10	mg

3. Results and Discussion

3.1. Baseline G1 Condition

The numerical spray model was first validated for the Spray G baseline condition (G1). The most important spray macroscopic parameters are compared with Sandia's experimental measurements for vapor and liquid penetration. In addition, the spray-air interaction and gas entrainment were assessed based on centerline axial gas velocity from PIV measurements and finally, the performance of the stripping and break up activity of the KHRT model was verified based on SMD measurements provided by GM at different time steps.

The results shown in this section are an outcome of an extensive calibration procedure carried out in order to establish a suitable baseline model able to predict the aforementioned variables and to be extended to flash boiling conditions for the various fuels evaluated in this study. Therefore, it must be said that the constants implemented in the models are not intended to be the ideal ones for one operating condition but rather provide a comprehensive setup in order to predict the spray evolution for all the conditions investigated.

The evolution of the axial vapor phase penetration is shown in Figure 5. Initially, the model slightly overpredicts the vapor speed and penetrates with a steeper slope for the first milliseconds. The curve then seems to follow the experimental profile reasonably well and is capable of capturing the shape of the experimental curve. After the end of injection, the momentum of the spray seems to be lower than the experimental one where a slight deviation initiates and the numerical vapor penetrates with a slightly lower rate. Overall, it could be stated that the adopted turbulence model and Pope correction for the C_1 constant predict the air–fuel mixing process quite well and thus the spray evaporation rate. The issue with the underprediction after the end of injection (EOI) could be related to the adopted numerical cell resolution, in other words, refining the domain with an additional level of refinement could enhance the results considering a fixed spray model setup. However, a minimum value of 0.5 mm was considered sufficient enough to provide a good compromise between simulation run time and accuracy.

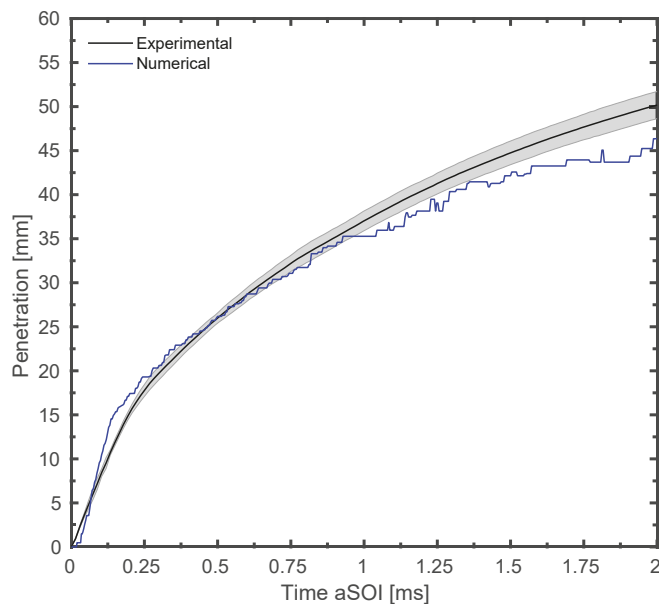


Figure 5. Numerical and experimental axial vapor phase penetration for the baseline condition (G1).

Liquid phase axial penetration results are displayed in Figure 6 where both thresholds are shown. Comparing results with two different thresholds provides detailed feedback on whether the deviations from experimental data is related to the tip of the spray plume or to the region nearby the liquid core. The low threshold captures most of the liquid length up to the spray plume tip whereas the high threshold only captures the dense liquid region. Observing the initial stage of injection, it could be seen that the axial liquid penetration for both thresholds is higher than the experimental curves. That is mainly attributed to the prolonged core length which allows larger droplets to evolve for a longer distance since the KH stripping activity is not active within this region. That being said, a shorter liquid core length could be implemented by decreasing the C_{BLI} constant in order to trigger the KH stripping activity sooner. However, considering the current setup, it was concluded by the authors that for the given stripping characteristics, very small droplets will be present in the near nozzle region which would negatively influence the gas entrainment and spray morphology and increase the error in droplet size prediction; therefore, the selected value is justified. Following the early stage of injection, the low threshold liquid penetration follows the experimental trace quite effectively for the remainder of the injection duration as well

as EOI. On the other hand, the high threshold trend develops with a lower penetration magnitude compared to the experimental trace. The liquid residence time matches that of experimental data where it can be seen that the penetration value goes to zero at approximately 1.25 ms. A sensitivity analysis done by the authors revealed that the reason for this underestimation of the high threshold is mainly due to two factors, the stripping intensity of the KH model, and the breakup of the RT model regulated by the C_{RT} constant. Hence, further tuning of the spray breakup model could enhance the trend of the high threshold liquid penetration curve, although the effect on the G2 cold condition should be carefully considered. It is of utmost importance to keep in mind the significance of these constants and their impact on the droplet diameters and consequently on the liquid evaporation rate when a calibration procedure is to be done.

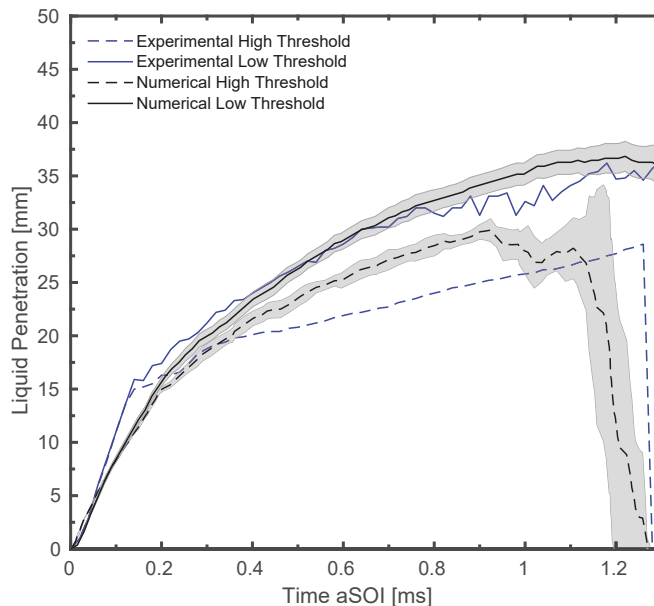


Figure 6. Numerical and experimental axial liquid phase penetration for the baseline condition (G1). High threshold corresponds to $2 \times 10^{-3} \text{ mm}^3/\text{mm}^2$ while low threshold corresponds to $2 \times 10^{-4} \text{ mm}^3/\text{mm}^2$ liquid volume fraction.

In order to accurately predict the mixture formation process, the spray induced gas velocity is of vital importance as it directly influences the spray evaporation rate. For this reason, the centerline axial gas velocity at 15 mm downstream of the injector is calculated and is shown in Figure 7. The magnitude of the axial velocity is highly dependent on the turbulence model adopted and the liquid core length, or in other words, the location at which the transition from primary atomization regime to secondary breakup occurs. The computed axial gas velocity presents an overestimation of the recirculating gas motion during the injection phase. This can be attributed to the prolonged liquid core length resulting in bigger droplets for a larger distance leading to a higher gas entrainment. Consequently, the reverse motion of the gas phase is delayed as seen by the gap after the end of injection, at 0.78 ms, and then follows the experimental trend with good accuracy.

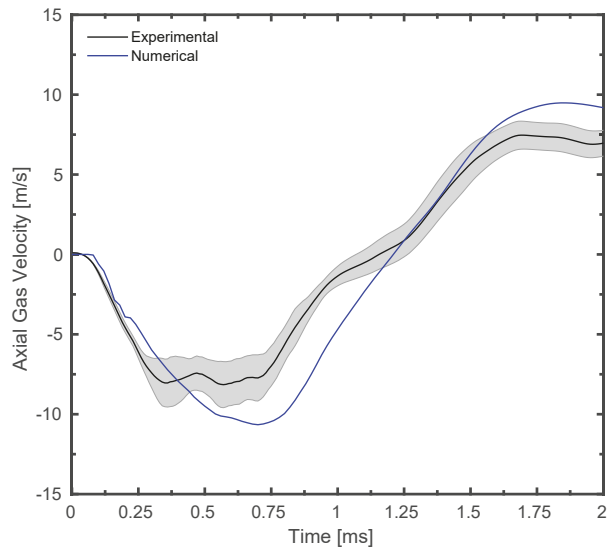


Figure 7. Numerical axial gas velocity comparison with PIV experimental data from Sandia for the baseline condition (G1).

The assessment of the droplet SMD allowed for the evaluation of the performance of the breakup and stripping phases that the liquid droplets undergo as they are injected into the ambient gas. Figure 8 depicts the SMD values at three different time steps. An intense KH stripping activity at 0.3 ms leads to small droplets compared with experimental PDI measurements whereas a better agreement is reached during the late stage of injection and after EOI.

Spray morphology and liquid evaporation were also investigated based on the projected liquid volume maps. This permits a one-to-one comparison between computed and experimental liquid profiles and allows one to further elaborate the liquid penetration trends. The PLV data used in this comparison was obtained from the University of Melbourne (UoM) [15]. From Figure 9, it can be clearly seen that the numerical spray has a smaller plume cone angle with respect to the measurements. In addition, the computed spray seems to be denser with a higher liquid concentration on the plume tips. At 0.9 ms, there is almost no liquid present in the domain which is not the case for the computed spray signifying a lower evaporation rate. Future efforts will investigate plume angles greater than the adopted value (16°) in order to be in agreement with the experimental morphology. Furthermore, the evaporation rate could also be simultaneously improved since the spray would entrain more air with a wider plume angle. It can also be noted that the numerical spray evolves with a larger spray width which could be attributed to the adopted drill angle in this study, 37° . There are various uncertainties in literature [15,42] regarding the optimal drill angle value. Therefore, the drill angle was not used as a tuning factor in this study and the value of 37° was kept constant for all the simulations. Overall, the computed macroscopic and microscopic variables were deemed accurate and suitable to proceed with the study.

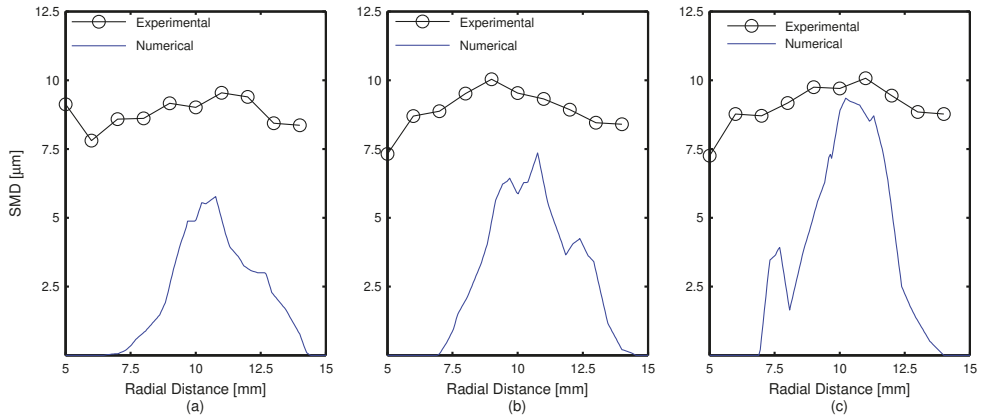


Figure 8. Numerical radial SMD profile comparison with experimental PDI data from GM for the baseline condition (G1). (a) 0.3 ms, (b) 0.6 ms and (c) 0.9 ms.

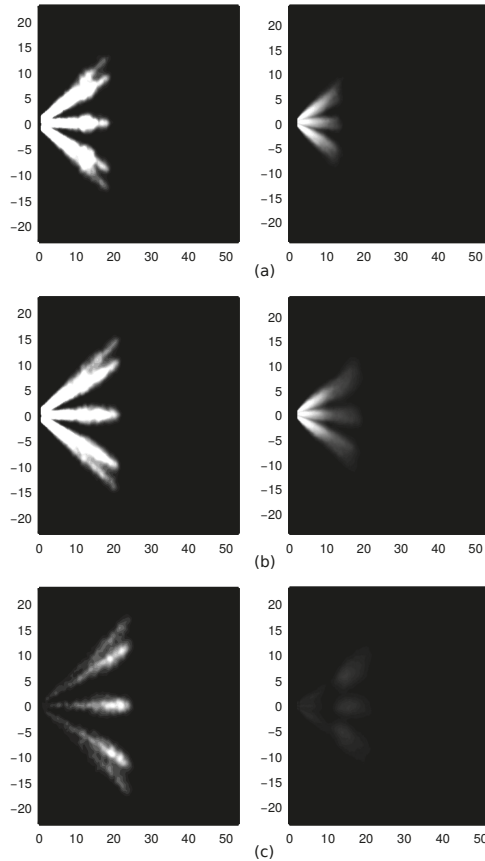


Figure 9. Numerical (left) vs. UoM experimental (right) PLV maps for the baseline condition (G1). (a) at 0.3 ms, (b) at 0.6 ms and (c) at 0.9 ms after SOI. Liquid volume fraction range is 0–0.01 mm³/mm².

3.2. G2 Cold Condition for iso-octane

Following a thorough validation of the baseline G1 condition, the spray model was then used to simulate the G2 cold condition. Iso-octane was first analyzed since it was the liquid fuel with which the model was developed and calibrated. The only parameter that was changed from the previous model setup was the spray cone angle and was increased to 26.5° to account for the mild flash boiling condition [43]. In the following analysis, for iso-octane and the different fuels that will be presented, the experimental data correspond to those described in Section 2.4 which were carried out at CMT. The numerical axial vapor and liquid penetrations are compared with the experimental ones and shown in Figure 10. The computed vapor penetration develops with a higher penetration magnitude for the majority of the injection duration as well as EOI. The trend, however, is captured by the numerical model. On the other hand, liquid penetration results agree with the experimental measurements although they present an overestimation during the steady phase of the injection duration due to the extended liquid core length. The slope of the curve is also predicted by the model well after the EOI. The results of vapor and liquid penetration indicate that there is more improvement to be done in terms of spray atomization and breakup in this weakly evaporative condition. The promotion of a more intense KH stripping activity, leading to a higher evaporation rate, would provide enhanced behavior in terms of the vapor penetration results. Overall, the results shown are quite promising given that the model is able to predict the main macroscopic variables under different ambient densities and temperatures.

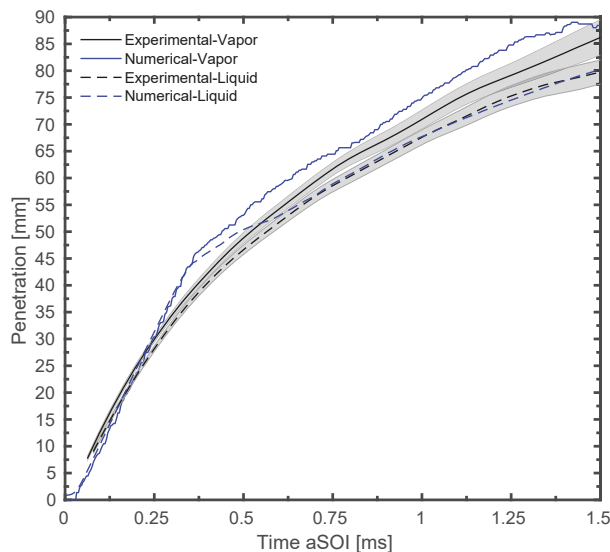


Figure 10. Numerical and experimental axial vapor and liquid phases penetration for the G2 cold condition for iso-octane.

Furthermore, the spray morphologies are analyzed in terms of DBI images and images of the numerical spray parcels. The previous comparison demonstrated in Section 3.1 based on the projected liquid volume fraction could not be done here since the experimental measurements were not post-processed in this manner. Nevertheless, this method of comparison outlines the overall spray shape and permits the assessment of the spray behavior under mild flashing conditions. Figure 11 reports the evolution of the liquid during the injection event, at 0.3 ms and 0.6 ms, as well as after the end of injection at 0.9 ms. The numerical model seems to capture the global spray shape and exhibits a certain degree of plume-to-plume interaction from the early stages of injection. In addition, the

spray tip liquid density is also well captured although numerical images indicate that the overall plume width is wider than the corresponding DBI images. The liquid distribution is also predicted by the numerical model, especially at 0.9 ms where few droplets appear in the liquid core region which agrees with the DBI images. It could then be stated that evaporation model utilized for the G2 cold condition is capable of reproducing the overall spray shape with good accuracy. That being said, the model is further analyzed in the next sections for several fuels which present different behaviors under mild flash boiling conditions.

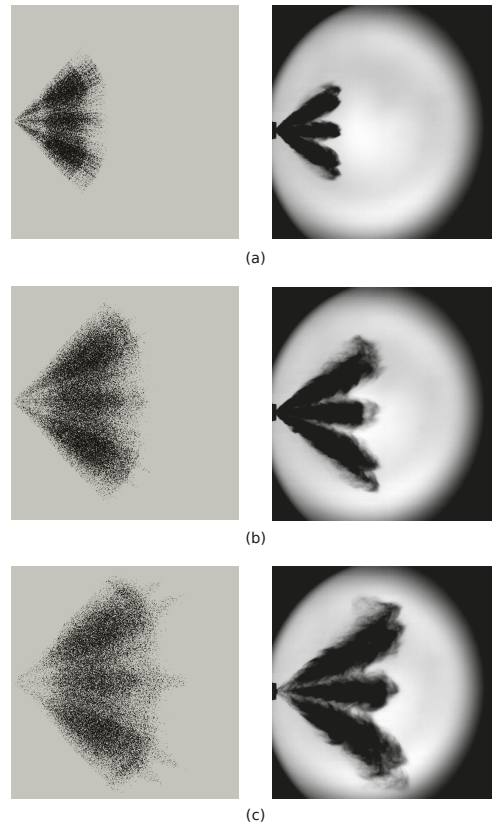


Figure 11. Numerical (left) vs. CMT experimental (right) liquid morphology images for the G2 cold condition for iso-octane. (a) at 0.3 ms, (b) at 0.6 ms and (c) at 0.9 ms after SOI.

3.3. G2 Cold Condition for *n*-heptane

This section is dedicated to the implementation of the numerical spray model with *n*-heptane. Given that *n*-heptane possesses similar liquid properties as iso-octane, the behavior under mild flashing conditions is expected to be similar as well. As what was previously discussed, the axial vapor and liquid phase penetrations are first examined and the spray morphologies through numerical and DBI images are then studied. Figure 12 shows the evolution of the vapor and liquid phases. The vapor phase follows the experimental trend quite well up to the end of injection. A slight underestimation can then be observed in the range of 0.8 ms to 1.0 ms; however, the deviation from the experimental trace is considered negligible. The same could be said for the axial liquid penetration, where the

slight overestimation during the initial stages of injection is present, as previously seen with iso-octane.

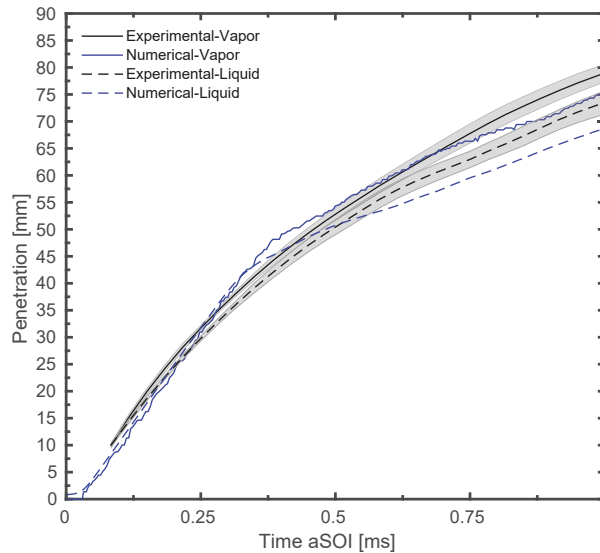


Figure 12. Numerical and experimental axial vapor phases penetration for the G2 cold condition for n-heptane.

The evolution of the spray morphology during and after the end of injection is shown in Figure 13. Experimental and numerical images resemble that of iso-octane where plume-to-plume interaction is evident. The effect of superheated liquid on the plume radial expansion as well as the Adachi Rutland flash boiling diameter reduction rate seem to accurately predict the flashing behavior using n-heptane as a fuel. So far, the fuel tested are said to be in mild flashing conditions since the R_p values are slightly greater than unity. The R_p value is generally used to indicate the presence of flash boiling and is computed according to the ratio of fuel saturation to ambient pressure p_{sat}/p_{amb} . The R_p value for n-heptane under the G2 cold condition is around 1.5. The next sections will feature the remaining fuels investigated in this study, n-hexane and n-pentane, which are characterized by a higher superheat degree compared to iso-octane and n-heptane.

3.4. G2 Cold Condition for n-hexane

N-hexane is usually employed to imitate the light component of gasoline and previous experimental studies under flash boiling conditions have shown that its behavior is more similar to gasoline compared to n-heptane and iso-octane [44]. Validation for the axial vapor and liquid phase penetrations is shown in Figure 14. The computed profiles correctly match the experimental trends for the whole injection duration and the model is able to reproduce the higher volatility characteristic of n-hexane compared to the previous fuels, as can be seen by the reduced penetration length. The Adachi Rutland implemented model thus proves to be accurate in computing the evaporation rate in weakly evaporative conditions and for fuels of different volatilities.

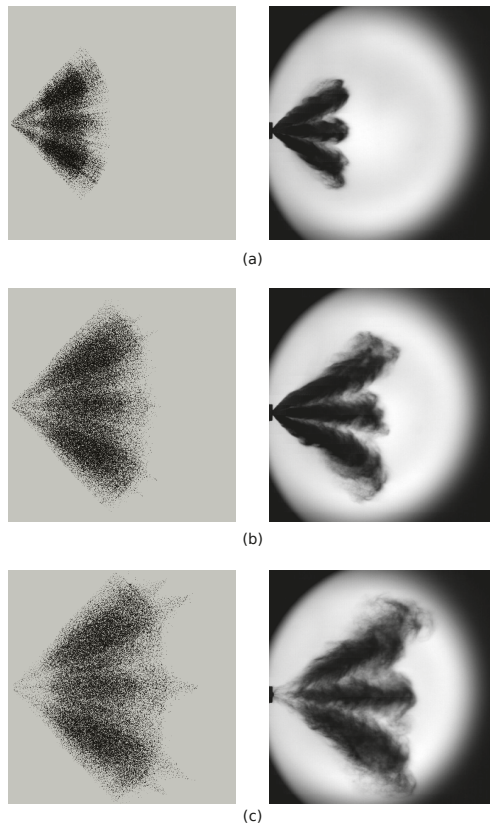


Figure 13. Numerical (left) vs. CMT experimental (right) liquid morphology images for the G2 cold condition for n-heptane. (a) at 0.3 ms, (b) at 0.6 ms and (c) at 0.9 ms after SOI.

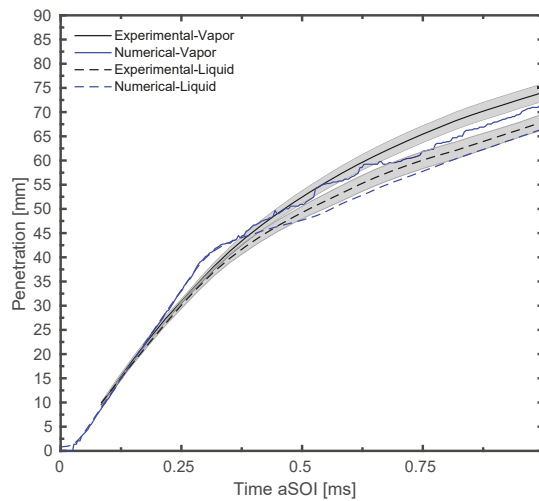


Figure 14. Numerical and experimental axial vapor and liquid phases penetration for the G2 cold condition for n-hexane.

To further assess the numerical results, the spray morphology is depicted in Figure 15. A clear difference can be seen in the DBI images compared to the fuels previously elaborated. Thicker plumes are now evident leading to a strong plume-to-plume interference although distinct spray plumes can still be observed. Therefore, the radial expansion of the plumes due to flash boiling is more evident for *n*-hexane. The numerical images further confirm the reduced liquid penetration of *n*-heptane. Moreover, the spray tip shape is also captured by the computed spray in the stable phase of injection at 0.6 ms. This could also be extended to 0.9 ms shortly after the injection has ended.

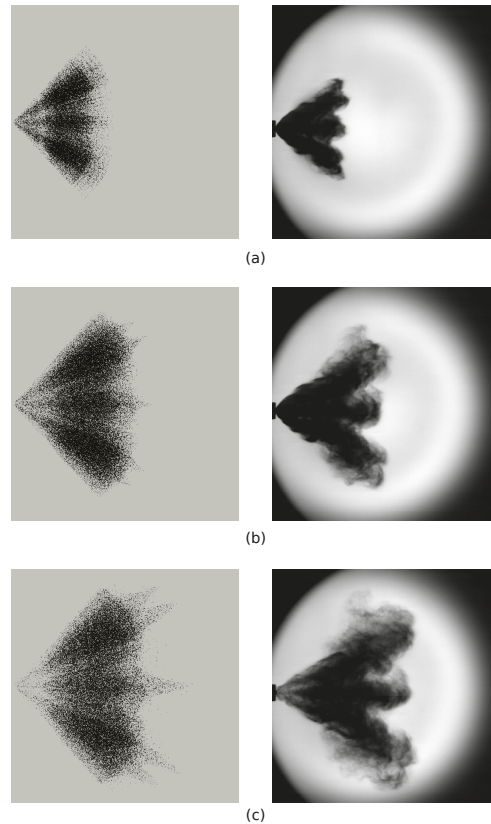


Figure 15. Numerical (left) vs. CMT experimental (right) liquid morphology images for the G2 cold condition for *n*-hexane. (a) at 0.3 ms, (b) at 0.6 ms, and (c) at 0.9 ms after SOL.

3.5. G2 Cold Condition for *n*-pentane

N-pentane encompasses the highest R_p value among all the fuels tested; therefore, a more extreme case of flash boiling is expected. After a thorough calibration procedure, the authors concluded that a slightly smaller plume cone angle, 23° , compared to the previous fuels should be adopted to accurately describe the spray development into the gas phase. Figure 16 shows the axial vapor and liquid penetrations. It can be clearly seen that the computed liquid phase evolution has a different slope than the experimental one which is magnified after the end of injection and a large deviation is present. This implies that the acceleration of penetration due to the spray collapse is not captured by the model.

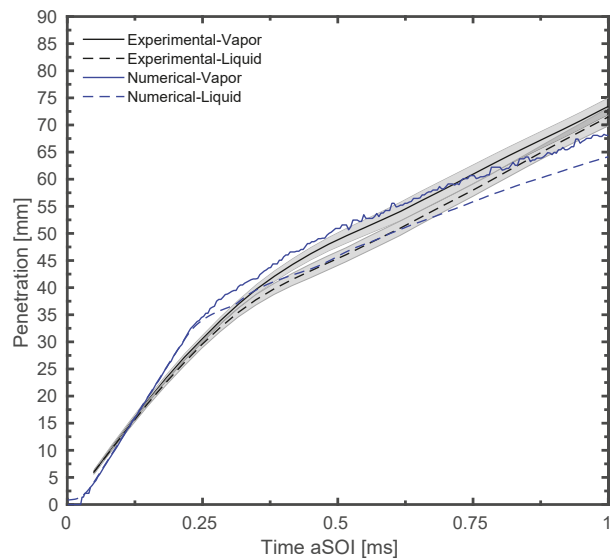


Figure 16. Numerical and experimental axial vapor and liquid phases penetration for the G2 cold condition for n-pentane.

A more detailed explanation of the deviation shown in Figure 16 could be drawn from the spray morphology images shown in Figure 17. A large discrepancy between the numerical and experimental images can be clearly seen. At 0.3 ms, the experimental spray is already collapsed towards the injector axis and evolves as a single entity. In addition, an initiation of the toroidal structure is seen at the spray radial extremities. This behavior is not reproduced by the numerical model where the plumes continue to penetrate in their original direction with minor plume-to-plume interactions. At 0.6 ms, the toroidal structure becomes more evident and a higher degree of recirculating motion is shown at the two radial extremities of the spray. The tip of the numerical spray slightly changes and becomes narrower. Finally, after the end of injection at 0.9 ms, the experimental spray penetrates faster due to the spray collapse. No spray collapse is evident in the numerical spray although a slight deviation of parcel direction at the spray tip can be noticed. The variation in the slopes of the liquid penetration curves between the numerical and experimental trends can then be justified by the spray images. The numerical model presents a drawback since the spray collapse is not predicted and therefore lags behind in terms of penetration. Duronio et al. [45] adjusted the plume direction and cone angle when moving towards more extreme case of flash boiling at an ambient density of 0.2 kg/m^3 and using iso-octane. The plume direction was decreased down to 19° , compared to the nominal 37° , and it was possible to reproduce the spray collapse by doing so. Modifying the plume cone angle and plume direction produced a higher radial velocity component in the spray simulations leading to the classical bell shape of the jet with two recirculation zones on each side. However, for the sake of implementing a comprehensive model, the plume direction was not modified in this study and the plume cone angle reduction alone was not able to predict the spray collapse behavior seen in the experimental images.

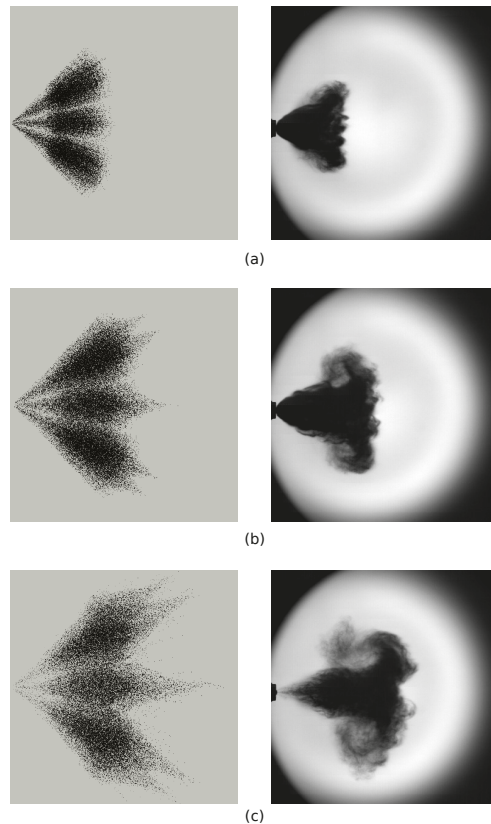


Figure 17. Numerical (left) vs. CMT experimental (right) liquid morphology images for the G2 cold condition for n-pentane. (a) at 0.3 ms, (b) at 0.6 ms and (c) at 0.9 ms after SOI.

4. Conclusions and Outlook

The current study comprised of the implementation of Lagrangian spray simulations for a multi-hole gasoline direct injector, Spray G from the ECN, and several mono-component fuels with different physical characteristics. The eight-hole injector was tested, both numerically and experimentally, under the baseline G1 condition typical of a late injection strategy in a GDI engine and under the mild flash boiling condition (G2 cold) typical of part load operation. The experimental analysis was carried out in a constant volume chamber constructed for GDI spray visualizations at CMT-Motores Térmicos, whereas the computational part was developed within the OpenFOAM framework coupled with the LibICE code, developed by the ICE group of Politecnico di Milano for specific CFD applications applied to internal combustion engines.

Due to the abundance of experimental data for the Spray G1 condition, preliminary work involved tuning the spray sub-models for that case, reproducing the main variables made available by the ECN. The model was then left unchanged for the subsequent stages of the study where only the spray cone angle was varied to account for flash boiling evaporation. To this end, the validation process of the spray model did not only cover the vapor and liquid penetration comparison but rather included the assessment of the spray gas interaction by analyzing the axial gas centerline velocity, SMD radial distributions, and finally liquid spray morphologies. The RANS standard $k - \epsilon$ turbulence model with the Pope correction provided accurate results for the vapor phase penetration and the

centerline axial gas velocity. A slight underestimation of the vapor penetration between 1.5 ms and 2.0 ms could be improved by further refining the grid; however, an increase in computational cost is expected. Likewise, adopting a fixed grid instead of using AMR could lead to a better prediction of the gas velocity since the centerline point bounded by the spray plumes would not be refined when AMR is utilized. Furthermore, liquid high and low threshold penetrations revealed that the liquid core of the spray is overpredicted which was verified by the morphology images although a better assessment would be done if PLV images from Sandia were available. Additionally, computed SMD values were quite a bit lower than the measured ones indicating that further tuning of the sub-models is required in order to accurately predict the diameters while maintaining an adequate liquid evaporation rate. Nonetheless, the adopted setup was evaluated to be suitable for the investigation of the flash boiling behavior of the various fuels.

Iso-octane and n-heptane both demonstrated similar behaviors under mild flashing conditions. The radial expansion of the spray was slightly overestimated as shown by the comparison of the numerical parcel and experimental DBI images. A more comparative assessment would be to compare the morphologies in the same way done for the Spray G1 condition since the same post-processing and thresholding procedure would be employed for both images. In any case, the plume-to-plume interaction was captured by the numerical model for both fuels. The Adachi-Rutland evaporation rate and flashing diameter reduction led to a good agreement between numerical and experimental penetration trends. Therefore, the adopted spray setup tuned for the G1 condition was also able to predict the main spray characteristics even at three times lower ambient density without the need of a re-calibration. The adopted methodology was also validated under a more intense flash boiling scenario by testing n-hexane under the same chamber conditions. The computed liquid and vapor penetrations were in good agreement with the measured profiles for the whole duration of injection. Spray morphology images indicated that the numerical model is weak in capturing the radial expansion of the dense liquid core region due to the intense flash boiling phenomenon although a good agreement is observed at the plume tips. The weakness of the DDM model is further magnified when n-pentane was investigated. The underestimation of the liquid phase penetration and liquid spray morphologies demonstrated that the numerical spray model did not contract and thus evolved with an overall lower penetration. This highlights an important limitation in the adopted methodology and lays the foundation for future development activities that must be carried out. In that sense, it must be said that the physics occurring inside the nozzle and near nozzle region cannot be neglected under extreme cases of flash boiling leading to spray collapse. Therefore, future activities are intended to implement a coupling between internal and external nozzle flow so that the initial plume direction and cone angle are calculated by the internal nozzle flow Eulerian model which initializes the Lagrangian simulation. This would be a more physical approach rather than imposing fixed injection direction and plume angle values, making the model less reliant on experimental measurements. In addition, the rapid phase change and plume expansion occurring at the nozzle exit under flash boiling conditions could be captured and transmitted to the subsequent Lagrangian simulation, thus improving the model fidelity.

Author Contributions: Conceptualization, R.P., R.A. and A.B.; methodology, P.M.-A., R.A. and A.B.; software, R.A. and A.B.; validation, P.M.-A. and R.A.; formal analysis, R.A.; investigation, R.P. and A.B.; resources, R.P.; data curation, R.P.; writing—original draft preparation, R.A.; writing—review and editing, R.P. and P.M.-A.; visualization, P.M.-A., R.A. and A.B.; supervision, R.P. and P.M.-A.; project administration, R.P.; funding acquisition, R.P. All authors have read and agreed to the published version of the manuscript.

Funding: This research was funded by Ministerio de Ciencia, Innovación y Universidades grant number RTI2018-099706-B-I00 in the frame of the project Study of Primary Early Atomization using DNS and Optical Ultra-high resolution Techniques (SPREAD OUT). Additionally, the PhD student Rami Abboud has been funded by Ayudas para la formación de profesorado universitario (FPU) program with reference FPU19/03838.

Institutional Review Board Statement: Not applicable.

Informed Consent Statement: Not applicable.

Conflicts of Interest: The authors declare no conflict of interest.

References

- Millo, F.; Gullino, F.; Rolando, L. Methodological approach for 1D simulation of port water injection for knock mitigation in a turbocharged DISI engine. *Energies* **2020**, *13*, 4297. [CrossRef]
- Tornatore, C.; Sjöberg, M. Optical investigation of a partial fuel stratification strategy to stabilize overall lean operation of a DISI engine fueled with gasoline and E30. *Energies* **2021**, *14*, 396. [CrossRef]
- Gong, C.; Si, X.; Liu, F. Combined effects of excess air ratio and EGR rate on combustion and emissions behaviors of a GDI engine with CO₂ as simulated EGR (CO₂) at low load. *Fuel* **2021**, *293*, 120442. [CrossRef]
- Huang, W.; Gong, H.; Moon, S.; Wang, J.; Murayama, K.; Taniguchi, H.; Arima, T.; Arioka, A.; Sasaki, Y. Nozzle Tip Wetting in GDI Injector at Flash-boiling Conditions. *Int. J. Heat Mass Transf.* **2021**, *169*, 120935. [CrossRef]
- Fach, C.; Rödel, N.; Schorr, J.; Krüger, C.; Dreizler, A.; Böhm, B. Multi-parameter imaging of in-cylinder processes during transient engine operation for the investigation of soot formation. *Int. J. Engine Res.* **2021**. [CrossRef]
- Kale, R.; Banerjee, R. Optical investigation of flash boiling and its effect on in-cylinder combustion for butanol isomers and iso-octane. *Int. J. Engine Res.* **2021**, *22*, 1565–1578. [CrossRef]
- Du, J.; Mohan, B.; Sim, J.; Fang, T.; Roberts, W.L. Study of spray structure under flash boiling conditions using 2phase-SLIPI. *Exp. Fluids* **2021**, *62*, 24. [CrossRef]
- Chang, M.; Lee, Z.; Park, S.; Park, S. Characteristics of flash boiling and its effects on spray behavior in gasoline direct injection injectors: A review. *Fuel* **2020**, *271*, 117600. [CrossRef]
- Engine Combustion Network. Available online: <https://ecn.sandia.gov/gasoline-spray-combustion/> (accessed on 30 September 2020).
- Mohapatra, C.K.; Schmidt, D.P.; Sforzo, B.A.; Matusik, K.E.; Yue, Z.; Powell, C.F.; Som, S.; Mohan, B.; Im, H.G.; Badra, J.; et al. Collaborative investigation of the internal flow and near-nozzle flow of an eight-hole gasoline injector (Engine Combustion Network Spray G). *Int. J. Engine Res.* **2020**. [CrossRef]
- Shahangian, N.; Sharifian, L.; Miyagawa, J.; Bergamini, S.; Uehara, K.; Noguchi, Y.; Marti-alzaravi, P.; Martinez, M.; Payri, R. Nozzle Flow and Spray Development One-Way Coupling Methodology for a Multi-Hole GDI Injector. *SAE Tech. Pap. Ser.* **2019**. [CrossRef]
- Kong, S.C.; Senecal, P.K.; Reitz, R.D. Developments in spray modeling in diesel and direct-injection gasoline engines. *Oil Gas Sci. Technol.* **1999**, *54*, 197–204. [CrossRef]
- Duronio, F.; Ranieri, S.; Montanaro, A.; Allocca, L.; De Vita, A. ECN Spray G injector: Numerical modelling of flash-boiling breakup and spray collapse. *Int. J. Multiph. Flow* **2021**, *2021*, 103817. [CrossRef]
- Wadekar, S.; Yamaguchi, A.; Oevermann, M. Large-Eddy Simulation Study of Ultra-High Fuel Injection Pressure on Gasoline Sprays. *Flow Turbul. Combust.* **2021**, *107*, 149–174. [CrossRef]
- Paredi, D.; Lucchini, T.; D'Errico, G.; Onorati, A.; Pickett, L.; Lacey, J. Validation of a comprehensive computational fluid dynamics methodology to predict the direct injection process of gasoline sprays using Spray G experimental data. *Int. J. Engine Res.* **2020**, *21*, 199–216. [CrossRef]
- Jiang, C.; Parker, M.C.; Helie, J.; Spencer, A.; Garner, C.P.; Wigley, G. Impact of gasoline direct injection fuel injector hole geometry on spray characteristics under flash boiling and ambient conditions. *Fuel* **2019**, *241*, 71–82. [CrossRef]
- Sun, Z.; Cui, M.; Ye, C.; Yang, S.; Li, X.; Hung, D.; Xu, M. Split injection flash boiling spray for high efficiency and low emissions in a GDI engine under lean combustion condition. *Proc. Combust. Inst.* **2021**, *38*, 5769–5779. [CrossRef]
- Sun, Z.; Yang, S.; Nour, M.; Li, X.; Hung, D.; Xu, M. Significant Impact of Flash Boiling Spray on In-Cylinder Soot Formation and Oxidation Process. *Energy Fuels* **2020**, *34*, 10030–10038. [CrossRef]
- Dong, X.; Yang, J.; Hung, D.L.; Li, X.; Xu, M. Effects of flash boiling injection on in-cylinder spray, mixing and combustion of a spark-ignition direct-injection engine. *Proc. Combust. Inst.* **2019**, *37*, 4921–4928. [CrossRef]
- Lacey, J.; Poursadegh, F.; Brear, M.J.; Gordon, R.; Petersen, P.; Lakey, C.; Butcher, B.; Ryan, S. Generalizing the behavior of flash-boiling, plume interaction and spray collapse for multi-hole, direct injection. *Fuel* **2017**, *200*, 345–356. [CrossRef]
- Li, Y.; Guo, H.; Zhou, Z.; Zhang, Z.; Ma, X.; Chen, L. Spray morphology transformation of propane, n-hexane and iso-octane under flash-boiling conditions. *Fuel* **2019**, *236*, 677–685. [CrossRef]
- Nocivelli, L.; Sforzo, B.A.; Tekawade, A.; Yan, J.; Powell, C.F.; Chang, W.; Lee, C.F.; Som, S. *Analysis of the Spray Numerical Injection Modeling for Gasoline Applications*; SAE Technical Papers; SAE International: Warrendale, PA, USA, 2020. [CrossRef]
- Weller, H.G.; Tabor, G.; Jasak, H.; Fureby, C. A tensorial approach to computational continuum mechanics using object-oriented techniques. *Comput. Phys.* **1998**, *12*, 620–631. [CrossRef]
- Lucchini, T.; D'errico, G.; Ettore, D. Numerical investigation of the spray-mesh-turbulence interactions for high-pressure, evaporating sprays at engine conditions. *Int. J. Heat Fluid Flow* **2011**. [CrossRef]
- Lucchini, T.; D'Errico, G.; Paredi, D.; Sforza, L.; Onorati, A. *CFD Modeling of Gas Exchange, Fuel-Air Mixing and Combustion in Gasoline Direct-Injection Engines*; SAE Technical Papers; SAE International: Warrendale, PA, USA, 2019. [CrossRef]

26. Paredi, D. CFD Modeling and Validation of Spray Evolution in Gasoline Direct Injection Engines. Ph.D. Thesis, Politecnico di Milano, Milan, Italy, 2020.
27. Pope, S.B. An explanation of the turbulent round-jet/plane-jet anomaly. *AIAA J.* **1978**, *16*, 279–281. [[CrossRef](#)]
28. Huh, K.Y.; Gosman, A.D. A Phenomenological Model of Diesel Spray Atomization. In Proceedings of the International Conference on Multiphase Flows, Tsukuba, Japan, 24–27 September 1991.
29. Paredi, D.; Lucchini, T.; D’Errico, G.; Onorati, A.; Montanaro, A.; Allocca, L.; Ianniello, R. *Combined Experimental and Numerical Investigation of the ECN Spray G under Different Engine-Like Conditions*; SAE Technical Papers; SAE International: Warrendale, PA, USA, 2018; [[CrossRef](#)]
30. Baumgarten, C. *Mixture Formation in IC Engines*; Springer: Berlin/Heidelberg, Germany, 2006.
31. Adachi, M.; McDonnell, V.G.; Tanaka, D.; Senda, J.; Fujimoto, H. *Characterization of Fuel Vapor Concentration inside a Flash Boiling Spray*; SAE Technical Papers; SAE International: Warrendale, PA, USA, 1997. [[CrossRef](#)]
32. Zuo, B.; Gomes, A.M.; Rutland, C.J. Modelling superheated fuel sprays and vapourization. *Int. J. Engine Res.* **2000**, *1*, 321–336. [[CrossRef](#)]
33. Engine Combustion Network. Available online: <https://ecn.sandia.gov/ecn-workshop/ecn6-workshop/> (accessed on 17 November 2020).
34. Available online: <http://www.philiplaven.com/mieplot.htm> (accessed on 3 March 2021).
35. Sphicas, P.; Pickett, L.M.; Skeen, S.; Frank, J.; Lucchini, T.; Sinoir, D.; D’Errico, G.; Saha, K.; Som, S. A Comparison of Experimental and Modeled Velocity in Gasoline Direct-Injection Sprays with Plume Interaction and Collapse. *SAE Int. J. Fuels Lubr.* **2017**, *10*, 184–201. [[CrossRef](#)]
36. ECN, Engine Combustion Network—Primary Spray G Datasets. Available online: <https://ecn.sandia.gov/gasoline-spray-combustion/target-condition/primary-spray-g-datasets/> (accessed on 25 January 2021).
37. Duke, D.J.; Kastengren, A.L.; Matusik, K.E.; Swantek, A.B.; Powell, C.F.; Payri, R.; Vaquerizo, D.; Itani, L.; Bruneaux, G.; Grover, R.O.; et al. Internal and near nozzle measurements of Engine Combustion Network “Spray G” gasoline direct injectors. *Exp. Therm. Fluid Sci.* **2017**, *88*, 608–621. [[CrossRef](#)]
38. Payri, R.; Salvador, F.J.; Abboud, R.; Viera, A. Study of evaporative diesel spray interaction in multiple injections using optical diagnostics. *Appl. Therm. Eng.* **2020**, *176*, 115402. [[CrossRef](#)]
39. Payri, R.; Bracho, G.; Gimeno, J.; Bautista, A. Rate of injection modelling for gasoline direct injectors. *Energy Convers. Manag.* **2018**, *166*, 424–432. [[CrossRef](#)]
40. Rodriguez, A.B. Study of the Gasoline Direct Injection Process under Novel Operating Conditions. Ph.D. Thesis, Universitat Politècnica de València, Valencia, Spain, 2021.
41. Lemmon, E.W.; McLinden, M.O.; Friend, D.G. Thermophysical Properties of Fluid Systems. In *NIST Chemistry WebBook, NIST Standard Reference Database Number 69*; Linstrom, P.J., Mallard, W.G., Eds.; National Institute of Standards and Technology: Gaithersburg, MD, USA, 2011; p. 20899. [[CrossRef](#)]
42. Payri, R.; Gimeno, J.; Marti-Aldaravi, P.; Martínez, M. *Nozzle Flow Simulation of Gdi for Measuring Near-Field Spray Angle and Plume Direction*; SAE Technical Papers; SAE International: Warrendale, PA, USA, 2019; pp. 1–11. [[CrossRef](#)]
43. Guo, H.; Li, Y.; Lu, X.; Zhou, Z.; Xu, H.; Wang, Z. Radial expansion of flash boiling jet and its relationship with spray collapse in gasoline direct injection engine. *Appl. Therm. Eng.* **2019**, *146*, 515–525. [[CrossRef](#)]
44. Araneo, L.; Donde’, R. Flash boiling in a multihole G-DI injector—Effects of the fuel distillation curve. *Fuel* **2017**, *191*, 500–510. [[CrossRef](#)]
45. Duronio, F.; De Vita, A.; Allocca, L.; Montanaro, A.; Ranieri, S.; Villante, C. *CFD Numerical Reconstruction of the Flash Boiling Gasoline Spray Morphology*; SAE Technical Papers; SAE International: Warrendale, PA, USA, 2020. [[CrossRef](#)]

Article

Deflagration Characteristics of N₂-Diluted CH₄-N₂O Mixtures in the Course of the Incipient Stage of Flame Propagation

Maria Mitu, Codina Movileanu and Venera Giurcan *

“Ilie Murgulescu” Institute of Physical Chemistry, Romanian Academy, 202 Spl. Independentei, 060021 Bucharest, Romania; maria_mitu@icf.ro (M.M.); cmovileanu@icf.ro (C.M.)

* Correspondence: venerab@icf.ro

Abstract: In this study, experimental measurements in a spherical combustion bomb were performed in order to investigate the flame propagation in N₂-diluted CH₄-N₂O mixtures with stoichiometric equivalence ratio, at several initial pressures (0.5–1.75 bar) and ambient initial temperatures. Methane was chosen as a test-fuel, since it is the main component of natural gas, a fuel often used as a substitute to gasoline in engines with internal combustion and industrial plants. The method approached in this study is based on a simple examination of the cubic law of pressure rise during the early (incipient) period of flame propagation. The incipient stage defined by a pressure rise equal or smaller than the initial pressure, was divided into short time intervals. The burnt mass fractions (obtained using three different Equations) and flame radii at various moments of the flame propagation in the course of the incipient stage were calculated. The cubic law coefficients and corresponding laminar burning velocities at considered time intervals were also reported.

Keywords: flame propagation; closed spherical bomb; incipient stage; methane; N₂O

Citation: Mitu, M.; Movileanu, C.; Giurcan, V. Deflagration Characteristics of N₂-Diluted CH₄-N₂O Mixtures in the Course of the Incipient Stage of Flame Propagation. *Energies* **2021**, *14*, 5918. <https://doi.org/10.3390/en14185918>

Academic Editors: Alexandre M. Afonso, Pedro Resende and Mohsen Ayooobi

Received: 21 August 2021

Accepted: 15 September 2021

Published: 17 September 2021

Publisher’s Note: MDPI stays neutral with regard to jurisdictional claims in published maps and institutional affiliations.



Copyright: © 2021 by the authors. Licensee MDPI, Basel, Switzerland. This article is an open access article distributed under the terms and conditions of the Creative Commons Attribution (CC BY) license (<https://creativecommons.org/licenses/by/4.0/>).

1. Introduction

Nitrous oxide (N₂O) is a naturally occurring gas, which has applications in different fields such as: pharmacologic agent to generate anesthesia; food additives; propellant in propulsion systems; refrigerant; additive for fuels. In small amounts, it is generated in nuclear waste storage tanks, along with methane, hydrogen and ammonia. The mixture of these gases can lead to a flammable gas mixture. In the unlikely event that an ignition source is present as this gas releases, an explosion can occur.

N₂O is a two-phase compound existing both as a liquid and a gas. Nitrous oxide in liquid form is inert, but in a vapor form at high temperatures, it can decompose rapidly and energetically. Due to its exothermic decomposition in N₂ and O₂ (N₂O → N₂ + 1/2O₂; ΔH = −82.1 kJ/mol), the combustion supported by nitrous oxide releases greatly the temperatures and explosion pressures compared to combustion occurring in the presence of air. Therefore, the explosions in fuel-N₂O systems are more powerful, and consequently the unanticipated events are more devastating. This situation motivates researchers in the combustion field to conduct studies on hydrocarbon–nitrous oxide combustion to deliver valuable information on the fundamental chemical kinetics significant to the intricate oxidation systems where nitrogen oxide is involved.

Due to unexpected accidents caused by nitrous oxide [1,2], there are many experimental and computed studies on fuel combustion supported by N₂O, especially regarding their flammability and propagation properties. Vandebroek et al. [3] conducted experiments in a closed spherical bomb at atmospheric pressure and at an initial temperature of 70 °C to determine the explosion characteristics and flammability limits of toluene-N₂O in comparison with toluene–air mixtures. Powell et al. [4–6] used a flat flame burner and numerical modeling to study the laminar burning velocities of hydrogen-, methane-, propane- and propylene-N₂O mixtures diluted with N₂, at near-atmospheric pressure. Shebeko et al. [7–9] reported the flammability limits, minimum inert concentrations, peak explosion

pressures, maximum rates of pressure rise and laminar burning velocities of hydrogen-, methane-, propane- and butane-N₂O mixtures in the presence of N₂, CO₂ and several halogen derivatives by experiments in closed vessels, at standard conditions. Mével et al. [10] carried out experimental studies in a spherical bomb and kinetic modeling at ambient conditions to study the flame propagation in H₂-N₂O-Ar mixtures. Koshiha et al. [11–13] studied the explosion properties (explosion limits, peak explosion pressures, and time to peak explosion pressure) of mixtures of *n*-alkanes, diethyl ether, diethylamine and *n*-butyraldehyde with nitrous oxide and nitrogen in a cylindrical vessel, at room temperature and atmospheric pressure. Bane et al. [14] determined the flame velocities and combustion parameters (peak explosion pressure and severity factor) for the H₂-N₂O mixture diluted or not with N₂ by experiments in a cylindrical bomb and numerical modeling, at different initial conditions (pressure, equivalence ratio, dilution level). Movileanu et al. [15] reported the explosion indices of N₂-diluted ethylene-N₂O mixtures in elongated vessels, at ambient temperatures and various initial pressures. Razus et al. [16,17] performed experiments in a spherical bomb and numerical modeling at room temperature and initial pressures different from ambient, to obtain the peak explosion pressures, maximum rates of pressure rise, deflagration indices and laminar burning velocities of methane-N₂O flames in the presence of inert additives. Shen et al. [18] conducted a study on stoichiometric C₂H₄/N₂O mixtures diluted with N₂ or CO₂ using a standard 20 L spherical bomb and sub-atmospheric initial pressures to assess the explosion mechanism and hazard. Li et al. [19] carried out an experimental study at standard conditions using cylindrical channels to investigate the flame propagation and thermal hazard of the premixed N₂O/fuel mixtures, including NH₃, C₃H₈ and C₂H₄. Wang et al. [20,21] performed experiments in a closed cylindrical vessel at atmospheric and sub-atmospheric pressures to investigate the explosion behaviors of hydrogen-, methane- and ethylene-N₂O mixtures diluted with N₂. Luo et al. [22] investigated the effects of the addition of ethane, ethylene, hydrogen and carbon monoxide on the flammability limits and limiting oxygen concentrations of methane under N₂ dilution in a pipeline at atmospheric temperature and pressure. Mitu et al. [23] studied the laminar burning velocities of N₂-diluted CH₄-N₂O flames by experiments in a spherical bomb, at various initial pressures and room temperature.

Despite the background described above, the research on CH₄ explosions supported by N₂O occurring in closed bombs (especially at initial pressures different from ambient) are still lacking, although the methane explosions have frequently been studied in the presence of other oxidants, such as O₂ or air. Therefore, the present research pays attention to explosion propagation occurring in another kind of hazardous mixture, which is motivated not only by the safety concerns in technical applications in which these mixtures are involved, but also in the handling and storage of nuclear waste, where they are generated.

The present work is focused on the study of flame propagation in the course of the early (incipient) period of explosions inside a closed-bomb with central ignition using N₂-diluted CH₄-N₂O mixtures. Methane was chosen as the test-fuel because it is the main component of natural gas, which is increasingly being used as a substitute to gasoline in engines with internal combustion and industrial plants [24]. On the other hand, the combustion of fuels in the presence of N₂O can lead to greatly turbulent deflagrations and unstable flames, which can fast self-accelerate and may shift from a deflagration to a detonation regime. Although methane and nitrous oxide are some of the more noxious greenhouse gases [25], they can be used together to obtain a synthesis gas and other hydrocarbons [26], which can be further used to obtain various useful chemicals. Both methane and nitrous oxide present a highly explosive potential and in the event of a spark they can ignite and lead to devastating explosions. Therefore, it is desired to carry out studies in order to provide data regarding the explosion propagations in methane-nitrous oxide mixtures, at pressures different from ambient, trying to get closer to conditions encountered in practice.

The early stage of flame propagation gives us useful information regarding the flame initiation and increase, associated with pressure increase and unstable heat generation.

Additionally, the pressure change in the course of this incipient period is useful for the design of venting devices, necessary for the mitigation of gaseous explosions which may occur accidentally in industrial installations or storage reservoirs. One of the conditions for a good work of vents is that the operating time of the suppression system must be lower than the induction period (the time required for the allowable pressure increase) [27]. In the incipient stage of flame development, the flame is smooth, has a negligible width and propagates in the absence of convection [28,29].

A detailed study of the early stage of flame development made it known that the pressure increase at the end of this period in the course of the combustion in a constant volume bomb can be linked with the time from initiation by means of a cubic law [28]. This law is plausible as long as the flame maintains its spherical aspect and its propagation is undisturbed. Moreover, it was empirically limited to a pressure variation less or equal to the initial pressure at which the experimental determination takes place [28,29]. Therefore, the examination of the incipient stage of flame development is necessary to find the most favorable duration of this stage of flame propagation. Shorter durations of the incipient period of explosion should be assessed in order to obtain valuable information regarding the flame propagation, mainly when near-limit flammable systems are considered or when non-spherical explosion cells are implied. It is known that the combustion in a non-spherical explosion vessel is not completed at the same time over the whole bomb area, but the early period of combustion is identical in any case [28].

Our approach is to carry out experiments in a small-closed bomb, using for ignition a punctiform source of energy. Measurements of pressure versus time are further used to determine the burnt mass fractions, flame radii and the cubic law constants of pressure increase. The last parameters were subsequently used to calculate the laminar burning velocities. The method approached in this research provides laminar burning velocities from a single experiment and is suitable for non-conventional mixtures such as those studied in the present research consisting of fuel-oxidizer (N_2O) and diluent.

This study aims to provide new experimental results on these fundamental combustion characteristics and to find the optimum duration of the incipient stage. These new data will contribute to safety enhancement in industrial facilities that handle and store nitrous oxide, expanding at the same time the combustion database regarding the fuel- N_2O flames. Additionally, to the lack of data referring to methane combustion in the presence of nitrous oxide, there is also a large discrepancy in the available reported results, no matter whether these data are obtained from experiments or from numerical modeling. Moreover, the study of hydrocarbon-nitrous oxide combustion can provide valuable information on the fundamental chemical kinetics relevant to complex oxidation systems involving nitrogen. Thus, it fully justifies the interest on a comprehensive study of their explosivity to help formulate answers related to three categories of problems: prediction, prevention and protection.

2. Experimental Apparatus and Procedure

In this study, the method of unstable flame propagation inside a spherical closed bomb with central ignition was used to investigate the flame propagation in N_2 -diluted CH_4 - N_2O mixtures.

The experimental set-up is schematically shown in the previous study [25]. Its main components are the combustion bomb, the ignition device, the pressure transducer coupled to an amplifier, the ionization gauges and the system for data acquisition. The experiments were conducted in a spherical bomb with an internal volume of 0.52 L and 5 cm radius, which was projected to withstand an internal pressure of 40 bar. The ignition was achieved by electric sparks produced between stainless-steel electrodes of 1 mm diameter and round tips, fixed at the center of the vessel. The ignition energies were maintained at a low value (1–5 mJ) to keep away from any turbulence that could appear due to an excessive energy input in the course of ignition.

CH₄-N₂O mixtures having initial temperature of 298 K, different initial pressures (0.5–1.75 bar) and stoichiometric equivalence ratio were used as test mixtures. For safety reasons, the CH₄-N₂O mixtures were diluted with N₂ between 40 and 60 vol%. N₂ was chosen as a diluent because it is inexpensive, widespread and is commonly used for explosions inhibition.

The stoichiometric mixture composition was chosen as a representative composition because it affords a complete fuel and oxidizer consumption and generally ensures diffusion stability of the flame front.

The test mixtures were prepared according to the partial pressure method, stored in a 10 L metallic reservoir and used 48 h later. Prior to every test, the experimental bomb was evacuated by means of a vacuum pump to a pressure under 1.0 mbar. The studied mixture is then introduced inside the bomb (at the desired initial pressure) and it is left to become quiescent. Once the mixture is ignited, the explosion evolution was collected by means of a piezoelectric pressure transducer (Kistler 601A, Kistler, Winterhur, Switzerland) coupled to a charge amplifier (Kistler 5001SN, Kistler, Winterhur, Switzerland). Two ionization gauges mounted in an equatorial place immersed at 0.3 cm from the wall were used to monitor the arrival time of the flame front. The signals from the charge amplifier and ionization gauge were recorded by a digital oscilloscope, usually at 10⁴ signals/s. To shun the effect of the combustion products that may still be present in the bomb and to mitigate the heating of the mixture produced by an eventual heating of the bomb's wall that may occur as a result of the flame propagation, the vessel was flushed with dry air after each test.

To minimize the operational errors, each experiment was repeated a minimum of three times to check the reproducibility and to ensure accurate results. Figure 1 compares the pressure histories measured in the experimental bomb for various N₂ dilutions. In this figure, the different color symbols refer to three repeated measurements for each N₂ dilution. The repeatability of the measurements led to satisfactory results, indicating that the mixtures have been accurately prepared. A strain gauge manometer (Edwards type EPS-10HM, Edwards Ltd., West Sussex, UK) was used to measure the initial pressures of the tested mixtures, p_0 . According to the information from the equipment manufacturer, the error of initial pressure measurement is less than 0.1%.

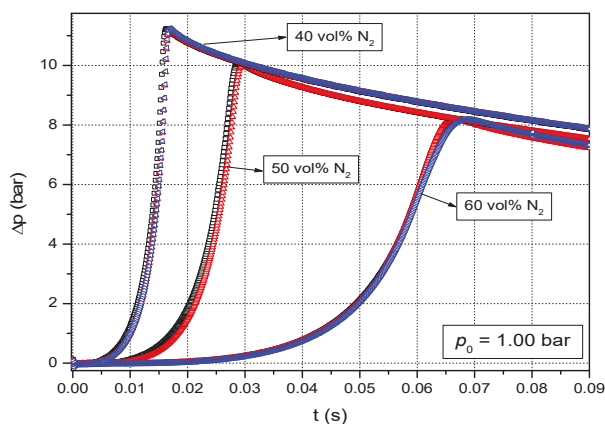


Figure 1. Experimental pressure-time history of the combustion process.

Methane (99.99%), N₂O and N₂ (both 99.999%) were provided by SIAD Italy and were used without any purification.

The uncertainties involved in the present study can be due to mixture preparation, data acquisition and data processing. The uncertainty due to the mixture preparation depends strongly on the accuracy of the pressure gauge manometer. In this study, very accurate pressure gauge manometers were used; therefore, the uncertainties due to the

mixtures preparation can be neglected. The uncertainty in the course of one experiment can be attributed to the initial conditions: temperature and pressure. During all experiments, the initial temperature of the mixtures was considered the room temperature (298 K). However, an estimated error of ± 2 K (about 0.7%) due to the temperature variation from one day to another can be considered a possible factor that may affect the overall precision of measurements. In addition to the errors that may be due to the initial temperature, other errors which may arise correspond to the accuracy of the pressure transducer and ignition sources. According to the piezoelectric pressure transducer manufacturer, the error given by this device is less or equal to 0.1%. Considering all of these possible sources of experimental errors, a total standard deviation of 3.5% was taken into account during this study. The errors due to data processing are generated by the accuracy of the equations used to calculate the unburnt mass fractions, flame radius and laminar burning velocity.

3. Data Evaluation

In the present research, the laminar burning velocities of N_2 -diluted CH_4 - N_2O mixtures with stoichiometric composition were calculated using the assessment of pressure-time curves in the early period of flame propagation, assuming an isothermal compression of the unburned gas, as proposed by Razus et al. [29]:

$$S_u = R \left(\frac{k}{\Delta p_{max}} \right)^{\frac{1}{3}} \left(\frac{p_0}{p_{max}} \right)^{\frac{2}{3}} \quad (1)$$

Here, R represent the radius of the bomb; k represent the cubic law coefficient of pressure rise, characteristic to the incipient period of the combustion; $\Delta p_{max} = p_{max} - p_0$ represent the maximum (peak) pressure rise.

Taking into account the initial moment of flame propagation in a closed bomb, Equation (1) can be used to calculate the laminar burning velocities of various mixtures. This Equation has the advantage that it allows us to obtain S_u without the necessity of other additional assumptions on explosion evolution after initiation.

The cubic law coefficient of pressure rise, characteristic for the incipient period of combustion, was obtained for each measurement by means of a nonlinear regression [29]:

$$\Delta p = a + k \cdot (t - b)^3 \quad (2)$$

In Equation (2), the coefficients a and b are used to correct the pressure and time, respectively. These corrections were made in order to eliminate any possible delays in the signal recording or in the signal shift of pressure transducer. In this study, for every experiment, the coefficients a and b were determined using a restricted number of points satisfying the following condition:

$$p_0 \leq p \leq 1.5p_0 \quad (3)$$

The flame radius at any instant (at pressure p), r_b , of the combustion propagation was calculated using the following equation [30,31]:

$$r_b = R \left[1 - (1 - n) \left(\frac{p_0}{p} \right)^{\frac{1}{\gamma_u}} \right]^{\frac{1}{3}} = R \left[1 - (1 - n) \pi^{\frac{-1}{\gamma_u}} \right]^{\frac{1}{3}} \quad (4)$$

Here, n represents the burnt mass fraction; p represents the pressure achieved at moment t ; γ_u represent the adiabatic compression factor of the unburnt gas; π represents the relative pressure defined as p/p_0 .

r_b is a characteristic property, which can be obtained from a continuous registering or from signals provided by some ionization gauges.

A limited range of the transient pressures into the interval $\Delta p \leq p_0$ was used in the flame radius calculation according to the works [32,33] in order to avoid the disturbing effects of the flame stretch and curvature on this parameter.

Over time, there were proposed a series of equations, which allow the calculation of the burnt mass fraction. Some of these are suitable for the incipient stage of flame propagation when the pressure and temperature of burned and unburned gas are quasi-constant [30,31].

In the present study, the burnt mass fraction was calculated using three different equations:

(I) the equation proposed by Manton et al. [31]:

$$n = \frac{(p - p_0)}{(p_e - p_0)} = \frac{(\pi - 1)}{(\pi_e - 1)} \quad (5)$$

Here, $\pi_e = p_e/p_0$; p_e represent the final explosion pressure in the course of the isochoric combustion.

The equation proposed by Manton et al. [31] is a simple relationship which links the burnt mass fraction with pressure. It states that the fraction of burned gas is equal with the fraction of the total pressure rise. Equation (5) is suitable for small values of burnt mass fraction. This equation was validated by Chen et al. [34] by numerical simulation of propagation of spherical flames in a closed spherical bomb. They used H_2 , CH_4 and C_3H_8 -mixtures and obtained a good agreement between data obtained by this equation and data delivered by numerical simulation, which indicates the robustness of Equation (5).

(II) the equation proposed by Grumer et al. [35]:

$$n = \frac{(p - p_0)}{p_0 \gamma_u (E_0 - 1)} = \frac{(\pi - 1)}{\gamma_u (E_0 - 1)} \quad (6)$$

where E_0 is the expansion factor of gases in the course of the initial period of the flame propagation. In this study, the expansion coefficients were calculated as the ratio between the volume of burned gas (V_b) and volume of unburned gas (V_u):

$$E_0 = \frac{V_b}{V_u} \quad (7)$$

The burned gas volumes were obtained from runs with the COSILAB 0-D package [36] in isobaric conditions.

The equation proposed by Grumer et al. [35] is a more accurate relation than the linear one proposed by Manton and co-workers. However, Equation (6) is valid only for a restricted region, defined as $p < 1.1 p_0$ [35].

(III) the equation proposed by Oancea et al. [37]:

$$n = \frac{\theta \left(\pi - \pi^{1 - \frac{1}{\gamma_u}} \right)}{\pi_e - \theta \pi^{1 - \frac{1}{\gamma_u}}} \quad (8)$$

In Equation (8): $\theta = \left(\frac{\pi_e}{\pi} \right)^{1 - \frac{1}{\gamma^*}}$; $\gamma^* = \frac{\ln \pi_e}{\ln \left(\frac{\pi_e}{\pi_0} \right)}$; $\theta_0 = \frac{T_{f,v}}{T_{f,p}}$.

$T_{f,v}$ represents the adiabatic flame temperature of isochoric combustion; $T_{f,p}$ represents the adiabatic flame temperature of isobaric combustion. Their values were also obtained by running the COSILAB 0-D software (Rotexo-Softpredict-Cosilab GmbH & Co KG: Bad Zwischenhahn, Germany) [36].

The equation proposed by Oancea et al. [37] is a simple method for calculating the burnt mass fraction over an extended domain of conditions achieved in the course of the constant volume combustion, taking into account an adjusted adiabatic compression law of burnt gas. This equation requires the knowledge of the final explosion pressure and flame temperatures (at constant volume and constant pressure, respectively), parameters that can be easily obtained using thermodynamic data and adequate computer software. The utility

and validity of the equation by Oancea et al. was tested by comparing the burnt gas radii obtained with this equation and measured data reported by other authors. Additionally, a good agreement was reported between the laminar burning velocities obtained with its help and data from the literature delivered using other methods [37,38].

Equations (5) and (6) can be applied to examine the early stage of the closed bomb explosions, while Equation (8) can also be applied for the later stages of the explosions. The only limitation of Equation (8) is that when the flame gets close to the vessel's wall, an important quantity of the heat is lost and therefore it is necessary to take this into account.

4. Results and Discussion

The method of unstable flame propagation in a spherical closed bomb with central ignition is generally acknowledged as being potentially both versatile and accurate. In this type of explosion bomb, a thin spherical flame front divides the inner gas mixtures in two zones: the burnt mixture zone and the unburnt mixture zone [39]. After ignition, the flame has a laminar propagation through the unburnt mixture until it reaches the bomb's walls. The flame evolution during the explosion in a spherical bomb is schematically drawn in Figure 2. To model spherical flames, the following assumptions are considered: the unburned and burned gases are ideal gases; the ignition source is quasi-punctiform; the flame propagation is spherical during the whole explosion; the flame front thickness is negligible in comparison with the flame radius; the heat transferred between the flame front and the electrodes and the vessel's wall, respectively, is also negligible.

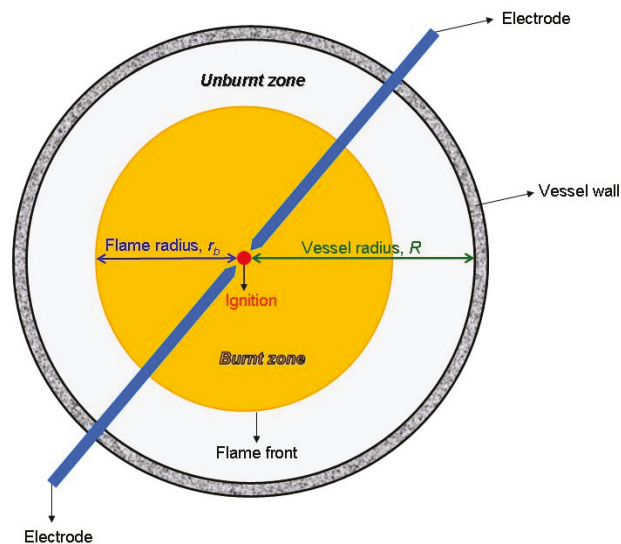


Figure 2. Flame front development in the spherical explosion bomb (equatorial view).

A representative diagram of pressure variation into the experimental bomb during the explosion of stoichiometric $\text{CH}_4\text{-N}_2\text{O}$ mixture diluted with 60% N_2 , at $p_0 = 1.50$ bar and ambient initial temperature is presented in Figure 3, together with the transient signal of the ionization gauge (U_{IP}) and the rate of pressure rise (dp/dt). In this diagram, the incipient (early) stage of the explosion defined by restriction $\Delta p = p_0 = 1.50$ bar was also indicated. As can be seen, the incipient period of flame propagation is much smaller than the time necessary to achieve the maximum rate of pressure rise (in the present research, 53.7 ms) when the heat losses become significant.

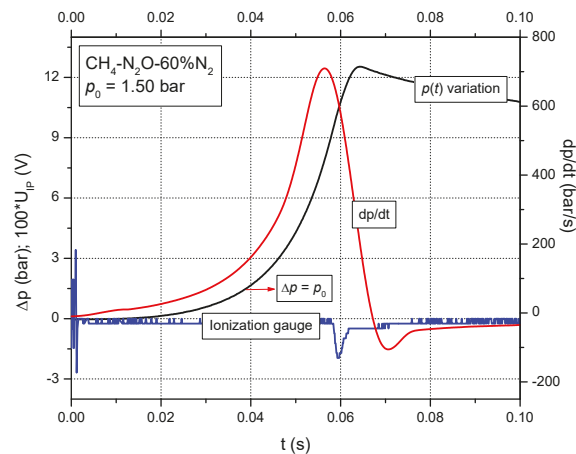


Figure 3. Pressure variation during the explosion in stoichiometric $\text{CH}_4\text{-N}_2\text{O-60\% N}_2$, at ambient initial temperature and $p_0 = 1.50$ bar.

Another representative diagram is given in Figure 4a for the stoichiometric $\text{CH}_4\text{-N}_2\text{O}$ mixture diluted with various amounts of N_2 , at ambient initial temperature and initial pressure of 1.75 bar. Curves with a similar aspect were registered for all tested pressures.

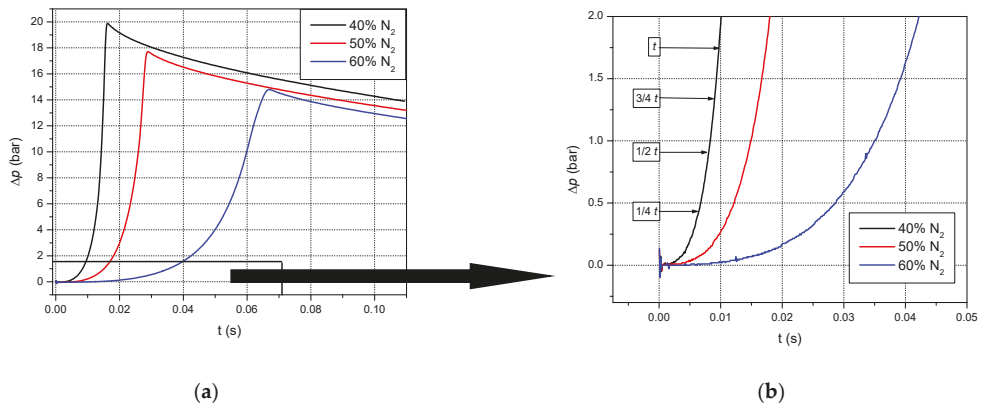


Figure 4. Pressure variation during the explosions in stoichiometric $\text{CH}_4\text{-N}_2\text{O}$ mixtures diluted with N_2 , at $p_0 = 1.75$ bar and ambient initial temperature. (a) the whole $p(t)$ curve; (b) a magnified diagram representing the incipient period of the flame propagation.

The incipient stage of pressure–time variation during propagation of laminar flames in closed bombs gives important information regarding the formation and development of the flame core trigger off an electric spark. This stage takes place over a specific period of time t , whose duration can be divided into the shorter time intervals of $1/4 t$, $1/2 t$ and $3/4 t$. In this incipient stage, the flame preserves its spherical form, the heat losses do not affect its growth, and the temperature gradients in both burned and unburned gas are low and so they may not be considered. A magnified diagram representing the incipient period of the flame propagation in the course of explosions that take place in the studied systems is presented in Figure 4b. Here, several arrows delimitate the possible lengths of the incipient stage: t is the length of a period where $\Delta p = p_0$; $3/4 t$ is the length of a period where $\Delta p = 3/4 p_0$ and so on.

Taking into account those presented above, the cubic law coefficients were obtained for corresponding shorter time intervals of $1/4 t$, $1/2 t$, $3/4 t$ and t by means of a nonlinear regression procedure of $p(t)$ data, assuming the validity of Equation (2). The cubic law coefficients are influenced by initial temperature and pressure, fuel and diluent content.

In Figure 5, the variation of cubic law coefficients with the initial pressure, together with error bars for the stoichiometric $\text{CH}_4\text{-N}_2\text{O}$ mixture diluted with 40% N_2 , at room temperature, are given. A linear increase in the cubic law coefficients was observed when the initial pressure increased. An increase in the cubic law coefficients with the initial pressure increase was already reported in [17,23]. Referring to the example in the Figure 5 and keeping the initial pressure constant (e.g., $p_0 = 1.00$ bar), the values of the cubic law coefficients increase from the time interval $1/4 t$ to the time interval t .

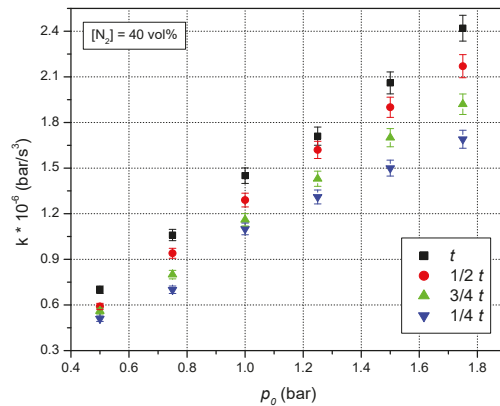


Figure 5. Variation of cubic law coefficients with initial pressure for stoichiometric $\text{CH}_4\text{-N}_2\text{O}$ mixture diluted with 40% N_2 , at ambient initial temperature.

As mentioned above, the cubic law coefficients depend not only on the initial pressure, but also on the diluent concentration. This dependence can be remarked also in Figure 6, where the data regarding the variation of the cubic law coefficients with the N_2 concentration at ambient initial temperature and $p_0 = 0.50$ bar are presented. The same comportment was observed for all the initial pressures considered in the present work.

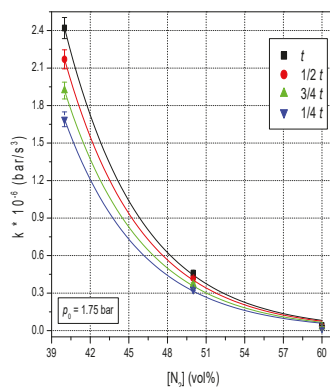


Figure 6. Variation of cubic law coefficients with diluent concentration for stoichiometric $\text{CH}_4\text{-N}_2\text{O}$ mixtures, diluted with N_2 , at $p_0 = 1.75$ bar and ambient initial temperature.

Representative values of the laminar burning velocities obtained using the cubic law coefficients are shown in Figures 7 and 8. Similar plots were obtained at all initial conditions studied in this work.

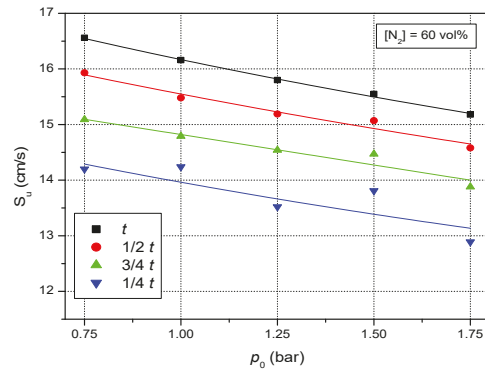


Figure 7. Variation of laminar burning velocities with initial pressure for stoichiometric $\text{CH}_4\text{-N}_2\text{O}$ mixture, diluted with 60% N_2 , at room temperature.

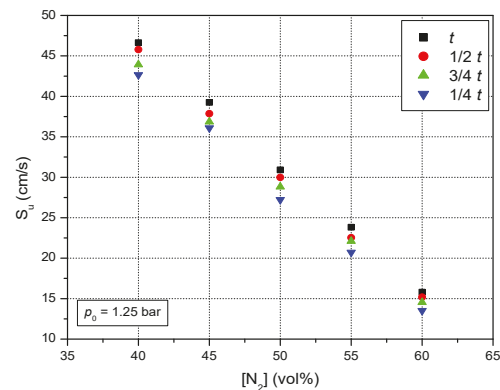


Figure 8. Variation of laminar burning velocities with diluent concentration for stoichiometric $\text{CH}_4\text{-N}_2\text{O}$ mixtures diluted with N_2 , at $p_0 = 1.25$ bar and ambient initial temperature.

In Figure 7, the laminar burning velocities of stoichiometric $\text{CH}_4\text{-N}_2\text{O}$ mixtures diluted with 60% N_2 , at ambient initial temperature and various initial pressures, are presented. As expected, a diminution of the laminar burning velocities is observed when the initial pressure increases. The dependence of the laminar burning velocity on initial pressure is based on the unburned gas density variation accordingly with the thermal theory of flame propagation [40]. When the initial pressure rises, the density of the unburned gas increases, and therefore, a diminution of the laminar burning velocity occurs.

In Figure 8, the laminar burning velocities of $\text{CH}_4\text{-N}_2\text{O}$ mixtures with stoichiometric composition diluted with various concentrations of N_2 , at $p_0 = 1.25$ bar, and ambient initial temperatures are illustrated. As expected, the rise in the diluent concentration causes a diminution of the laminar burning velocity at all studied initial pressures. The influence of diluents on the laminar burning velocity can be attributed to their ability to modify the thermal properties of flammable mixtures by changing the heat capacity, and thus the flame temperature. Moreover, diluent addition leads to a decrease in the fuel content, and therefore of the heat released and the reaction rate. Therefore, diluent addition influences

both the oxidation reaction kinetics and the thermal diffusivity of the reacting mixture, and thus the laminar burning velocity.

Lee et al. [41] conducted an experimental study on syngas mixtures diluted with N_2 , CO_2 and steam, in order to examine the dilution effects on a gas turbine combustion performance. The results revealed that the dilution of syngas decreases NO_x emissions and that the reduction of NO_x emissions is related to the diluent's heat capacity. Zhang et al. [42] examined the MILD (moderate or intense low-oxygen dilution) combustion in the presence of N_2 and CO_2 by experiments and numerical modeling. They used natural gas (CH_4) and liquefied petroleum gas (LPG) as tested fuels and concluded that the CO_2 has a dilution effect that is better than N_2 due to its heat capacity, which is bigger than the heat capacity of N_2 . The dilution with CO_2 conducted to lower adiabatic temperature rise, and thus to a good occurrence of MILD combustion compared with N_2 dilution. In this case, the physical factor plays an important role compared to the chemical factor. On the other hand, Zhang et al. [42] found that the ignition delay time of methane diluted with CO_2 is notably longer in comparison with the ignition delay time of methane diluted with N_2 , which makes easier the occurrence of MILD combustion. In this case, the chemical factor plays a major role compared with the physical factor. Later, Ceriello et al. [43] showed that the role of the internal exhaust gas recirculation is decisive in establishing the MILD regimes. They proposed a tabulated chemistry model and concluded that dilution with CO_2 led to much more satisfactory results in comparison with dilution with N_2 due to the lower reaction rates of CO_2 .

The laminar burning velocities at the end of the incipient period of explosion defined by $\Delta p = p_0$ can be compared with the literature data reported by other groups of researchers. On the one hand, the present data are higher compared with reported laminar burning velocities obtained using other experimental methods or computation. For example, at 0.75 bar and ambient initial temperature, the value of the laminar burning velocity for stoichiometric CH_4 - N_2O mixture diluted with 50 vol% N_2 found in the present study is $S_u = 33.03$ cm/s. In comparison, Powell et al. [4–6] obtained $S_u = 24.20$ cm/s from experiments using a burner with a flat flame and $S_u = 21.50$ cm/s from computation with an adjusted PPD mechanism. They used a stoichiometric CH_4 - N_2O mixture diluted with 52 vol% N_2 at 0.8 atm. These differences could be due to the fact that Powell et al. reports experimental data on the unstretched adiabatic flame velocity.

On the other hand, the results reported in this study are close to those reported by D'Olieslager and van Tiggelen [44] on stoichiometric CH_4 - N_2O mixture diluted with 40 and 50 vol% N_2 , respectively. The experiments from [44] were performed using a Bunsen burner at $p_0 = 1$ bar. For the mixture diluted with 40 vol% N_2 , D'Olieslager and van Tiggelen reported $S_u = 46.50$ cm/s ($S_u = 47.58$ cm/s in this study), while for the mixture diluted with 50 vol% N_2 , they reported $S_u = 30.10$ cm/s ($S_u = 31.11$ cm/s in this study). A summative table, which includes the comparison between present data and those from the literature is presented in Table 1.

Table 1. Comparison between present data and data reported in the literature.

p_0 (bar)	(N_2) (vol%)	Method	S_u (cm/s)	Reference
0.75	50	Spherical expanding flames	33.03	Present data
0.81	52	Flat flame burner	24.20	[4–6]
0.81	52	Numerical modeling	21.50	[4–6]
1.00	40	Spherical expanding flames	47.58	Present data
1.00	40	Bunsen burner	46.50	[44]
1.00	50	Spherical expanding flames	31.11	Present data
1.00	50	Bunsen burner	30.10	[44]

For all the considered systems, the coefficients of cubic law k drop when shorter time durations of the incipient stage are evaluated. Therefore, a diminution of the laminar burning velocities S_u was observed. This could be due to a large perturbation in pressure

measurements right after initiation of the explosion. Thus, a statistical analysis of the results is necessary in order to establish the optimum length of the incipient period. In Table 2, the determination coefficients (r^2) obtained at fitting the data using Equation (1), together with the value of the statistical factors (F_s), are given. The example given in Table 2 refers to the data achieved during one experimental measurement. In this example, the measurements were conducted at atmospheric pressure and temperature. Similar results were achieved for all tests performed under the same conditions realized in order to check the reproducibility of the results and also at initial pressures, different to the ambient ones considered in this research.

Table 2. The determination coefficients (r^2) and the value of the statistical factors (F_s).

Time Interval	(N ₂) = 40 (vol%)		(N ₂) = 50 (vol%)		(N ₂) = 60 (vol%)	
	r^2	F_s	r^2	F_s	r^2	F_s
t	0.998	19159	0.997	29648	0.998	116931
$3/4 t$	0.997	12136	0.995	17272	0.998	89100
$1/2 t$	0.992	4748	0.989	6843	0.996	42722
$1/4 t$	0.973	1112	0.962	1549	0.983	8181

From Table 2, it can be concluded that the best values of the cubic law coefficients and thus of the laminar burning velocities are obtained when the condition $\Delta p = p_0$ is fulfilled. The fact that a shorter duration of the incipient stage is not optimal is also observed from the scattering of the data obtained for short periods of the early stage ($1/4 t$, $1/2 t$) studied in this research and presented in Figure 7. Therefore, these short time intervals of the incipient stage of the flame propagation do not bring an improvement in obtaining accurate values of the laminar burning velocities, an important parameter in the process of understanding a large range of flammable mixtures.

The assessment of pressure-time curves in the incipient stage of flame propagation allows the calculation of other explosion parameters, such as burnt mass fraction and flame radius.

In Table 3, the burnt mass fractions of stoichiometric CH₄-N₂O mixture diluted with 40 vol% N₂ at atmospheric initial pressure and temperature obtained using Equations (5), (6) and (8) at different moments of the early stage, are presented. The same behavior was observed for all studied mixtures and initial pressures. Close values of the burnt mass fraction were obtained when Equations (6) and (8) were used. The Equation of Manton et al. [31] is an approximate linear relationship which relates the burnt mass fraction from the vessel to the fractional pressure rise. Although Equation (5) is often cited in the literature [34,45,46], Luijten et al. [47] showed that this linear relationship has obvious errors and proposed corrections to the burnt mass fraction considering different disturbing aspects. However, the error involved in this assumption is not large in the incipient stage of combustion, so that the Equation (5) can be used for small values of n , as already was mentioned in [48].

Table 3. The burnt mass fractions of stoichiometric CH₄-N₂O mixture diluted with 40 vol% N₂, at atmospheric initial pressure and temperature.

Duration of the Early Stage	n		
	Equation Manton et al. [31]	Equation Grumer et al. [35]	Equation Oancea et al. [37]
t	0.0846	0.0762	0.0792
$3/4 t$	0.0608	0.0548	0.0564
$1/2 t$	0.0425	0.0383	0.0391
$1/4 t$	0.0203	0.0183	0.0184

The values of the burnt mass fractions were further used to calculate the flame radii at different moments of the early stage of combustion considered in this work using Equation (4). The flame radii obtained using the mass fractions presented above in Table 3 are presented in Table 4.

Table 4. The flame radius of stoichiometric CH₄-N₂O mixture diluted with 40 vol% N₂, at atmospheric initial pressure and temperature.

Duration of the Early Stage	r_b		
	n from Manton et al. [31]	n from Grumer et al. [35]	n from Oancea et al. [37]
t	3.878	3.865	3.870
$3/4 t$	3.637	3.624	3.627
$1/2 t$	3.362	3.350	3.352
$1/4 t$	2.784	2.775	2.775

Similar results were obtained at all initial pressures and diluent concentrations examined in this work. As can be seen, all three equations used to obtain the burnt mass fractions deliver close results of flame radius for all time lengths taken into account in this study. At constant initial pressures and diluent composition, the flame radius increases from $1/4 t$ to t , indicating that the flame front travels from the burnt to the unburnt zone.

In our previous study [32] on propane-air mixtures in a spherical and two cylindrical bombs, a dimensionless flame radius defined as $\mathfrak{R}_b = \frac{r_b}{R}$ was considered. The study revealed that, for a particular burnt mass fraction in the course of the incipient period of the explosion, the dimensionless flame radius is by far higher than the relative pressure rise (p/p_0). Indeed, this is also true in the present case for mixtures in which the oxidant is N₂O. This can be seen from Table 5, where results obtained from a stoichiometric CH₄-N₂O mixture diluted with 60 vol% N₂ at ambient initial temperature and $p_0 = 1.25$ bar are given.

Table 5. Dimensionless flame radius and relative pressure of stoichiometric CH₄-N₂O mixture diluted with 60 vol% N₂, at ambient initial temperature and $p_0 = 1.25$ bar.

Duration of the Early Stage	n from Grumer et al. [35]	\mathfrak{R}_b	π
t	3.871	3.856	3.859
$3/4 t$	3.653	3.639	3.641
$1/2 t$	3.338	3.325	3.326
$1/4 t$	2.810	2.800	2.799

In all of the studied mixtures, the flame achieved a dimensionless radius $\mathfrak{R}_b = 0.55$ – 0.56 at the end of an incipient period with the length $1/4 t$ and a dimensionless radius $\mathfrak{R}_b = 0.76$ – 0.77 at the end of an incipient period with the length t . Therefore, it can be said that the flame curvature and stretch effect (significant when $\mathfrak{R}_b \leq 0.10$) should not affect the value of the laminar burning velocity. Thus, it shows that any length between $1/4 t$ and t is suitable for application in Equation (1). As discussed above, a rigorous selection of the optimum length of the incipient period can be due after inspection of the fit parameters achieved for regressions between the pressure rise Δp and time t . From this inspection results that the optimal duration of the incipient is reached when $\Delta p = p_0$.

The burnt mass fraction and flame radius play an important role in the incipient detection of the explosion initiation, and therefore in obtaining accurate laminar burning velocities using the constant volume combustion method.

Using the flame radii and burnt mass fractions, the laminar burning velocities can be calculated from the transient pressure record in the closed bomb using the following equation, which includes both measurable and calculable parameters [31]:

$$S_u = \frac{R^3}{3r_b^2} \left(\frac{1}{\pi} \right)^{1/\gamma_u} \frac{dn}{dt} \quad (9)$$

The time derivative of the burned mass fraction, dn/dt , was analytically calculated at every moment, after detecting the best-fit Equation $n(t)$ by a nonlinear least-square procedure.

A set of representative data regarding the stoichiometric CH₄-N₂O mixture diluted with 40 vol% N₂, at atmospheric initial temperature and pressure obtained using the Equation (9), along with the laminar burning velocities obtained with the help of the cubic law coefficients, are given in Table 6.

Table 6. Laminar burning velocities of CH₄-N₂O mixture with stoichiometric composition diluted with 40 vol% N₂, at ambient initial temperature and pressure.

Calculation Method	S_u (cm/s)
Using cubic law coefficient k	47.58
Using n from Manton et al. [31]	46.30
Using n from Grumer et al. [35]	42.33
Using n from Oancea et al. [37]	40.07

Similar values of the laminar burning velocities were obtained by means of Equation (9) only when the burnt mass fraction is calculated using the linear Equation of Manton et al. [31]. In the case of burnt mass fractions obtained using the equations proposed by Grumer et al. [35] and Oancea et al. [37], lower values of the laminar burning velocities were obtained. Such behavior was observed for all initial pressures and diluent compositions studied here. This is also valid when comparing these values with those obtained by D’Olieslager and van Tiggelen [44] (e.g., $S_u = 46.50$ cm/s for stoichiometric mixture diluted with 40 vol% N₂).

The laminar burning velocity plays an important role in the combustion process. It contains fundamental information regarding the reactivity, diffusivity, and exothermicity of a combustible mixture. The accurate values of the laminar burning velocities are still needed as inputs for computation of turbulent flames and for validation of chemical kinetic mechanisms for conventional and alternative fuels. Moreover, the knowledge of the laminar burning velocity is needed for the design of new internal combustion engines where the initial combustion takes place as laminar combustion.

5. Conclusions

The present paper uses the transient pressure records in a small-closed spherical bomb in order to investigate the flame propagation in N₂-diluted CH₄-N₂O mixtures with stoichiometric equivalence ratio, at various initial pressures (0.5–1.75 bar) and ambient initial temperature. In this respect, the flame radii, burnt mass fractions, cubic law coefficients and corresponding laminar burning velocities at various moments of the flame propagation in the incipient period of the flame propagation were analyzed and reported.

The burnt mass fractions achieved using three different equations reported in the literature led to similar results of the flame radius, but only the simple equation proposed by Manton et al. [31] conducted to a good agreement between the laminar burning velocities obtained in this study and data reported by other authors.

The cubic law coefficients and corresponding laminar burning velocities obtained in the preset research depend on the initial pressure and diluent concentration. Furthermore, the laminar burning velocities obtained in the present study using the cubic law coefficients were found to be far from those reported from experiments using a burner with a flat flame

or from computation with an adjusted PPD mechanism, but close to those obtained from experiments performed using a Bunsen burner. Accurate values of the laminar burning velocities are necessary for computation of turbulent flames, validation of chemical kinetic mechanisms and design new internal combustion engines.

The incipient stage (whose duration was considered t and which was limited to $\Delta p = p_0$) was divided into smaller time intervals of $3/4 t$, $1/2 t$ and $1/4 t$. This was done in order to establish the optimum duration of the incipient stage of flame propagation. After a rigorous inspection of the fit parameters achieved for regressions of Δp vs. t , the optimum duration of the early stage was set to be at $\Delta p = p_0$. The incipient stage of flame propagation gives us useful information regarding the flame initiation and growth, while the pressure variation in the course of this stage is useful for the design of venting devices.

Author Contributions: Conceptualization, V.G.; software, M.M.; validation, V.G., M.M. and C.M.; investigation, V.G. and M.M.; data curation, M.M.; formal analysis, V.G.; writing—original draft preparation, V.G.; writing—review and editing, V.G., M.M. and C.M.; visualization, V.G., M.M. and C.M. All authors have read and agreed to the published version of the manuscript.

Funding: This research received no external funding.

Acknowledgments: The present study was partially supported by the Romanian Academy under research project “Dynamics of fast oxidation and decomposition reactions in homogeneous systems” of Ilie Murgulescu Institute of Physical Chemistry.

Conflicts of Interest: The authors declare no conflict of interest.

References

- Hirano, T. Accidental explosions of semiconductor manufacturing gases in Japan. *J. Phys. IV Fr.* **2002**, *12*, 253–258. [[CrossRef](#)]
- Merrill, C. *Nitrous Oxide Explosive Hazards*; Technical Report; Air Force Research Laboratory: Edwards AFB, CA, USA, 2008.
- Vandebroek, L.; Van den Schoor, F.; Verplaetsen, F.; Berghmans, J.; Winter, H.; van't Oost, E. Flammability limits and explosion characteristics of toluene–nitrous oxide mixtures. *J. Hazard. Mater.* **2005**, *120*, 57–65. [[CrossRef](#)]
- Powell, O.A.; Miller, J.E.; Dreyer, C.; Papas, P. Characterization of hydrocarbon/nitrous oxide propellant combinations. In Proceedings of the 46th AIAA Aerospace Sciences Meeting and Exhibit, Reno, NV, USA, 7–10 January 2008.
- Powell, O.A.; Papas, P.; Dreyer, C. Laminar burning velocities for hydrogen-, methane-, acetylene- and propane-nitrous oxide flames. *Combust. Sci. Technol.* **2009**, *181*, 917–936. [[CrossRef](#)]
- Powell, O.A.; Papas, P.; Dreyer, C.B. Hydrogen- and C1–C3 hydrocarbon-nitrous oxide kinetics in freely propagating and burner-stabilized flames, shock tubes, and flow reactors. *Combust. Sci. Technol.* **2010**, *182*, 252–283. [[CrossRef](#)]
- Shebeko, Y.; Korolchenko, A.; Ylin, A.; Malkin, V. Concentration limits for flame propagation in fuel-diluent-nitrous oxide mixtures. *Fiz. Gorenyia Vzryva* **1988**, *24*, 48–51.
- Shebeko, A.; Shebeko, Y.; Zuban, A.; Navzenya, V. An experimental investigation of an inertization effectiveness of fluorinated hydrocarbons in relation to premixed H₂-N₂O and CH₄-N₂O flames. *J. Loss Prev. Process Ind.* **2013**, *26*, 1639–1645. [[CrossRef](#)]
- Shebeko, A.; Shebeko, Y.; Zuban, A.; Navzenya, V. Influence on fluorocarbons flammability limits in the mixtures of H₂-N₂O and CH₄-N₂O. *Russ. J. Phys. Chem. B* **2014**, *8*, 65–70. [[CrossRef](#)]
- Mével, R.; Lafosse, F.; Chaumeix, N.; Dupré, G.; Paillard, C.E. Spherical expanding flames in H₂-N₂O-Ar mixtures: Flame speed measurements and kinetic modelling. *Int. J. Hydrog. Energy* **2009**, *34*, 9007–9018. [[CrossRef](#)]
- Koshiha, Y.; Takigawa, T.; Matsuoka, Y.; Ohtani, H. Explosion characteristics of flammable organic vapors in nitrous oxide atmosphere. *J. Hazard. Mater.* **2010**, *183*, 746–753. [[CrossRef](#)] [[PubMed](#)]
- Koshiha, Y.; Nishida, T.; Morita, N.; Ohtani, H. Explosion behavior of n-alkane/nitrous oxide mixtures. *Process. Saf. Environ. Prot.* **2015**, *98*, 11–15. [[CrossRef](#)]
- Koshiha, Y.; Hasegawa, T.; Ohtani, H. Numerical and experimental study of the explosion pressures and flammability limits of lower alkenes in nitrous oxide atmosphere. *Process Saf. Environ. Prot.* **2018**, *118*, 59–67. [[CrossRef](#)]
- Bane, S.P.M.; Mevel, R.; Coronel, S.A.; Shepherd, J.E. Flame burning speeds and combustion characteristics of undiluted and nitrogen-diluted hydrogen-nitrous oxide mixtures. *Int. J. Hydrog. Energy* **2011**, *36*, 10107–10116. [[CrossRef](#)]
- Movileanu, C.; Mitu, M.; Razus, D.; Giurcan, V.; Oancea, D. Propagation indexes of C₂H₄-N₂O-N₂ deflagrations in elongated closed vessels. *Rev. Roum. Chim.* **2017**, *62*, 357–363.
- Razus, D.; Mitu, M.; Giurcan, V.; Oancea, D. Propagation indices of methane-nitrous oxide flames in the presence of inert additives. *J. Loss Prev. Process Ind.* **2017**, *49*, 418–426. [[CrossRef](#)]
- Razus, D.; Mitu, M.; Giurcan, V.; Movileanu, C.; Oancea, D. Methane-unconventional oxidant flames. Laminar burning velocities of nitrogen-diluted methane-N₂O mixtures. *Proc. Saf. Environ. Prot.* **2018**, *114*, 240–250. [[CrossRef](#)]

18. Shen, X.; Zhang, N.; Shi, X.; Cheng, X. Experimental studies on pressure dynamics of C₂H₄/N₂O mixtures explosion with dilution. *Appl. Therm. Eng.* **2019**, *147*, 74–80. [CrossRef]
19. Li, Y.; Jiang, R.; Li, Z.; Xu, S.; Pan, F.; Xie, L. Studies on the flame propagation characteristic and thermal hazard of the premixed N₂O/fuel mixtures. *Def. Technol.* **2020**, *16*, 564–570. [CrossRef]
20. Wang, L.Q.; Ma, H.H.; Shen, Z.W. Explosion characteristics of H₂/N₂O and CH₄/N₂O diluted with N₂. *Fuel* **2020**, *260*, 116355. [CrossRef]
21. Wang, L.Q.; Ma, H.H.; Shen, Z.W.; Pan, J. A comparative study of the explosion behaviors of H₂ and C₂H₄ with air, N₂O and O₂. *Fire Saf. J.* **2021**, *119*, 103260. [CrossRef]
22. Luo, Z.; Liang, H.; Wang, T.; Cheng, F.; Su, B.; Liu, L.; Liu, B. Evaluating the effect of multiple flammable gases on the flammability limit of CH₄: Experimental study and theoretical calculation. *Process Saf. Environ. Prot.* **2021**, *146*, 369–376. [CrossRef]
23. Mitu, M.; Giurcan, V.; Movileanu, C.; Razus, D.; Oancea, D. Propagation of CH₄-N₂O-N₂ flames in a closed spherical vessel. *Processes* **2021**, *9*, 851. [CrossRef]
24. Mehra, R.K.; Duan, H.; Juknelevičius, R.; Maa, F.; Li, J. Progress in hydrogen enriched compressed natural gas (HCNG) internal combustion engines—A comprehensive review. *Renew. Sustain. Energy Rev.* **2017**, *80*, 1458–1498. [CrossRef]
25. Popoola, A.I.; Ponle, A.L.; Ogunlua, B.O.; Oluyamo, S.S. Design and implementation of an instrument for methane (CH₄) and nitrous oxide (N₂O) measurements. *J. Sci. Technol. Res.* **2019**, *1*, 92–104.
26. Branco, J.B.; Ferreira, A.C.; Botelho do Rego, A.M.; Ferraria, A.M.; Almeida-Gasche, T. Conversion of methane over bimetallic copper and nickel actinide oxides (Th, U) using nitrous oxide as oxidant. *ACS Catal.* **2012**, *2*, 2482–2489. [CrossRef]
27. Babkin, V.S.; Babushok, V.I. Initial stage of gas combustion in a closed volume. *Combust. Explos. Shock Waves* **1977**, *13*, 19–23. [CrossRef]
28. Zabetakis, M. *Flammability Characteristics of Combustible Gases and Vapors*; BM-BULL-627; U.S. Bureau of Mines: Pittsburgh, PA, USA, 1964.
29. Razus, D.; Movileanu, C.; Oancea, D. Burning velocity evaluation from pressure evolution during the early stage of closed-vessel explosions. *J. Loss Prev. Process Ind.* **2006**, *19*, 334–342. [CrossRef]
30. Fiock, E.; Marvin, C. The measurement of flame speeds. *Chem. Rev.* **1937**, *21*, 367–387. [CrossRef]
31. Manton, J.; Lewis, B.; von Elbe, G. Burning-velocity measurements in a spherical vessel with central ignition. *Proc. Symp. Int. Combust.* **1953**, *4*, 358–363. [CrossRef]
32. Brinzea, V.; Mitu, M.; Movileanu, C.; Razus, D.; Oancea, D. Deflagration parameters of stoichiometric propane-air mixture during the initial stage of gaseous explosions in closed vessels. *Rev. Chim.* **2011**, *62*, 201–205.
33. Razus, D.; Brinzea, V.; Mitu, M.; Movileanu, C.; Oancea, D. Burning velocity of propane-air mixtures from pressure-time records during explosions in a closed spherical vessel. *Energy Fuels* **2012**, *26*, 901–909. [CrossRef]
34. Chen, Z.; Burke, M.P.; Ju, Y. Effects of compression and stretch on the determination of laminar flame speeds using propagating spherical flames. *Combust. Theor. Model.* **2009**, *13*, 343–364. [CrossRef]
35. Grumer, J.; Cook, E.B.; Kubala, T.A. Considerations pertaining to spherical vessel combustion. *Combust. Flame* **1959**, *3*, 437–446. [CrossRef]
36. COSILAB; Version 3.0.3; Rotexo-Softpredict-Cosilab GmbH & Co KG: Bad Zwischenhahn, Germany, 2013.
37. Oancea, D.; Razus, D.; Ionescu, N.I. Burning velocity determination by spherical bomb technique. I. A new model for burnt mass fraction. *Rev. Roum. Chim.* **1994**, *39*, 1187–1196.
38. Razus, D.; Oancea, D.; Ionescu, N.I. Burning velocity determination by spherical bomb technique. II. Propylene-air mixtures of various compositions, pressures and temperatures. *Rev. Roum. Chim.* **2000**, *45*, 319–330.
39. Nagy, J.; Conn, J.; Verakis, H. *Explosion Development in a Spherical Vessel*; US Bureau of Mines Report, No. 7279; U.S. Department of the Interior: Washington, WC, USA, 1969. Available online: <https://ncsp.tamu.edu/reports/MSHA/sphericalvessel.pdf> (accessed on 16 September 2021).
40. Glassman, I.; Yetter, R. *Combustion*, 4th ed.; Elsevier: Amsterdam, The Netherlands; Boston, MA, USA; London, UK, 2008.
41. Lee, M.C.; Seo, S.B.; Yoon, J.; Kim, M.; Yoon, Y. Experimental study on the effect of N₂, CO₂, and steam dilution on the combustion performance of H₂ and CO synthetic gas in an industrial gas turbine. *Fuel* **2012**, *102*, 431–438. [CrossRef]
42. Zhang, J.; Mi, J.; Li, P.; Wang, F.; Dally, B.B. Moderate or intense low-oxygen dilution combustion of methane diluted by CO₂ and N₂. *Energy Fuels* **2015**, *29*, 4576–4585. [CrossRef]
43. Ceriello, G.; Sorrentino, G.; Cavaliere, A.; Sabia, P.; de Joannon, M.; Ragucci, R. The role of dilution level and canonical configuration in the modeling of MILD combustion systems with internal recirculation. *Fuel* **2020**, *264*, 116840. [CrossRef]
44. D’Olieslager, J.; van Tiggelen, A. Kinetic study of hydrocarbon-nitrous oxide flames. *Bull. Soc. Chim. Belg.* **1964**, *73*, 135–153. [CrossRef]
45. Dahoe, A.; Zevenbergen, J.; Lemkowitz, S.; Scarlett, B. Dust explosions in spherical vessels: The role of flame thickness in the validity of the ‘cube-root’ law. *J. Loss Prev. Process Ind.* **1996**, *9*, 33–44. [CrossRef]
46. Faghhi, M.; Chen, Z. The constant-volume propagating spherical flame method for laminar flame speed measurement. *Sci. Bull.* **2016**, *61*, 1296–1310. [CrossRef]
47. Luijten, C.C.M.; Doosje, E.; de Goey, L.P.H. Accurate analytical models for fractional pressure rise in constant volume combustion. *Int. J. Therm. Sci.* **2009**, *48*, 1213–1222. [CrossRef]
48. O’Donovan, K.H.; Rallis, C.J. A modified analysis for the determination of the burning velocity of a gas mixture in a spherical constant volume combustion vessel. *Combust. Flame* **1959**, *3*, 201–214. [CrossRef]

Article

Computational Analysis of Premixed Syngas/Air Combustion in Micro-channels: Impacts of Flow Rate and Fuel Composition

Sunita Pokharel ¹, Mohsen Ayoobi ^{2,*} and V'yacheslav Akkerman ¹

¹ Center for Innovation in Gas Research and Utilization (CIGRU), Department of Mechanical and Aerospace Engineering, West Virginia University, Morgantown, WV 26506, USA; sp0078@mix.wvu.edu (S.P.); vyacheslav.akkerman@mail.wvu.edu (V.A.)

² Division of Engineering Technology, Wayne State University, Detroit, MI 48202, USA

* Correspondence: mohsen.ayoobi@wayne.edu

Abstract: Due to increasing demand for clean and green energy, a need exists for fuels with low emissions, such as synthetic gas (syngas), which exhibits excellent combustion properties and has demonstrated promise in low-emission energy production, especially at microscales. However, due to complicated flame properties in microscale systems, it is of utmost importance to describe syngas combustion and comprehend its properties with respect to its boundary and inlet conditions, and its geometric characteristics. The present work studied premixed syngas combustion in a two-dimensional channel, with a length of 20 mm and a half-width of 1 mm, using computational approaches. Specifically, a fixed temperature gradient was imposed at the upper wall, from 300 K at the inlet to 1500 K at the outlet, to preheat the mixture, accounting for the conjugate heat transfer through the walls. The detailed chemistry of the ignition process was imitated using the San Diego mechanism involving 46 species and 235 reactions. For the given boundary conditions, stoichiometric premixed syngas containing various compositions of carbon monoxide, methane, and hydrogen, over a range of inlet velocities, was simulated, and various combustion phenomena, such as ignition, flame stabilization, and flames with repeated extinction and ignition (FREI), were analyzed using different metrics. The flame stability and the ignition time were found to correlate with the inlet velocity for a given syngas mixture composition. Similarly, for a given inlet velocity, the correlation of the flame properties with respect to the syngas composition was further scrutinized.

Keywords: micro-combustion; syngas; repetitive extinction and ignition (FREI); numerical simulations; flame instabilities

Citation: Pokharel, S.; Ayoobi, M.; Akkerman, V. Computational Analysis of Premixed Syngas/Air Combustion in Micro-channels: Impacts of Flow Rate and Fuel Composition. *Energies* **2021**, *14*, 4190. <https://doi.org/10.3390/en14144190>

Academic Editor: Giuseppe Pascazio

Received: 13 June 2021

Accepted: 7 July 2021

Published: 11 July 2021

Publisher's Note: MDPI stays neutral with regard to jurisdictional claims in published maps and institutional affiliations.



Copyright: © 2021 by the authors. Licensee MDPI, Basel, Switzerland. This article is an open access article distributed under the terms and conditions of the Creative Commons Attribution (CC BY) license (<https://creativecommons.org/licenses/by/4.0/>).

1. Introduction

Due to expanding interest in and development of cutting-edge, highly-effective miniaturized and portable power generation devices, such as unmanned aerial vehicles (UAVs), microsatellite thrusters, miniature reactors, and sensors, the demand exists for more advanced technologies with reduced weight and high durability. Further, the combination of heat and power microsystems and thermo-photovoltaic applications, in which micro-combustion systems play a significant role, is advancing [1,2]. Although new energy resources such as batteries are emerging rapidly, they still have considerably lower energy densities compared to combustion-based sources [3]. In particular, the density of the energy stored in a typical hydrocarbon fuel is orders of magnitude higher than that in a typical lithium-ion battery [4]. Therefore, combustion-based power generation cannot be phased out immediately, especially in aviation and aerospace applications, and other devices such as micro satellites, for which weight is a critical and deciding factor. Thus, because combustion has been and remains the most reliable energy source, due to the high energy density of fossil fuels [5,6], and due to the increasing need for clean, green, and sustainable (CGS) energy, a critical need exists for an efficient method to sustain such micro-combustion.

Regarding CGS energy and its compatibility with other power generation systems based on combustion, numerous studies have been conducted on the application of synthetic gas (syngas), and have proven that syngas is potentially more advantageous than conventional fuels [7], with advantages ranging from cheaper production to lower emissions [8]. Syngas is mainly produced through gasification of heavy hydrocarbons (C_xH_y), biomass, or coal-based feedstocks, with carbon dioxide (CO_2) eliminated from the environment. The composition of syngas also varies depending on the raw material and the production process [9–12]. For instance, it exhibits high adiabatic flame temperatures in the presence of hydrogen (H_2) and carbon monoxide (CO) [13]. Furthermore, the combination of H_2 and CO provides a lower flammability limit than methane (CH_4) and a higher upper limit than other hydrocarbons, having a wider flammability range than conventional fuels such as oil or natural gas. Thus, the presence of H_2 and CO in syngas exhibits flame-retardant characteristics, whereas the presence of inert gases such as nitrogen (N_2) and CO_2 reduces the flammability limits of syngas.

Regarding the unstretched laminar burning velocity, S_L , using a detailed chemical kinetics mechanism, Pio et al. [14] studied the effect of syngas composition on reactivity, adiabatic flame temperature, T_a , energy, and pollutant production rate. Comparing their work with the data from the literature, the authors of Ref. [14] found that the volumetric increment of CO_2 and CO reduced S_L , in addition to which the kinetic effect of CO_2 led the maximum values of S_L and T_a to shift towards the stoichiometric compositions. Syngas explosion properties in closed vessels and the impacts of different operating conditions, such as the equivalence ratio and syngas composition, on the flame characteristics have also been the subject of many studies [15–17]. The impact of H_2 -addition to CH_4 on the properties of syngas combustion was studied by Mardani et al. [18]. It was shown that H_2 -enrichment led to higher volumes of the hot regions and faster upstream movement, in addition to an increase in the distance between the locus of the maximum temperature and that of the stoichiometric mixture fraction, so that the maximum temperature exceeded the adiabatic flame temperature. Zhang et al. [19] studied the effect of fuel variability for high hydrogen-containing syngas and demonstrated a good performance of the combustion process for certain fractions of H_2 and CO. Further, the effects of CO_2 and N_2 at various equivalence ratios were compared by Dam et al. [20]. Similarly, the effect of varying syngas composition (based on different production methods) at different pressures was studied by Monteiro et al. [21]. Although all the studies listed above showed important contributions of different fuel components to the combustion properties, the systems of interest were very large compared to micro-combustors. Wei et al. [22] identified the operating cost as the major issue for syngas production, which was then suggested to have significantly reduced unit costs for higher production when industrialized with better manufacturing and optimization techniques. Research in this area is still in its rudimentary phases as burning at microscales and macroscales shows different behaviors [23–25]. Therefore, further research is critically needed to study syngas combustion at microscales.

In a microscale system, the surface area to the volume ratio is higher than that at larger scales, which promotes heat losses from the system [25–28], thereby reducing the efficiency of a combustor. Further, a smaller size of the system leads to a reduced characteristic length scale of the flow and, therefore, a lower Reynolds number. Consequently, the flow is laminar. Although experimental analysis of combustion at both conventional scales and microscales is essential to validate the computational or analytical models and results, numerical simulations allow researchers to minimize the investments in experimental trials; in particular, preliminary results from numerical simulations can help researchers be more objective with their experimental setup and analysis. In microscale and mesoscale combustors, the stabilizing and destabilizing effects of the flame stretch, due to the wall heat losses, further complicate the analysis.

Various studies have been conducted in the past to sustain the microscale combustion process by incorporating a bluff body and a cavity into a micro-combustor [29], and some researchers focused on the impact of the adiabatic walls on the flame stability in micro-

combustors [30]. In particular, Pizza et al. [31] conducted extensive numerical simulations to study the characteristics of H₂-air combustion in a two-dimensional (2D) channel, employing various channel heights and inlet velocities of a reactant. Further studies have been conducted for other fuels, such as methane (CH₄) [26,32,33], propane (C₃H₈) [34–36], and syngas [24,37,38]. The numerical work of Kousheshi et al. [39] also analyzed the effect of syngas composition on the engine exhaust, with the reduction of the ignition delay time, sharper heat release rate, more NO_x, and less soot, CO, and unburned hydrocarbon production obtained for an H₂-rich mixture. These computational findings on the flame instabilities have also been confirmed experimentally [40]. Brambilla et al. [24] studied lean-premixed, syngas-air combustion in a microchannel of 7 mm height, by varying the equivalence ratios in the range $0.35 \leq \phi \leq 0.42$, the volumetric CO:H₂ ratio from 1:1 to 20:1, and the wall temperatures from 550 to 1320 K. As a result, the steady V-shaped and asymmetric flames, with the stationary and oscillatory modes, were observed in this work. Further, the stable flames, in addition to the flames with repetitive extinction and ignition (FREI), were shown for CH₄-air burning in a microchannel of 2 mm diameter by Maruta et al. [41]. This experimental work investigated how the flame behavior depends on the equivalence ratio, identifying the stable flames for $\phi < 1.3$, and the FREI were observed for $1.3 < \phi < 1.5$. The flat and stationary flames, with the cyclic oscillatory and the FREI behavior, were also observed for CH₄-air and C₃H₈-air combustion in another study by Maruta et al. [23], with a fixed temperature gradient maintained at the channel wall. The phenomenon of repetitive extinction/ignition has been also observed in several other experimental studies for various fuels such as CH₄ [42,43] and ethane (C₂H₆) [44].

Although syngas combustion at microscales has been studied previously, comprehensive studies accounting for detailed chemistry are necessary at these scales to further scrutinize the combustion characteristics, and the impacts of the mixture composition and the flow rate on various properties of syngas combustion at such small scales.

The present work is a step in this direction. Specifically, stoichiometric premixed syngas combustion in a microscale 2D channel was simulated by means of a detailed San Diego mechanism [45], aiming to scrutinize the flame behavior for various mixture compositions and inlet velocities. The remainder of the manuscript is organized as follows: the methodology is explained in Section 2; various combustion phenomena, such as extinction and ignition, stabilization, and instabilities, are observed and scrutinized in Section 3; and the conclusions are summarized in Section 4.

2. Methodology

In the following, the governing equations, operating conditions, and metrics guiding the analyses and conclusions are elucidated.

2.1. Governing Equations

The governing equations are the general balance equations for mass, momentum, species, and energy, which read:

$$\frac{\partial \rho}{\partial t} + \nabla \cdot (\rho \vec{v}) = 0, \quad (1)$$

$$\frac{\partial}{\partial t} (\rho \vec{v}) + \nabla \cdot (\rho \vec{v} \vec{v}) = -\nabla p + \nabla \cdot (\bar{\tau}) + \rho \vec{g} + \vec{F}, \quad (2)$$

$$\frac{\partial}{\partial t} (\rho Y_i) + \nabla \cdot (\rho \vec{v} Y_i) = -\nabla \cdot \vec{J}_i + R_i, \quad (3)$$

$$\rho C_p \frac{\partial T}{\partial t} + \rho C_p v \nabla T = -\nabla q - \rho \sum_{i=1}^N C_{p,i} Y_i V_i - \sum_{i=1}^N h_i \Omega_i, \quad (4)$$

respectively. Here ρ is the density of the system, C_p is the specific heat at constant pressure, p is the static pressure, $\bar{\tau}$ is the stress tensor, T is the temperature, \vec{g} and \vec{F} are the

gravitational and external body forces, respectively; and R_i is the net rate of production for the i th species in the chemical reactions. The local mass fraction of each species Y_i is predicted by solving the convection-diffusion equation for the i th species, and V_i , h_i and Ω_i are, respectively, the diffusion velocity, the specific enthalpy, and the net rate of production of the i th species, $i = 1 \dots N$, with the total number of species N . \vec{J}_i in Equation (3) represents the diffusion flux of the i th species due to the gradients of the concentration and temperature. Fick's law is employed to approximate mass diffusion due to the concentration gradient:

$$\vec{J}_i = -\rho D_{i,m} \nabla Y_i - D_{T,i} \frac{\nabla T}{T}. \quad (5)$$

Here, $D_{i,m}$ is the mass diffusion coefficient of the i th species in the mixture, and $D_{T,i}$ is the thermal diffusion (Soret) coefficient. The simulations were performed using the commercial CFD package Ansys FLUENT (version 18.2) [46], employing the finite-volume discretization method. The following model options were chosen in the Ansys FLUENT simulation setup: pressure-based coupling, absolute velocity formulation, laminar viscosity, and volumetric species transport model. In addition, the semi-implicit method for pressure-linked equations (SIMPLE) was used as a numerical scheme to solve the Navier–Stokes equations. The methods and models employed in this work are widely used and accepted in the literature.

2.2. Operating Conditions

The computational domain is a 2D channel of length 20 mm and half-width 1 mm, as schematically shown in Figure 1. It is noted that 2D simulations were preferred in this work because (i) with the large number of the cases simulated here, it would have been very challenging (in terms of time and computational resources) to use a 3D domain, and (ii) although considering 3D impacts could possibly provide further detail of the combustion characteristics, 2D simulations provide sufficient insights into the fundamental processes occurring in narrow channels [31–33]. Both extremes of the channel were open, and the pressure at the inlet and outlet was atmospheric. To save the computational cost twice, the upper half of the channel was imitated by imposing the axisymmetric boundary conditions at the lower wall. The upper wall was imposed with a temperature gradient such that the wall temperature grows linearly, from 300 K at the inlet to 1500 K at the outlet, to account for the conjugate heat transfer at the wall. The temperature gradient of 60 K/mm was selected to ensure relatively high exit temperature (1500 K), where auto ignition of the air/fuel mixtures downstream of the channel can be guaranteed. The inlet mixture flowed with a uniform velocity profile, with a constant temperature and no-slip boundary conditions at the wall. A uniform square mesh of cell size 0.05 mm and a time step of 10 μ s were used in all simulations. It is important for the grid resolution to sufficiently resolve the flame thickness. Although the flame thickness depends on the operating conditions, including fuel composition, it remains in the same order of magnitude (≈ 1 mm) for the different cases studied here. Correspondingly, the selected grid resolution ensures that the flames are resolved, with around 20 cells inside the thickness of the flame front.

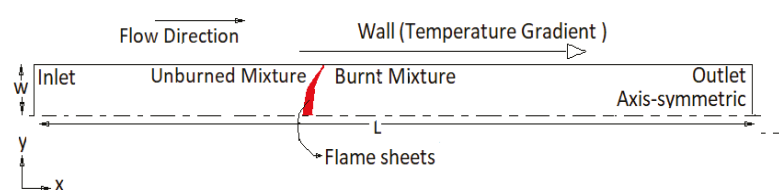


Figure 1. A schematic of the computational domain.

Stoichiometric premixed combustion of syngas comprised of CO, CH₄, and H₂ was considered, with three various mixture compositions, A, B and C, as listed in Table 1. Various inlet flow velocities were employed, from 0.1 to 3.0 m/s. To calculate the mass fractions of the species at the inlet, the following global mechanism of syngas combustion was used:

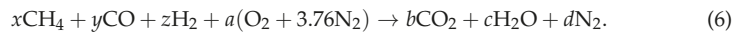


Table 1. The syngas mixture compositions studied in this work.

$x\text{CH}_4 + y\text{CO} + z\text{H}_2 + a(\text{O}_2 + 3.76\text{N}_2) \rightarrow \text{Products}$			
Fuel Mixture	$x(\%)$	$y(\%)$	$z(\%)$
A	30	5	65
B	70	5	25
C	60	10	30

The indexes x , y , and z in Equation (6) represent the fuel composition, and the coefficients a , b , c , and d are defined as:

$$a = \frac{4x + y + z}{2}, \quad (7)$$

$$b = x + y, \quad (8)$$

$$c = 2x + z, \quad (9)$$

$$d = 3.76 \left(\frac{4x + y + z}{2} \right). \quad (10)$$

The chemical kinetics obeys the San Diego mechanism with 46 species and 235 reactions [45].

2.3. Resolution Test

To verify the accuracy of the simulations and to ensure that the results do not depend on the grid size or time steps, two different resolution tests, for the grid and time resolutions, respectively, were performed and analyzed as described below.

Grid Resolution. The numerical simulation tool that was used in this work, Ansys FLUENT, is based on a finite-volume discretization, where the small volumes, also regarded here as mesh elements, play a very important role in accurately mimicking the physical phenomena and producing the effective results. The optimum mesh size needs to be chosen to obtain accurate results by nevertheless utilizing as minimal resources as possible. Because 2D simulations were of interest in this work, the simulation domain was discretized with an evenly sized square grid. Numerical simulations were performed over three different grid sizes: 0.02 mm (fine), 0.05 mm (moderately fine), and 0.1 mm (coarse), with all other conditions kept identical. To evaluate the simulation performance over these three grid sizes, the time evolution of the total heat release rate (HRR_T) is compared for all cases (see Figure 2). It is observed that although HRR_T experiences some variations depending on the mesh size, the ignition time (the time when HRR_T peaks), determining most of the combustion parameters, is practically the same for all three meshes. However, the time it took the software to complete the simulations almost doubled and the memory usage by the simulation almost tripled as the mesh size was refined from 0.1 to 0.05 mm, and from 0.05 to 0.02 mm. As expected, the results of the simulations with the finest mesh size (0.02 mm) were smoother compared to those with other two mesh sizes. Considering the number of simulations needed for this study, to more efficiently use time and memory resources, the moderately fine mesh size (0.05 mm) was chosen for all the simulations.

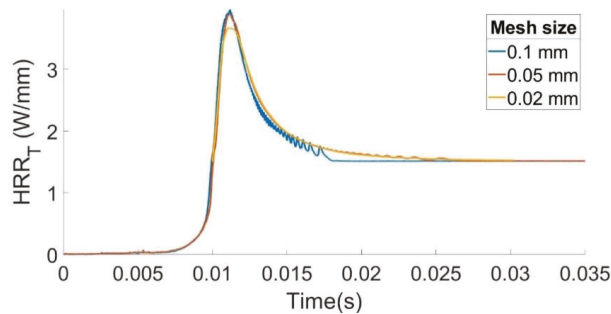


Figure 2. The grid resolution test for mixture A with the inlet velocity of 1.0 m/s.

Time Resolution. Due to the transient nature of the simulations in this work and, in particular, the significant variation of most properties with time, it was important to ensure that the results were not affected by the selected time step. Therefore, a baseline case was first simulated with various time steps (1, 10, and 50 μ s), while all other conditions were kept identical. Similar to the grid resolution test, the time evolution of HRR_T was compared for all time steps; see Figure 3. The results suggest that the time step of 50 μ s does not allow predicting the ignition time as accurately as the cases of smaller time steps (10 and 1 μ s), whereas the difference is minor when comparing the results associated with the time steps of 10 and 1 μ s. Again, to be most efficient with the time and memory resources, and to avoid sacrificing accuracy, the time step of 10 μ s was selected for all the simulations.

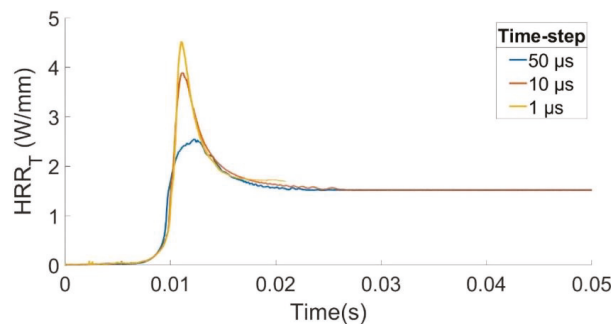


Figure 3. The time resolution test for mixture A with the inlet velocity of 1.0 m/s.

It is noted that there are no experimental results in the literature for the operating conditions, used in this paper, against which the results of this work could be compared. However, similar behavior (such as ignition process or FREI) observed in the literature [20,23,25,30,42–44] for different fuels and operating conditions, in addition to the resolution tests conducted here, confirm that the simulation results of this work are physically possible and valid. Therefore, the findings of this work could inspire future experiments, while being used as a guidance to design and perform such experiments.

2.4. Metrics

To scrutinize various combustion properties from the raw simulation data, the following metrics are introduced:

Heat release rate (HRR): This is a local property in the system, and is calculated by obtaining the summation of the net heat release rates for all the reactions involved in each computation cell. Due to the implementation of detailed chemistry in this work, comprehensive information about all species and reactions is available. Because the heat

release rate integrates the impact of all species and reactions into one parameter, and it is known to peak at the flame front, this was chosen as the most precise criterion to demarcate the flame front and understand its behavior.

Total heat release rate (HRR_T): This is the total amount of heat released over the domain.

Ignition time and extinction time: The quantity HRR_T explained above varies with time, and thus the ignition time is defined as the time when HRR_T reaches the maximum value before the flame stabilizes. Similarly, the time at which HRR_T becomes minimal (near-zero) is defined as the extinction time.

Ignition location and length: These quantities are defined based on the temperature distribution in the simulation domain at the time of ignition.

Stabilization location and flame span: These quantities are defined using the axial temperature distribution after the flame stabilizes.

FREI and FREI period: For lower inlet velocities, flame extinction is followed by ignition. This kind of flame is known as the FREI. For these cases, the time required for a flame to gain two consecutive ignition incidents is defined as the FREI period (τ_{FREI}).

How these metrics are obtained and what they represent physically are elaborated in Section 3.

3. Results and Discussion

In this section, various combustion phenomena, such as ignition, stable/unstable flame behaviors, and the impacts of various operating conditions (such as the flow rate and the fuel composition) on such characteristics, are analyzed.

3.1. Ignition Process

The ignition process, which showed similar behavior for all the simulation runs, was analyzed as follows: when a syngas/air mixture flows in the channel with an inlet temperature of 300 K, it is heated up due to the positive temperature gradient imposed at the wall. Such a preheating facilitates the chain-branching reactions, which trigger ignition when the temperature is sufficiently high and produce a flame kernel somewhere downstream the channel. In this work, the ignition process is characterized by the transient total heat release rate in the domain, HRR_T , which is calculated by integrating the local heat of reaction in the computational domain at each time step,

$$HRR_T = \sum_m HRR = \sum_m \sum_n \dot{h}_r, \quad (11)$$

where m is the number of cells in the domain and n is the number of species. Because HRR_T varies with time, the ignition time is defined as the time at which HRR_T peaks,

$$t_{ig} = t_{(HRR_T)_{max}}. \quad (12)$$

Similarly, the extinction time is defined as the time at which HRR_T falls to near-zero,

$$t_{ex} = t_{(HRR_T=0)}. \quad (13)$$

This is further explained by Figure 4, associated with the inlet velocity of 1 m/s and the mixture composition A, where the time evolution of HRR_T is used to determine the ignition time. Figure 5 complements Figure 4 for further explanation of the ignition process. Here, the temperature contour plots for the selected time steps in Figure 4 are provided. Specifically, the chain branching reaction starts at time (a) and goes through time (b), indicating the beginning of the ignition process. At time (b), HRR_T of this system is maximal, and a flame front is formed, separating the unburnt and burnt mixtures. State (b) determines the ignition time (t_{ig}). From time (b) to time (c), the flame starts propagating upstream until it either becomes stable or is extinguished, depending on the boundary conditions, which are discussed in the next sections.

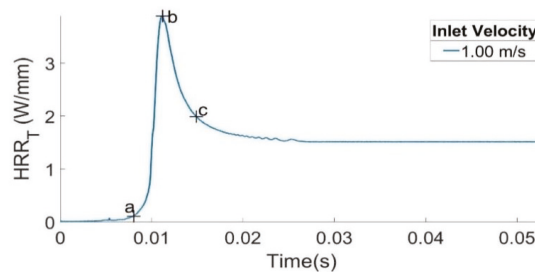


Figure 4. The total heat release rate (HRR_T) vs. time for mixture A with the inlet velocity of 1.0 m/s. The markers (a), (b) and (c) indicate selected time steps for further explanation in Figure 5.

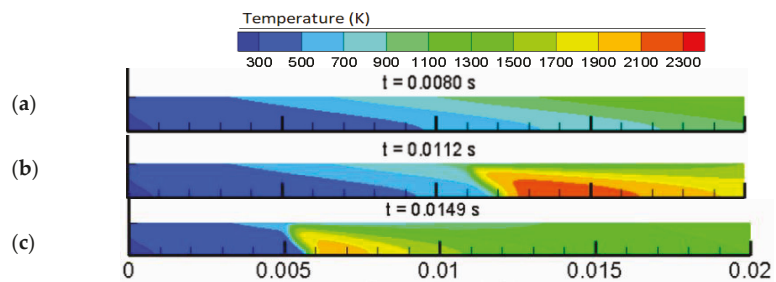


Figure 5. The temperature distribution at the selected consecutive time steps (a)–(c) for the ignition process for mixture A with the inlet velocity of 1.0 m/s. The length is measured in meters.

In addition to the ignition time, the ignition location is another metric that was defined in this work to characterize the ignition process. The axial temperature at the ignition time is analyzed in Figure 6a, and the temperature contour during the time of ignition is presented in Figure 6b. The spans over which the positive temperature gradient peaks, to where the negative temperature gradient peaks, are defined as the ignition locations. That is, $x_{(ig-st)}$ and $x_{(ig-e)}$ indicate the points where the temperature, respectively, jumps and drops, abruptly.

$$x_{ig-st} = \left(x_{\left(\frac{dT}{dx} \right)_{max}} \right)_{t_{ig}}, \quad (14)$$

$$x_{ig-e} = \left(x_{\left(\frac{dT}{dx} \right)_{min}} \right)_{t_{ig}}. \quad (15)$$

Further, the difference between these two points defines the ignition length, Δx_{ig} , as

$$\Delta x_{ig} = x_{ig-st} - x_{ig-e}. \quad (16)$$

3.2. Flame Behaviour

After ignition, the flame front propagates downstream. Under the operating conditions employed in this work, and as the wall temperature decreases towards the upstream, the V-shaped flame may become stable at a certain location, or it may lose its stability and go through repeated extinctions and ignitions. These types of behaviors are analyzed in detail for selected operating conditions in Sections 3.2.1 and 3.2.2. The impact of all operating conditions used in this work on the ignition process and the flame behavior are subsequently elaborated in Section 3.3.

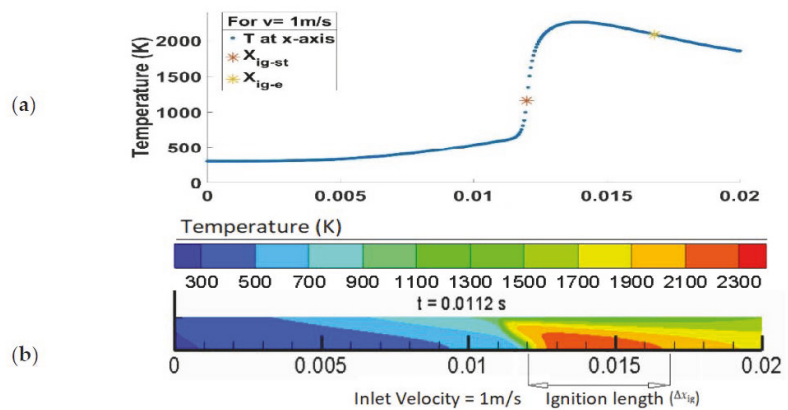


Figure 6. The temperature distribution at the time of ignition for mixture A with the inlet flow velocity of 1.0 m/s. The length is measured in meters. (a) the temperature profile along the x-axis, (b) the temperature contour in the simulation domain at the selected time step.

3.2.1. Stable Flames

In the stable modes, the flame propagates further upstream and becomes stable at a certain location. This behavior is expected in cases with higher inlet velocities (discussed in Section 3.3), in which flame propagation is balanced with the inlet velocity, resulting in a stable flame that is not too close to the inlet, where the wall temperature is sufficiently high to sustain the flame. To scrutinize this process, similar to Figures 4–6, the case with the inlet velocity of 1 m/s and the fuel mixture composition A is selected. As seen in Figure 4, HRR_T decreases after ignition until it becomes constant, indicating that the flame front has become stable. This is also confirmed by the temperature contour plots of Figure 5, where flame propagation eventually stops.

Similar to the ignition process, the properties of a stable flame front are characterized by the stabilization location. According to Figure 7, the location at which the stable flame lies is known as the stabilization location, and is obtained from the axial temperature variation in the domain for the stabilized flame. Here, the starting point of the stabilized location, $x_{(sz-st)}$, is defined as the location at which the axial temperature grows abruptly.

$$x_{sz-st} = \left(x_{\left(\frac{dT}{dx} \right)_{max}} \right)_{t_{st}} \quad (17)$$

Similarly, the ending point of the stabilized flame, $x_{(sz-e)}$, is the locus with the least temperature gradient,

$$x_{sz-e} = \left(x_{\left(\frac{dT}{dx} \right)_{min}} \right)_{t_{st}} \quad (18)$$

It is recalled that both these points are obtained at the time t_{st} , when the solution is converged and the flame front is stabilized. The difference between these points defines the flame length after the flame stabilization,

$$\Delta x_{sz} = x_{sz-st} - x_{sz-e} \quad (19)$$

3.2.2. Flames with Repeated Extinctions and Ignitions (FREI)

Under some operating conditions, the flame does not stabilize after the ignition, i.e., as it propagates further upstream, towards the inlet, the temperature is not high enough for the reactions to be sustained, so the flame is extinguished. However, with the continuous supply at the inlet, the fuel-air mixture subsequently reaches the high-temperature zone and the flame is ignited again. Such a repetitive scenario has been observed, both computationally and experimentally, and is referred to as flames with repetitive extinctions and

ignitions (FREIs) in the literature [20,25,30]. To further understand this process, one of the operating conditions resulting in such a behavior is chosen (mixture A; the inlet velocity of 0.2 m/s), with the corresponding metrics elaborated.

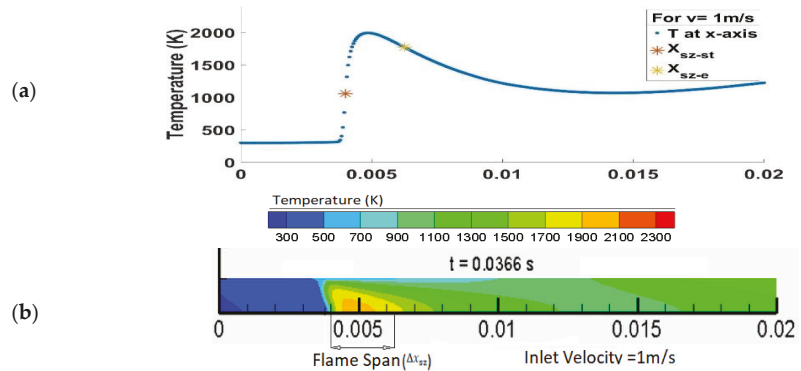


Figure 7. The temperature distribution for the stabilized flame for mixture A with the inlet flow velocity of 1.0 m/s. The length is measured in meters. (a) the temperature distribution along the x-axis, (b) the temperature contour in the simulation domain at the selected time step.

Figure 8 illustrates the variations of HRR_T , accompanied by the temperature contours of Figure 9, which correspond to the selected time steps of Figure 8. States (a)–(c) describe the ignition process discussed earlier in Section 3.1. Once ignition is completed, the flame starts propagating upstream, from state (c) to state (d). In contrast to the stable mode, the flame front does not stabilize here and continues propagating further towards the inlet, where the wall temperature is not high enough to sustain a flame. Consequently, HRR_T drops to zero and extinction occurs in state (e). With the continuous premixed fuel-air flow at the inlet, the premixture ignites again as observed between states (e) and (f). The flame is then extinguished again, from state (f) to state (h). This repeats periodically. That is, at lower inlet velocities, the flame propagation speed will not be balanced by the inlet velocity, resulting in a flame propagating farther upstream. Because the flame is closer to the inlet, where the wall temperature is not high enough, the heat transfer rates are not balanced, the flame extinguishes, and the FREI phenomenon happens.

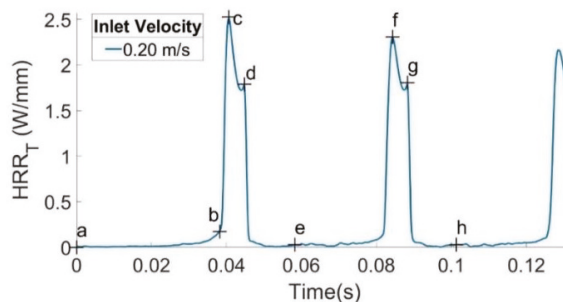


Figure 8. The total heat release rate (HRR_T) vs. time for a flame with FREI mode for mixture A with the inlet velocity of 0.2 m/s. The markers (a) to (h) indicate selected time steps for further explanation of the FREI phenomenon in Figure 9.

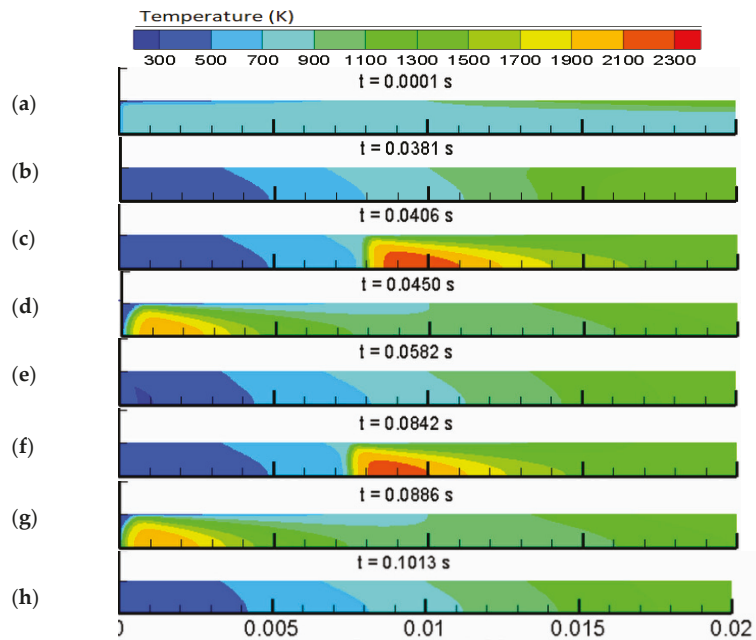


Figure 9. The temperature contours at the selected time steps for a flame with FREI mode for mixture A with the inlet velocity of 0.2 m/s. The length is measured in meters. The snapshots (a)–(h) correspond to the respective markers in Figure 8 for the selected time steps.

3.3. Impacts of Operating Conditions

The aim of the previous Sections 3.1 and 3.2 was to scrutinize the ignition process, in addition to the stable and FREI modes of syngas combustion after ignition, with the corresponding metrics defined and elaborated for a number of the cases selected from the simulation runs performed in this work. A comprehensive and fundamental understanding of how these syngas combustion properties could be altered due to slight variations in the operating conditions will help researchers and industries make more informed decisions before spending time and money on prototypes and tests. In this subsection, these characteristics are analyzed over a range of operating conditions by varying the flow rate and the syngas fuel composition.

Findings from this subsection are essentially important in understanding how changing the fuel composition or the fuel/air mixture flow rate could impact the important combustion properties, such as the ignition time/delay, the ignition location, the flame location, and the flame stability.

3.3.1. Impact of the Flow Rate (Inlet Velocity)

Various inlet velocities, in the range from 0.1 m/s to 3.0 m/s, were used to design a total of eight (8) different cases and characterize the impact of the flow rate on ignition and the flame behavior. The ignition properties, such as the ignition time, the ignition locations, and the ignition length, defined in Section 3.1, were computed for each of these eight cases and are listed in Table 2. It is shown that the ignition time is smaller for the higher inlet velocities, which is attributed to lower residence times for higher velocities (the fuel-air mixture reaches the temperatures, required for autoignition, faster). It should be noted that the ignition times/delays presented in this work are of the order of 10 ms (from 5 to 80 ms), whereas the selected time step in the simulations is 10 μ s, i.e., three orders of magnitude smaller than the ignition times, which makes it sufficiently fine to resolve the ignition time in all cases. In addition, although, to the best of our knowledge, there are no experimental

studies employing the same operating conditions as this work, the ignition times in this work are qualitatively comparable (being of the same order of magnitude) with the syngas ignition delays existing in the literature [47].

Table 2. Ignition metrics against inlet velocity for fuel mixture A.

Inlet Velocity (m/s)	Ignition Time (ms)	Ignition Location (mm)		Ignition Length (mm)
	t_{ig}	x_{ig-st}	x_{ig-e}	Δx_{ig}
0.10	77.14	6.35	9.70	3.35
0.15	52.49	6.45	9.80	3.35
0.20	40.56	7.95	11.60	3.65
0.50	18.96	9.95	13.60	3.65
0.75	13.73	12.00	16.00	4.00
1.00	11.17	12.00	16.80	4.80
1.50	8.32	13.60	19.30	5.70
3.00	5.25	16.00	20.00	4.00

The values of the ignition locations x_{ig-st} and x_{ig-e} indicate that, at higher inlet velocities, the ignition kernel appears further downstream. Moreover, it is shown that the ignition length also correlates with the inlet velocity such that the higher the velocity, the larger the ignition length. Consequently, the mixture requires higher temperatures and reaction areas to ignite at higher inlet velocities.

After completion of the ignition process, the flame behavior and stability were also found to depend on the inlet velocity. The results are presented in Figure 10, which shows a stable flame mode for the intermediate and higher inlet velocities (exceeding 0.2 m/s). For such stable flames, similar to the ignition time, the time required for the flame to stabilize also significantly decreases with the inlet flow velocity. In addition to the stabilization time, the stabilization location and the flame span (x_{sz-st} , x_{sz-e} , Δx_{sz}) were also obtained and compared in Table 3. It is shown that for higher inlet velocities, the stable flame (i) is eventually positioned further away from the inlet, and (ii) has a larger span.

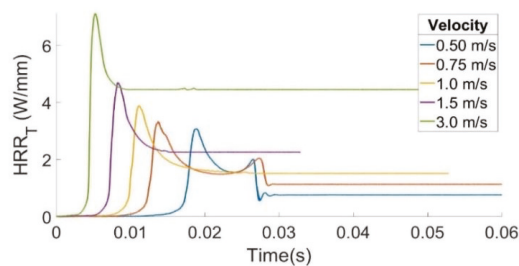


Figure 10. The total heat release rate (HRR_T) vs. time for mixture A with the inlet velocities resulting in a stable mode.

As mentioned previously, in some cases, the flame may not end up in a stable location after ignition is completed. Here, with smaller inlet velocities (≤ 0.2 m/s), the flame experiences a FREI mode. These cases with the FREI mode are further analyzed by comparing their FREI time periods, τ_{FREI} , in Table 4. It is shown that τ_{FREI} remains the same for each given inlet velocity, but diminishes with the reduction in the inlet velocity.

Table 3. The stabilization location for the stable cases for fuel mixture A.

Inlet Velocity (m/s)	Flame Location (mm)		Flame Span (mm)
	x_{sz-st}	x_{sz-e}	Δx_{sz}
0.50	0.10	1.85	1.75
0.75	0.10	2.35	2.25
1.00	4.00	6.25	2.25
1.50	7.05	9.70	2.65
3.00	10.70	15.35	4.65

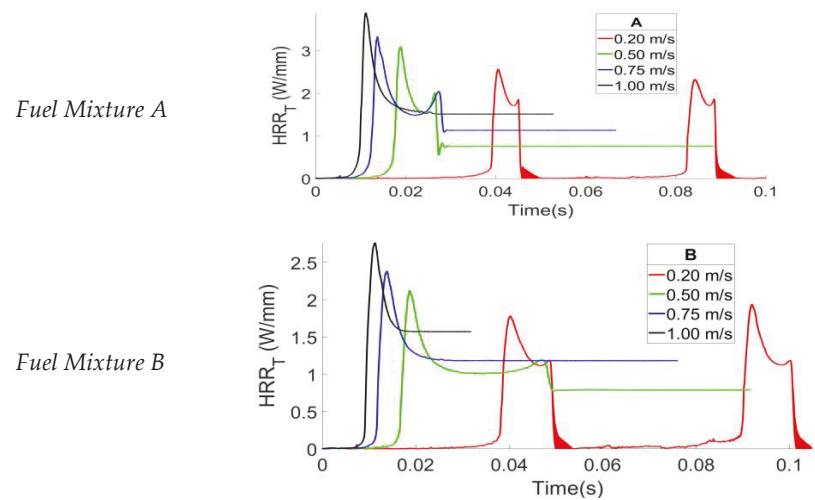
Table 4. The FREI period for the corresponding inlet velocities for fuel mixture A.

Inlet Velocity (m/s)	0.10	0.15	0.20
τ_{FREI} (ms)	82.27	55.93	42.00

3.3.2. Impact of Fuel Composition

In this section, the impact of the syngas mixture composition on the ignition and the flame behavior is analyzed. In particular, three various syngas mixtures of Table 1 are studied over various inlet flow velocities, ranging from 0.2 to 1.0 m/s. Therefore, a total of twelve cases are studied.

Figure 11 presents the time variations of HRR_T for fuel mixtures A, B, and C at various inlet flow velocities, in which both the stable flames and the FREI are observed for the lower inlet velocities for all three mixtures under consideration. As the inlet velocity exceeds 0.2 m/s, the corresponding flame stabilizes. However, the combustion characteristics are found to depend on both the fuel composition and the inlet velocity.

**Figure 11.** Cont.

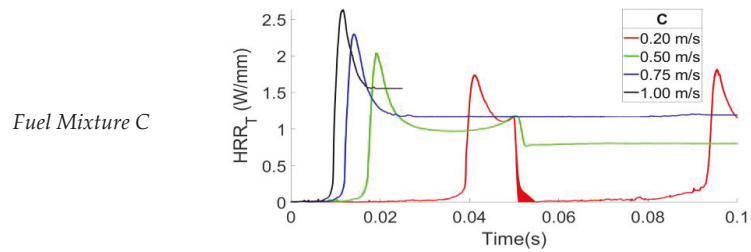


Figure 11. The total heat release rate (HRR_T) vs. time for the syngas mixtures from Table 1 at various inlet velocities.

In general, the ignition time increases as the inlet velocity decreases; see Table 5. Although the ignition time does not vary much between various fuel mixtures, the ignition length is found to be very sensitive to the fuel composition. For example, for any given inlet velocity, the ignition length, Δx_{ig} , is larger for the fuel mixture A compared to that for mixture C, and such a correlation is not observed for mixture B. Similarly, for the ignition location, ignition occurred further from the inlet for the higher inlet velocities in each case, i.e., it occurs at the locus, where the temperature of the unburnt mixture is higher due to the imposed temperature gradient at the wall. The ignition location is further from the inlet for mixtures B and C compared to mixture A.

Table 5. The ignition time and location for all cases.

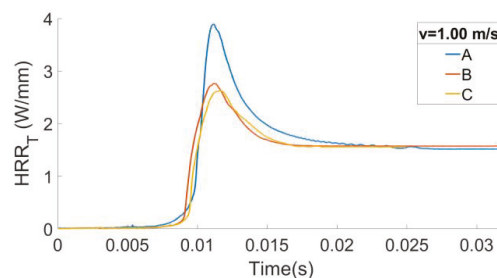
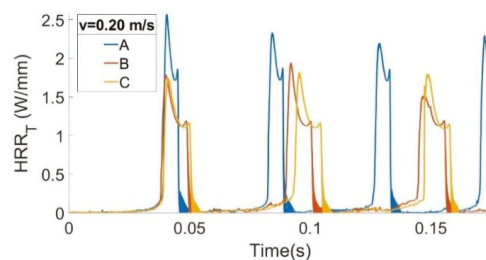
	Velocity (m/s)	t_{ig} (ms)	x_{ig-st} (mm)	x_{ig-e} (mm)	Δx_{ig} (mm)
Mixture A	0.2	40.56	7.95	11.60	3.65
	0.5	18.96	9.95	13.60	3.65
	0.75	13.73	12.00	16.00	4.00
	1.0	11.17	12.00	16.80	4.80
Mixture B	0.2	40.19	8.75	12.20	3.45
	0.5	18.66	11.35	15.50	4.15
	0.75	13.80	12.15	15.80	3.65
	1.0	11.31	12.75	16.80	4.05
Mixture C	0.2	41.20	9.15	12.15	3.00
	0.5	19.15	10.35	13.80	3.45
	0.75	14.15	12.80	16.55	3.75
	1.0	11.65	13.30	17.70	4.40

Table 6 summarizes the combustion characteristics in the cases when the stable flame has been observed. Here, the stable flame locations for these cases are compared in terms of their $x_{(sz-st)}$, which is found to be larger for mixture C compared to the other two mixtures for any given inlet velocity, whereas it is larger for mixture B compared to A. However, the difference between mixtures A and B exceeds that between mixtures B and C. The same tendency is also seen for $x_{(sz-e)}$. Further, for mixture A, in addition to the flame being stabilized closer to the inlet, it is also observed to have a shorter flame span than the other two mixtures for any given inlet velocity. The fact that these combustion metrics of mixture A differ substantially from those of mixtures B and C, while the difference between the combustion characteristics of mixtures B and C is less profound, is attributed to the higher percentage of H_2 in mixture A, which plays a major role in controlling the stable flame location and length.

Table 6. The location of the stabilized flame.

	Velocity (m/s)	x_{sz-st} (mm)	x_{sz-e} (mm)	Δx_{sz} (mm)
Mixture A	0.5	0.10	1.85	1.75
	0.75	0.10	2.35	2.25
	1.0	4.00	6.25	2.25
Mixture B	0.5	0.10	2.20	2.10
	0.75	7.15	9.40	2.25
	1.0	9.15	11.60	2.45
Mixture C	0.5	0.10	2.20	2.10
	0.75	7.50	9.65	2.15
	1.0	9.50	12.00	2.50

To further study the impact of syngas composition on the flame behavior, the quantities HRR_T are compared for all three mixtures at two inlet velocities. First, we chose the inlet velocity of 1.0 m/s, where all three mixtures resulted in stable flames, see Figure 12. Here, mixture A (containing 65% of H_2) provides the largest HRR_T peak compared to the other two mixtures, thereby showing the high energy density of H_2 . In addition, it took longer for the flame to be stabilized for mixture A compared to mixtures B and C. Second, we chose the inlet velocity of 0.2 m/s, where the FREI phenomenon was observed for all three mixtures, see Figure 13. Specifically, the time evolution of HRR_T is depicted in Figure 13 for mixtures A, B, and C, thereby representing the unstable cases, in which each ignition is followed by the extinction, in a repetitive manner.

**Figure 12.** The total heat release rate (HRR_T) vs. time for the stable flame cases with the inlet velocity of 1.0 m/s.**Figure 13.** The total heat release rate (HRR_T) vs. time for the FREI cases with the inlet velocity of 0.2 m/s.

These repetitive ignition times are given in Table 7 for all cases. Here, t_{ig-x} represents the x^{th} ignition time, and $t_{ig-y,x}$ represents the difference between the y^{th} and x^{th} ignition

times. It is observed that the consecutive ignition time remains almost the same for each case, with a slight discrepancy that can be attributed to numerical artifacts. However, the FREI cases for mixture A show a higher maximum heat release rate compared to those of mixtures B and C, which can be attributed to a higher hydrogen composition in mixture A because H_2 possesses higher energy density. Similarly, it is seen that τ_{FREI} is smaller for mixture A. Thus, the burning process of mixture A can be regarded as an oscillating flame. However, τ_{FREI} increases for mixture B by 2.0 ms, whereas for mixture C, τ_{FREI} decreases by 2.0 ms, which cannot be ignored. As we know, mixture C differs from the other two mixtures in terms of the CO percentage (i.e., it has almost twice the amount of the other two). Thus, we can suggest that this significantly higher percentage of CO in mixture C reduces τ_{FREI} , causing the FREI incident to occur more quickly. Among the two mixtures having the same CO percentage (A and B), mixture B has a higher percentage of CH_4 and a lower percentage of H_2 ; thus, for mixture B, τ_{FREI} is observed to be larger by 2.0 ms. A similar trend can be seen when comparing mixtures C and A. It is observed that although CH_4 and H_2 are the main driving forces to generate the FREI behavior, a CO fraction in the fuel mixture plays an important role in controlling the FREI frequency.

Table 7. Ignition time for the FREI cases given in Figure 13.

	t_{ig-1} (ms)	t_{ig-2} (ms)	t_{ig-3} (ms)	$\Delta t_{ig-2,1}$ (ms)	$\Delta t_{ig-3,2}$ (ms)
Mixture A	40.4	84.3	128.6	43.9	44.3
Mixture B	40.2	92.0	146.5	51.8	54.5
Mixture C	41.3	95.6	148.2	54.3	52.6

4. Conclusions

In this work, microscale combustion of syngas mixtures was studied, computationally, with the use of detailed chemical kinetics. The key agent of conjugate wall heat loss, which is inherent to microscale combustion, was addressed by imposing a temperature gradient on the wall, which also preheated the fuel mixture. The flame dynamics and other combustion characteristics at microscales were studied for various inlet flow velocities (ranging from 0.1 to 3.0 m/s) and syngas compositions (mixture A: 30% CO, 5% CH_4 , and 65% H_2 ; mixture B: 70% CO, 5% CH_4 , and 25% H_2 ; and mixture C: 60% CO, 10% CH_4 , and 30% of H_2). Two different phenomena—the stable flames and the FREI—were observed with respect to the inlet velocities, such that for high inlet velocities ranging from 0.5 to 3.0 m/s, the flame was stable, whereas for the velocity range from 0.1 to 0.2 m/s, the flame became unstable and the FREI was observed. The ignition time, ignition location, and ignition length were analyzed for each case, and the stabilization characteristics, such as the stabilized flame location for the stable flames, were scrutinized. The ignition time and location, in addition to the stabilized flame location, where maximum domain temperatures are expected, are significantly important factors in designing micro-combustion-related technologies with syngas as a fuel. In particular, conjugate heat transfer/heat losses play an important role in micro-combustion devices, in which the ratio of the surface area to the volume is relatively higher than that of the conventional combustion devices. Further, the FREI properties were calculated and compared for the unstable cases. Regarding the fuel mixture composition, in the stable cases, mixture A showed more variations in terms of the total heat release, stabilization time, flame location, and flame span compared to those in mixtures B and C. Similarly, for the unstable cases, the time difference between the consecutive ignitions varied for all of the cases. Mixture A, which had a higher percentage of H_2 , was found to have a higher total heat release in the domain, and significantly different characteristics compared to the other two mixtures. This corroborates the major role and dominance of an H_2 fraction in syngas combustion. Similarly, the effect of CO can be projected in the FREI mode for mixtures B and C in terms of the FREI period (τ_{FREI}). From a practical perspective, because syngas is generated from a variety of sources and methodologies, and can consist of different species of a wide range of concentrations, the

findings of this work are critically important in selecting the appropriate composition of syngas depending on the application.

This research can be further extended in the following directions:

- (a) to conduct in situ experiments for the operating conditions used in this work;
- (b) to study the impact of the equivalence ratio on the flame behavior and instabilities;
- (c) to consider 3D geometries and compare the results with those from 2D simulations; and
- (d) to study the geometrical impacts on syngas combustion at microscales, while undertaking both experimental and numerical analyses over different geometries.

Author Contributions: Conceptualization, M.A. and V.A.; Data curation, S.P., M.A. and V.A.; Formal analysis, S.P., M.A. and V.A.; Funding acquisition, S.P., M.A. and V.A.; Investigation, S.P., M.A. and V.A.; Methodology, S.P., M.A. and V.A.; Project administration, M.A. and V.A.; Resources, V.A.; Software, S.P.; Supervision, M.A. and V.A.; Validation, S.P. and M.A.; Visualization, S.P.; Writing—original draft, S.P.; Writing—review & editing, M.A. and V.A. All authors have read and agreed to the published version of the manuscript.

Funding: The work at West Virginia University was supported by the National Science Foundation (NSF), through CAREER Award #1554254 (V.A.), as well as by West Virginia Higher Education Policy Commission, through Grant #HEPC.dsr.18.7 (V.A.). Wayne State University’s Research reported in this publication was supported in part by funding provided by the National Aeronautics and Space Administration (NASA), under award number 80NSSC20M0124, Michigan Space Grant Consortium (MSGC).

Institutional Review Board Statement: Not applicable.

Informed Consent Statement: Not applicable.

Data Availability Statement: The data presented in this study are available on request from the corresponding author.

Conflicts of Interest: The authors declare no conflict of interest.

References

1. Chen, W.L.; Huang, C.W.; Li, Y.-H.; Kao, C.-C.; Cong, H.T. Biosyngas-fueled platinum reactor applied in micro combined heat and power system with a thermophotovoltaic array and Stirling engine. *Energy* **2020**, *194*, 116862. [\[CrossRef\]](#)
2. Yang, W.M.; Chou, S.K.; Shu, C.; Xue, H.; Li, Z.W.; Li, D.T.; Pan, J.F. Microscale combustion research for application to micro thermophotovoltaic systems. *Energy Convers. Manag.* **2003**, *44*, 2625–2634. [\[CrossRef\]](#)
3. Fernandez-Pello, A. Micropower generation using combustion: Issues and approaches. *Proc. Combust. Inst.* **2002**, *29*, 883–899. [\[CrossRef\]](#)
4. Kaisare, N.; Vlachos, D. A review on microcombustion: Fundamentals, devices and applications. *Prog. Energy Combust. Sci.* **2012**, *38*, 321–359. [\[CrossRef\]](#)
5. Walther, D.C.; Ahn, J. Advances and challenges in the development of power-generation systems at small scales. *Prog. Energy Combust. Sci.* **2011**, *37*, 583–610. [\[CrossRef\]](#)
6. Ju, Y.; Maruta, K. Microscale combustion: Technology development and fundamental research. *Prog. Energy Combust. Sci.* **2011**, *37*, 669–715. [\[CrossRef\]](#)
7. Wang, Z.; Bai, Z.; Yu, G.; Yelishala, S.; Metghalchi, H. The critical pressure at the onset of flame instability of syngas/air/diluent outwardly expanding flame at different initial temperatures and pressures. *J. Energy Resour. Technol.* **2019**, *141*, 082207. [\[CrossRef\]](#)
8. Ali, K.; Kim, C.; Lee, Y.; Oh, S.; Kim, K. A Numerical study to investigate the effect of syngas composition and compression ratio on the combustion and emission characteristics of a syngas-fueled HCCI engine. *J. Energy Resour. Technol.* **2020**, *142*, 092301. [\[CrossRef\]](#)
9. Islam, S.; Dincer, I. A comparative study of syngas production from two types of biomass feedstocks with waste heat recovery. *J. Energy Resour. Technol.* **2018**, *140*, 092002. [\[CrossRef\]](#)
10. Al-Zareer, M.; Dincer, I.; Rosen, M.A. Influence of selected gasification parameters on syngas composition from biomass gasification. *J. Energy Resour. Technol.* **2018**, *140*, 041803. [\[CrossRef\]](#)
11. Liu, X.; Burra KR, G.; Wang, Z.; Li, J.; Che, D.; Gupta, A.K. Syngas characteristics from catalytic gasification of polystyrene and pinewood in CO₂ atmosphere. *J. Energy Resour. Technol.* **2021**, *143*, 052304. [\[CrossRef\]](#)
12. Ayoobi, M.; Schoegl, I. Non-catalytic conversion of glycerol to syngas at intermediate temperatures: Numerical methods with detailed chemistry. *Fuel* **2017**, *195*, 190–200. [\[CrossRef\]](#)
13. Othman, N.F.; Boosroh, M.H. Effect of H₂ and CO contents in syngas during combustion using Micro Gas Turbine. In *IOP Conference Series: Earth and Environmental Science*; IOP Publishing: Bristol, UK, 2016; Volume 32.

14. Pio, G.; Ricca, A.; Palma, V.; Salzano, E. Experimental and numerical evaluation of low-temperature combustion of bio-syngas. *Int. J. Hydrog. Energy* **2020**, *45*, 1084–1095. [CrossRef]
15. Salzano, E.; Basco, A.; Cammarota, F.; Di Sarli, V.; Di Benedetto, A. Explosions of Syngas/CO₂ mixtures in oxygen-enriched air. *Ind. Eng. Chem. Res.* **2012**, *51*, 7671–7678. [CrossRef]
16. Xie, Y.; Wang, J.; Cai, X.; Huang, Z. Pressure history in the explosion of moist syngas/air mixtures. *Fuel* **2016**, *185*, 18–25. [CrossRef]
17. Sun, Z.Y. Laminar explosion properties of syngas. *Combust. Sci. Technol.* **2018**, *192*, 166–181. [CrossRef]
18. Mardani, A.; Mahalegi HK, M. Hydrogen enrichment of methane and syngas for MILD combustion. *Int. J. Hydrog. Energy* **2019**, *44*, 9423–9437. [CrossRef]
19. Zhang, K.; Jiang, X. Uncertainty quantification of fuel variability effects on high hydrogen content syngas combustion. *Fuel* **2019**, *257*, 116111. [CrossRef]
20. Dam, B.; Ardha, V.; Choudhuri, A. Laminar flame velocity of syngas fuels. *J. Energy Resour. Technol.* **2010**, *132*, 044501. [CrossRef]
21. Monteiro, E.; Rouboa, A. Measurements of the laminar burning velocities for typical syngas-air mixtures at elevated pressures. *J. Energy Resour. Technol.* **2011**, *133*, 031002. [CrossRef]
22. Wei, L.; Pordesimo, L.O.; Filip To, S.D.; Herndon, C.W.; Batchelor, W.D. Evaluation of micro-scale syngas production costs through modeling. *Trans. ASABE* **2009**, *52*, 1649–1659. [CrossRef]
23. Maruta, K.; Kataoka, T.; Kim, N.; Minaev, S.; Fursenko, R. Characteristics of combustion in a narrow channel with a temperature gradient. *Proc. Combust. Inst.* **2005**, *30*, 2429–2436. [CrossRef]
24. Brambilla, A.; Schultze, M.; Frouzakis, C.E.; Mantzaras, J.; Bombach, R.; Boulouchos, K. An experimental and numerical investigation of premixed syngas combustion dynamics in mesoscale channels with controlled wall temperature profiles. *Proc. Combust. Inst.* **2015**, *35*, 3429–3437. [CrossRef]
25. Resende, P.R.; Ayoobi, M.; Afonso, A. Numerical investigations of micro-scale diffusion combustion: A Brief Review. *Appl. Sci.* **2019**, *9*, 3356. [CrossRef]
26. Akkerman, V.; Bychkov, V.; Petchenko, A.; Eriksson, L.-E. Flame oscillations in tubes with nonslip at the walls. *Combust. Flame* **2006**, *145*, 675–687. [CrossRef]
27. Ayoobi, M.; Schoegl, I. Numerical analysis of flame instabilities in narrow channels: Laminar premixed methane/air combustion. *Int. J. Spray Combust. Dyn.* **2017**, *9*, 155–171. [CrossRef]
28. Resende, P.R.; Afonso, A.; Pinho, C.; and Ayoobi, M. Impacts of Dilution on Hydrogen Combustion Characteristics and NO_x Emissions. *ASME. J. Heat Transfer* **2019**, *141*, 012003. [CrossRef]
29. Zhang, Z.; Wu, K.; Yao, W.; Yuen, R.; Wang, J. Enhancement of combustion performance in a microchannel: Synergistic effects of bluff-body and cavity. *Fuel* **2020**, *265*, 116940. [CrossRef]
30. Malushte, M.; Kumar, S. Flame dynamics in a stepped micro-combustor for non-adiabatic wall conditions. *Therm. Sci. Eng. Prog.* **2019**, *13*, 100394. [CrossRef]
31. Pizza, G.; Frouzakis, C.E.; Mantzaras, J.; Tomboulides, A.G.; Boulouchos, K. Dynamics of premixed hydrogen/air flames in microchannels. *Combust. Flame* **2008**, *152*, 433–450. [CrossRef]
32. Kim, N.; Maruta, K. A numerical study on propagation of premixed flames in small tubes. *Combust. Flame* **2006**, *146*, 283–301. [CrossRef]
33. Norton, D.G.; Vlachos, D.G. Combustion characteristics and flame stability at the microscale: A CFD study of premixed methane/air mixtures. *Chem. Eng. Sci.* **2003**, *58*, 4871–4882. [CrossRef]
34. Munir, F.A.; Mikami, M. A numerical study of propane-air combustion in meso-scale tube combustors with concentric rings. *J. Therm. Sci. Technol.* **2015**, *10*, JTST0008. [CrossRef]
35. Konakov, S.A.; Dzyubanenko, S.V.; Krzhizhanovskaya, V.V. Computer simulation approach in development of propane-air combustor microreactor. *Procedia Comput. Sci.* **2016**, *101*, 76–85. [CrossRef]
36. Wang, W.; Zuo, Z.; Liu, J. Experimental study and numerical analysis of the scaling effect on the flame stabilization of propane/air mixture in the micro-scale porous combustor. *Energy* **2019**, *174*, 509–518. [CrossRef]
37. Takbiri-Borujeni, A.; Ayoobi, M. Application of physics-based machine learning in combustion modeling. In Proceedings of the 11th US National Combustion Meeting, Pasadena, CA, USA, 24–27 March 2019.
38. Pokharel, S.; Ayoobi, M.; Akkerman, V. Characterizing premixed syngas combustion and flame dynamics in micro scales. In Proceedings of the 2020 28th Conference on Nuclear Engineering Joint with the ASME 2020 Power Conference ICONE28-POWER2020, Virtual Conference, 4–5 August 2020; pp. 1–7. Available online: <https://event.asme.org/POWER-2020> (accessed on 10 July 2021).
39. Kousheshi, N.; Yari, M.; Paykani, A.; Mehr, A.S.; de la Fuente, G.F. Effect of syngas composition on the combustion and emissions characteristics of a syngas/diesel RCCI engine. *Energies* **2020**, *13*, 212. [CrossRef]
40. Chuahy, F.D.F.; Kokjohn, S.L. High efficiency dual-fuel combustion through thermochemical recovery and diesel reforming. *Appl. Energy* **2017**, *195*, 503–522. [CrossRef]
41. Maruta, K.; Parc, J.K.; Oh, K.C.; Fujimori, T.; Minaev, S.S.; Fursenko, R.V. Characteristics of microscale combustion in a narrow heated channel. *Combust. Explos. Shock Waves* **2004**, *40*, 516–523. [CrossRef]
42. Baumgardner, M.E. Microreactor combustion of simple hydrocarbons. In Proceedings of the 11th U.S. National Combustion Meeting, Pasadena, CA, USA, 24–27 March 2019.

43. Di Stazio, A.; Chauveau, C.; Dayma, G.; Dagaut, P. Oscillating flames in micro-combustion. *Combust. Flame* **2016**, *167*, 392–394. [[CrossRef](#)]
44. Di Stazio, A.; Chauveau, C.; Dayma, G.; Dagaut, P. Pulsating combustion of ethylene in micro-channels with controlled temperature gradient. In *Combustion Science and Technology*; Taylor & Francis: Abingdon, UK, 2018; pp. 1–11.
45. Chemical-Kinetic Mechanisms for Combustion Applications, San Diego Mechanism, Mechanical and Aerospace Engineering (Combustion Research), University of California at San Diego. Available online: <http://combustion.ucsd.edu> (accessed on 10 July 2021).
46. ANSYS Fluent [online]. Available online: <https://www.ansys.com/products/fluids/ansys-fluent> (accessed on 10 July 2021).
47. Lee, H.C.; Jiang, L.Y.; Mohamad, A.A. A review on the laminar flame speed and ignition delay time of Syngas mixtures. *Int. J. Hydrog. Energy* **2014**, *39*, 1105–1121. [[CrossRef](#)]

Article

Numerical and Experimental Study of a Jet-and-Recirculation Stabilized Low Calorific Combustor for a Hybrid Power Plant

Felix Grimm *, Timo Lingstädt, Peter Kutne and Manfred Aigner

German Aerospace Center (DLR), Pfaffenwaldring 38-40, 70569 Stuttgart, Germany; timo.lingstaedt@dlr.de (T.L.); peter.kutne@dlr.de (P.K.); manfred.aigner@dlr.de (M.A.)

* Correspondence: felix.grimm@dlr.de

Abstract: An atmospheric prototype burner is studied with numerical and experimental tools. The burner system is designed for operation in a hybrid power plant for decentralized energy conversion. In order to realize such a coupled system, a reliable combustion system has to be established. Numerical and experimental findings in the presented study demonstrate the capabilities of the novel burner system in suitable operation conditions. In this system, a solid oxide fuel cell (SOFC) is mounted upstream of the burner in the gas turbine system. The combination of both realizes a large operational flexibility with comparably high overall efficiency. Since the combustor is operated with SOFC off-gas, several challenges arise. Low calorific combustion needs careful burner design and numerical modeling, since the heat-loss mechanisms occur to be in the order of magnitude of thermal power output. Thus, different modeling strategies are discussed in the paper. The numerical studies are compared with experimental results and high-quality simulation results complement limited measured findings with easy-to-use low fidelity RANS models. A priori measurements are employed for the selection of investigation points. It is shown that the presented combustor system is able to cover low-calorific combustion over a large range of operation conditions, despite major heat-loss effects, which are characterized by means of numerical CFD (Computational Fluid Dynamics) modeling.

Citation: Grimm, F.; Lingstädt, T.; Kutne, P.; Aigner, M. Numerical and Experimental Study of a Jet-and-Recirculation Stabilized Low Calorific Combustor for a Hybrid Power Plant. *Energies* **2021**, *14*, 537. <https://doi.org/10.3390/en14030537>

Keywords: jet-and-recirculation stabilized combustion; OH* measurements; numerical CFD analysis; RANS modeling; detailed chemistry schemes; heat-loss modeling; low-calorific combustion; syngas fuel

Academic Editor: Alexandre M. Afonso, Pedro Resende and Mohsen Ayooobi

Received: 17 December 2020

Accepted: 15 January 2021

Published: 21 January 2021

Publisher's Note: MDPI stays neutral with regard to jurisdictional claims in published maps and institutional affiliations.



Copyright: © 2021 by the authors. Licensee MDPI, Basel, Switzerland. This article is an open access article distributed under the terms and conditions of the Creative Commons Attribution (CC BY) license (<https://creativecommons.org/licenses/by/4.0/>).

1. Introduction

In the present study a novel FLOX[®] burner system (FLOX: Flameless Oxidation) is analyzed by means of experimental and numerical diagnostics. The most distinct characteristic of this burner system is the ability to run with very low calorific fuels near lean blow off. Low fuel energy content gives rise to operational difficulties of the burner system, since especially heat loss mechanisms play a more important role and have to be carefully assessed in burner design.

This particular burner was developed to serve as a combustor in a hybrid power plant cycle, with a solid oxide fuel cell (SOFC) that is placed upstream. It features a comparably steady state flow field with stable and locally restricted combustion and is therefore highly suitable for energy related applications, where the low emissions are required. Combined SOFC/GT (GT: Gas Turbine) concepts are promising, since due to combined power generation and heat extraction, they are highly efficient energy systems. They are capable of achieving similar or higher efficiencies compared to conventional gas and vapor cycles. Electrical efficiencies of hybrid systems are usually in the range of $\eta_{el} \in [45\%; 75\%]$ at a power range of 0.01MW to 100 MW [1–5].

The SOFC/MGT (MGT: Micro gas turbine) hybrid power plant in the actual context has been built and is being investigated at the German Aerospace Center (DLR) [6]. In the coupled facility, an SOFC is placed into a standard micro gas turbine cycle before

actual combustion. This stands in contrast to hybrid SOFC systems as reported in the literature, where only few works are given. Approaches are mainly based on non-premixed combustion with catalytic support [7–13] or reforming processes [14–18].

In this work, prior to operation in the actual machine, the burner system is isolated and investigated in an optically accessible atmospheric test stand. There, optical measurements can be applied in order to characterize the burner and validate numerical methods. The burner at hand is coupled with an SOFC emulator [19]. This, the so called super-heated steam generator mimics the exhaust properties of an actual SOFC. Thus, the burner system has to function with low calorific fuel, since it operates with fuel cell off-gas. Combustion stability at part load condition is ensured by natural gas addition. This emulation of the SOFC ensures virtual coupling that was established before the actual coupling in the hybrid power plant rig.

The hybrid power plant demonstrator is required to provide operational flexibility. The burner system investigated in this work therefore has to fulfill certain requirements. A large operational range has to be covered, from SOFC off-gas usage to usual micro gas turbine operation. The jet-and-recirculation-stabilization based burner, which is investigated here, stems from a family of burner systems known as FLOX[®] and is particularly suited for this purpose.

The FLOX[®] burner systems can be placed in the MILD (Moderate or Intense Low-Oxygen Dilution) regime. They first appeared for a furnace application [20,21], where homogeneous temperature distribution is a major requirement. However, during the later adaptations those burner system featured more and more discrete flames and therefore the term jet-and-recirculation stabilized combustion is more suitable. Still, homogeneous temperature distribution with comparably low peak temperatures are achieved.

The fuel is induced into the combustor in a co-flow alignment. This is usually followed by a short air and fuel mixing section leading to partially premixed combustion. Circumferentially aligned jet nozzles with the air-fuel mixture induce a large axial momentum and therefore a prominent inner recirculation region develops that leads to hot-gas re-transport to the reaction zones. This enhances combustion stability and contributes to homogeneous combustor temperatures. As a consequence, jet-and-recirculation stabilized burner systems usually show a wide operational range and low emissions [22,23]. Circumferentially aligned jets with high momentum furthermore ensure a low risk of flame flashback and makes this burner technology a promising application for hydrogen combustion and synthetic fuels [24,25].

Consecutively, jet-and-recirculation stabilized burners were combined with swirl-stabilized staging, for further extension of operational range, depending on the respective application [26–28]. The burner concept has undergone many adaptations, mainly for energy applications and even fundamental investigations [29–33] in pressurized combustion in order to analyze the flame stabilization and emissions formation mechanisms with elaborate measurement techniques have been carried out. Combustion dynamics and thermoacoustic phenomena were analyzed by means of experiments [34] and numerics [35], only to name a few. A later adaption in view of possible aero-engine applications was the transition to liquid fuel operation [36–38]. Explicit developments for aero-engine applications are subject to on-going studies [39].

More recent variants of jet-and-recirculation stabilized burner systems are located in the micro gas turbine sub-MW power range, e.g., for combination with gasification processes [40–42] or single and multiple household energy applications with conventional fuels [43–45].

The low-calorific burner system at hand has twelve circumferentially aligned nozzles [19]. Main design criteria were a low pressure loss with at the same time large operational flexibility and combustion stability.

The combustion system has been optimized and further developed by Lingstädt et al. [46–49]. Therefore, several aspects of the system development can be found in the literature. In the present work, this is concentrated to major findings and combined with

an elaborated CFD study that allows for the quantification of heat-loss, which has not been carried out for preceding burner developments and therefore provides grounds for future machine-integration design of the low-calorific burner system. Furthermore, CFD temperature distributions are compared with measurements of pointwise combustor temperatures.

As mentioned previously, hybrid power plants of fuel cells combined with gas turbine systems have the opportunity to provide electricity and heat at comparably high efficiencies. There, combustor development and investigation is a key factor. In the presented work this is addressed with careful and detailed numerical and experimental investigation. It was shown [46] that the burner system at hand is also able to process higher calorific fuel and therefore is a multi-fuel burner, potentially saving costs and combining several burner systems in one. It features low emissions and stable combustion over a large operational range. This is demonstrated for the low-calorific end in the presented paper.

Furthermore, to the authors' knowledge, combinations of fuel cells with gas turbine systems are extremely rare in the literature. So the presented concept poses a promising energy conversion solution at high efficiencies. It is thoroughly examined with numerical modeling and highly consistent experimental findings. The comprehensive study of schemes with the incorporation of heat loss mechanisms underlines the importance of careful modeling, the less energy content is present in the fuel. The presented studies are therefore beneficial for other works and raise awareness for the required conscientiousness in combustion modeling under low-calorific conditions.

The structure of the paper is as follows: First, the combustion system operating at low-calorific conditions is introduced and the measurement setup is explained. This is followed by a choice of investigated reference operation points based on carbon monoxide emissions measurements. Subsequently, numerical setups are introduced and the approach for estimation of heat transfer coefficients is elaborated. Results are first discussed based on a reference case at nominal load for the lowest CO emissions, where the order of magnitude of a system heat loss is elaborated from numerical findings. Finally, a case study for all the investigation points is carried out and experimental results are supported by numerical simulations in terms of averaged flow field and temperature distribution. This is accompanied by comparison of point-wise temperatures in the combustor from measurements. Opposition of numerical results with experimental findings demonstrates feasibility of the pursued approach. All the numerical CFD simulations shown are based on steady state RANS modeling with detailed chemistry approaches.

2. Materials and Methods

In the preceding section, the burner system that is investigated in this work was placed into context of a hybrid power plant. In order to be able to conduct structured atmospheric experiments that depict realistic conditions, several specifics have to be taken into consideration for a test stand. Therefore, the test stand setup for low-calorific combustion analysis is elaborated in the following. Atmospheric tests are carried out prior to actual machine integrated performance studies, due to optical access, therefore the possibility of methodical assessment of the system, and lower cost of atmospheric testing is used. Furthermore, numerical simulation approaches are introduced.

2.1. The Low-Calorific Burner System

The burner system, namely F20OG.1, is shown in Figure 1. "F" denotes FLOX similar design, the number 20 relates to the order of magnitude of thermal load and "OG" indicates operation with SOFC Off Gas. The last number simply labels the development version of the burner system.

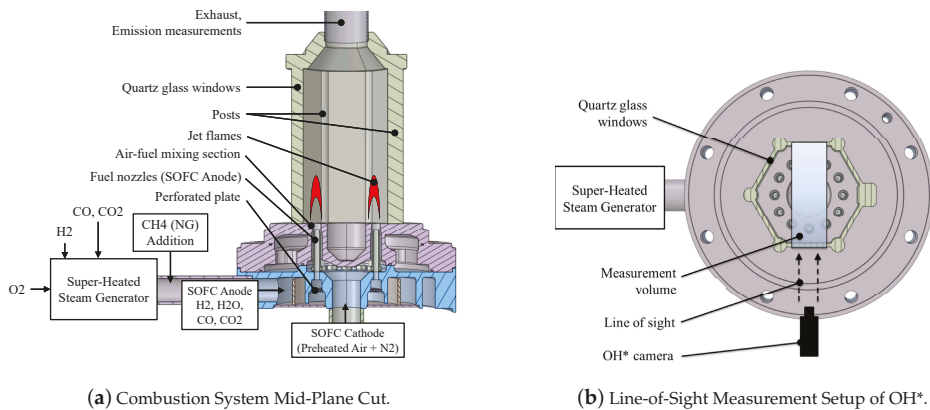


Figure 1. The low-calorific burner system, F20OG.1, with upstream heat generator system (solid oxide fuel cell (SOFC) emulator), combustion chamber components, and measurement techniques [48].

In the context of this work, atmospheric tests are the choice of analysis, since they provide optical access at low running costs and therefore allow for a thorough analysis of the system. As stated earlier, the solid oxide fuel cell is imitated by an auxiliary upstream H₂/O₂ burner. It is operated in a way that it mimics anode gas compositions and temperatures as would be present with a real fuel cell in the power plant rig.

Besides the delivery of H₂O content on the anode side, CO and CO₂ are injected downstream of the super-heated steam generator. Additionally, in certain part load conditions, natural gas is introduced after the auxiliary burner to ensure reliable and stable combustion. Fuel heating values are particularly low in part load mode. The resulting gas stream from the auxiliary system is the combustor input from the anode side, as indicated in Figure 1a. It is led to the optically accessible chamber via twelve nozzles in circumferential alignment. In a standard atmospheric test rig, this would be labeled the fuel stream.

The cathode side consists of oxygen-depleted but preheated air. This is achieved by N₂ addition to air under atmospheric conditions. The cathode flow stream is led to combustion via an upstream plenum to a co-flow alignment around the fuel jets. As stated previously, this leads to a partially premixed combustion regime due to a short mixing section, labeled Air-fuel mixing section in Figure 1a. Consequently, lifted-off reaction zones are present in the combustion chamber over each axially aligned nozzle.

In the present study, the burner system is characterized via certain reference conditions. Their choice is based on exhaust gas emissions measurements with carbon-monoxide as the main criterion. Measurement of NO_x in the off-gas poses major challenges with prevailing high water contents after combustion. However, measurement attempts indicated that NO_x emissions are in the single digit order of magnitude, referring to parts per million at dry conditions. At off-gas combustion conditions, low adiabatic flame temperatures are present, so that thermal NO_x plays a subordinate role. A measurement device is installed in the center of the downstream exhaust duct following the combustion chamber. It records averaged CO emissions in a discrete point.

Optical measurements characterizing the flame locations and spatial extensions are based on OH* chemiluminescence. Averaged radical OH* emission profiles are then used for validation of numerical results. Details and specifications on the measurement techniques can be found in the literature [46,47].

OH* chemiluminescence is a line-of-sight measurement technique. In the current combustor it is set up in a way that it covers the range of a rectangular corresponding with the size of one of the quartz-glass windows. Measurement setup alignment is displayed in Figure 1. Since it is a line-of-sight method, OH* signals are recorded and averaged

over three front flames and three corresponding rear flames that are in-line with the front flames due to the annular alignment of the jet flames. Therefore, the OH* results shown here display six flames in total, where the two flames are in line of sight, respectively. The numerical studies are evaluated accordingly.

2.2. Reference Operating Conditions

The combustion system has to be capable of undergoing a large range of operation in the context of the power plant setup. Therefore, striking operation conditions have to be picked for further analysis, in order to cover the full characteristics of the system. This is done by means of CO exhaust gas emissions measurements. The choice of investigated operation conditions is emphasized in Figure 2, where emissions are displayed over the air fuel equivalence ratio.

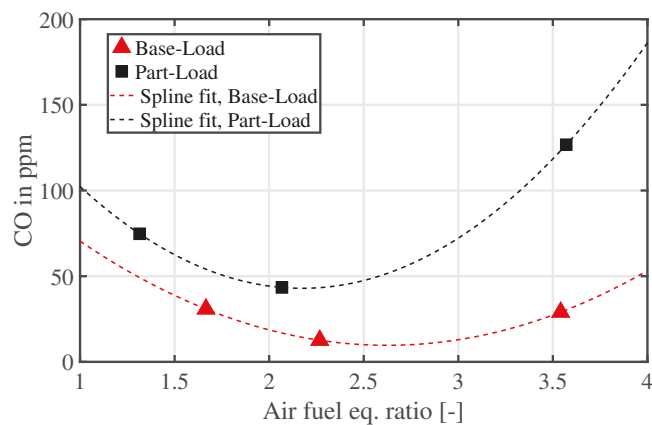


Figure 2. Investigated reference operation conditions normalized to 15% oxygen content [48] from exhaust gas emission measurements. Base-load fit: $CO = 23\lambda^2 - 121\lambda + C_1$, with $C_1 = 168.33$. Part-load fit: $CO = 43\lambda^2 - 187\lambda + C_2$, with $C_2 = 246.4$.

According to Figure 2, the respective base-load and part-load points are labeled as “lean”, “optimum” and “rich” with respect to their global air fuel ratio $\lambda = 1/\Phi$. Φ denotes global equivalence ratio. The reference case is defined at near-optimum conditions w.r.t. CO emissions. The burner is operated with SOFC off-gas and therefore at extremely low calorific conditions. The reference case thermal load is about $P_{th} = 4$ kW. Adiabatic flame temperatures of the base-load cases are in the range of 1500 K to 1650 K. Due to the upstream SOFC, pre-heating temperatures are of the order of magnitude of 1000 K. Therefore, combustion itself realizes temperature deltas in the order of magnitude of $\Delta T \approx 600$ K.

The fuel consists of H_2 , H_2O , CO_2 and CO. The oxidizer is nitrogen-diluted air, with mass fractions $Y_{O_2} \approx 0.17$ and $Y_{N_2} \approx 0.83$. In this application, the oxidizer is oxygen-depleted air, as would be present for the cathode-side of the fuel cell output. The categories base-load and part-load refer to power plant operation at full rotational shaft-speed and 70% fraction, respectively. The rotational shaft speed of the system operation is limited to 240 krpm at base- or full-load.

For this particular case of operation with SOFC off-gas, the inlet conditions are rather complex, therefore an overview on operation conditions for the respective cases is given in Table 1. Estimated temperature deltas due to combustion are evaluated from Cantera simulations and reflect the low energy content of the off-gas fuel. Since part-load cases are close to lean blow-off, a small amount of methane is added to the fuel after the super heated steam generator in part-load mode for combustion stabilization.

Table 1. Combustion system operation conditions in the context of post-SOFC alignment. Y_i : Mass fractions of fuel composition, $\sum Y_i = 1$. $T_{in,a,c}$: Inlet temperatures of anode (fuel) and cathode (air). T_{ad} : Adiabatic flame temperature, ΔT : Expected temperature capacity by combustion. Values were measured in the test rig. Measurement uncertainties in Table 3.

Operation Point	$T_{in,a}$ [K]	$T_{in,c}$ [K]	Y_{H_2} [%]	Y_{H_2O} [%]	Y_{CO_2} [%]	λ [-]	T_{ad} [K]	ΔT [K]
Base-load								
Lean	797.3	1113.8	1.507	39.47	49.44	3.54	1490.7	446.4
Near Optimum	806.8	1119.6	1.509	39.68	49.67	2.27	1606.5	583.3
Rich	803.3	1126.1	1.511	39.88	49.69	1.67	1685.8	681.9
Part-load								
Lean	879.5	1122.7	0.892	41.88	51.82	3.57	1401.3	337.0
Near Optimum	866.3	1128.3	0.887	41.83	51.82	2.07	1501.2	465.5
Rich	856.7	1137.4	0.889	41.83	51.83	1.31	1583.3	575.6

2.3. Numerical Modeling

Numerical simulations are carried out with two major objectives. Foremost, experimental data is limited to exhaust gas emissions and flame location by OH^* chemiluminescence analysis. Therefore, numerical results are validated against experimentally obtained flame position. By capturing flame position and extension accurately, numerical flow field results complement experimental findings.

Additionally, heat-loss mechanisms play a major role in low-calorific combustion and therefore, this aspect is carefully addressed in the numerical modeling and validated with experiments by means of local temperature measurements. Especially for the later transition to machine testing, it is crucial to narrow down heat-loss effects. Obviously, atmospheric test rigs will show much larger heat loss compared to isolated gas turbines, but information from numerical modeling gives also insight into phenomena upstream to the actual combustion chamber. This makes machine-integrated design much more reliable and helps with gathering experience upfront.

Numerical simulations are conducted with Ansys Fluent, version 19.1. The incompressible, steady state Navier-Stokes equations are solved with an additional energy equation based on specific enthalpy and a species transport equation.

2.3.1. Modeling Theory

In the numerical simulations, the incompressible averaged Navier-Stokes equations for reacting flow are solved with the segregated SIMPLE solution strategy for pressure-velocity coupling. The energy equation solved in the gas phase reads

$$\nabla \cdot (\mathbf{u}(\rho e + p)) = \nabla \cdot (k_{eff} \nabla T - \sum_i h_i \mathbf{j}_i + (\overline{\tau}_{eff} \mathbf{u})) + S_R. \quad (1)$$

Vectors are bold and tensor notation is given as bold and over-lined. The energy in Equation (1) is in turn given as $e = h - p/\rho + 0.5\mathbf{u}^2$. There, the sensible enthalpy h is the sum over all the species of products $\sum h_i Y_i + p/\rho$ with the species mass fractions Y_i . p and ρ denote pressure and density, respectively. k_{eff} is the effective thermal conductivity, consisting of a laminar and a turbulent fraction. \mathbf{j}_i are the diffusion coefficients of species i . The heat sources S_R stand for energy entries due to chemical reactions and are subject to combustion modeling. The sensible enthalpies of species i are computed as the interval integral of heat capacity $c_{p,i}$ over temperature, via

$$h_i = \int_{T_0}^{T_1} c_{p,i} dT. \quad (2)$$

On the contrary, for solid regions (quartz glass and metal structures), the energy transport equation is the only transport equation solved and has the form

$$\nabla \cdot (\mathbf{u}\rho h) = \nabla \cdot (k\nabla T). \quad (3)$$

Note that Equation (3) is solved without source terms, since radiation is not modeled in the investigated case, due to relatively low peak temperatures in the combustor. Results of the numerical analyses will be analyzed with regard to this assumption.

Therefore, convective and conductive heat transfer is assumed to be the most dominant heat loss mechanism. In Equation (3), the sensible enthalpy is accordingly evaluated from Equation (2). Thus, heat capacities and thermal conductivities of the specific solid materials are modeled with piecewise-linear relations, as exemplarily shown in Figure 3 for the thermal conductivity.

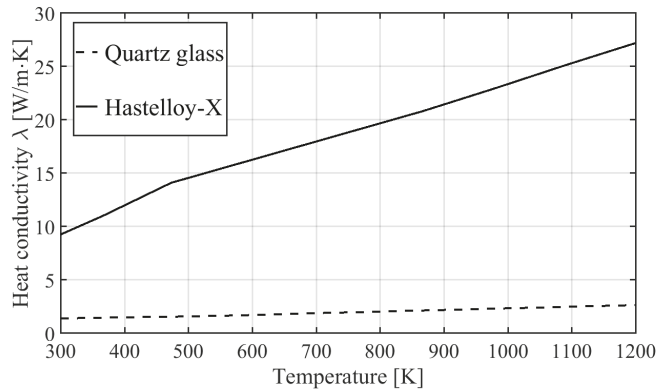


Figure 3. Used region-wise linear approximation of thermal dependency of solid structure materials' thermal properties. Example for thermal conductivity of hastelloy and quartz glass as employed in the coupled simulations. Adapted from [49].

Essential for the correct depiction of heat transfer mechanisms due to conduction and convection is the grid resolution at combustor walls. Since also a $k - \omega$ based turbulence model is used, the first cell in wall-normal direction is chosen according to $y^+ = 1$.

In terms of thermal boundary conditions, several variants are used in the presented study. Adiabatic boundaries are not considered. They are the simplest, but do not account for any local temperature gradients and heat transfer mechanisms. In the presented study, the heat transfer is modeled threefold, by applying

- Temperature boundary conditions (isothermal),
- Heat flux boundary conditions
- Conduction of fully coupled simulations.

The governing energy equation at the interface of fluids and solids without consideration of radiation generally is $\dot{q}_{conv_int} = \dot{q}_{conv_ext}$, which means $h_f(T_W - T_f) = h_{ext}(T_{ext} - T_W)$. h_f and h_{ext} are the respective conjugate heat transfer coefficients on the fluid "f" and exterior flow "ext" side.

For isothermal boundary conditions, T_W is prescribed,

$$h_f(\overline{T_w} - T_f) = h_{ext}(T_{ext} - T_w). \quad (4)$$

For the general heat flux boundary conditions, convection is considered, therefore \dot{q}_{int} is specified, which has to be assumed a priori. Either knowledge about heat flux exists, or it has to be estimated. For this work, it was estimated by a coupled test-case with forced convection, as shown in Figure 4.

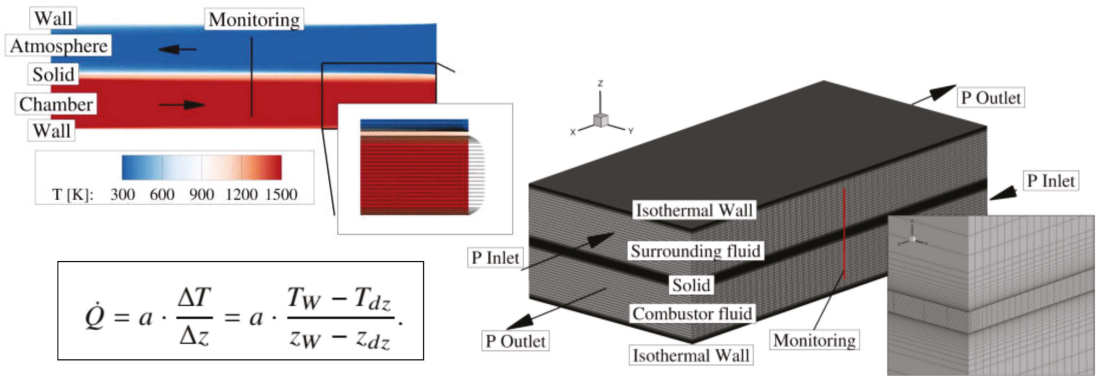


Figure 4. CHT (Conjugated Heat Transfer) numerical setup for the evaluation of heat transfer coefficients for heat-flux boundary prescription. Emulation of a cutout of near-wall conditions in the actual combustion chamber. P: Pressure boundary conditions. Adapted from [48]. z : Wall normal distance in the given coordinate system. a : Thermal conductivity.

Heat transfer coefficients are extracted from this setup by assuming thermodynamic conditions inside the combustion chamber and in the ambient, while the combustor wall is explicitly modeled. Detailed results on this investigation can be found in [48].

For a global balancing, in fully coupled simulations, the heat flux from fluid to solid and vice versa is evaluated with

$$q = \frac{k_{f/s}}{\Delta z} (T_{W,f/s} - T_{f/s}), \tag{5}$$

with the respective thermal conductivity k and the wall normal distance Δz . The subscript f/s means fluid or solid. For fully coupled simulations, temperature gradients in the solid walls develop and therefore the formula in Equation (5) has to be expanded. Depending on which side (combustor- or ambient-oriented medium) the heat flux is evaluated, the internal $T_{W,int}$ or external $T_{W,ext}$ wall temperature has to be taken into consideration.

2.3.2. Numerical CFD Setup

The overall computational domain is shown in Figure 5. A segment of 120 degrees is directly modeled, in order to exploit symmetry for computational efficiency. At the same time, 120 degrees mean the inclusion of four nozzles and therefore the accountance for nozzle-nozzle interaction. Periodic boundaries are applied in the rotational direction. Fully coupled CHT simulations are carried out with the domain in Figure 5a, whereas the isothermal and heat-flux modeling is carried out on the combustor domain only, where outer extensions are marked with the red line in Figure 5b. The grid consists of 4.4 million cells and 9.5 million nodes. Polyhedral elements are used, which provide a good quality resolution and representation of flow field and combustion, compared to conventional tetrahedral discretization due to a larger number of interpolation points. Wall resolution of $y^+ = 1$ is achieved with prism layer cells. The grid is refined in the reaction zone regions and in particular in the anode-cathode mixing zone, following the fuel nozzles. Model assumptions as presented were tested on a simplified setup, regarding grid resolution and influence of periodic boundary setting but are not explicitly shown for conciseness.

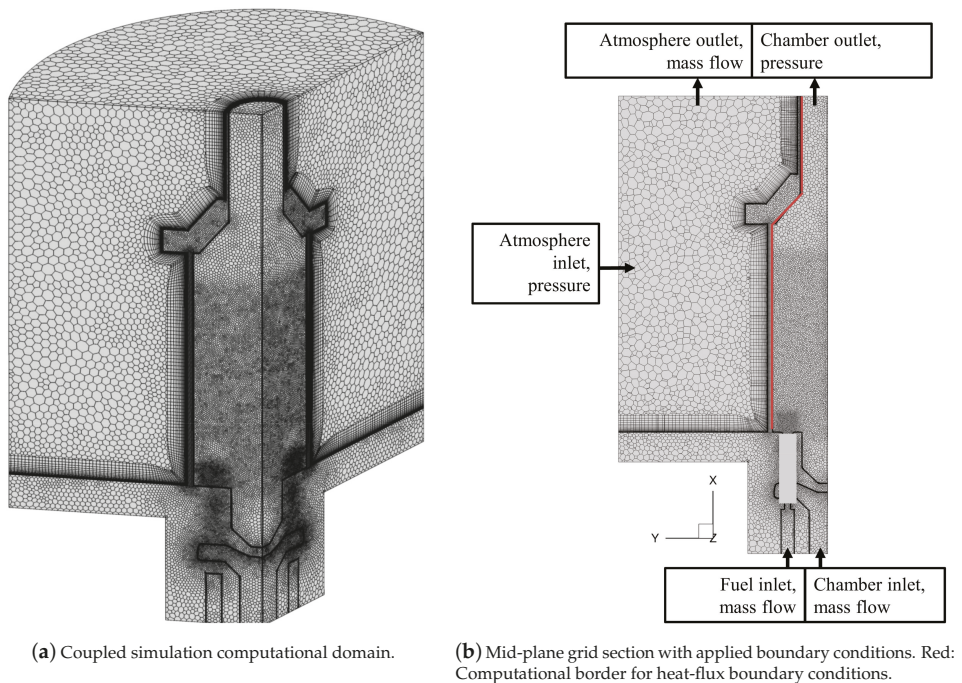


Figure 5. Numerical setup and computational grids.

In the solid regions of posts and glass walls, the grid is structured and composed of mainly hexahedral cells. Solid cells are in total 3.778 million elements with 0.82 million nodes. For simplicity reasons, only two different solid materials are applied. Those are quartz-glass for the combustion chamber windows and hastelloy-x steel for the posts, the combustor, the combustor stand and the exhaust duct.

Numerical simulations are carried out with Ansys Fluent, version 19.1. Turbulence is modeled with a $k - \omega$ SST approach [50]. Pressure-velocity coupling is covered with the SIMPLE solution strategy. Spatial discretization of transport and conservation equations is the second order upwind. At first, cold flow solutions are established. Combustion is then initialized with a global EDM (Eddy Dissipation Model) approach, based on a simple reaction equation for hydrogen. Finally, combustion is depicted using the Eddy Dissipation Concept (EDC) from Magnussen [51] and a detailed mechanism for synthetic gas combustion from Li et al. [52]. Judging from previous jet-and-recirculation stabilized burner simulations, this combination of chemical reaction modeling is best suited. Detailed combustion modeling is necessary in order to be able to depict the complex chemistry of lifted-off jet flames. Applied flow boundary conditions are sketched in Figure 5b.

In the case of heat-flux and isothermal modeling, constant values are prescribed for characteristic zones, namely the upstream burner section, the combustor front plate, combustor walls and the exhaust duct. For the isothermal case, an estimated temperature of $T_W = 1150$ K is defined for the combustion chamber walls.

Air and fuel mass flow rates are defined at the inlets according to experimentally used flow rate values, whereas the chamber outlet is modeled as a pressure outlet condition, where the gauge static pressure is set to zero. On the contrary, for the air surrounding the combustor (atmosphere), at the inlet, static pressure is prescribed, whereas the outlet is forced with mass flow (velocity), leaving the computational domain. In this way, an exhaust fan is imitated, as is present in the actual rig. The external flow conditions are estimated with simple flow-meter measurements and numerical boundaries are set in

order to mimic those conditions. The combination of mass flow and pressure boundary conditions prove to be superior over pressure boundary conditions only.

All the simulations were carried out on an Intel® Xeon E5-2695v2 architecture. The coupled cases were conducted on 6*24 cores, whereas isothermal and heat-flux computations were run with 5*24 cores. Overall turnaround times amount to 18.2 k CPU-h for the coupled cases and 11 k and 9.8 k CPU-h for the heat-flux and isothermal simulations, respectively. Therefore, the overall turnaround times are still very low compared to scale resolving approaches like LES (Large Eddy Simulation) or SAS (Scale Adaptive Simulation).

3. Results

3.1. Results-Reference Case

At first, numerical and experimental findings of the reference case are presented. The reference case is defined as full-load at near optimum conditions from Figure 2. Numerical results for different heat-loss modeling approaches are compared with experimental findings and then the flow field and temperature characteristics are discussed. The reference case data serves furthermore as a basis for evaluation of convective and conductive heat-loss in this investigation.

Reference case results are shown in Figure 6. Note that averaged OH^* can be evaluated only qualitatively. The measurement results are usually scaled within one order of magnitude in intensity and there is a certain high level cut-off. In the numerical simulations, absolute values of O and H concentrations are taken into consideration and the results are consistently scaled between the three modeling approaches for heat-loss.

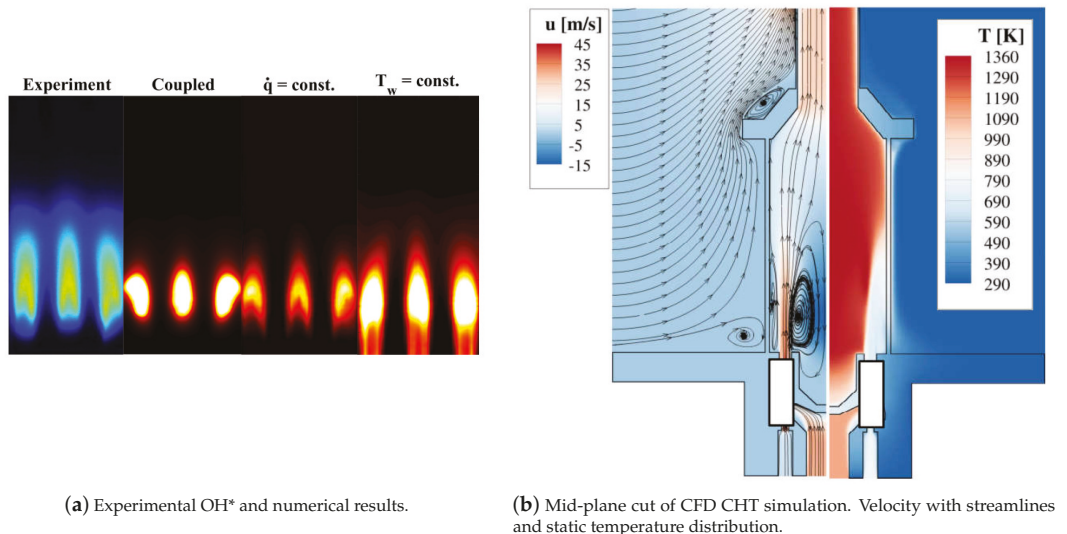


Figure 6. Experimental and numerical results of nominal load, optimum case.

Experiments in the reference case (Figure 6a), and, as will be shown later, in all the investigated cases, show compact, discrete flames with a certain lift-off from the nozzles but still a limited elongation in the downstream direction. This is important for later gas turbine integration, since in this way there is no interaction to be encountered with downstream mixing air and therefore no increased CO emissions are expected. Another characteristic of the reaction zones is an inverse u-shape distribution of the single flames. Judging from the averaged images, it is assumed that the reaction zones are distributed regularly in circumferential direction for different nozzles.

Numerical simulation approaches reproduce flame lift-off nicely, except the isothermal case. This is probably due to poor estimation of upstream wall temperatures that heat the upstream flow and foster reactivity. The best reproduction of experiments is achieved by the heat-flux modeling approach, where also the u-shape flame characteristics is reproduced. However, in all the cases, reaction zones are significantly short in axial direction. This is due to mixing deficiencies of the RANS approaches and probably the employment of simplified chemical reaction schemes.

Since comparison in terms of flame anchoring and position seems to be sufficient for the reference case, numerical results for velocity and temperature distribution are further analyzed in Figure 6b. The combustor averaged flow field shows the distinct characteristics of a jet-and-recirculation stabilized burner. Axial jets with high momentum issuing into the combustion chamber cause development of a large inner recirculation zone that helps with combustion stability by hot gas retransport to the flame root. As a consequence, remarkably homogeneous temperature distributions are achieved in the chamber, leading to the lower peak temperatures with NO_x levels to be expected to be in the order of single digit values in parts per million. NO_x could not be measured due to very large water contents in the combustor off-gas.

The mid-plane results for different simulation approaches are shown in Figure 7. In this context it becomes evident that different ways of treating the heat-loss mechanisms can have significant impact on flow field and temperatures.

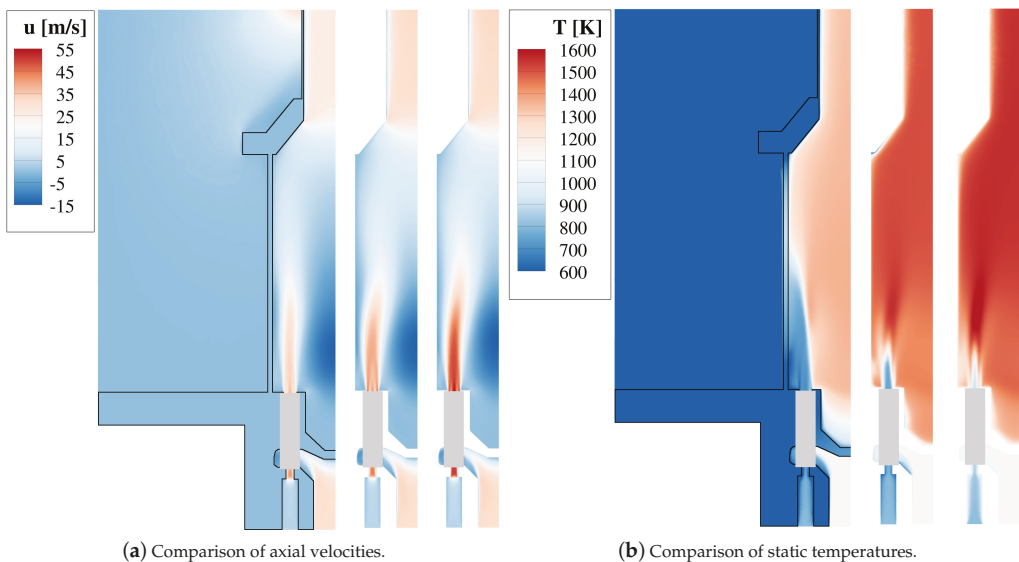


Figure 7. Combustor mid-plane of numerical results. **Left:** fully-coupled CHT, **mid:** Heat-flux modeled, **right:** isothermal boundaries.

Jet axial velocities are the lowest for the coupled case, whereas they increase for the heat-flux modeling and are the highest for isothermal walls. This circumstance is closely related to temperature distributions, since they affect the local density. In the coupled case, heat discharge is the greatest, therefore lower temperatures in the combustor develop and, as a consequence, lower velocities are present. At the same time, when jet velocities are higher, the formation and magnitude of the inner recirculation zone becomes more prominent, leading to an increased re-transport of hot gases to the reaction zones and therefore stabilizes and enhances combustion. In the balanced, averaged scenario of reacting steady state RANS simulations, the two effects are superimposed but can not be

separated. However, this leads to the distinct differences in velocity magnitudes and peak temperatures between the single modeling strategies [49].

Another reason contributing to the highest velocities in the isothermal case is that, due to the zonal prescription of temperature values, the fuel is slightly heated upstream, as can be seen on the bottom of the right picture in Figure 7. This heat entry into the system leads to lower fuel densities and therefore enhanced axial velocities. This denotes one downside of isothermal modeling, since the temperature profiles would have to be particularly refined and elaborated, if one would want to depict correct heat loss in the whole computational domain, requiring a large amount of modeling effort.

The main reason for the modeling endeavor with three variants for the heat losses is to achieve a high quality assessment of heat loss in the atmospheric burner tests. This is studied for the reference case in Figure 8. Componentwise discharged heat is shown in Figure 8a, whereas the total heat loss is balanced in Figure 8b. It becomes obvious from Figure 8a that most heat is discharged in the coupled case, while isothermal and heat-flux modeling are comparable. Confirmation of the situation with unwanted upstream flow heating from Figure 6a is given by burner and combustor stand results in the isothermal case, where heat is even induced due to defined wall temperatures. Upstream temperatures are generally hard to estimate due to complex test stand construction and strongly depends on the outer extension choice of the computational domain. A solution would be to further distinguish local regions for the scalar temperature definition, which comes however with significantly increased modeling effort prior to simulation.

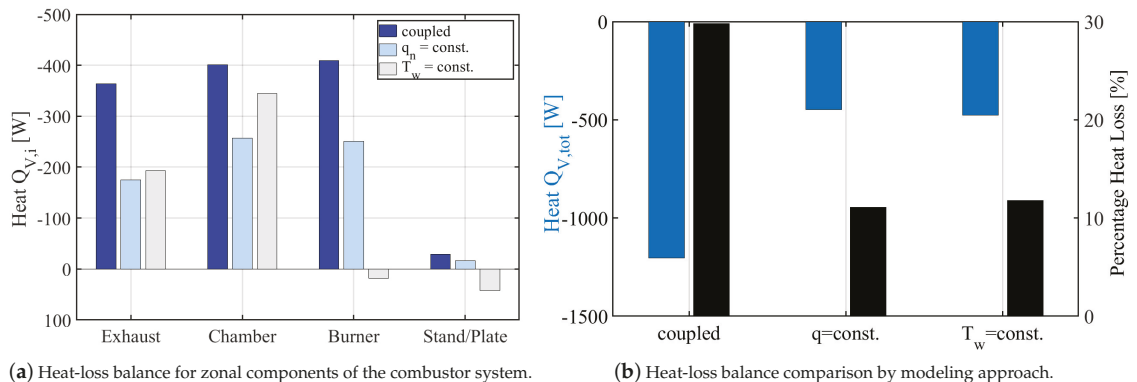


Figure 8. Heat loss balance based on numerical simulation approaches for isothermal, heat-flux, and coupled modeling.

The total balance in Figure 8b confirms the observation that discharged heat is probably overpredicted in the fully coupled CHT case, whereas heat-flux and isothermal case are in the same range. The most remarkable aspect is that the overall heat loss with respect to total thermal power amounts to 15–20%. Therefore, careful insulation assessment in the experiment is crucial, not only in atmospheric tests but also for later machine configuration. This is especially important in the investigated case of low calorific combustion, where slightly increased heat loss can make a big difference for combustion stability.

3.2. Results-Case Study

A bigger picture of combustion characteristics of the F20OG.1 is given by studying all the cases as defined in Figure 2. This is carried out in Figure 9. As mentioned earlier, all investigated points show discrete and compact flames, as is highly desirable for machine integration of the combustion system. Reaction zone elongation is the longest and most critical in part load situations, which are however very close to lean blow-off. The measured trends in base-load show the longest flames with lowest intensities in the rich regime, which

is counter-intuitive. However, one has to consider that air temperatures are at high levels, as can be seen in Table 1. Especially in the lean case this leads, in relation to the lower fuel mass flow, to larger impulse ratios between air and fuel stream and therefore enhances mixing. Additionally, the anode side that is considered as fuel is exhaust gas from the super heated steam generator. Therefore, naturally, the fuel has significant fractions of inert content (H_2O , CO_2), so rich cases can be relatively non-reactive compared to the lean mixture, leading to elongated reaction zones and lower radicals emission levels.

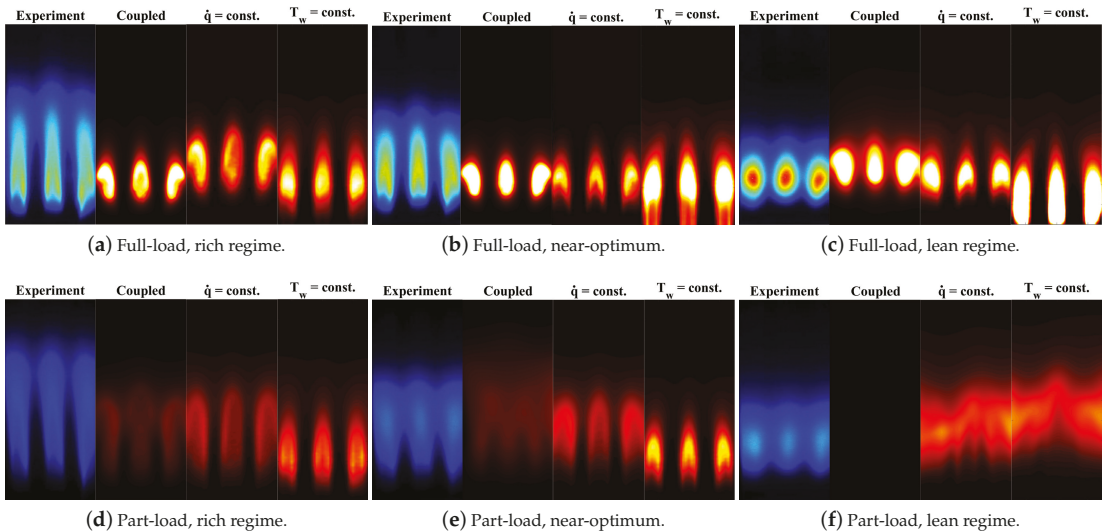


Figure 9. Comparison of experimental and numerical results for OH^* for nominal base- and part-load conditions. Subfigure titles from left to right: Experiment, Coupled, $\dot{q} = \text{const.}$, $T_w = \text{const.}$

Numerical simulations generally deliver a good reproduction of experimental findings. Especially the fully coupled CHT and the heat-flux modeling approach deliver sensible results in terms of qualitative lift-off height and reaction zone extensions. Major deviations are observed for the isothermal cases, which are linked to lack of detail in upstream prescription of temperatures and therefore enhanced reactivity of the mixture. Previously, it was discussed that in the coupled case the largest amount of heat is extracted from the combustion system. Judging from the part-load results, especially in the lean regime, where the CHT simulation shows no reaction, indicates that the heat-loss is overestimated in the coupled CHT case. This could be linked to overprediction of forced convective heat transfer due to uncertainties in the modeling of atmospheric flow. The outer flow situation is hard to determine due to very low velocities that are driven by an exhaust fan.

Measured emissions are listed in Table 2. The CO values are low for the base-load cases but distinctly higher in part-load, due to more unsteadiness in the vicinity of lean blow-off. Values for NO_x emissions are given where possible. However, they are prone to large insecurities due to the high water content in the exhaust gas, as can also be seen in Table 2. Indications are that NO_x are in the single digit order of magnitude w.r.t. parts per million.

Table 2. Experimental results of emissions measurements. x: no sensible value obtainable. ppm values unreferenced to oxygen content. Measurement uncertainties in Table 3. Measurement standard deviation: ± 0.1 ppm.

Operation Point	λ [-]	CO [ppm]	NO [ppm]	NO ₂ [ppm]	H ₂ O [ppm]
Base-load					
Lean	3.54	29.02	0.55	6.31	222,921.2
Near Optimum	2.27	12.61	1.17	6.09	338,094.6
Rich	1.67	30.85	2.08	5.07	400,266.0
Part-load					
Lean	3.57	126.72	1.19	x	238,987.2
Near Optimum	2.07	43.43	0.46	x	386,449.9
Rich	1.31	74.75	x	x	400,302.0

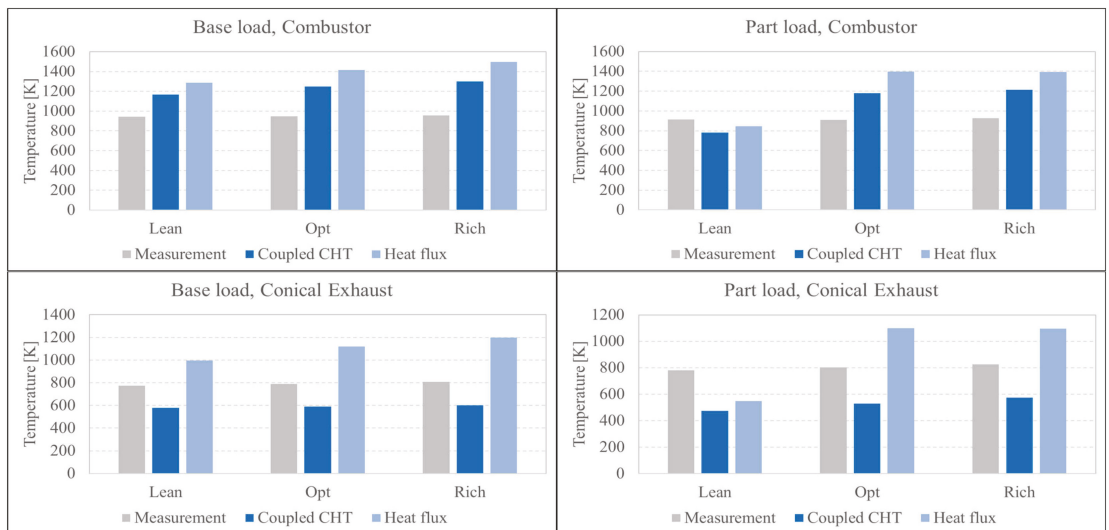


Figure 10. Pointwise temperature measurements and comparison with numerical results for the coupled CHT and heat flux modeling. Combustor: Downstream in the combustor strut. Conical Exhaust: Mid-height on the conical exhaust section wall. Measurement uncertainties in Table 3. Measurement standard deviation: ± 0.01 °C.

Table 3. Uncertainties of temperature and CO emissions measurements (thermo-couples) [53,54].

Measurement	Type and Class	Range	Accuracy
Static Temperature	Type N and K, Class 2	−40 to 333 °C	± 2.5 °C
		333 to 1200 °C	$\pm 0.0075T$
Emissions	AO2000, ABB	≤ 8 ppm	± 0.1 ppm
		≤ 80 ppm	± 1 ppm

As round off analysis, pointwise temperature measurements are shown in Figure 10. Temperatures are evaluated for the coupled CHT and heat-flux modeling of heat loss and balanced with experimental findings.

In general, in the combustion chamber near-wall regions simulations overpredict the measured findings, but are within the same order of magnitude. The coupled simulation

performs better in terms of absolute temperature values, especially in the downstream conical section but consistently for all operation points.

A possible reason for deviations between measurements and numerical modeling are radiation effects. Especially for the cases with heat-flux boundary modeling, large deviations to measured temperatures are present. In those cases, it is difficult to quantify radiation effects, since pre-simulation efforts like the extraction of heat transfer coefficients as shown in Figure 4 will not be able to quantify radiation heat-loss, since it does not fully depict gas radiation of the whole combustion chamber molecules. Therefore, it is concluded that radiation should not be neglected, even in the case of low-calorific combustion, unless a deviation in temperature in the order of magnitude 10–20% is acceptable in the design process. From our experience, this order of magnitude of radiation heat-loss does contribute to flame stabilization, but does not fundamentally change reaction zone location and spatial extensions.

Another aspect adding possibly up to temperature differences between experiment and simulation are measurement uncertainties of the thermo-couples, which are however hard to quantify.

With regard to the modeling values being in the same range as measured values, it can be stated that the modeling approach, especially the RANS based fully coupled scheme, finds absolute temperature levels in the right order of magnitude with a certain level of overprediction. The approach can therefore be used for the machine integration design as the worst case estimation for thermal load of the combustor structure in a gas turbine, when combustor temperature regimes are viewed.

4. Conclusions

A novel combustor based on jet-and-recirculation stabilized combustion, formerly known as FLOX[®] was investigated by means of optical measurements, exhaust gas analysis and numerical CFD simulations. The combustion system operates in the context of a hybrid power plant, processing off-gas from an upstream fuel cell. This leads to the main peculiarity of the burner system that it has to be able to process low-calorific fuel. It was however shown in previous works that the combustor is also able to run with conventional natural gas.

It was demonstrated that the burner system is able to cover a large operational range in the lean regime with indication of the low NO_x emissions in the single digit order of magnitude, despite low fuel energy contents. Lean blow-off was reached with off-gas around an air fuel ratio of 3.6. The burner features discrete and compact flames, as was demonstrated by means of OH* chemiluminescence measurements.

Numerical simulations were conducted and compared with measured data and the CFD conveniently complemented measurement data with information on flow field and temperature distribution. It is possible to support measurements with low-fidelity CFD, if careful treatment of boundary conditions is provided and detailed chemistry is used.

Different modeling strategies for the heat-loss were taken into consideration, in order to quantify heat-loss effects in the system reliably, which is of special relevance in low calorific combustion. It was shown that for this burner configuration, the heat loss is within range of 20–30% of overall thermal power.

Findings of the investigations carried out are of particular relevance for integration of the combustion system into the actual power plant. Although the combustor in the plant will have the lower heat-loss, the studies conducted raise awareness for critical thermal design and it was shown that it is feasible to use the employed CFD tools for reliable thermal design of the machine-integrated combustor. It is expected that low emission behavior of the combustion system will be reflected in machine operation.

As a major conclusion from the numerical studies, a careful assessment of thermal boundaries is crucial, especially with lower fuel energy contents. Different choices of thermal boundaries can have significant influence on flow field and combustion. Low-fidelity boundary conditions, like heat-flux and isothermal temperature prescription, have

the advantage of lower modeling effort and more efficient computations, are however seen critical if no detailed a priori knowledge on heat transfer is available in the modeling process. Fully coupled CHT simulations have a high modeling effort but deliver high quality results, not necessarily in terms of reproduction of a flame position and extensions but in terms of temperature prediction, which is important in the combustor design process. In order to increase the predictive accuracy of the numerical simulations for design and construction, a major improvement would be the incorporation of radiation models.

In general, the choice of simulation method should depend on the respective target values of the design process. In case combustion systems are designed in view of flame stabilization and reaction zone extensions, it can be a sensible approach to neglect radiation effects, especially in the case of low-calorific combustion, judging from the good match between OH* measurements and numerical simulation as presented in the paper. If however temperature level prediction for further analyses, e.g., life-span estimation with FEM (Finite Element Method) is important, radiation effects should be taken into account in the numerical model, despite the much higher computational effort.

The presented burner system is able to run with high and low calorific fuels at low emissions with stable combustion and covers a large operational range. The design is therefore integrated in an actual hybrid power plant application, where one crucial point for successful transition is the match of operational assumptions in the atmospheric tests with actual plant behavior, which will require future analysis. Apart from this, the burner system can be used in applications with higher power levels by applying common scaling rules based on geometric ratios and Mach number similarities. The presented burner system is basis for further burner development at DLR, going towards applications like biogas or hydrogen combustion in decentralized energy applications.

Author Contributions: Conceptualization, F.G. and T.L.; formal analysis and investigation, F.G. and T.L.; writing—original draft preparation, F.G.; writing—review and editing, T.L.; supervision, P.K.; funding acquisition, P.K. and M.A. All authors have read and agreed to the published version of the manuscript.

Funding: This project had received funding from the European Union’s Horizon 2020 research and innovation programme under grant agreement No. 641073 (www.bio-hypp.eu).

Data Availability Statement: Numerically and experimentally obtained data in this work are not publically available.

Conflicts of Interest: The authors declare no conflict of interest. The funders had no role in the design of the study; in the collection, analyses, or interpretation of data; in the writing of the manuscript, or in the decision to publish the results.

Abbreviations

The following abbreviations are used in this manuscript:

CHT	Conjugated Heat Transfer	—
DLR	German Aerospace Center	—
EDC	Eddy Dissipation Concept	—
EDM	Eddy Dissipation Model	—
FEM	Finite Element Method	—
FLOX®	Flameless Oxidation	—
LES	Large Eddy Simulation	—
LHV	Lower Heating Value	—
MGT	Micro Gas Turbine	—
MILD	Moderate or Intense Low-Ox. Dilution	—
NG	Natural Gas	—

RANS	Reynolds Averaged Navier Stokes	–
SAS	Scale Adaptive Simulation	–
SOFC	Solid Oxide Fuel Cell	–
a	Thermal conductivity	W/(m · K)
$c_{p,i}$	Heat capacity	J/(kg · K)
E	Energy	J/kg
h_f	Heat transfer coefficient	W/(m ² K)
h_i	Enthalpy, species i	J/kg
J_i	Diffusion flux, species i	kg/(m ² s)
k_{eff}	Effective thermal conductivity	W/(m · K)
Δz	Wall normal distance	m
p	Pressure	Pa
q	Heat flux	W/m ²
Q	Heat	W
T	Temperature	K
\mathbf{u}	Velocity vector	m/s
x, y, z	Spatial coordinates	m
y^+	Wall distance	–
Φ	Equivalence ratio	–
λ	Air-fuel number	–
ρ	Density	kg/m ³
τ	Shear stress	Pa

References

- Azizi, M.A.; Brouwer, J. Progress in solid oxide fuel cell-gas turbine hybrid power systems: System design and analysis, transient operation, controls and optimization. *Appl. Energy* **2018**, *215*, 237–289. [\[CrossRef\]](#)
- Kobayashi, Y.; Tomida, K.; Nishiura, M.; Hiwatashi, K.; Kishizawa, H.; Takenobu, K. Development of next-generation large-scale SOFC toward realization of a hydrogen society. *Mitsubishi Heavy Ind. Techn. Rev.* **2015**, *52*, 111.
- Konle, M.; Sattelmayer, T. Interaction of heat release and vortex breakdown during flame flashback driven by combustion induced vortex breakdown. *Exp. Fluids* **2009**, *47*, 627. [\[CrossRef\]](#)
- Veyo, S.E.; Lundberg, W.L.; Vora, S.D.; Litzinger, K.P. Tubular SOFC Hybrid Power System Status. In Proceedings of the ASME Turbo Expo 2003, Collocated with the 2003 International Joint Power Generation Conference, Atlanta, GA, USA, 16–19 June 2003; GT2003-38943.
- Veyo, S.E.; Shockling, L.A.; Dederer, J.T.; Gillett, J.E.; Lundberg, W.L. Tubular Solid Oxide Fuel Cell/Gas Turbine Hybrid Cycle Power Systems -Status. In *ASME Turbo Expo 2000: Power for Land, Sea and Air*; ASME: New York, NY, USA, 2000.
- Hohloch, M.; Huber, A.; Aigner, M. Analysis of Operational Strategies of a SOFC/MGT Hybrid Power Plant. In *Proceedings of the ASME Turbo Expo*; ASME: New York, NY, USA, 2017; GT2017-65013.
- Frenzel, I.; Loukou, A.; Trimis, D. An Innovative Burner Concept for the Conversion of Anode Off-gases from High Temperature Fuel Cell Systems. In Proceedings of the 11th Conference on Energy for a Clean Environment, Lisbon, Portugal, 5–8 July 2011.
- Frenzel, I.; Loukou, A.; Trimis, D.; Schroeter, F.; Mir, L.; Marin, R.; Egilegor, B.; Manzanedo, J.; Raju, G.; de Bruijne, M.; et al. Development of an SOFC based Micro-CHP System in the Framework of the European Project FC-DISTRICT. *Energy Procedia* **2012**, *28*, 170–181. [\[CrossRef\]](#)
- Hermann, F.; Palsson, J.; Mauss, F. Combustor Design Analysis for SOFC Off-gases. In Proceedings of the 5th Solid Oxide Fuel Cell Forum, Lucerne, Switzerland, 1–5 July 2002.
- Mathiak, J.; Heinzl, A.; Roes, J. Coupling of a 2.5 kW steam reformer with a 1 kWel PEM fuel cell. *J. Power Sources* **2004**, *131*, 112–119. [\[CrossRef\]](#)
- Sundaresan, M.; Ramaswamy, S.; Moore, R.M.; Hoffman, M.A. Catalytic burner for an indirect methanol fuel cell vehicle fuel processor. *J. Power Sources* **2003**, *113*, 19–36. [\[CrossRef\]](#)
- Pianko-Oprych, P.; Jaworski, Z. Numerical investigation of a novel burner to combust anode exhaust gases of SOFC stacks. *Pol. J. Chem. Technol.* **2017**, *19*, 20–26. [\[CrossRef\]](#)
- Severin, C.; Pischinger, S.; Ogrzewalla, J. Compact gasoline fuel processor for passenger vehicle APU. *J. Power Sources* **2005**, *145*, 675–682. [\[CrossRef\]](#)
- Frauhammer, J.; Eigenberger, G.; Hippel, L.V.; Arntz, D. Ein neuartiges Reaktorkonzept für endotherme Hochtemperaturreaktionen. *Chem. Ing. Tech.* **1998**, *70*, 1393–1397. [\[CrossRef\]](#)
- Schmid, H.P.; Wüning, J.A. FLOX Steam Reforming for PEM Fuel Cell Systems. *Fuel Cells* **2004**, *4*, 256–263. [\[CrossRef\]](#)
- Rampe, T. Entwicklung eines Bioethanol-Dampfreformers zur Erzeugung von Wasserstoff für den Einsatz in einem PEM-Brennstoffzellen-BHKW. Ph.D. Thesis, Duisburg-Essen University, Duisburg, Germany, 2004.
- Gritsch, A.; Kolios, G.; Eigenberger, G. Reaktorkonzepte zur autothermen Führung endothermer Hochtemperaturreaktionen. *Chem. Ing. Tech.* **2004**, *76*, 722–725. [\[CrossRef\]](#)

18. Wuenning, J. Flammlose Oxidation für Reformier. *Chem. Ing. Tech.* **2002**, *74*, 1606–1609. [\[CrossRef\]](#)
19. Bücheler, S.; Huber, A.; Aigner, M. Development of a Jet-Stabilized Combustion System for the use of Low-Caloric SOFC Off-Gas. In *ASME Turbo Expo*; ASME: New York, NY, USA, 2017; GT2017-64447.
20. Wünnig, J.; Wünnig, J. Flameless oxidation to reduce thermal NO-formation. *Prog. Energy Combust. Sci.* **1997**, *23*, 81–94. [\[CrossRef\]](#)
21. Cavaliere, A.; Joannon, M. Mild Combustion. *Prog. Energy Combust. Sci.* **2004**, *30*, 329–366. [\[CrossRef\]](#)
22. Flamme, M. Low NO_x Combustion Technologies for High Temperature Applications. *Energy Convers. Manag.* **2001**, *42*, 1919–1935. [\[CrossRef\]](#)
23. Lueckerath, R.; Meier, W.; Aigner, M. FLOX[®] Combustion at High Pressure With Different Fuel Compositions. *J. Eng. Gas Turbines Power* **2008**, *130*. [\[CrossRef\]](#)
24. Flamme, M. New combustion systems for gas turbines (NGT). *Appl. Therm. Eng.* **2004**, *24*, 1551–1559. [\[CrossRef\]](#)
25. Lammel, O.; Stöhr, M.; Kutne, P.; Dem, C.; Meier, W.; Aigner, M. Experimental Analysis of Confined Jet Flames by Laser Measurement Techniques. In *ASME Turbo Expo*; ASME: New York, NY, USA, 2011; GT2011-45111.
26. Rödiger, T.; Lammel, O.; Aigner, M.; Beck, C.; Krebs, W. Part-Load Operation of a Piloted FLOX[®] Combustion System. *J. Eng. Gas Turbines Power* **2013**, *135*, 031503-01. [\[CrossRef\]](#)
27. Zanger, J.; Monz, T.; Aigner, M. Experimental Investigation of the Influence of Combustor Cooling on the Characteristics of a FLOX[®]-Based Micro Gas Turbine Combustor. *Prog. Gas Turbine Perform.* **2013**, 165–184. [\[CrossRef\]](#)
28. Monz, T.; Stöhr, M.; O’Loughlin, W.; Zanger, J.; Hohloch, M.; Aigner, M. Experimental characterization of a swirl stabilized MGT combustor. In *Proceedings of the ASME Turbo Expo*; ASME: New York, NY, USA, 2015; GT2015-42387.
29. Ax, H.; Lammel, O.; Lueckerath, R.; Severin, M. High Momentum Jet Flames at Elevated Pressure, C: Statistical Distribution of Thermochemical States Obtained from Laser-Raman-Measurements. *J. Eng. Gas Turbines Power* **2020**, *142*, 071011. [\[CrossRef\]](#)
30. Severin, M.; Lammel, O.; Ax, H.; Lueckerath, R.; Meier, W.; Aigner, M.; Heinze, J. High Momentum Jet Flames at Elevated Pressure, B: Detailed Investigation of Flame Stabilization with Simultaneous PIV and OH-LIF. In *ASME Turbo Expo 2017: Power for Land, Sea and Air*; ASME: New York, NY, USA, 2017; GT2017-64556.
31. Yin, Z.; Nau, P.; Boxx, I.; Meier, W. Characterization of a single-nozzle FLOX[®] model combustor using kHz laser diagnostics. In *ASME Turbo Expo 2015: Power for Land, Sea and Air*; ASME: New York, NY, USA, 2015; GT2015-43282.
32. Severin, M.; Lammel, O.; Meier, W.; Aigner, M. Experimental Investigation of Flame Stabilization in a Turbulent Premixed Recirculation-Stabilized Jet-Flame with Simultaneous kHz Laser Diagnostics. In *Proceedings of the 57th AIAA Aerospace Sciences Meeting*, San Diego, CA, USA, 7–11 January 2019; Paper AIAA 2019-0183.
33. Lammel, O.; Severin, M.; Ax, H.; Lueckerath, R.; Tomasello, A.; Emmi, Y.; Noll, B.; Aigner, M.; Panek, L. High Momentum Jet Flames at Elevated Pressure, A: Experimental and Numerical Investigation for Different Fuels. In *ASME Turbo Expo 2017: Power for Land, Sea and Air*; ASME: New York, NY, USA, 2017; GT2017-64615.
34. Yin, Z.; Boxx, I.; Stöhr, M.; Lammel, O.; Meier, W. Confinement-induced instabilities in a jet-stabilized gas turbine model combustor. *Flow Turbulence Combust.* **2017**, *98*, 217–235. [\[CrossRef\]](#)
35. Grimm, F.; Lourier, J.M.; Lammel, O.; Noll, B. A Selective Fast Fourier Filtering Approach Applied to High Frequency Thermoacoustic Instability Analysis. In *ASME Turbo Expo 2017: Power for Land, Sea and Air*; ASME: New York, NY, USA, 2017; GT2017-63234.
36. Gounder, J.D.; Zizin, A.; Lammel, O.; Rachner, M.; Aigner, M.; Kulkarni, S.R. Experimental and numerical investigation of spray characteristics in a new FLOX[®] based combustor for liquid fuels for Micro Gas Turbine Range Extender (MGT-REX). In *Proceedings of the 52nd AIAA/SAE/ASEE Joint Propulsion Conference*, Salt Lake City, UT, USA, 25–27 July 2016; AIAA-2016-4698.
37. Izadi, S.; Zanger, J.; Kislal, O.; Enderle, B.; Grimm, F.; Kutne, P.; Aigner, M. Experimental Investigation of the Combustion Behavior of Single-Nozzle Liquid-FLOX[®]-Based Burners on an Atmospheric Test Rig. In *ASME Turbo Expo 2020: Power for Land, Sea and Air*; ASME: New York, NY, USA, 2020; GT2020-14564.
38. Schaefer, D.; Gounder, J.D.; Lammel, O.; Ax, H.; Lueckerath, R.; Aigner, M. High momentum jet flames at elevated pressure, D: Simultaneous measurement of OH/PAH PLIF and Mie scattering on liquid fuels. In *ASME Turbo Expo 2019: Power for Land, Sea and Air*; ASME: New York, NY, USA, 2019; GT2019-91177.
39. Schmitz, O.; Kaiser, S.; Klingels, H.; Kufner, P.; Obermueller, M.; Henke, M.; Zanger, J.; Grimm, F.; Schuldt, S.; Marcellan, A.; et al. Aero Engine Concepts Beyond 2030: Part3-Experimental Demonstration of Technological Feasibility. In *ASME Turbo Expo 2020: Power for Land, Sea and Air*; ASME: New York, NY, USA, 2020; GT2020-15397.
40. Bower, H.; Roth, J.; Grimm, F.; Zornek, T.; Schwärzle, A.; Kutne, P. Experimental Analysis of the Fuel Flexibility of a Jet-stabilized Micro Gas Turbine Combustor Designed for Low Calorific Gases. In *Proceedings of the Global Power and Propulsion Society Conference (GPPS)*, Zurich, Switzerland, 7–9 May 2018. GPPS-NA-2018-0012.
41. Bower, H.; Schwärzle, A.; Grimm, F.; Zornek, T.; Kutne, P. Experimental Analysis of a Micro Gas Turbine Combustor Optimized for Flexible Operation with Various Gaseous Fuel Compositions. In *ASME Turbo Expo 2019: Power for Land, Sea and Air*; ASME: New York, NY, USA, 2019; GT2019-90183.
42. Zornek, T.; Monz, T.; Aigner, M. Performance analysis of the micro gas turbine Turbec T100 with a new FLOX-combustion system for low calorific fuels. *Appl. Energy* **2015**, *159*, 276–284. [\[CrossRef\]](#)

43. Seliger-Ost, H.; Kutne, P.; Zanger, J.; Aigner, M. Experimental Investigation of the Impact of Biogas on a 3 kW Micro Gas Turbine FLOX[®]-based Combustor. In *ASME Turbo Expo 2020: Power for Land, Sea and Air*; ASME: New York, NY, USA, 2020; GT2020-15556.
44. Hasemann, S.; Seliger, H.; Kutne, P.; Aigner, M. Experimental and numerical design study for a small scale jet-stabilized micro gas turbine combustor. In *ASME Turbo Expo 2018: Power for Land, Sea and Air*; ASME: New York, NY, USA, 2018; GT2018-75050.
45. Seliger, H.; Stöhr, M.; Yin, Z.; Huber, A.; Aigner, M. Experimental and Numerical Analyses of a FLOX[®]-based Combustor for a 3 kW Micro Gas Turbine under Atmospheric Conditions. In *ASME Turbo Expo 2017: Power for Land, Sea and Air*; ASME: New York, NY, USA, 2017; GT2017-63317.
46. Lingstädt, T.; Grimm, F.; Krummrein, T.; Bücheler, S.; Aigner, M. Experimental Investigation of a SOFC Off-Gas Combustor for Hybrid Power Plant Usage with Low Heating Values Realised by Natural Gas Addition. In *Proceedings of the GPPS Forum 2018, Global Power and Propulsion Society, Zurich, Switzerland, 7–9 May 2018*; GPPS-2018-0052.
47. Lingstädt, T.; Grimm, F.; Krummrein, T.; Kutne, P.; Aigner, M. Atmospheric Experimental Investigations of a Jet-Stabilized SOFC Off-Gas Combustor for a Hybrid Power Plant operated with Biogas. In *Proceedings of the 57th AIAA Aerospace Sciences Meeting, San Diego, CA, USA, 7 January 2019*; AIAA 2019-1677.
48. Lingstädt, T.; Grimm, F.; Drude, A.; Kutne, P.; Aigner, M. Numerical Investigation of a Jet-Stabilized Combustion System Operated with Low-Calorific SOFC Off-Gas. In *Proceedings of the 57th AIAA Aerospace Sciences Meeting, San Diego, CA, USA, 7 January 2019*; AIAA 2019-1675.
49. Grimm, F.; Spörl, K.; Drude, A.; Lingstädt, T.; Kutne, P.; Aigner, M. Modeling Variants of Heat Loss in RANS Based Simulation of Jet-and-Recirculation-Stabilized Combustion. In *Proceedings of the ASME Turbo Expo*; ASME: New York, NY, USA, 2020; GT2020-14160.
50. Menter, F. Two-Equation Eddy-Viscosity Turbulence Models for Engineering Applications. *AIAA J.* **1994**, *32*, 1598–1605. [[CrossRef](#)]
51. Magnussen, B. On the Structure of Turbulence and a Generalized Eddy Dissipation Concept for Chemical Reaction in Turbulent Flow. In *Proceedings of the Nineteenth AIAA Meeting, St. Louis, MO, USA, 12–15 January 1981*.
52. Li, J.; Zhao, Z.; Kazakov, A.; Chaos, M.; Dryer, F. A Comprehensive Kinetic Mechanism for CO, CH₂O, and CH₃OH Combustion. *Int. J. Chem. Kinet.* **2007**, *39*, 109–136. [[CrossRef](#)]
53. Hohloch, M. Entwicklung und Experimentelle Untersuchung Eines Betriebskonzepts für die Mikrogasturbine in Einem MGT/SOFC Hybridkraftwerk. Ph.D. Thesis, Stuttgart University, Stuttgart, Germany, 2020.
54. Zanger, J. Experimentelle Charakterisierung Eines atmosphärisch Betriebenen, FLOX-Basierten Mikrogasturbinenbrenners für Erdgas. Ph.D. Thesis, Stuttgart University, Stuttgart, Germany, 2015.

Article

Numerical Investigation of the Impact of H₂ Enrichment on Lean Biogas/Air Flames: An Analytical Modelling Approach

Filipe M. Quintino * and Edgar C. Fernandes

Center IN+, Instituto Superior Técnico, University of Lisbon, 1049-001 Lisbon, Portugal; edgar.fernandes@tecnico.ulisboa.pt

* Correspondence: filipe.marques.quintino@tecnico.ulisboa.pt

Abstract: The transition from natural gas to renewable gases such as biogas and hydrogen creates an interchangeability challenge. The laminar flame speed S_L is a critical parameter in appliance design as it is a unique characteristic of the flame mixture. It is thus essential to evaluate the impact of renewable gases on S_L . In this work, 1D simulations were conducted in Cantera with the USC-Mech 2.0 kinetic mechanism. The S_L of three base biogas blends (BG100, BG90 and BG80) was computed for H₂ enrichment up to 50% in volume, equivalence ratio $0.8 \leq \phi \leq 1.0$, $p = 1$ atm and $T_u = 298$ K. It was found that the effect of H₂ enrichment is higher for base blends with higher CO₂ content as the thermal-diffusive and dilution effects of carbon dioxide are mitigated by hydrogen. The introduction of H₂ also increases the H radical pool, which is linked with the increase in S_L . A new correlation to model the impact of H₂ enrichment, $S_L(x_{H_2}) = (\zeta(\phi)/S'_L(x_{CO_2}))x_{H_2}e^{x_{H_2}} + S'_L(x_{CO_2})$, is proposed, which exhibits good agreement with the literature data and simulations. This equation can be directly used to estimate S_L without the need for a priori adaptations of fit parameters as the contributions of CO₂ and H₂ are isolated in independent variables.

Keywords: biogas; hydrogen; laminar flame speed; premixed combustion; correlation

Citation: Quintino, F.M.; Fernandes, E.C. Numerical Investigation of the Impact of H₂ Enrichment on Lean Biogas/Air Flames: An Analytical Modelling Approach. *Energies* **2021**, *14*, 369. <https://doi.org/10.3390/en14020369>

Received: 16 December 2020

Accepted: 6 January 2021

Published: 11 January 2021

Publisher's Note: MDPI stays neutral with regard to jurisdictional claims in published maps and institutional affiliations.



Copyright: © 2021 by the authors. Licensee MDPI, Basel, Switzerland. This article is an open access article distributed under the terms and conditions of the Creative Commons Attribution (CC BY) license (<https://creativecommons.org/licenses/by/4.0/>).

1. Introduction

Natural gas is a widely used fuel in applications ranging from heating and electricity generation to cooking and vehicle fuel [1]. However, the increasingly ambitious greenhouse gas (GHG) emission reduction targets, set by governments and institutions, means that it will likely be phased out in the future. As many of its current applications are not easily adaptable to consume electricity, renewable gases will be required. Recent developments in technology and public policy have opened a pathway where hydrogen and biogas are the likely candidates to replace natural gas [2–5].

Biogas is a biofuel obtained from the anaerobic digestion of organic matter. Its main components are CH₄ and CO₂, and it is often upgraded to biomethane by removing the excess carbon dioxide [6]. As biogas exhibits a similar composition to natural gas, with methane occupying the largest volume share in both, it has been widely used in its place in the past. In Denmark, for example, more than 50% of the biogas produced in the country is upgraded and injected in the national gas grid [7]. However, the limited feedstock for biogas production in most countries indicates that it cannot solely meet the gas demand. Therefore, green hydrogen has been pointed out as a more scalable alternative. It can be produced through electrolysis, requiring only a source of water and electricity [8]. By producing hydrogen through electrolysis, it is possible to couple the gas and electricity sectors, taking advantage of off-peak hours electricity production. However, replacing natural gas with hydrogen raises additional concerns as the two fuels have significantly different properties. The introduction of hydrogen and biogas in the energy sector is expected to be gradual by incorporating larger shares of renewable gases as time goes on. Several countries have already established targets for the use of renewable gases,

particularly hydrogen, at least until 2030. Based on national strategies and roadmaps, a summary of these for selected countries is provided in Table 1:

Table 1. Hydrogen related targets in selected countries for 2030. Data collected from national hydrogen roadmaps.

Country	Electrolyser Capacity (GW)	Hydrogen Refuelling Stations	Hydrogen Share in Gas Networks (%)
France	6.5	400–1000	-
Germany	5	-	-
Japan	-	900	-
Netherlands	3–4	-	-
New Zealand	-	-	20
Portugal	2–2.5	50–100	10–15
South Korea	-	310–1200	-
Spain	4	100–150	-

A major challenge in the transition from natural gas to renewable gases in the gas system is the interchangeability in end-use equipment [9]. These devices are often tailored for a specific fuel composition, thus having a unknown performance when this changes. Therefore, it is crucial to effectively determine the impact of different levels of renewable gas incorporation in current gas systems in a fast and accessible way. Significant impacts on reaction chemistry are expected due to high concentrations of CO₂ and H₂ in the gas composition resulting from hydrogen and biogas admixture. The sub-mechanism of the water-gas shift (WGS) reaction ($\text{CO} + \text{H}_2\text{O} \rightleftharpoons \text{CO}_2 + \text{H}_2$) is of particular importance in hydrogen applications. This reaction appears through the combination of the CO oxidation and a radical shuffle reaction [10]:



Changes in reaction kinetics will ultimately have an impact on the laminar flame speed S_L , a critical parameter in appliance design. This unique characteristic of a premixed combustion mixture depends on the reaction rate, thermal diffusivity and temperature in the flame region [11]. Consequently, a precise determination of S_L is of the utmost importance in design and equipment performance.

The estimation of S_L is often time-consuming. It can be experimentally measured, which often makes the process expensive, or obtained using numerical models. However, these methods require extensive and detailed kinetics mechanisms, which increase the computational cost [12]. As a result, there has been an effort to develop empirical and analytical relations to estimate S_L for varied blends and conditions [13]. Several authors have focused on the impact of diluents in S_L to address a challenge posed by exhaust gas recirculation (EGR) systems. Metgalchi and Keck [14], in 1982, established a “power-law” relation, which has been widely adopted [15,16]:

$$S_L = S_{L,ref} \left(\frac{p}{p_{ref}} \right)^\sigma \left(\frac{T_u}{T_{u,ref}} \right)^\gamma (1 - 2.1y_{dil}) \quad (3)$$

where $S_{L,ref}$ is the laminar flame speed at pressure $p = p_{ref}$ and unburned gas temperature $T_u = T_{u,ref}$ for a determined equivalence ratio ϕ . $\sigma = \sigma(\phi)$ and $\gamma = \gamma(\phi)$ are fit parameters and y_{dil} the mass fraction of diluents in the premixed combustion mixture. The formulation of Equation (3) was based on experimental data obtained for propane, methanol, isooctane and indolene tested in a constant volume bomb experiment. The diluent simulated an EGR gas mixture (85%N₂/15%CO₂). Since then, other authors explored alternative formulations. Han et al. [17] tested CH₄/EGR mixtures, where EGR=81.5%N₂/18.5%CO₂, obtaining the

following correlation from empirical data: $S_{L,ref} = 229.7D^2 - 157.6D + 35.26$, where D is the volume fraction of EGR in the mixture. Elia et al. [18] proposed the following expression for a diluent mixture composed of 86%N₂/14%CO₂: $S_L/S_{L,ref} = 1 - a_1D + a_2D^2 + a_3D^3$, where D is the diluent volume fraction (in %) and a_i are model parameters.

Biogas composition is highly variable depending on the substrate used in production, as well as on the anaerobic digestion process, which, in turn, is affected by several technical aspects. As a result, the weight of CH₄ and CO₂ in the blend composition varies significantly, thus changing the laminar flame speed. Hydrogen can be used to compensate the changes in S_L caused by increases in CO₂ content to attain a relatively steady value of S_L that ensures adequate equipment performance and safety. However, to do this, an accurate estimation of the H₂ enrichment impact on the laminar flame speed is necessary, to ensure that changes in S_L are not over- or under-compensated by the hydrogen admixture. In 2011, based on the original formulation of Metgalchi and Keck (Equation (3)), Bougrine et al. [19] proposed a new correlation to model S_L in CH₄/H₂ flames. To this end, the authors performed one-dimensional simulations and collected literature data across a wide set of conditions. Even though the resulting model exhibited good agreement with premix simulations, it required the determination of 40 fit parameters, making its use not expeditious. Furthermore, biogas was not directly addressed in this research.

Recently, Quintino and Fernandes [20] explored the possibility of using an analytical correlation to model the impact of CO₂ content on the S_L of biogas/air lean flames. Based on the formulation of Equation (3), a new expression was obtained, exhibiting good results for a mass fraction of CO₂ ($y_{CO_2,dil}$) in the flame up to 0.38. The model parameters were estimated using data from one-dimensional numerical simulations. Furthermore, the expression performance was also evaluated with available literature results. The final model took the form of Equation (4):

$$S_L = S_{L,ref} \left(\frac{p}{p_{ref}} \right)^\sigma \left(\frac{T_u}{T_{u,ref}} \right)^\gamma \left(1 + \alpha y_{dil} + \beta y_{dil}^2 \right) \quad (4)$$

where p and T_u are the pressure and temperature of the unburned mixture, respectively, $p_{ref} = 1$ atm and $T_{u,ref} = 298$ K, $S_{L,ref} = S_{L,ref}(\phi)$ is the laminar flame speed at reference conditions and $y_{dil} = 0$ and $\alpha = \alpha(\phi)$, $\beta = \beta(\phi)$, $\sigma = \sigma(\phi)$ and $\gamma = \gamma(\phi)$ are model parameters. More details on the model can be found in the original paper [20]. This correlation failed to incorporate the possibility of hydrogen enrichment, making it possible to assess the drop in S_L for a determined CO₂ content, but not to estimate the H₂ admixture necessary to compensate such a drop.

This work aims to study the impact of H₂ enrichment on the laminar flame speed of lean biogas/air flames and to develop an analytical correlation to model S_L , extending the application range of Equation (4). To that end, one-dimensional simulations in Cantera software are conducted for three base biogas blends (BG100, BG90 and BG80), with the equivalence ratio between 0.8 and 1.0 and hydrogen content in the fuel mixture up to 50% in volume. The impacts of thermal-diffusive, dilution and chemical effects of CO₂ and H₂ on S_L at $p = 1$ atm and $T_u = 298$ K are analysed. A correlation is proposed and validated with simulations and literature data.

2. Methods

2.1. Modelling

Simulations were conducted using the CANTERA toolkit [21] in the Python (Version 3.7) programming language (Python Software Foundation, <http://www.python.org/>). The laminar flame speed S_L for each blend and condition were obtained with a one-dimensional freely propagating flame routine (FPF). Steady-state and uniform inlet conditions were assumed in every run. The computational domain was defined with a sufficient size to ensure negligible heat and mass diffusion through the boundary. Inlet pressure and temperature were set to $p = 1$ atm and $T_u = 298$ K, respectively.

The 1D FPF routine was fed with the USC Mech 2.0 kinetics mechanism [22], published in 2007 by the Combustion Kinetics Laboratory of the University of Southern California. It comprises 111 chemical species and 784 reactions and is tailored for the combustion of H₂/CO/C₁-C₄ based blends. This mechanism has overall presented good results with CH₄/CO₂/H₂ fuels in engine simulations [23] and in the estimation of laminar premixed combustion characteristics [24,25].

Three base biogas blends were adopted for the conducted simulations: BG100, BG90 and BG80. Under the notation BGXX, XX indicates the volume content (*v/v* %) of CH₄ in the blend, while the remainder is assumed to be CO₂. Previous research has shown that the presence of small quantities of other ballast components in biogas have little impact on *S_L* values [20], indicating that modelling of biogas as a CH₄/CO₂ mixture is a valid assumption for this work. The impact of hydrogen enrichment for each biogas blend was also evaluated. H₂ content by volume in the fuel (*x_{H₂}*) varied between 0% and 50%, with 1 p.p.steps. It was calculated as:

$$x_{H_2} = \frac{n_{H_2}}{n_{CH_4} + n_{CO_2} + n_{H_2}} \quad (5)$$

where *x_{H₂}* is the hydrogen content in the fuel blend and *n_i*[mol] the amount of species *i*. The combustion reaction equivalence ratio *φ* varied in the interval 0.8 ≤ *φ* ≤ 1.0, with 0.05 steps. Air was assumed to be only O₂ and N₂ in a 21/79% proportion. Every base biogas blend was simulated at every *φ* and *x_{H₂}*, detailed above.

2.2. Correlation

As stated before, this work intends to develop an analytical correlation to model the impact of H₂ enrichment on the *S_L* of lean biogas/air flames. Based on the model outputs, a correlation was obtained using a best fit routine. To do so, several formulations based on the exponential behaviour were tested. This was performed using the `curve_fit()` function of the SciPy (Version 1.5.4) module in Python. The routine tests a function formulation and determines the parameters that provide the best fit. Simplicity was prioritized in the choice of the mathematical formulation. It was ensured that the obtained correlation attained an *R*² ≥ 0.99 for every base blend and *φ*. Furthermore, it was also guaranteed that correlation parameters were independent of CO₂ content (*x_{CO₂}*) in the base biogas blend except for an intermediate flame speed *S'_L*, which already accounts for the carbon dioxide contribution. The expressions tested assumed the following formulation:

$$S_L = S_L(x_{H_2}, \phi, S'_L) \quad (6)$$

where *S_L*[m/s] is the laminar flame speed, *x_{H₂}* is the H₂ enrichment given by Equation (5), *φ* is the equivalence ratio and *S'_L* = *S'_L*(*x_{CO₂}*)[m/s] is an intermediate flame speed (*x_{CO₂}* is the CO₂ content in the base biogas blend such that *x_{CO₂}* = *n_{CO₂}*/(*n_{CO₂}* + *n_{CH₄}*)).

3. Results and Discussion

This discussion is divided into three complementary sections. In Section 3.1, the impact of H₂ content in the *S_L* of biogas/air flames is discussed. Literature data on this topic were found to be scarce and, when present, focused on a narrow subset of conditions that did not support the development of a new correlation. Therefore, a numerical analysis was conducted to quantify the different effects of H₂ and CO₂ content on *S_L* and to provide fundamental support for the model development. Here, the results obtained from the 1D-FPF simulations are presented, and the coupling effect of CO₂ and H₂ on *S_L* is depicted. Section 3.2 describes the analytical model proposed in this work. The criteria used for model development are presented, and the improvement on Equations (3) and (4) is described. Furthermore, the new model's novelty is explained. Finally, the proposed correlation is validated with reliable H₂/CO₂/CH₄/air *S_L* measurements in Section 3.3.

Model predictions are compared with literature data to assess performance, and relevant cases for model application are described.

3.1. Hydrogen Content Impact on S_L

The fuel blends tested in this work are ternary mixtures of CH_4 , CO_2 and H_2 in varying proportions. Each of these species impacts the laminar flame speed by changing the mixture properties: producing thermal-diffusive, kinetic and concentration effects [26,27]. Thermal-diffusive effects are caused by changes in thermal diffusivity and the specific heat capacity of the mixture. Kinetic or chemical effects occur by the participation of species in chemical reactions or pathways [28]. Concentration effects result from a reduced amount of a determined species caused by the increase of any other. Methane, carbon dioxide and hydrogen exhibit largely different properties, making their impact on any of these effects highly asymmetric. While CH_4 and H_2 are reactive species, CO_2 can be generally considered an inert gas. Regarding density, that of CO_2 is around 20 times higher than that of H_2 . Thus, an understanding of these species' contributions on the effects that ultimately impact S_L is of paramount importance.

Simulations were performed for three base biogas blends: BG100 (pure CH_4), BG90 and BG80. For each of these, the range of hydrogen enrichment, as defined by Equation (5), varied within the interval $0\% \leq x_{\text{H}_2} \leq 50\%$. The equivalence ratio ϕ range was set from 0.8 to 1.0, with 0.05 steps. The obtained results are exhibited in S_L vs. x_{H_2} plots in Figures 1–3, for BG100, BG90 and BG80, respectively.

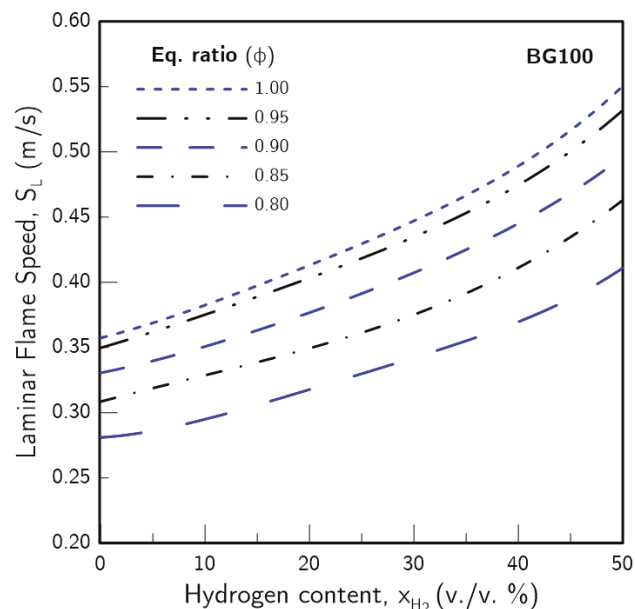


Figure 1. The laminar flame speed of biogas (BG100)/air flames enriched with H_2 . Each line corresponds to the model results for a determined equivalence ratio (ϕ). Conditions were set at $p = 1$ atm and $T_u = 298$ K.

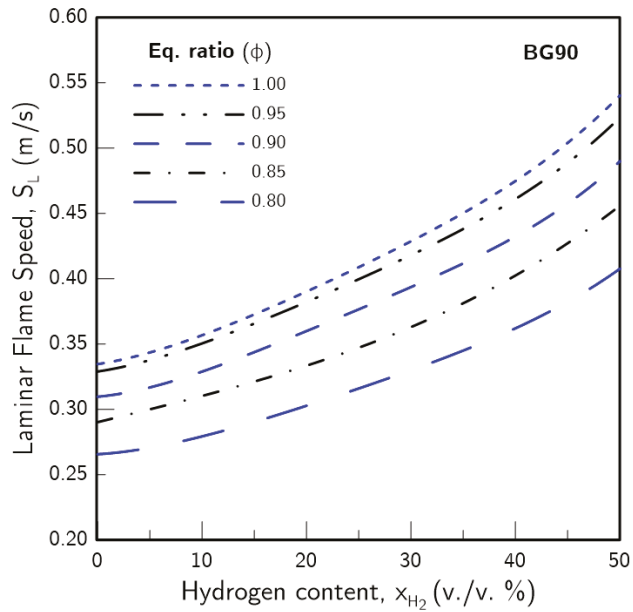


Figure 2. Laminar flame speed of BG90/air flames enriched with H₂. Each line corresponds to the model results for a determined equivalence ratio (ϕ). Conditions were set at $p = 1$ atm and $T_u = 298$ K.

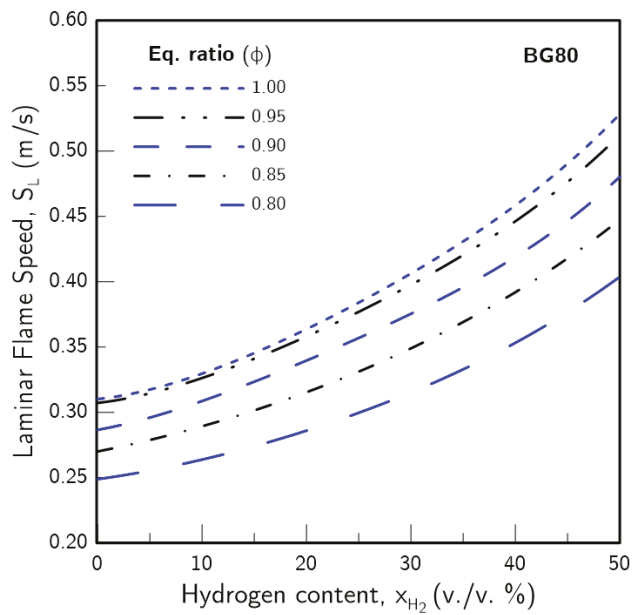


Figure 3. Laminar flame speed of BG80/air flames enriched with H₂. Each line corresponds to the model results for a determined equivalence ratio (ϕ). Conditions were set at $p = 1$ atm and $T_u = 298$ K.

Naturally, in all three cases, an increased x_{H_2} produced an increase in S_L . The thermal flame theory of Mallard and Le Chatelier [29] states that S_L is dependent on the reaction rate ($\dot{\omega}$), thermal diffusivity (α) and temperature (T (b —burned, u —unburned, i —ignition)) in the flame region in the form of Equation (7):

$$S_L = \sqrt{\alpha \dot{\omega} \left(\frac{T_b - T_i}{T_i - T_u} \right)} \quad (7)$$

Hydrogen enrichment increases α and $\dot{\omega}$, as well as temperature, thus raising S_L . A comparison of the curves exhibited in Figures 1–3 shows that hydrogen enrichment of biogas blends attenuates the negative effects of CO_2 in a non-linear fashion, with a greater proportion the higher x_{H_2} is. If an S_L average for every ϕ tested is taken at $x_{H_2} = 0\%$, it is observed that from BG100 to BG90, there is a S_L drop of 6.3%, due to the contribution of CO_2 . The difference increases between BG100 and BG80, reaching 13%. However, the same calculation performed at $x_{H_2} = 50\%$ yields a drop of 1.3% from BG100 to BG90 and of 3.1% from BG100 to BG80. As a consequence, the impact of hydrogen enrichment on S_L is greater when CO_2 content is higher in the base biogas blend. On average, the S_L increase caused by $x_{H_2} = 50\%$ is of 47.3% for BG100, 58.3% for BG90 and 67.5% for BG80.

Numerical simulations conducted by Wei et al. [30] indicate that the concentration of the H radical in the flame region affects the S_L of BG/ H_2 flames. Whereas H_2 increases the presence of H through the reactions R1: $OH + H_2 \rightarrow H_2O + H$ and R2: $O + H_2 \rightarrow H + OH$, CO_2 produces the opposite phenomena through R3: $OH + CO \rightarrow H + CO_2$ and R4: $O + CH_3 \rightarrow H + CH_2O$. As introduced in Section 1, R1 and R3 are the steps of the water-gas shift (WGS) sub-mechanism, which seems to be responsible for the adjustments in the H radical pool that derive from modifications in the reaction kinetics. Furthermore, CO_2 also decreases the H radical pool by diluting the mixture. Wei et al. found that the coupling effects of CO_2/H_2 for lean mixtures, as CO_2 content is increased, give rise to evident improvements of S_L through the kinetic effects of H_2 . This conclusion is consistent with the results discussed above. The non-linear increase of S_L with x_{H_2} , such that $d^2S_L/dx_{H_2}^2 > 0$, supports the hypothesis that the H_2 related kinetics gradually takes over the CH_4 dominated chemical pathways. Furthermore, it seems that a larger CO_2 concentration in the base blend increases the weight of the H_2 related chemistry for lower x_{H_2} .

When considering the impact of CO_2 and H_2 on S_L , thermal-diffusive effects must also be taken into account. It is known that on top of a kinetic effect, CO_2 also produces a significant impact due to its high specific heat capacity [31]. Carbon dioxide acts as a heat sink in the flame, thus reducing the adiabatic flame temperature T_{ad} and increasing the mixture ignition temperature T_i [32,33]. In a numerical study on the impact of CO_2 dilution on CH_4 /air premixed flames, Halter et al. [34] showed that for small concentrations in the flame mixture (<5%), this effect contributes to approximately 50% of the S_L reduction experienced. On the other hand, H_2 enrichment increases S_L not only through kinetics, but also as a result of thermal-diffusive effects. The increased thermal diffusivity of hydrogen produces a positive effect on S_L (see Equation (7)), counterbalancing the negative impacts of carbon dioxide. Furthermore, the lower T_i and higher T_{ad} of H_2 produce a temperature increase throughout the flame region. This effect has been reported by Rocha et al. [35] in a numerical and experimental work where the impact of H_2 on the chemiluminescence of $CH_4/CO_2/H_2$ /air flames was evaluated. The simulation results of the present work (Figures 1–3) are congruent with previous research, manifesting an overall positive effect of H_2 enrichment on the S_L of biogas/air flames, even though it varies with base blend composition due to coupling CO_2/H_2 effects.

To evaluate the effects of CO_2 when combined with H_2 enrichment on S_L , further simulations were conducted. To this end, two base blends were selected: BG100 and BG80. However, to isolate the different effects of CO_2 presence, simulations were also conducted with fake CO_2 (FCO₂) in the biogas blend. This species possesses the same transport and thermodynamic properties of CO_2 , but does not participate in any chemical reaction.

Thus, with ϕ set at 0.9, three S_L curves were obtained for BG100, BG80 and BG80 (FCO₂). The results are provided in Figure 4.

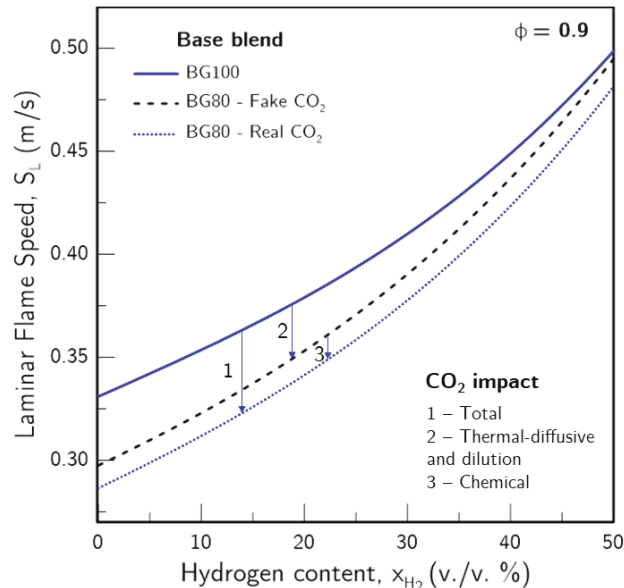


Figure 4. Laminar flame speed of BG100, BG80 and BG80 (FCO₂)/air flames enriched with H₂. Each line corresponds to the model results for a determined base blend. Conditions were set at $p = 1$ atm and $T_u = 298$ K.

The different impacts CO₂ produces in S_L for varying levels of H₂ enrichment can be seen in Figure 4. As FCO₂ does not take part in the reaction chemistry, the difference between the BG100 and BG80 (FCO₂) curves can be attributed to the dilution and thermal-diffusive effects produced by CO₂, whereas the step from BG80 (FCO₂) to BG80 stems from the CO₂ impact on the kinetics. The results show that for low H₂ content, most of the CO₂ impact on S_L can be attributed to dilution and thermal-diffusive effects. When $x_{H_2} = 0\%$, the S_L of BG80 is 0.041 m/s lower than that of BG100, with 73% of this reduction caused by thermal-diffusive and dilution effects and 27% by kinetics. However, as x_{H_2} is increased, the weight of thermal-diffusive and concentration effects is reduced. At $x_{H_2} = 50\%$, the S_L drop between the same base blends is of 0.016 m/s, with 84% of it resulting from changes in chemistry due to the presence of CO₂. Thus, whereas CO₂ thermal-diffusive and dilution effects gradually subside as H₂ content is increased, CO₂ chemistry maintains a consistent contribution in S_L reduction. The simulation results indicate that the coupling of H₂ enrichment with CO₂ in the base biogas blend tends to mitigate the negative thermal-diffusive and dilution effects on S_L caused by the latter.

As stated previously, the impact of H₂ and CO₂ on the H radical pool is linked to variations in laminar flame speed [30]. Additionally, as the dominant decomposition product of methane, the radical CH₃ is an indicator of the CH₄ related chemistry [36]. Thus, to assess in further detail the H₂ and CO₂ chemical impact on S_L , the evolution of CH₃ and H was analysed for the conditions of this study. For the same blends that produced the results exhibited in Figure 4 at $\phi = 0.9$, a CH₃ and H weight was estimated to evaluate the radical pool of both species. The contribution for each blend was computed by integrating the molar fraction of each species along the reaction distance: $\int x_{H,CH_3} dz$. This calculation is illustrated in Figure 5 through the shadowed areas. Figure 6 exhibits the evolution of the CH₃ and H radical pool with H₂ content.

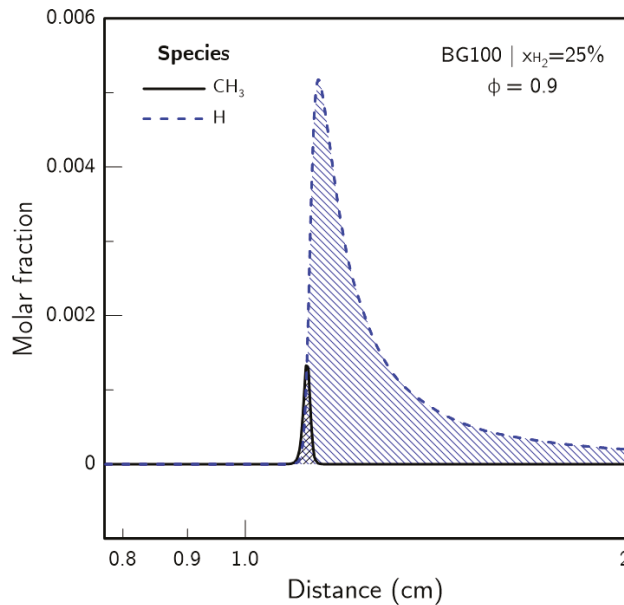


Figure 5. CH_3 and H molar fraction profile for BG100 with $x_{\text{H}_2} = 25\%$ and $\phi = 0.9$. The X axis is in the base 10 logarithmic scale. Conditions were set at $p = 1$ atm and $T_u = 298$ K.

Figure 6 shows that the CH_3 evolution with H_2 content is non-linear, such that $d^2\text{CH}_{3,w}/dx_{\text{H}_2}^2 < 0$. As CH_3 is a marker of CH_4 related chemistry, it would be expected that its weight diminishes as x_{H_2} is increased. However, the reduction of CH_3 weight is not proportional to the CH_4 concentration in the flame mixture. Even though CO_2 lowers the overall presence of CH_3 , mostly through thermal-diffusive and concentration effects, it seems to have little impact on the evolution of the CH_3 radical weight with x_{H_2} . This trend indicates that as H_2 content is increased, a transition occurs, consisting of a weakening of the CH_4 related chemistry and improvement of the H_2 related kinetics. As Wei et al. [30] reported in their work, the H radical evolution appears to follow the variations in laminar flame speed through changes in the WGS sub-mechanism. However, when comparing the curves of Figures 4 and 6, it can be seen that as x_{H_2} increases, the difference between the BG100 and BG80 S_L curves reduces faster than the difference between the H radical weight. It appears that as H_2 content is increased, the CO_2 thermal-diffusive and dilution effects maintain a more relevant impact on the H radical pool than on S_L . For the BG80 base blend, a $x_{\text{H}_2} \approx 25\%$ is required to raise the H radical weight levels to those of BG100 without H_2 enrichment even though S_L is matched at $x_{\text{H}_2} \approx 17\%$. As CO_2 thermal-diffusive and dilution effects seem to produce a greater impact on H evolution than on S_L , this indicates that H_2 not only increases S_L through a more efficient H radical production, but also due to its own thermal-diffusive and concentration effects.

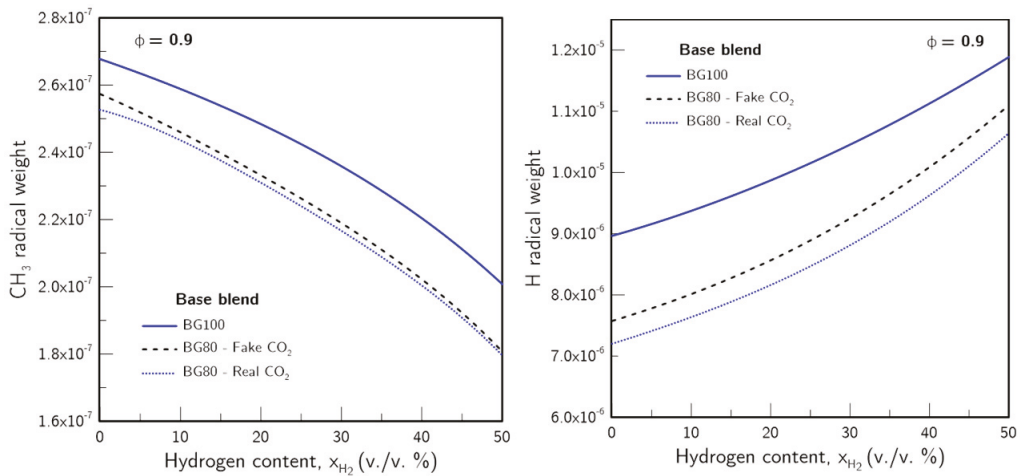


Figure 6. CH_3 and H weight BG100, BG80 and BG80 (FCO_2)/air flames with varying x_{H_2} . The equivalence ratio is 0.9. Conditions were set at $p = 1$ atm and $T_u = 298$ K.

The above-mentioned effect of CO_2 and H_2 on S_L turns the modelling of their impact into a complex task. In the next section, the steps taken to obtain a simple analytical model to quantify the impact of H_2 enrichment on the S_L of lean biogas/air flames are described.

3.2. Analytical Model

As stated in Section 1, this work aims to develop a correlation to model the impact of H_2 enrichment (up to 50%) on the S_L of lean biogas/air flames. Currently, available correlations are either too complex to allow an expeditious use or are not tailored to hydrogen-enriched biogas blends [19,37]. Because of this, existing expressions require a priori undertakings to determine several fit parameters or to adapt mathematical formulations. Their complexity requires, in some cases, the estimation of several fit parameters on a case-by-case basis, hindering the expeditious aim of a correlation of this sort. Hence, it seems that these alternatives only seem applicable in an academic or advanced industry environment where computational cost might not be a significant issue. Additionally, these alternatives fail to specifically address the case of H_2 -enriched biogas, thus combining the contributions of hydrogen and carbon dioxide in fit parameters that also depend on other variables. This implies that the user of any of these models has to determine new fit parameters every time the base biogas blend or the hydrogen enrichment level are changed, as x_{H_2} and x_{CO_2} are not function arguments. Here, simplicity and fast use were adopted as priorities to improve on the options already available in the literature.

In a previous work, Quintino and Fernandes [20] quantified the impact of CO_2 dilution on the S_L of CH_4 /air lean flames and introduced a new analytical model to predict this effect. The final model is presented in Equation (4), and its details can be found in the original research. Thus, for the new model, it was intended to achieve an expression that isolated in different terms the contributions of CO_2 and H_2 for the S_L of CH_4 / CO_2 / H_2 /air lean flames. To this end, Equation (4) was adopted to estimate an intermediate flame speed $S'_L(x_{\text{CO}_2})$ that encompasses the effect of CO_2 in the base biogas blend. Based on the simulation outputs presented in the previous section, an iterative procedure as described in Section 2 was employed to obtain the model. Considering the curves in Figures 1–3, the following constraints were set: $dS_L/dx_{\text{H}_2} > 0$ and $d^2S_L/dx_{\text{H}_2}^2 > 0$ for $0\% \leq x_{\text{H}_2} \leq 50\%$. Furthermore, a minimum coefficient of determination (R^2) of 0.99 was ensured. For the formulations tested that complied with all established criteria, the choice was based on the expression's simplicity.

Based on this approach, the following correlation for the impact of H₂ enrichment on the S_L of biogas/air lean flames is proposed:

$$S_L(x_{H_2}) = \frac{\zeta(\phi)}{S'_L(x_{CO_2})} x_{H_2} e^{x_{H_2}} + S'_L(x_{CO_2}) \quad (8)$$

where $S_L = S_L(x_{H_2})$ is the laminar flame speed of the H₂-enriched flame mixture, $S'_L = S'_L(x_{CO_2})$ is the intermediate flame speed computed with Equation (4), x_{CO_2} is the CO₂ content of the base biogas blend, x_{H_2} is the hydrogen fraction in the flame mixture (Equation (5)) and $\zeta = \zeta(\phi)$ is a fit parameter that varies with the equivalence ratio ϕ . The variation of ζ with ϕ was evaluated, and a data fit was performed. The values obtained and the correspondent data fit can be found in Figure 7. The obtained expression took the form: $\zeta(\phi) = -0.3143 \times \phi^2 + 0.7437 \times \phi - 0.35$, with $R^2 = 0.9974$.

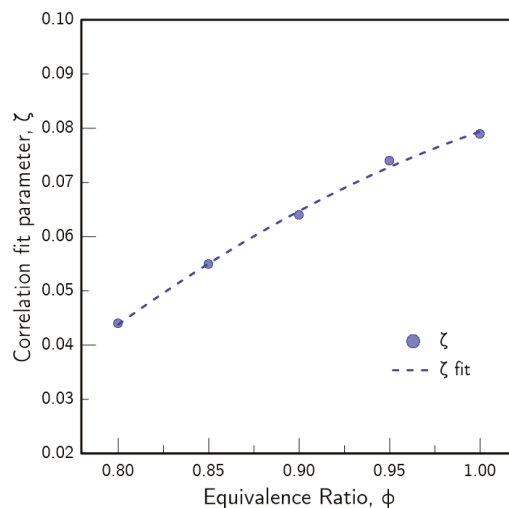


Figure 7. Variation of the fit parameter ζ with the equivalence ratio. The correspondent data fit curve is also displayed.

The final model compared well with the numerical results. The lowest coefficient of determination ($R^2 = 0.9903$) was found for BG80 at $\phi = 1.0$ and the highest ($R^2 = 0.9983$) for BG100 at $\phi = 1.0$.

The model proposed by Quintino and Fernandes [20] in 2018 improved the original correlation established by Metgalchi and Keck [14] in 1982 by re-defining fit parameters and modifying the term that quantifies the impact of diluents in the mixture. Equation (4) models the effect of CO₂ concentration on the laminar flame speed of biogas/air flames, which permits a fast estimation of S_L for varying biogas composition. Equation (4) proved to be a significant improvement on Equation (3), which was shown to fail for biogas blends [20]. Thus, Equation (4) extended the original range of application of Equation (3) by accurately predicting the impact of CO₂ content on S_L . However, this improved correlation did not account for the possibility of blending other fuels with biogas. The model proposed in Equation (8) predicts the S_L of biogas when enriched with H₂, thus extending the range of application of Equations (3) and (4). The most significant novelty of this work is that the developed model (Equation (8)) only requires a single fit parameter $\zeta(\phi)$ for the S_L prediction of H₂-enriched biogas/air flames. In opposition to alternative correlations, where lookup tables are required to readjust parameters according to blend composition, the new model proposed in this work is ready to use for CO₂ content up to 20% in the biogas blend and H₂ enrichment up to 50%.

3.3. Validation

As stated above, the analytical model of Equation (8) presented values in agreement with the numerical simulations performed. To validate the developed model, a collection of results from the literature was compared to the model predictions. These publications encompassed different numerical and experimental methods of S_L determination, as well as base blends with two levels of CO_2 content (BG100 and BG80). This collection is compiled and summarized in Table 2.

Table 2. Published work on laminar flame speed of lean $\text{CH}_4/\text{CO}_2/\text{H}_2$ /air flames used to validate the correlation of this work.

Authors	Method	ϕ	p	T_u	Ref.
Hermanns	Heat flux burner	0.8, 0.9, 1.0	1 atm	298 K	[38]
Coppens et al.	Heat flux burner	0.8, 0.9, 1.0	1 atm	298 K	[37]
Halter et al.	Constant volume bomb	0.8, 0.9, 1.0	1 bar	298 K	[39]
Yadav et al.	Flat flame burner and Ansys (GRI3.0)	0.8, 0.9, 1.0	1 bar	298 K	[40]
Wei et al.	Premix Code (GRI3.0)	0.9, 1.0	1 atm	298 K	[30]

The first two references of Table 2 employ the heat flux burner method to estimate S_L [37,38]. A constant volume bomb experiment is also included [39], as well as tests with a flat flame burner [40]. Simulations ran with Ansys [40] and Premix Code [30] fed with the GRI-Mech 3.0 mechanism [41] were also used.

Based on the developed model (Equation (8)) and on available literature results, two data sets are plotted, for BG100 and BG80. For each base blend, literature data are plotted against model predictions in the range $0\% \leq x_{\text{H}_2} \leq 50\%$ and for $\phi = 0.8, 0.9, 1.0$. The resulting graphs are exhibited in Figures 8 and 9, for BG100 and BG80, respectively.

Overall, the correlation predictions exhibited good concordance with the literature data. The agreement was better at $\phi = 0.9$ and 1.0 , with similar performance whether the base blend was BG100 or BG80. A detailed evaluation of the data in both plots shows that the average percentage difference between the correlation prediction and literature data was 4.44% for BG100 (Figure 8) and 4.02% for BG80 (Figure 9). For the case of BG100, differences lied within the interval $[0.09, 15.62]\%$, whereas for BG80 this interval was $[0.09, 12.02]\%$. The highest differences were found for $\phi = 0.8$, where the correlation tended to overestimate the literature data, even though the difference never exceeded 0.056 m/s. The highest differences were found in the data of Figure 8, where the correlation prediction was considerably higher than the data collected from the work developed by Halter et al. [39]. In their work, a spherical combustion chamber was coupled to a shadowgraphy system, and flame pictures were captured by a high-speed camera. Experiments were conducted for CH_4/H_2 /air flames with the global equivalence ratio varying from 0.7 to 1.2. These were then compared to CHEMKIN simulations fed with the GRI-Mech 3.0 kinetics mechanism [41]. Measurements performed by Halter et al. (Figure 7 of reference [39]) at $\phi = 0.8$ exhibited the poorest agreement with CHEMKIN simulations and seemed to contrast with other published data. Thus, it appears that the impact of H_2 content on S_L was well captured by the model of the present work. The literature data also exhibited a non-linear S_L increase with x_{H_2} . This supports the hypothesis, stated in Section 3.1, that the H_2 related kinetics takes over the CH_4 related one as x_{H_2} is increased.

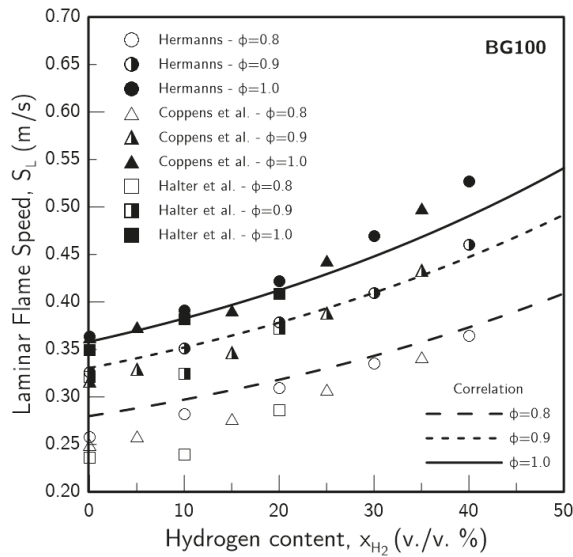


Figure 8. Laminar flame speed of H₂-enriched BG100/air flames. Symbols are literature results, and lines are the application of the correlation of this work.

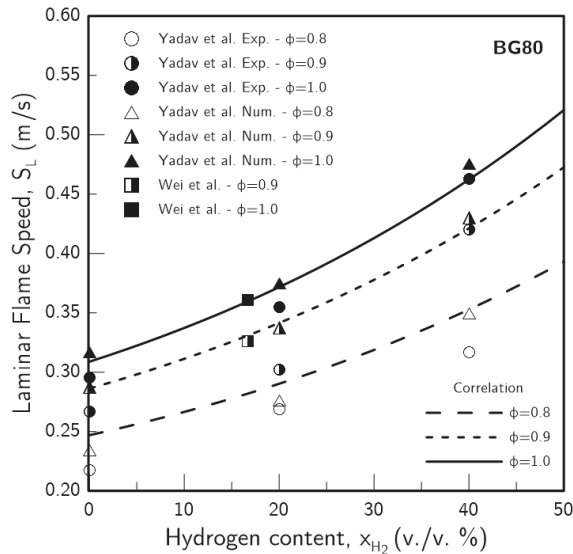


Figure 9. Laminar flame speed of H₂-enriched BG80/air flames. Symbols are the literature results, and lines are the application of the correlation of this work.

On top of the comparison with the literature data, model predictions were evaluated with every S_L value resulting from the performed simulations. Numerical results were compared to model predictions to evaluate if any subset of points were poorly captured by the developed correlation. Figure 10 exhibits this analysis' output.

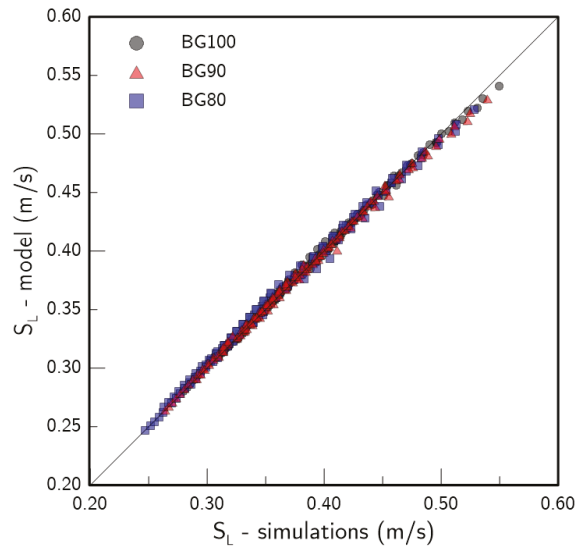


Figure 10. Model predictions vs. the numerical results of laminar flame speed S_L . Symbols indicate base biogas compositions. All equivalence ratio and H_2 enrichment conditions produced in this work are included.

The data in Figure 10 demonstrate that the correlation displayed a good performance not only on average, but also for the complete set of numerical data produced in this work. There were no significant accuracy differences identified among BG100, BG90 and BG80. The percentage difference between the correlation predictions and simulations never exceeded 2.91%, with an average difference of 0.74%. Thus, the model in Equation (8) can be considered an accurate representation of the S_L values yielded by the simulations conducted in Cantera with USC-Mech 2.0. Overall, the analytical model exhibited a good agreement with the experiments, indicating that numerical simulations also compared well with the literature data.

This new model should be particularly relevant in burner design and gas interchangeability analysis involving $CH_4/CO_2/H_2$ blends. Examples of this are the research developed by Jones et al. [42] and Vries et al. [43], where flashback and blowoff limits for domestic appliances were evaluated in a context where hydrogen is blended in the fuel feed. The determination of the theoretical flame stability first requires a prediction of the flame speed as a function of hydrogen content. The model developed in this work is tailored for these sorts of analysis, given its low average uncertainty of 0.74% when compared with simulations and 4.44% when compared with literature data. Therefore, it provides an accurate description of S_L for CO_2 content up to 20% in the biogas blend and H_2 enrichment up to 50%.

4. Conclusions

In this work, 1D PPF simulations were conducted in Cantera to assess the impact of H_2 enrichment on the S_L of biogas/air lean flames. Furthermore, numerical results were employed in the development of an analytical correlation to model this effect. Simulations were conducted for three base biogas blends (BG100, BG90 and BG80) with H_2 content in the fuel mixture (x_{H_2}) up to 50% and an equivalence ratio (ϕ) between 0.8 and 1.0. The approach undertaken in this work allowed the quantification of CO_2 and H_2 effects on S_L , by evaluating the dilution, thermal-diffusive and chemical impacts. The numerical model made it possible to run simulations with both real (CO_2) and fake (FCO_2) carbon

dioxide to isolate the different effects of its presence on S_L . Finally, the analytical correlation was tested against data from the literature. The main findings are summarized below:

1. The introduction of H_2 in the fuel blends produced a greater effect on S_L the higher the CO_2 content was. Furthermore, the increase in S_L due to H_2 enrichment was non-linear, with a more pronounced effect the higher x_{H_2} was. This was found to be linked with an increase in the H radical pool, which resulted from greater H production through the sub-mechanism of the water-gas shift (WGS) reaction.
2. The presence of H_2 in the fuel blend tended to mitigate the thermal-diffusive and concentration effects of CO_2 on S_L . These effects were the highest contributor for S_L reduction for low x_{H_2} . However, these gradually subsided as x_{H_2} increased, while the CO_2 chemistry maintained a consistent impact. Thus, for practical applications, higher amounts of H_2 -enrichment may avoid the need to completely remove carbon dioxide from biogas blends.
3. H_2 enrichment was found to weaken the CH_4 related chemistry as the CH_3 radical pool was significantly impacted. The reduction of the CH_3 radical presence was found to be not directly proportional to the CH_4 concentration, with an acceleration of its reduction with increasing x_{H_2} .
4. Based on the numerical results, a new correlation to model the impact of H_2 enrichment on the S_L of lean biogas/air flames was proposed:

$$S_L(x_{H_2}) = \frac{\zeta(\phi)}{S'_L(x_{CO_2})} x_{H_2} e^{x_{H_2}} + S'_L(x_{CO_2}) \quad (9)$$

where $S_L = S_L(x_{H_2})$ is the laminar flame speed of the H_2 -enriched flame mixture, $S'_L = S'_L(x_{CO_2})$ is the intermediate flame speed computed with Equation (4), x_{CO_2} is the CO_2 content of the base biogas blend, x_{H_2} is the hydrogen fraction in the flame mixture (Equation (5)) and $\zeta = \zeta(\phi)$ is a fit parameter. The correlation exhibited good agreement with literature data and with simulations for all of the tested conditions. This new model isolates the contribution of H_2 and CO_2 as both are arguments of the function that yield $S_L = S_L(x_{H_2}, \phi, S'_L(x_{CO_2}))$. Thus, the final model can be directly used to estimate S_L without the need for a priori adaptations of fit parameters for varying base blends as the correlation itself accomplishes that goal. The fast and reliable estimation of S_L for H_2 -enriched biogas blends makes this model useful for the adaptation or development of existing devices that rely on these blends.

Concluding remarks:

The model proposed in this work provides an engineering approach to estimate S_L for fuel-lean combustion of H_2 -enriched biogas blends. In contexts where biogas is widely available, the admixture of renewable hydrogen can improve equipment performance or even allow the possibility of using lower quality biogas blends, which would otherwise remain unused or burned in flares. Future research could address fuel-rich conditions. These configurations, typically found in the ceramics and glass industry for radiative heat transmission purposes, will eventually shift from natural gas to renewable gases. The use of biogas will likely require hydrogen admixture to compensate for the loss in CH_4 . The development of an analytical model for fuel-rich conditions will require a reassessment of reaction kinetics and an adaptation of the original model proposed by Quintino and Fernandes in 2018 [20]. The USC Mech 2.0, employed in this research, should cope well with such conditions since it was subject to validation with proven $H_2/CO/C_1-C_4$ combustion data. However, the development of a new correlation for fuel-rich conditions must cope with the variability of the maxima location in relation to the equivalence ratio. The hydrogen enrichment of biogas, in fuel-rich conditions, will push the maximum value of S_L for higher values of ϕ as x_{H_2} is increased. This phenomena must be well captured by any new model proposed in the future.

Author Contributions: Conceptualization, F.M.Q. and E.C.F.; methodology, F.M.Q.; software, F.M.Q.; validation, F.M.Q. and E.C.F.; formal analysis, F.M.Q.; investigation, F.M.Q.; resources, E.C.F.; data curation, F.M.Q.; visualization, F.M.Q.; writing, original draft preparation, F.M.Q.; writing, review and editing, E.C.F.; supervision, E.C.F. All authors read and agreed to the published version of the manuscript.

Funding: F.M. Quintino acknowledges Fundação para a Ciência e Tecnologia for the provision of the scholarship PD/BD/140184/2018.

Conflicts of Interest: The authors declare no conflict of interest.

Abbreviations

The following abbreviations are used in this manuscript:

1D	One-dimensional
BG	Biogas
EGR	Exhaust gas recirculation
FPF	Freely propagating flame
USC	University of Southern California
WGS	Water-gas shift

References

- Gillingham, K.; Huang, P. Is abundant natural gas a bridge to a low-carbon future or a dead-end? *Energy J.* **2019**, *40*. [CrossRef]
- Speirs, J.; Balcombe, P.; Johnson, E.; Martin, J.; Brandon, N.; Hawkes, A. A greener gas grid: What are the options. *Energy Policy* **2018**, *118*, 291–297. [CrossRef]
- Glenk, G.; Reichelstein, S. Economics of converting renewable power to hydrogen. *Nat. Energy* **2019**, *4*, 216–222. [CrossRef]
- Lantz, M. *Biogas in Sweden—Opportunities and Challenges from a Systems Perspective*; Lund University: Lund, Sweden, 2013.
- Patricio, R.; Sales, A.; Sacramento, E.; De Lima, L.; Veziroglu, T. Wind hydrogen energy system and the gradual replacement of natural gas in the State of Ceará—Brazil. *Int. J. Hydrogen Energy* **2012**, *37*, 7355–7364. [CrossRef]
- Roubík, H.; Mazancová, J.; Le Dinh, P.; Dinh Van, D.; Banout, J. Biogas quality across small-scale biogas plants: A case of central Vietnam. *Energies* **2018**, *11*, 1794. [CrossRef]
- Korberg, A.D.; Skov, I.R.; Mathiesen, B.V. The role of biogas and biogas-derived fuels in a 100% renewable energy system in Denmark. *Energy* **2020**, *199*, 117426. [CrossRef]
- Saccani, C.; Pellegrini, M.; Guzzini, A. Analysis of the Existing Barriers for the Market Development of Power to Hydrogen (P2H) in Italy. *Energies* **2020**, *13*, 4835. [CrossRef]
- Quintino, F.M.; Fernandes, E.C. Interchangeability Analysis of Biogas and Hydrogen Blends. In Proceedings of the 27th European Biomass Conference and Exhibition Proceedings, Lisbon, Portugal, 27–30 May 2019; pp. 736–741. [CrossRef]
- Barlow, R.; Frank, J.; Karpetis, A.; Chen, J.Y. Piloted methane/air jet flames: Transport effects and aspects of scalar structure. *Combust. Flame* **2005**, *143*, 433–449. [CrossRef]
- Turns, S.R. *Introduction to Combustion*; McGraw-Hill Companies: New York, NY, USA, 1996; Volume 287.
- Lu, T.; Law, C.K. Toward accommodating realistic fuel chemistry in large-scale computations. *Prog. Energy Combust. Sci.* **2009**, *35*, 192–215. [CrossRef]
- Lu, T.; Law, C.K. A directed relation graph method for mechanism reduction. *Proc. Combust. Inst.* **2005**, *30*, 1333–1341. [CrossRef]
- Metghalchi, M.; Keck, J.C. Burning velocities of mixtures of air with methanol, isooctane, and indolene at high pressure and temperature. *Combust. Flame* **1982**, *48*, 191–210. [CrossRef]
- Gülde, O. Burning velocities of ethanol–air and ethanol–water–air mixtures. *AIAA Progr Astronaut Aeronaut* **1984**, *95*, 181–197.
- Liao, S.; Jiang, D.; Cheng, Q. Determination of laminar burning velocities for natural gas. *Fuel* **2004**, *83*, 1247–1250. [CrossRef]
- Han, P.; Checkel, M.D.; Fleck, B.A.; Nowicki, N.L. Burning velocity of methane/diluent mixture with reformer gas addition. *Fuel* **2007**, *86*, 585–596. [CrossRef]
- Elia, M.; Ulinski, M.; Metghalchi, M. Laminar burning velocity of methane–air–diluent mixtures. *J. Eng. Gas Turbines Power* **2001**, *123*, 190–196. [CrossRef]
- Bougrine, S.; Richard, S.; Nicolle, A.; Veynante, D. Numerical study of laminar flame properties of diluted methane–hydrogen–air flames at high pressure and temperature using detailed chemistry. *Int. J. Hydrogen Energy* **2011**, *36*, 12035–12047. [CrossRef]
- Quintino, F.; Fernandes, E. Analytical correlation to model diluent concentration repercussions on the burning velocity of biogas lean flames: Effect of CO₂ and N₂. *Biomass Bioenergy* **2018**, *119*, 354–363. [CrossRef]
- Goodwin, D.G.; Moffat, H.K.; Speth, R.L. *Cantera: An Object-Oriented Software Toolkit for Chemical Kinetics, Thermodynamics, and Transport Processes*; Caltech: Pasadena, CA, USA, 2009.
- Wang, H.; You, X.; Joshi, A.V.; Davis, S.G.; Laskin, A.; Egolfopoulos, F.; Law, C.K.; Version II, U.M. High-Temperature Combustion Reaction Model of H₂. Technical Report; CO/C1–C4 Compounds. 2007. Available online: http://ignis.usc.edu/Mechanisms/USC-MechII/USC_MechIII.htm (accessed on 14 December 2020).

23. Zhang, Y.; Jiang, X.; Wei, L.; Zhang, J.; Tang, C.; Huang, Z. Experimental and modeling study on auto-ignition characteristics of methane/hydrogen blends under engine relevant pressure. *Int. J. Hydrogen Energy* **2012**, *37*, 19168–19176. [CrossRef]
24. Ren, F.; Chu, H.; Xiang, L.; Han, W.; Gu, M. Effect of hydrogen addition on the laminar premixed combustion characteristics the main components of natural gas. *J. Energy Inst.* **2019**, *92*, 1178–1190. [CrossRef]
25. Qian, Y.; Sun, S.; Ju, D.; Shan, X.; Lu, X. Review of the state-of-the-art of biogas combustion mechanisms and applications in internal combustion engines. *Renew. Sustain. Energy Rev.* **2017**, *69*, 50–58. [CrossRef]
26. Xie, Y.; Wang, J.; Xu, N.; Yu, S.; Huang, Z. Comparative study on the effect of CO₂ and H₂O dilution on laminar burning characteristics of CO/H₂/air mixtures. *Int. J. Hydrogen Energy* **2014**, *39*, 3450–3458. [CrossRef]
27. Chen, Z.; Tang, C.; Fu, J.; Jiang, X.; Li, Q.; Wei, L.; Huang, Z. Experimental and numerical investigation on diluted DME flames: Thermal and chemical kinetic effects on laminar flame speeds. *Fuel* **2012**, *102*, 567–573. [CrossRef]
28. Stylianidis, N.; Azimov, U.; Birkett, M. Investigation of the effect of hydrogen and methane on combustion of multicomponent syngas mixtures using a constructed reduced chemical kinetics mechanism. *Energies* **2019**, *12*, 2442. [CrossRef]
29. Law, C.K. *Combustion Physics*; Cambridge University Press: Cambridge, UK, 2010.
30. Wei, Z.; He, Z.; Zhen, H.; Zhang, X.; Chen, Z.; Huang, Z. Kinetic modeling investigation on the coupling effects of H₂ and CO₂ addition on the laminar flame speed of hydrogen enriched biogas mixture. *Int. J. Hydrogen Energy* **2020**, *45*, 27891–27903. [CrossRef]
31. Glarborg, P.; Bentzen, L.L. Chemical effects of a high CO₂ concentration in oxy-fuel combustion of methane. *Energy Fuels* **2008**, *22*, 291–296. [CrossRef]
32. Xie, Y.; Wang, J.; Zhang, M.; Gong, J.; Jin, W.; Huang, Z. Experimental and numerical study on laminar flame characteristics of methane oxy-fuel mixtures highly diluted with CO₂. *Energy Fuels* **2013**, *27*, 6231–6237. [CrossRef]
33. Westbrook, C.K.; Dryer, F.L. Chemical kinetic modeling of hydrocarbon combustion. *Prog. Energy Combust. Sci.* **1984**, *10*, 1–57. [CrossRef]
34. Halter, F.; Foucher, F.; Landry, L.; Mounaïm-Rousselle, C. Effect of dilution by nitrogen and/or carbon dioxide on methane and iso-octane air flames. *Combust. Sci. Technol.* **2009**, *181*, 813–827. [CrossRef]
35. Rocha, N.; Quintino, F.; Fernandes, E. H₂ enrichment impact on the chemiluminescence of biogas/air premixed flames. *Int. J. Hydrogen Energy* **2020**, *45*, 3233–3250. [CrossRef]
36. Zhang, X.; Mei, B.; Ma, S.; Pan, H.; Wang, H.; Li, Y. Experimental and kinetic modeling investigation on laminar flame propagation of CH₄/CO mixtures at various pressures: Insight into the transition from CH₄ related chemistry to CO related chemistry. *Combust. Flame* **2019**, *209*, 481–492. [CrossRef]
37. Coppens, F.; De Ruyck, J.; Konnov, A.A. Effects of hydrogen enrichment on adiabatic burning velocity and NO formation in methane+ air flames. *Exp. Therm. Fluid Sci.* **2007**, *31*, 437–444. [CrossRef]
38. Hermanns, R.T.E. Laminar Burning Velocities of Methane-Hydrogen-Air Mixtures. Ph.D. Thesis, Technische Universiteit Eindhoven, Eindhoven, The Netherlands, 2007.
39. Halter, F.; Chauveau, C.; Djebaili-Chaumeix, N.; Gökalp, I. Characterization of the effects of pressure and hydrogen concentration on laminar burning velocities of methane-hydrogen-air mixtures. *Proc. Combust. Inst.* **2005**, *30*, 201–208. [CrossRef]
40. Yadav, V.K.; Ray, A.; Ravi, M. Experimental and computational investigation of the laminar burning velocity of hydrogen-enriched biogas. *Fuel* **2019**, *235*, 810–821. [CrossRef]
41. Smith, G.P.; Golden, D.M.; Frenklach, M.; Moriarty, N.W.; Eiteneer, B.; Goldenberg, M.; Bowman, C.T.; Hanson, R.K.; Song, S.; Gardiner, W., Jr.; et al. GRI-Mech 3.0, 1999. 2011. Available online: http://www.me.berkeley.edu/gri_mech (accessed on 14 December 2020).
42. Jones, D.R.; Al-Masry, W.A.; Dunnill, C.W. Hydrogen-enriched natural gas as a domestic fuel: An analysis based on flash-back and blow-off limits for domestic natural gas appliances within the UK. *Sustain. Energy Fuels* **2018**, *2*, 710–723. [CrossRef]
43. De Vries, H.; Mokhov, A.V.; Levinsky, H.B. The impact of natural gas/hydrogen mixtures on the performance of end-use equipment: Interchangeability analysis for domestic appliances. *Appl. Energy* **2017**, *208*, 1007–1019. [CrossRef]

Article

An Artificial Neural Network for the Low-Cost Prediction of Soot Emissions

Mehdi Jadidi, Stevan Kostic, Leonardo Zimmer and Seth B. Dworkin *

Department of Mechanical and Industrial Engineering, Ryerson University, Toronto, ON M5B 2K3, Canada; mehdi.jadidi@ryerson.ca (M.J.); stevan.kostic@ryerson.ca (S.K.); leonardo.zimmer@ryerson.ca (L.Z.)

* Correspondence: seth.dworkin@ryerson.ca

Received: 14 August 2020; Accepted: 11 September 2020; Published: 14 September 2020

Abstract: Soot formation in combustion systems is a growing concern due to its adverse environmental and health effects. It is considered to be a tremendously complicated phenomenon which includes multiphase flow, thermodynamics, heat transfer, chemical kinetics, and particle dynamics. Although various numerical approaches have been developed for the detailed modeling of soot evolution, most industrial device simulations neglect or rudimentarily approximate soot formation due to its high computational cost. Developing accurate, easy to use, and computationally inexpensive numerical techniques to predict or estimate soot concentrations is a major objective of the combustion industry. In the present study, a supervised Artificial Neural Network (ANN) technique is applied to predict the soot concentration fields in ethylene/air laminar diffusion flames accurately with a low computational cost. To gather validated data, eight different flames with various equivalence ratios, inlet velocities, and burner geometries are modeled using the CoFlame code (a computational fluid dynamics (CFD) parallel combustion and soot model) and the Lagrangian histories of soot-containing fluid parcels are computed and stored. Then, an ANN model is developed and optimized using the Levenberg-Marquardt approach. Two different scenarios are introduced to validate the network performance; testing the prediction capabilities of the network for the same eight flames that are used to train the network, and for two new flames that are not within the training data set. It is shown that for both of these cases the ANN is able to predict the overall soot concentration field very well with a relatively low integrated error.

Keywords: soot concentration; soot emissions; artificial neural network; estimator; computational fluid dynamics; combustion

1. Introduction

Soot emissions from combustion processes have damaging effects on both the environment and human health. Soot is the general term used for the class of pollutants known as PM 2.5, which constitutes particulate matter with a diameter less than or equal to 2.5 micrometers [1,2]. The minute nature of the soot particle makes it especially harmful when inhaled by an individual as it quite easily reaches the lungs and bloodstream. It can then lead to a host of serious issues including heart attacks, bronchitis, asthma, strokes, and even death [3]. Furthermore, soot is a notable contributor to climate change, second only to CO₂ [4]. Larger soot aggregates and the smaller soot particulate matter both contribute to the problem. The smaller, lighter particulates remain in the air absorbing sunlight and subsequently warming the surrounding air. On the other hand, the larger, heavier aggregates fall to the ground and absorb sunlight there. As a result, any surrounding snow or ice is melted far faster [4].

The problems outlined above are concerning, thus stricter regulations on soot emissions are becoming commonplace. This is true especially in current times, when efforts to be environmentally

sustainable are at an all-time high and are at the forefront of much in-depth research. For example, new vehicles sold in the European Union and European Economic Area (EEA) member states have rigorous regulations placed upon them [5]. Unfortunately for engine designers worldwide, soot formation is an exceptionally complex phenomenon dependent on numerous physical and chemical processes such as reaction kinetics, thermodynamics, heat transfer, and particle dynamics. The implementation of Computational Fluid Dynamics (CFD) throughout the engine design process has now become mainstream. However, if soot formation mechanisms were considered as part of these simulations, the computational costs would quickly become intractable if any respectable accuracy is to be obtained [6]. Currently, prototypes must be manufactured in order to be certain of the soot emissions a given engine will produce. This time-consuming, expensive, and strenuous method has limited the improvement in this area as many manufacturers are not willing to put forth this great effort to discover the soot emissions of a given engine. The balance between computational cost and accuracy of results quickly presents itself as an obstacle for this industry, as it often does for many others.

In CFD simulations, numerical accurate modelling and prediction of soot properties, such as concentration and particle size and shape, remains challenging due to the collective chemical, physical and thermodynamic interactions, and multiphase flow [7,8]. Previous numerical studies of soot evolution in laminar and turbulent flames have been based on different levels of fidelity. Many of these previous studies have utilized semi-empirical soot models coupled with simplified combustion models. In these studies, soot concentrations have generally not been predicted with acceptable accuracy, with errors in soot concentration ranging from one to two orders of magnitude or more [7,9–11]. Conversely, some studies use more accurate soot models, like the soot model explained in the CoFlame code [12] and hybrid method of moments (HMOM) developed by Mueller et al. [13], that allow for the description of soot volume fraction, number density, and morphology of the aggregates. In these models, in addition to the influence of local concentrations of various species, temperature, and pressure, the effects of various chemical and physical phenomena such as particle nucleation from Polycyclic Aromatic Hydrocarbons (PAHs), PAH dimer condensation, physical coagulation, surface growth by the hydrogen-abstraction-carbon-addition (HACA) mechanism, oxidation, and oxidation-induced fragmentation on soot evolution are considered [12,14,15]. Simulating all the aromatic precursors and the phenomena mentioned above causes the high-fidelity soot models to be computationally expensive.

To model soot evolution in turbulent flames, several Large Eddy Simulation (LES) studies have been attempted [7,8,11]. In general, in addition to modelling soot and precursor chemistry, the high fidelity LES-based models comprise models for turbulence-soot-chemistry interactions at the subfilter scale [8]. In this case, uncertainties related to the models of subfilter fluctuations would be added to the uncertainties associated with the soot model and the chemical kinetic mechanism [8,16]. It should be pointed out that the models of subfilter fluctuations depend on the employed soot model (for instance, state-of-the-art models of subfilter fluctuations are based on HMOM soot model [8,13]). Therefore, by changing the soot model, the models of subfilter fluctuations need to be modified [7]. Furthermore, one of the most important issues relates to the errors associated with combustion models [8,16], which can affect the soot prediction significantly. As an example, the recent work of Wick et al. [16] is worth mentioning here. They performed an investigation to show how errors related to combustion models (for example, flamelet models) propagate through into the mechanisms of soot characteristic prediction via interactions between the gas and solid phase. In their work, the coupling of a Flamelet/Progress Variable model with the HMOM soot model was analysed using Direct Numerical Simulation (DNS) results [15], where the same soot model (HMOM) was used. It was found that there are significant errors in the predicted soot field, which are traced back to tabulated quantities in the flamelet library propagating through the computation via PAH-based growth rates. Overall, this body of work indicates that LES-based soot models are still limited and more studies should be conducted to improve these models. However, it is clear that to model soot evolution, not only is a combustion model needed, along with a soot model and models for subfilter scale turbulence-soot-chemistry interactions, but all the aromatic precursors as well as the physics involved (for instance, aromatic collision or

PAH condensation) should be simulated, which is a challenging task and computationally expensive. Conversely, as mentioned above, the low-cost and precise estimation of soot properties, such as concentration, has become highly desired for industry. Therefore, to tackle this controversy, a novel soot estimator concept has been recently developed and validated [6,17–19].

The idea of linking a post-processing tool to CFD simulations to estimate soot characteristics accurately with a low computational cost was first proposed by Bozorgzadeh [19]. As a proof of concept, a post-processing technique for laminar flames was proposed by Alexander et al. [6] in 2018. The aforementioned work has been further amended where accuracy was improved and turbulent flame data was used, albeit with limited success [18,19]. The prediction method described in these papers is a rudimentary library consisting of a collection of data arrays from which desired values can be interpolated. The most recent work [18] demonstrates exceptional success when estimating the soot volume fraction of nine different steady laminar flames when the library comprises data of the same nine flames being tested.

Theoretically, the rate of soot formation (or destruction) can be thought to depend entirely on local system characteristics at any point in time t as

$$\frac{df_v(t)}{dt} = f(T(t), Y_i(t), P(t), f_v(t), A_s(t), \dots), \quad (1)$$

where T , Y_i , P , f_v and A_s are the temperature, the mass fraction of species i , the pressure, the soot volume fraction (concentration), and the average soot surface area, respectively. The idea of a soot estimator was based on this assumption that to calculate f_v , libraries (like the thermodynamic tables) can be created in which the values of different variables such as temperature and mass fractions are stored. However, due to the longer timescales of soot formation as compared to those of flow and gas-phase chemistry, and the inherent non-linearity of the problem, soot characteristics cannot be considered to be related only to especially local properties [18]. Veshkini et al. [20] and Kholghy et al. [21] showed that soot evolution is a stronger function of the temporal history of soot particles than just local flame characteristics. Therefore, within the soot estimator approach [6,17,18], it was assumed that the local instantaneous soot volume fraction f_v is a function of the temporal history of key variables in a combustion process. The fundamental formula from which the soot estimator concept was developed is as follows:

$$f_v(t) = f(T_h(t), Y_{i,h}(t), P_h(t), f_{v,h}(t), A_{s,h}(t), \dots), \quad (2)$$

where T_h , $Y_{i,h}$, P_h , $f_{v,h}$ and $A_{s,h}$ are the temperature time-integrated history, the mass fraction history of species i , the pressure history, the time-integrated history of soot volume fraction, and the average soot surface area history, respectively.

By using the soot estimator approach, Alexander et al. [6] and Zimmer et al. [18] showed that it is possible to estimate soot volume fraction, in an uncoupled manner, by tracking the histories of certain properties (temperature, species concentration) of fluid parcels. Therefore, only the gas phase conservation equations for mass, momentum, energy, and species mass fraction need to be solved in a simulation, and different soot-related terms such as soot nucleation, coagulation, etc., which are typically included in advanced soot models as well as the statistical particle dynamics equations (for example, see the equations of conservation of soot aggregate number density and conservation of soot primary particle number density in the CoFlame code [12]) are not required to be solved. Therefore, much less computational effort would be needed.

For applying the soot estimator approach, at first, the gas-phase temperature, pressure, species mass fractions, etc. (the parameters on the right side of Equation (2)) should be obtained from a validated sooting flame model. Alexander et al. [6] and Zimmer et al. [18] used the CoFlame code to gather these parameters for nine different flames. Then, in these studies, the Lagrangian temporal histories of soot-containing fluid parcels were stored. They defined a specific number of dimensions to the library, corresponding to the variable histories that were being considered, and a specific number of bins in each dimension. The soot volume fraction resulting from each fluid parcel history, corresponding

to those variable histories, were then stored in each bin. Due to practical constraints encountered in those works, only a few parameters could be stored in the library. In Reference [18], three data dimensions (the histories of temperature, mixture fraction, and hydrogen radical concentration) were used to estimate f_v :

$$f_v(t) \approx f(T_h(t), MF_h(t), H_{2,h}(t)), \quad (3)$$

where MF_h is the mixture fraction history. In their work [18], 300 bins of refinement in each dimension was also assumed so that a $300 \times 300 \times 300$ bin library, from which to interpolate, was created. Using this approach, the computational cost was kept moderate due to the reasons stated above. Furthermore, compared to the detailed numerical simulations (obtained from the CoFlame code where the gas-phase, as well as soot partial differential equations, were solved numerically), the average integrated error for prediction of the entire soot field across all flames was 0.42% [18]. However, the drawback of the method became evident when extending to transient and turbulent flows, where the timescales of the data are much larger, and the limited refinement of the data array becomes evident [17].

From the above discussion, it becomes clear that the accuracy of the approach developed previously [6,17,18] depends on the number of data dimensions and the number of bins. The work presented in Reference [18] was limited to three data dimensions and 300 bins of refinement in each dimension to avoid memory and compute time issues associated with dimensionality. The memory requirement in this approach [6,17,18] is a serious hindrance. Considering the example of a $300 \times 300 \times 300$ library, the method implemented in the previous work requires multiple arrays that have lengths equal to the total number of bins, that is $300 \times 300 \times 300 = 27,000,000$. Creating a $1 \times 27,000,000$ array using MATLAB R2018a requires 0.216 GB. This allows many arrays of the same size to be created with no issues. However, scaling to an additional dimension in search of further algorithm capability, the mesh now becomes a $300 \times 300 \times 300 \times 300$ field with a total of 8,100,000,000 bins. Creating a similar array to the one mentioned earlier with the updated number of bins will cost 60.3 GB, and therefore multiple arrays of this size cannot be created on a personal computer. A compromise in the number of dimensions used, or the number of bins per dimension, must then be made, hindering the scientific assessment of accuracy.

If the latter approach is chosen and the number of dimensions is increased to four while the number of bins is decreased to compensate, the idea of sparsity becomes more evident. When increasing the dimensions of the data field being analyzed, the available data quickly fills a smaller and smaller area of the entire field. With respect to the bin approach used in previous works, this would mean that the data would only fill a tiny portion of the millions of available bins. This is an inefficient use of memory and computational power. However, if added dimensions are not considered, plenty of available data is essentially discarded as it is not considered at all. These reasons, amongst others, inspired the notion of discovering a new method with which the post-processing tool can be implemented.

In the current work, a Neural Network is generated and taught by data from the CoFlame code [12] as a post-processing tool to estimate the soot volume fraction numerically with a low computational cost at various conditions. As mentioned above, this tool is necessary because, in industrial device simulations, soot formation is typically neglected or rudimentarily approximated due to high computational cost. The tool developed in this study would be able to estimate soot characteristics while it only needs properties from the gas-phase conservation equations (mass, momentum, energy and species mass fractions) as inputs. Therefore, the cost-benefit would be considerable since the soot-related terms and equations are not required to be solved in the flow model (the soot quantities such as volume fraction are obtained from the trained network using the model data as inputs). In the present study, issues of dimensionality that were observed previously in the library-based soot estimator models are less prevalent. This advantage will be crucial toward extending the concept of the soot estimator to transient and turbulent flames. However, it is worth mentioning that any error in the CFD model results can propagate into the estimator framework because the input/output datasets are directly obtained from the CFD simulations. As CFD simulations get more accurate, and more and more data are used to teach the network, this error propagation

effect will diminish. It should be noted that, to the authors' best knowledge, the present work is the first attempt to train artificial neural networks (ANNs) based on detailed modeling of soot formation. The methodology, fundamentals of ANN, data pre-processing, and network training are discussed in the following section. In the results section, the ANN predictions as well as its performance and error analysis are explained.

2. Methodology

Although not an entirely new concept, ANNs have recently become more prevalent due to their amazing flexibility and plethora of use cases. Before investigating the advantages of this method and precisely why it was preferred to others, it is important to establish an introductory level of knowledge about the actual processes going on within the model. A basic representation of the architecture of an ANN can be seen in Figure 1 below.

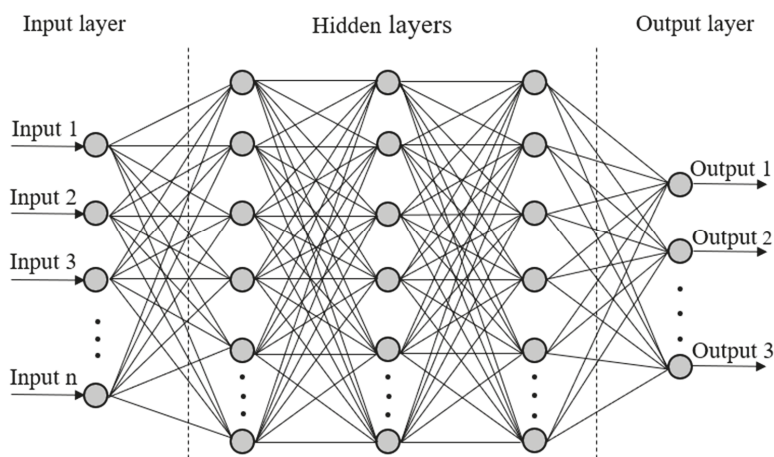


Figure 1. A schematic representation of an artificial neural network.

Inspecting this architecture, it is clear to see that there are three main sections to examine. Each section can be referred to as a layer; at a minimum, every ANN will have at least three layers, the input, output, and hidden layers. While every single network is limited to only one input and one output layer, the number of hidden layers between them can be arbitrarily set to any number, wholly dependent on the desired accuracy and available computational power [22]. In general, the simplest ANN has only one hidden layer, while deep neural networks have multiple hidden layers. Similarly, each layer consists of a number of hidden nodes, or neurons, where calculations take place. The input and output layers are limited in the number of neurons they can have by the number of input variables being provided and the number of output variables desired by the user. Once again, the hidden layers are the flexible part of the network. As such, the number of neurons in the hidden layers remains unlimited in theory [22]. The basic premise of the network is that any neuron in a given layer is connected to every single neuron in the layers immediately surrounding it. Each connection between two neurons has a weight associated with it. The output from a given neuron is obtained by applying a non-linear function to the weighted sum of inputs to that neuron and an overall bias. The weights and biases are initially random; however, they are adjusted as the network *learns* from the data provided to it. The non-linear function within each neuron that is central to the calculations is referred to as the activation function [22]. Many functions are available for use; however, two commonly used ones are the hyperbolic tangent and the rectified linear unit (*ReLU*) functions [23]. Figure 2 shows a schematic representation of an individual neuron unit, including the various inputs and outputs. The figure depicts inputs x_1, x_2, \dots, x_j , each with a corresponding weight

$w_1, w_2, \dots w_j$, the summation function with bias, b , and the activation function f , which leads to the output. In addition, the hyperbolic tangent as well as $ReLU$ activation functions are shown in Figure 3. As can be seen, $tanh$ can only vary between -1 and 1 . Moreover, $tanh$, as well as its derivative, are both monotonic functions. Put more explicitly, the output of a neuron with the hyperbolic tangent activation function is

$$f(s) = \tanh(s) = \frac{(e^s - e^{-s})}{(e^s + e^{-s})}, s = \sum_{i=1}^j w_i x_i + b, \tag{4}$$

and for the $ReLU$ activation function, it is

$$f(s) = ReLU(s) = \begin{cases} 0, & s < 0 \\ s, & s \geq 0 \end{cases}, \tag{5}$$

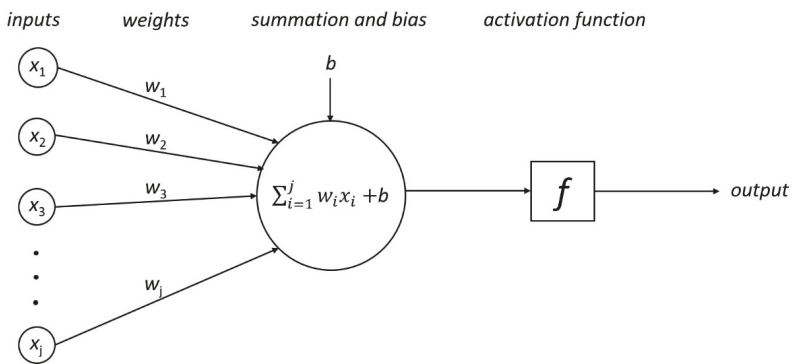


Figure 2. A schematic representation of a single neuron.

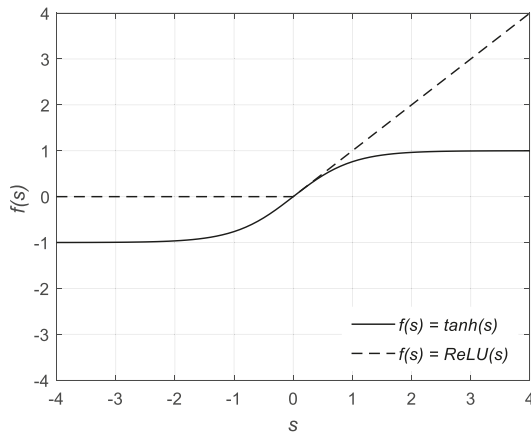


Figure 3. The hyperbolic tangent and the rectified linear unit ($ReLU$) functions.

In the present study, the concept of supervised learning is utilized. Supervised learning is a type of machine learning model in which the relationship between the input and output of a system is obtained based on a given training sample of input-output pairs. The objective of supervised learning is to teach an artificial system like the neural network a way to map inputs to outputs, using the prescribed structure, so that the output can quickly be determined for any set of inputs fed [24]. For supervised learning, the entire data set is often split into three subsections; the training, validation, and testing sets.

The training set is usually the largest and it comprises the data that is fed into the network as a way for it to learn from the data and adjust itself based on the error. The validation set is used to measure the generalization of the network—essentially how well the network will perform with unseen data. This subset is particularly important because it will serve to provide an indicator as when to stop training. If the generalization of the network stops improving, the training will be discontinued as a means of preventing overfitting, which is when the neural network over-trains itself such that it is well-suited to the particular training data, but will not reproduce results well that are outside of this data set. The testing data set is very similar to the validation set, in that they both consist of unseen data not used for training, with the only difference being the fact that the testing set has no impact on the learning done by the network. Therefore, it simply exists as a way to provide an independent measure of success.

In the current study, a backpropagation algorithm is applied to train the network. The specific algorithm used is referred to as ‘Levenberg-Marquardt backpropagation’. The method is used to determine the optimal network weights and biases which minimize error. In general, in the backpropagation algorithms, for every input-output pair in the training set, the input is first received and processed by the network and an output is obtained. The output on the first iteration is calculated by using randomly assigned weights and biases. The calculated output is then compared to the actual desired output from the input-output pair and an error is found. This error is then propagated back through the layers of the network and the weights of each connection and the biases of each neuron are adjusted accordingly. The process is then simply repeated until a global minimum of the error is found. For example, in the Levenberg-Marquardt training algorithm, the weight and bias values are updated using the following formula [25,26]:

$$X_{k+1} = X_k - [J^T J + \mu I]^{-1} J^T e_r, \quad (6)$$

where X stands for the weights or biases, e_r is the vector of network errors, μ is called regularization parameter or combination coefficient and is a positive number adjusted by the algorithm, and J is the Jacobian matrix comprising first derivatives of the network errors with respect to the weights and biases. The J matrix is typically calculated using the backpropagation algorithm stated above [25,26]. It is worth mentioning that the Levenberg-Marquardt algorithm is the combination of the gradient descent and the Newton algorithms. When μ is very close to zero, the Levenberg-Marquardt algorithm converts to the Newton algorithm. Conversely, when μ is very large, it becomes the gradient descent method. It should be also noted that the mentioned algorithm does not always work properly, as the network may get stuck on a local minimum. More information about the Levenberg-Marquardt algorithm as well as proof of the above equation are available in Reference [26].

ANNs have been successfully used to represent the chemistry in the simulation of laminar and turbulent flames with satisfactory results, negligible memory demand, and low computational cost (see References [27–37]). In addition, it should be pointed out that in a few fundamental studies, ANNs were trained using experimental data and then applied to predict soot properties. For instance, Inal et al. [38] experimentally studied soot characteristics in laminar, premixed, hydrocarbon fuel/oxygen/argon flames, and utilized ANN models to forecast the soot concentrations and particle sizes. At first, the soot characteristics were measured using classical light scattering techniques. Then, by using the input/output data sets obtained from the experiments, two neural network models were developed. In that work, the authors explained that they were not able to train and test a network to predict the soot number density with sufficient accuracy, due to great uncertainty in the determination of this parameter and a large minimum-maximum range.

In another study, Inal [39] developed a network to estimate PAH concentrations in laminar, premixed n-heptane/oxygen/argon and n-heptane/oxygen/oxygenate/argon flames. For data acquisition, an experimental study was performed. It was shown that the PAH amount was a strong function of

equivalence ratio, mole fractions of C_4 species, and presence of fuel oxygenates. The present study advances upon these works with full ex-situ prediction of soot concentration using ANNs.

In the present work, the input/output datasets are obtained from the CoFlame code [12]. CoFlame has been used extensively by multiple research groups to study a wide variety of axisymmetric laminar diffusion flames including those at microgravity and high pressure [40–42]. It is worth mentioning that CoFlame solves for soot primary particle number density and soot aggregate number density equations in addition to the conservation equations for mass, momentum, energy, and species mass [12]. The CoFlame sectional particle dynamics model contains nucleation, PAH condensation, HACA surface growth, surface coagulation, oxidation, fragmentation, particle diffusion, and thermophoresis. Radiation is also modeled using the discrete-ordinates method [12]. The boundary conditions and the coordinates (r and z) utilized in the code as well as the structure of a laminar coflow diffusion flame are shown in Figure 4.

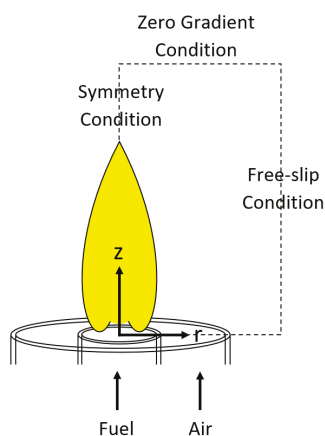


Figure 4. A schematic representation of a laminar diffusion flame along with the coordinates (r , z) and the boundary conditions used in the CoFlame code (adapted from Reference [40]).

The results of the simulations of eight different ethylene–air laminar flames at atmospheric pressure are considered in the current study (see Table 1). These flames range from low to moderate soot volume fraction. The computed peak values, obtained from the CoFlame code (Veshkini et al. [20]), are reported in Table 1. For each flame, the values of eleven key variables including temperature (T), mixture fraction (MF), oxygen (O_2), carbon monoxide (CO), carbon dioxide (CO_2), hydrogen (H_2), water (H_2O), hydroxide (OH), acetylene (C_2H_2), benzene ($A1$), and soot volume fraction (f_v) are gathered. As an example, the temperature contours for the flames SM32 and SM80 are shown in Figure 5. It should be pointed out that the first eight variables are considered key variables found in any combustion system. However, acetylene and benzene are included since they are the major species which result in PAH formation and hence affect soot inception and surface reactions. The soot volume fraction is the output in the present study.

Table 1. The main characteristics of eight laminar flames (Experimental works of ^a Smooke et al. [43], and ^b Shaddix and Smyth [44] referred to as “SMXX” and “SYXX”, respectively).

Flame Code	Fuel Composition (Volume)	Fuel Velocity (cm/s)	Air Velocity (cm/s)	Inner Diameter (mm)	Computed Peak f_v (ppm)
SM32 ^a	32% C ₂ H ₄ /68% N ₂	35	35	4	0.12
SM40 ^a	40% C ₂ H ₄ /60% N ₂	35	35	4	0.36
SM60 ^a	60% C ₂ H ₄ /40% N ₂	35	35	4	1.68
SM80.2 ^a	80% C ₂ H ₄ /20% N ₂	17.5	17.5	4	1.80
SM80 ^a	80% C ₂ H ₄ /20% N ₂	35	35	4	3.21
SY41 ^b	100% C ₂ H ₄	4.1	8.7	11	12.65
SY46 ^b	100% C ₂ H ₄	4.6	8.7	11	14.76
SY48 ^b	100% C ₂ H ₄	4.8	8.7	11	16.39

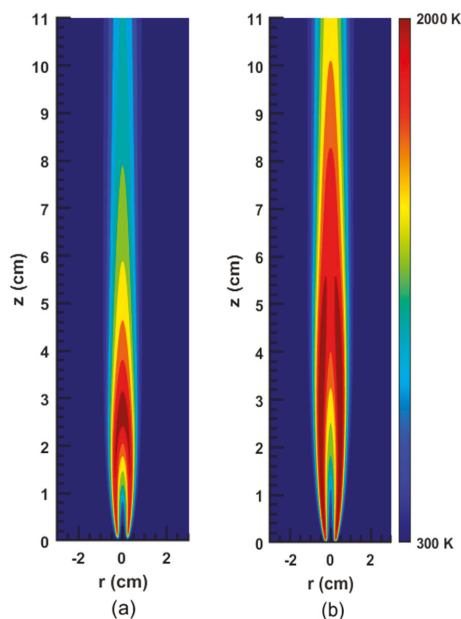


Figure 5. 2D contour plots of the temperature for the flames: (a) SM32; (b) SM80; obtained from the CoFlame code.

As previously mentioned, one of the problems associated with the binning process that was used in previous works is that it scales extremely poorly to added dimensions [6,17,18]. This also leads to large amounts of data being left unused (compare Equation (3) with Equation (2)). As a result, one of the first aspects that were explored with the ANN model was to increase the input parameters to exceed the three or four previously used.

In this study, similar to the work of Zimmer et al. [18], the Lagrangian histories of soot-containing fluid parcels are considered as the input datasets, and one network is trained for all the flames. In other words, the temperature history ($T_{i,t}$), mixture fraction history ($MF_{i,t}$), oxygen history ($O_{2,i,t}$), carbon monoxide history ($CO_{i,t}$), carbon dioxide history ($CO_{2,i,t}$), hydrogen history ($H_{2,i,t}$), water history ($H_2O_{i,t}$), hydroxide history ($OH_{i,t}$), acetylene history ($C_2H_{2,i,t}$), and benzene history ($A1_{i,t}$) are calculated and considered as the input dataset. To calculate the Lagrangian histories and create the library/data-frame the following steps are taken:

- (1) Gathering numerical data: as mentioned, the values of different parameters (such as temperature and oxygen) for the eight flames are gathered.

- (2) Extracting pathlines: each pathline p was computed from the following ordinary differential equation:

$$\frac{d\vec{X}_p}{dt} = \vec{u}(\vec{X}_p(t), t), \quad X_{p,t_0} = X_{p,0}, \quad p = 1, 2, \dots, N_p, \quad (7)$$

where \vec{X}_p is the current point in space of a fluid parcel which may contain soot, and which follows the fluid velocity \vec{u} with respect to time t . In addition, $X_{p,0}$ is the initial position for each pathline and N_p is the total number of pathlines.

- (3) Computing histories from pathlines: The history of a variable referred to the time integration of a given variable over its entire existence; for soot that is from inception to oxidation (that is along a pathline). For instance, for a general variable (Z), the history of Z is defined as:

$$Z_h = \int_{\text{pathline}} Z(\vec{X}, t) dt, \quad (8)$$

In previous studies [6,17,18], a specific number of bins was defined to divide the range of each history.

- (4) Storing soot concentrations: once the histories were computed for each fluid parcel pathline, the histories, as well as the associated soot concentration values, were stored in the libraries [6,17,18].
 (5) Concatenating the eight libraries/data-frames and generating one library/data-frame.

The key parts of the mentioned steps and the model flow are shown schematically in Figure 6. As can be seen, after training the network and finding the soot volume fraction along each fluid parcel pathline, linear interpolation is used to distribute the estimated f_v on the r - z coordinate system (see Figure 6). It should be noted that in previous works [6,17,18], the aforementioned steps, as well as the interpolation method, were comprehensively discussed. Therefore, the interested reader is referred to those studies for more information.

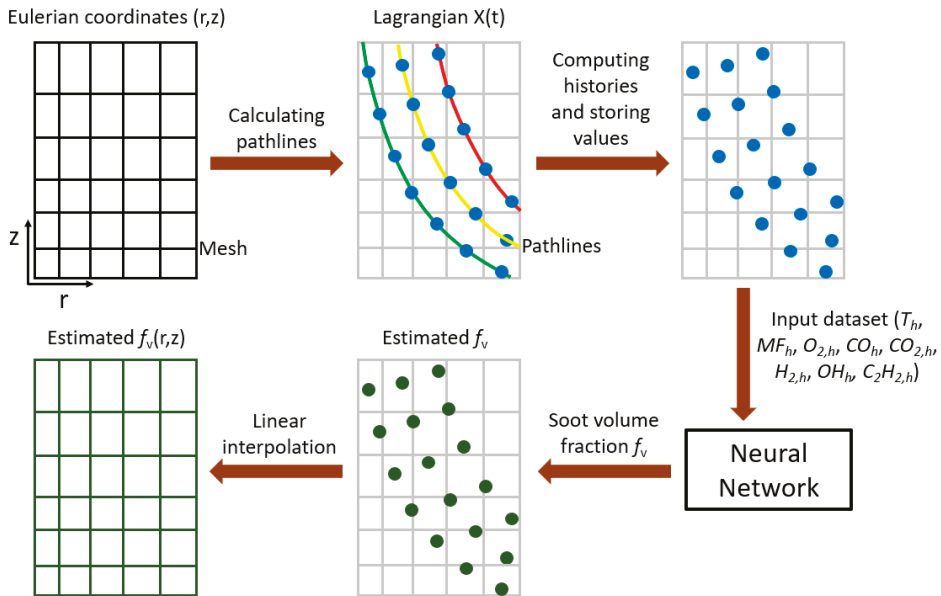


Figure 6. A schematic representation of the ANN-based soot estimator approach.

Initially, all the ten input variables mentioned above were fed to the ANN. However, it was found that this would lead to the network finishing training within one iteration and thus returning extremely poor results. When this occurs, it is almost always indicative of an issue with the data or the network. Upon further investigation, it was determined that there were two variables, namely $A1_h$ and H_2O_h , which when used in any combination with other variables would lead to the same issues. This behavior might be due to multicollinearity [45–48]. In fact, multicollinearity happens when the input variables are highly correlated (for instance, in the soot formation study, there is a strong correlation between $C_2H_{2,h}$ and $A1_h$) and they have a strong correlation with the output. In regression analysis, this may result in poor fitting [45–48]. In the current work, the two variables ($A1_h$ and H_2O_h) were simply omitted from subsequent training of the network (it should be noted that from a physical perspective, it is not that $A1_h$ is not an important driver of aromatic growth and soot formation in this case, but rather that other input sets produce better results). Upon completion of some brief testing, it was determined that using all of the remaining eight variables as input parameters showed the most promise in terms of decreasing the overall error and improving reliability. It is important to emphasize again that these inputs were histories of variables as opposed to values in a given instant of time. This hysteresis method is necessary because the timescales associated with soot formation tend to be much longer than those of combustion chemistry. Furthermore, it should be noted that the concept of tracking the time history was also used by Aceves et al. [49] for fast prediction of HCCI combustion with an ANN linked to the KIVA3V fluid mechanics code. In addition, in the work of Christo et al. [28], in order to reduce the dependency of the ANN model on the selection of training sets for modeling turbulent flames, the input parameters were integrated over a prescribed reaction time.

As expected, an increase in runtime along with significantly improved results was realized with the additional input parameters when compared to the original three input variables (T_h , MF_h , $H_{2,h}$) from previous work [18]. Furthermore, the repeatability of the results, where previously the exact same network would give largely varying results on several subsequent runs, was now much better. Nonetheless, variation will always be present to some degree, so it is a matter of limiting it as opposed to eliminating it. The reason this issue exists is the random nature behind the assignment of the initial weights paired with the random splitting of the entire data set into the training, validation, and testing sets (in this work, 80% of the entire dataset was randomly selected for training, 10% for validation, and 10% for testing). The randomness of the initial weights has a far smaller impact due to the fact that if the network works successfully it will always reach the global minimum. However, the data splitting does have a significant effect on the final results since the same network may be learning with different training data sets in successive runs, depending on how it is split. In this study, as an overall trend, the variability of these results decreased dramatically with the introduction of more input parameters.

From the onset of this study, there were some items of interest that were identified to have the potential to improve the performance of the ANN. Namely, these included data pre-processing, the number of input variables, the combination of input variables, the training method, the number of hidden layers and the number of neurons per hidden layer, and the activation function used.

As will be shown, data pre-processing had a considerable impact in this study. The results prior to the pre-processing were especially poor as they were not always physically realistic. Even though in the area where the flame is sooting the ANN returned fairly accurate results, the surrounding area where the soot volume fraction should be zero still had soot predicted for it. Not only was soot predicted there, but there were also regions of the predicted 2D field with negative concentrations. As negative values are unphysical, this was a very concerning result that had to be fixed if the estimators were to be of any use in the future.

The idea of data pre-processing was implemented in a work by Christo et al. [28]. In their study, a data pre-processing technique, called the histogram redistribution, was used to overcome the difficulties in achieving convergence of the network. This technique was based on using a nonlinear function, such as a natural logarithm, to transform the distorted or skewed distribution of the PDF into a more uniform one without changing the structure of the samples. Then, the transformed input

datasets were used to train and test the neural network. Berger et al. [50] also suggested that taking the logarithm of the data before feeding it into the network significantly reduced errors when exploring data in a 3D or higher-dimensional space. After implementing the log transformation concept in the present study, significantly improved results were obtained. In the subsequent paragraphs, the process by which extensive fine-tuning of the network was completed is discussed. It is worth mentioning that several soot concentration predictions from the ANN with and without data pre-processing are presented in the results section.

The training method of an ANN refers to the actual method by which the weights and the biases of connections are adjusted during training. MATLAB R2018a allows for the selection of a variety of training methods [51]. For a given problem it is difficult to judge which training method will have the best performance without rigorous testing, as it is dependent on a concoction of factors, including the complexity of the problem, the number of data points, the number of weights and biases in the network, and many more. In this study, only two training methods were considered. The first method that was considered was the default method, called 'Levenberg-Marquardt' (which was explained in the methodology section) [25,26,52]. Additionally, the Scaled Conjugate Gradient (SCG) method [53] was also examined. This method is a class of conjugate gradient algorithms which are typically used for large-scale unconstrained optimization. However, since the theory behind this method is complex and beyond the scope of the present study, only the fundamentals are briefly discussed here. Consider the minimization of a function $f(x)$ of n variables. Conjugate gradient methods minimize this function with iterations of the form $x_{k+1} = x_k + \alpha_k d_k$, where α_k and d_k are called the step length (always positive) and the search direction, respectively. It should be noted that if $d_k = -\nabla f(x_k)$, the steepest descent method is obtained. While by assuming $d_k = -\nabla f(x_k) \cdot [\nabla^2 f(x_k)]^{-1}$, the Newton algorithm is attained [54]. However, the SCG method proposed by Moller [53] is much more complicated. It is based on conjugate directions, but unlike other conjugate gradient methods, a line search at each iteration is not performed in this algorithm [53,55]. In the current study, the SCG was only brought into consideration due to the fact that if it were used as opposed to the Levenberg-Marquardt method, it would allow for the use of GPU (graphics processing unit) processing [51]. Since GPUs are effective at completing matrix mathematics, they prove to be extremely efficient for use in complex neural networks [56–58]. However, in our study, upon completing initial testing it was clear to see that the Scaled Conjugate Gradient gave far worse results which were not compensated for by the faster runtime. Therefore, the method was disregarded and further testing in the study was conducted with Levenberg-Marquardt training.

The last three parameters that were outlined to be tested initially were all done in tandem through the use of a grid search [59,60]. This technique essentially involves running through every possible combination of parameters to determine which single combination would give the best results. It should be pointed out that in general, manual search and grid search are the most extensively used approaches for hyper-parameter optimization. The major disadvantage of manual search is the fact that although a good result may be obtained, it is easy to miss the best result as only a select amount of combinations is considered. On the other hand, grid search suffers from the curse of dimensionality, as it quickly becomes too computationally-taxing to go through every single possibility for the network. However, in general, grid search is reliable in low dimensional spaces and typically results in a better configuration than would be obtained by purely manual sequential optimization in the same amount of time [61]. In the present study, 110 different combinations of the number of hidden layers and number of neurons per hidden layer were considered, along with two different activation functions (rectified linear unit and hyperbolic tangent). In fact, the number of hidden layers in the grid search was changed from 2 to 7, while the number of neurons per hidden layer was in the range of 3 to 25 (as demonstrated in the results, increasing the number of neurons causes the computational time to increase significantly). Consequently, the number of neurons per hidden layer was limited to 25). Additionally, each of the combinations was run five times to ensure repeatability. The main trends obtained from this study will be shown in the next section. Since the procedure was computationally expensive, parallel processing was used. The testing process utilized Compute Canada's Niagara

supercomputer and 40 CPUs. Using multiple clusters on Niagara allowed for several networks to be run concurrently as opposed to having to run one at a time. This allowed for far more testing to take place and ultimately helped in obtaining the final network architecture much faster than otherwise would have been possible.

3. Results and Discussion

Before going into detailed predictive results from the network, it is important to first examine the vast improvements associated with data pre-processing. This simple change in the network process led to the greatest advancement of the network's predictive accuracy. As mentioned above, a detailed examination of the training dataset showed that the model accuracy and convergence depend on the nonuniformity and skewness in the distribution of the input dataset. A typical example is shown in Figure 7a for a highly skewed distribution of samples for the temporal history of oxygen ($O_{2,t}$) before data pre-processing.

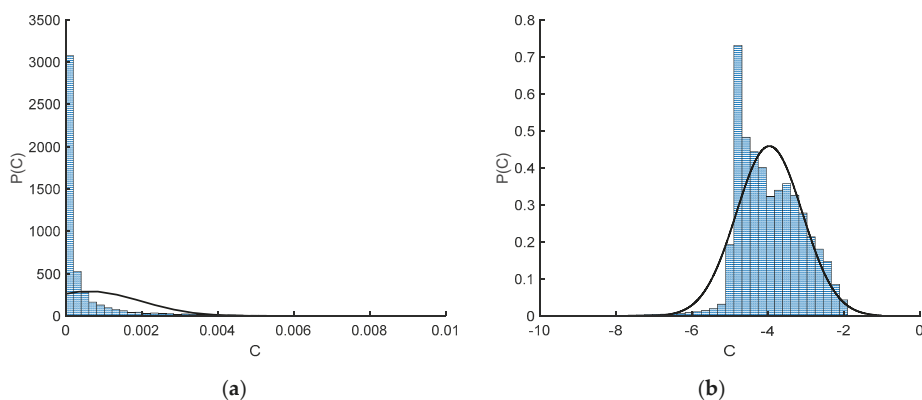


Figure 7. The probability density function (PDF) of oxygen history ($O_{2,t}$): (a) before data pre-processing; (b) after data pre-processing.

In statistical analyses, the data transformation concept is widely used to address skewed data [62]. Quite often data arising in real studies are far from the symmetric bell-shaped distribution and are so skewed that standard statistical analyses of these data become difficult and may yield inaccurate results [62]. Therefore, when the data distribution is non-normal and skewed, data transformations are utilized to make the data as 'normal' as possible [62]. The log transformation is the most common among the different kinds of data transformations [62,63]. Figure 7b shows that after using the log transformation in the present study, the data distribution (the histogram) has improved significantly and is closer to bell-shaped and resembles a normal distribution. Similar results were observed by Christo et al. [28]. For testing normality, the easiest approach is to compare the histograms to the normal probability curves (shown as solid lines in this figure). The log transformation was used here for the entire input set (since the data distribution of all the input variables were skewed), and then the transferred set was used as the training set for the neural network.

The results shown in Figure 8 depict the 2D soot volume fraction contours for the SY48 flame (see Table 1) obtained from the network with architecture of {8,5,3} (this notation means we have 3 hidden layers; 8 neurons in the first layer, 5 neurons in the second layer, and 3 neurons in the third layer (see Figure 1 for more information about the hidden layers)), eight inputs/one output (shown in Figure 6 and discussed in the previous section), and the *tanh* activation function. The stark difference between the results before and after the pre-processing was applied can be seen. Figure 8b highlights the poor results obtained without pre-processing when compared to the computed data (Figure 8a). As is experimentally known, only the flame and the area directly surrounding it can produce soot while

the area outside of that has a soot volume fraction equal to zero. However, in Figure 8b there is soot predicted in the areas farther from the flame (notice the color difference between the computed and predicted figures). Furthermore, there are significant areas where the prediction is negative—something that is physically impossible. When examining Figure 8c, it is clear that these issues are no longer present, and the network is able to predict a soot volume fraction of zero where appropriate. However, it is important to note the apparent deterioration in results obtained in the sooting area in Figure 8c. Clearly, even though the overall results improved significantly (in terms of relative integrated error calculated over the entirety of the 2D field), the soot accuracy in the producing area suffered as a result, and thus the ensuing attempts at improving the network were focused on this region in particular.

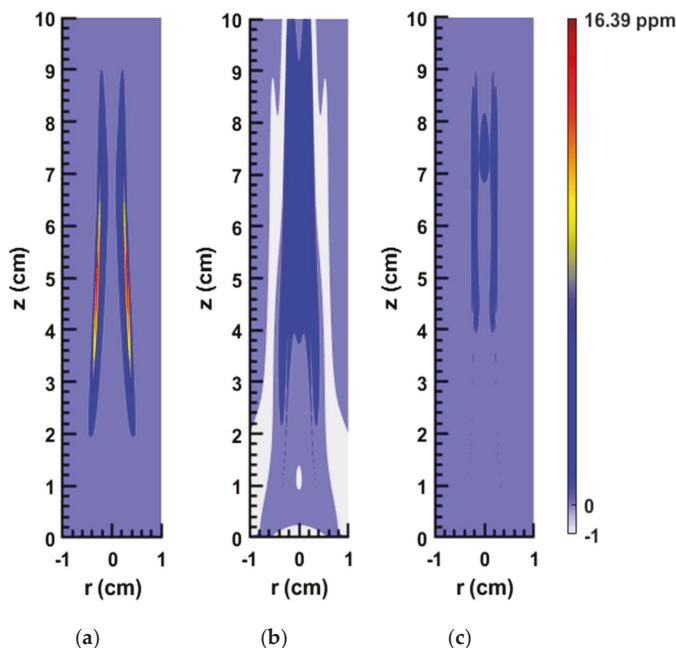


Figure 8. 2D contour plots of the soot volume fraction for the SY48 flame: (a) computed; (b) predicted by ANN without data pre-processing; (c) predicted by ANN with data pre-processing.

Aside from only examining particular results, it is imperative to look for overall trends that can be found in the grid search results. The grid search procedure reveals numerous trends in the results that can provide valuable information toward understanding these highly complex algorithms. The first trend that was observed is that calculations of complex architectures of several hidden layers and many neurons within each layer took significant runtime even with the parallelization in place. For instance, total run time (5 executions) for the networks with architectures of {15,15,15,15,15} (that is 5 hidden layers and 15 neurons within each layer), {15,15,15,15,15,15}, and {25,25,25} were 20.07, 27.45, and 47.08 h, respectively. In addition, the network predictions were often incorrect and unreliable, and the errors were extremely large. This is most likely due to the problem of overfitting where the model tunes itself so well to the training data that it no longer generalizes well to other data. In fact, deep neural networks make models more complex, and in a complex model it is more likely to have overfitting. Therefore, to develop a computationally efficient model (which is one of the main purposes of this study) and to prevent the problem of overfitting, shallower networks were focused on hereafter.

Furthermore, it was found that out of the two activation functions tested, the rectified linear unit gave far worse results when compared with the hyperbolic tangent. For instance, the average

relative error of the peak f_v (over 5 executions and based on the input/output datasets obtained from the eight flames in Table 1 (training errors)) for the networks with architectures of {15,10}, {10,5,3}, and {5,5,5,5} with the rectified linear unit activation function were 445.66, 1.3×10^4 and 165.25%, respectively. However, by using the hyperbolic tangent activation function, the error for the mentioned architectures was reduced to 73.23, 139.28, and 42.58%, respectively. Similar trends were observed for other networks considered in the grid search. Therefore, only the hyperbolic tangent function was considered after this point.

As mentioned, a variety of architectures were tested, including some where the number of neurons in each layer remains the same and some where the number of neurons in each layer decreases with layer number, as if converging towards the output. It was found that networks with equal-numbered amounts of neurons in each layer were more consistent overall and delivered better results (for example, see the errors related to the networks with architectures of {15,10}, {10,5,3}, and {5,5,5,5} mentioned above). Similar observations were reported by Christo et al. [27] and de Villiers and Barnard [64]. In the work of Christo et al. [27], it was explained that substantial differences in the number of neurons result in a bottleneck junction of information so that the convergence of the algorithm is severely affected.

In the previous section, it was discussed that each network in our grid search was run five times to ensure repeatability. Overall, in this investigation, a lot of architectures showed good results for three or four out of the five runs. As an example, consider the network with the architecture of {10,5,3}. For this network, the relative errors of the peak f_v for five executions were 15.21, 36.63, 16.98, 601.2, and 26.38% (average: 139.28%). As mentioned before, the variability is caused by the random splitting of the data into training/validation/testing subsets as well as random initialization of weights and biases. In the current study, a slightly higher error along with consistent results was preferred over a very low error occurring sporadically for the purpose of practical usability.

It is worth mentioning that, in the present study, to choose the optimal network architecture out of the 110 potential options, in addition to the analyses stated above (for instance, monitoring the network performance, the mean squared error, the relative error of the peak soot volume fraction (f_v) and the computational time), other errors such as the integrated f_v relative errors were examined. The integrated f_v represents the volumetric integration of the soot concentration in the whole domain and was calculated as [18]:

$$f_{v,int} = \iint_V 2\pi r f_v(r, z) dr dz, \quad (9)$$

where $f_{v,int}$ provides quantification of the overall soot formation in the whole domain.

Upon analyzing all the results (eliminating networks with inconsistent results, large errors, and high computational cost), the final network that was chosen was the {10,10,10,10} (4 hidden layers and 10 neurons within each layer) since this network architecture exhibited excellent balance between runtime and performance. Its average $f_{v,int}$ error over five runs was 10.9%, peaking at 13.9% and going as low as 7.4%. When compared to the average error of 10.2% for the {10,10,10,10,10} architecture, the small decrease in error was accompanied by an increase in runtime of 0.9 h.

As stated in the introduction, the network was first trained with eight laminar flames and then used to predict the soot volume fraction for the exact same flames. This sort of evaluation is done to ensure that the network is able to accurately predict the flame characteristics for which it is trained. In addition to that test, two more rigorous tests were performed using two new datasets to check the ability of the network to predict the soot concentration for new laminar diffusion flames. As shown in Table 2, the first rigorous test is based on the experimental study of Santoro et al. [65] and the second one is based on the work of Cepeda et al. [66]. In order to perform these tests, Lagrangian fluid parcel tracking was employed with pre-computed CFD simulation data and the following histories were first calculated: T_h , MF_h , $O_{2,h}$, CO_h , $CO_{2,h}$, $H_{2,h}$, OH_h , and $C_2H_{2,h}$. Then, these eight parameters were used as input variables and the soot concentrations that were predicted by the network were compared with the CFD results.

Table 2. The characteristics of two flames used as unseen data for the rigorous test (experimental work of ^a Santoro et al. [65]; experimental and numerical studies of ^b Cepeda et al. [66]).

Flame Code	Fuel Composition (Volume)	Fuel Velocity (cm/s)	Air Velocity (cm/s)	Inner Diameter (mm)	Computed Peak f_v (ppm)
SA ^a	100% C ₂ H ₄	5.06	13.3	11.1	10.74
CE ^b	100% C ₂ H ₄	2.42	26.55	10.32	6.13

The chosen network architecture ((10,10,10,10)) was run another five times, this time one at a time as opposed to consecutively, such that the error could be analyzed after every run instead of only at the end of the 5th one. This was done in search of the lowest possible error for the different tests mentioned above. Even though the network returns consistent results, there is still potential for it to have an even lower error due to the inherent variability present in the network predictions from run-to-run. It is worth mentioning that the runtime was approximately 50 min for a single training to complete and was done using four available cores on an average desktop computer through the use of MATLAB's Parallel Computing Toolbox and the `parpool` function. This can be done much faster through the use of supercomputer clusters, but was timed on a regular workstation to act as a gauge for how long the typical user would have to run the tool.

At the end, one network which had the best performance among five trained networks for both tests mentioned above (namely, eight flames explained in Table 1 and two flames discussed in Table 2) was selected. Table 3 shows the relative errors in predicting soot concentration for all eight flames that were used to train this network. It includes the relative errors of integrated f_v along the centerline and the streamline of maximum soot, the maximum f_v , and the integrated f_v in the whole domain. As shown, the average integrated soot volume fraction error over the whole domain is 8.08%.

Table 3. Relative errors between the CFD and the predicted data by ANN for eight flames used to train the network.

Flame Code	f_v along the Centerline (%)	f_v along the Streamline of Max Soot (%)	Peak f_v (%)	Integrated f_v (%)
SM32	31.54	8.59	11.15	6.07
SM40	7.66	15.83	29.69	31.64
SM60	11.09	25.36	6.23	4.79
SM80.2	45.3	8.24	10.2	1.91
SM80	12.65	6.03	16.74	2.14
SY41	2.71	16.82	39.92	10.91
SY46	3.85	21.66	33.98	6.25
SY48	1.79	13.76	23.99	0.93
Average	14.58	14.54	21.49	8.08

Table 4, by contrast, shows the relative errors obtained from our rigorous tests for SA and CE flames using this network. As can be seen, for the SA flame, the relative errors are less than 20% and, in particular, the integrated f_v error is 4.66%. However, for the CE flame, the errors are higher and the integrated f_v error reaches 63.43%, mainly due to deviation of its dataset from the model's dynamic range (similar observations were reported by Christo et al. [27] and Heinlein et al. [67]). For example, in the simulation of the CE flame, the fuel inlet velocity was assumed to be uniform and equal to 2.42 cm/s. For other nine flames discussed in the present work, the CFD results were based on the parabolic inlet velocity assumption and the minimum averaged fuel velocity was 4.1 cm/s (hence, the minimum fuel inlet velocity was 8.2 cm/s at the centerline, which was around 3.4 times more than the inlet velocity in the simulation of the CE flame). This degradation of accuracy, which occurs when the modelled samples are far enough outside the model's working range, highlights the importance of broadening the training datasets to represent the input/output combinations over a wide dynamic range. It should be pointed out that the lack of data is one of the main reasons why machine-learning programs often fail to predict expected results [68]. Therefore, in future research, more flames will be simulated and validated, and more data will be added to the training dataset so that the network's dynamic range will be expanded, making it the major advantage of this framework. It is worth

mentioning that although more rigorous tests must be conducted to find the network performance, the range of errors for the CE flame is still very promising compared to many available CFD models that predict soot properties with about a one or two order-of-magnitude error.

Table 4. Relative errors between the CFD and the predicted data by ANN for two flames used to test the network.

Flame Code	f_v along the Centerline (%)	f_v along the Streamline of Max Soot (%)	Peak f_v (%)	Integrated f_v (%)
SA	12.07	3.5	19.64	4.66
CE	61.22	73.09	52.79	63.43

Figures 9–11 demonstrate how our proposed network predicts the soot volume fraction (concentration) field for the eight flames stated in Table 1. To obtain these results, as explained in the methodology and demonstrated in Figure 6, the linear interpolation was performed. As shown in these figures, the network predicts the overall soot concentration field very well. The magnitude of the point of maximum soot is accurately predicted. All areas around the sooting region have a concentration value of zero. Furthermore, soot concentration distributions along the centerline and the streamline of maximum values are also properly estimated. It is worth mentioning that to keep the paper concise and to explain the details of the network predictions in different ways, 2D plots are presented for 4 flames (see Figure 9), and variations along the centerline and the streamline of maximum soot are revealed for the other 4 flames (see Figures 10 and 11). These figures are discussed in more details in the following paragraphs.

As shown in Figure 9a, for the flame SM80, the shape of the soot field is accurately captured by the ANN prediction. However, compared to the original case, the high-soot zone predicted by the ANN is slightly longer and thicker. Near the centerline when the distance from the burner exit is between 4.8 and 6 cm, the discrepancy is more noticeable. At the centerline, the maximum soot values are 1.176 and 1.038 ppm for the ANN and the original cases, respectively. In addition, the peak soot values in the entire domain are 3.75 and 3.21 ppm (see Table 1) for the ANN and the original cases, respectively.

Figure 9b shows the soot volume fraction fields for the SY41 flame. In general, the ANN prediction is in good agreement with the CFD results. The sooting region predicted by the ANN is slightly longer in comparison with the original case. However, the high-soot zone (where soot is more than 6 ppm) estimated by the network is slightly shorter and thinner. Moreover, as shown, f_v predicted by the network reaches a peak at 17.70 ppm, while the original f_v obtained from CFD peaks at 12.65 ppm (see Table 1). To present more details, it should be pointed out that, at the centerline, the soot volume fraction peaks at 1.96 and 1.91 ppm for the original and the ANN cases, respectively. In addition, there are slight and insignificant fluctuations in the ANN prediction when z is between 1.5 and 3 cm (see the red arrow in Figure 9b). It only happens in a limited small area at the boundary of the soot domain and can be due to the overfitting problem. Attempts were made to eliminate these fluctuations by changing our network architecture, but were unsuccessful.

In Figure 9c the soot volume fraction fields for the SY46 flame are shown. As can be seen, the length of sooting region predicted by the network is 20% greater than that obtained from the CoFlame code. In addition, the length of the high-soot concentration zone (where soot is more than 6 ppm) estimated by the network is 23% longer and 6% thicker. In this figure, the fluctuations in the ANN prediction at the boundary of the soot domain when z is between 1.4 and 3.2 cm are also visible. Additionally, the maximum f_v predicted by the network and calculated by the CoFlame code are 19.78 and 14.76 ppm, respectively. For the f_v along the centerline, the relative error is only 3.85% in this case.

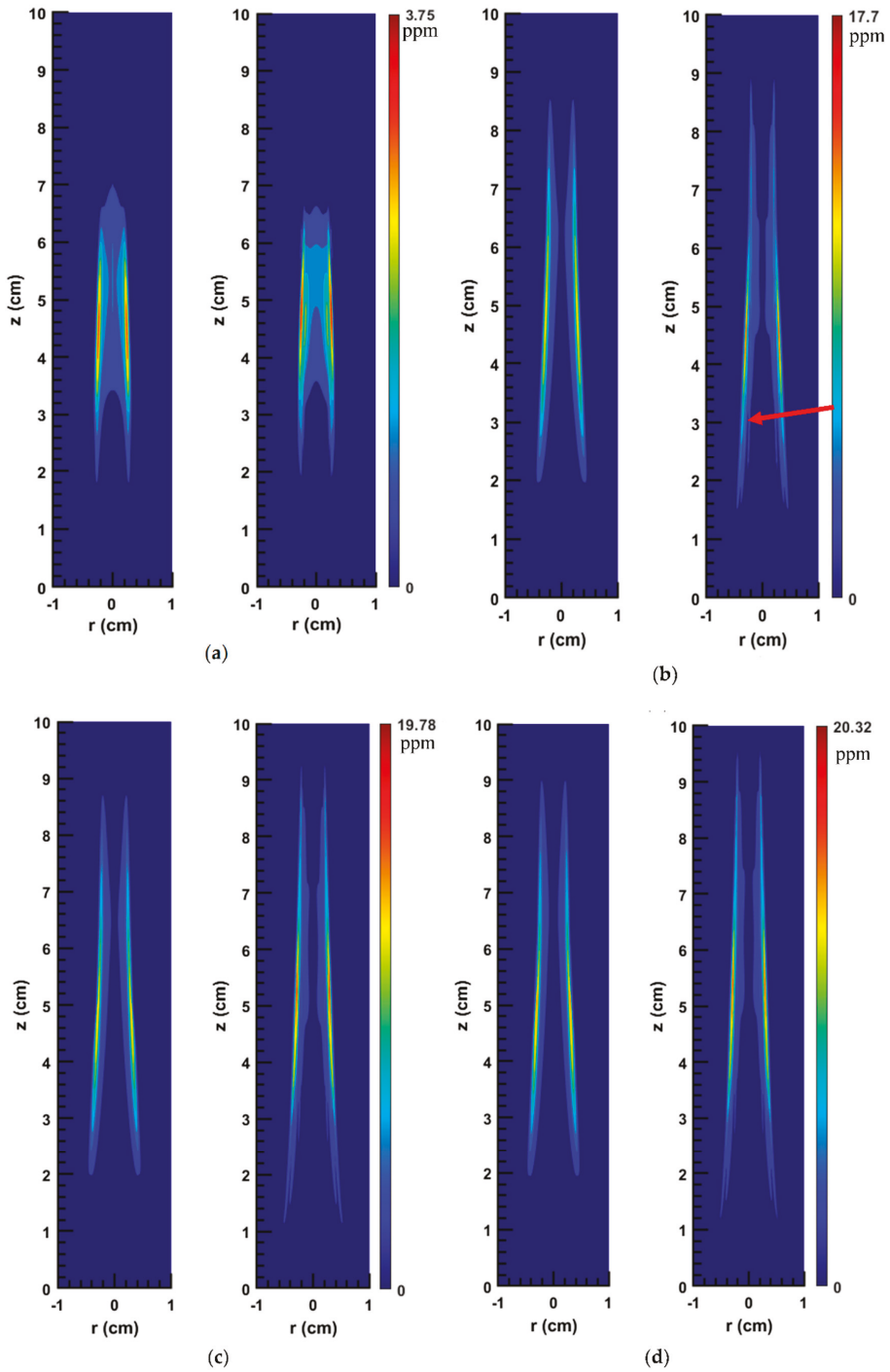


Figure 9. 2D soot concentration fields (ppm) for different flames: (a) SM80; (b) SY41; (c) SY46; (d) SY48; as obtained by two methods, using the original numerical solution (left image in each pair) and using the ANN prediction (right image in each pair).

The original and ANN predicted soot volume fraction fields for the SY48 flame are shown in Figure 9d. As illustrated, both the length of the soot domain (non-zero values) and the length of the high-soot zone (where soot is more than 8 ppm) predicted by the network are greater compared to the original cases. Meanwhile, the thickness of high-soot zone is almost the same. Moreover, the f_v reaches a peak at 20.32 and 16.39 ppm for the ANN and the original cases, respectively. In this figure, slight fluctuations in the ANN prediction when z is between 1.5 and 3.5 cm are also present.

Figures 10 and 11 show the variations of soot volume fraction along the centerline and the streamline of maximum soot for flames SM32, SM40, SM60, and SM80.2. The predictions of the proposed network as well as the CFD results are plotted. As can be seen, in general, there is very good agreement between the ANN and the CFD results and the trends of changes are accurately captured. However, it is worth mentioning that for the SM32 flame, in general, the network underestimates the soot concentration along the centerline and the streamline of maximum soot. A different tendency can be seen in SM40 flame, where the network underestimates and overestimates f_v along the centerline and along the streamline of maximum soot, respectively. For the SM60 flame, the network underestimates the soot concentration along the streamline of maximum soot, while it shows very good prediction along the centerline. Conversely, for the SM80.2 flame, the network underestimates the soot concentration along the centerline, while its prediction along the streamline of maximum soot is slightly shifted compared with the CFD results.

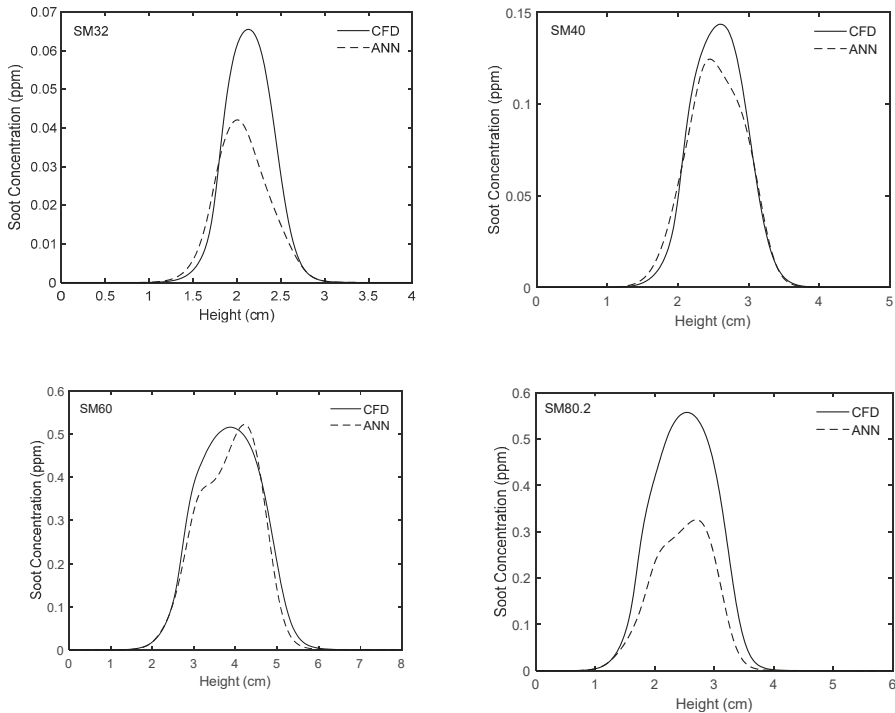


Figure 10. Comparison of experimentally-validated CFD results and those obtained from the ANN for different flames along the centerline.

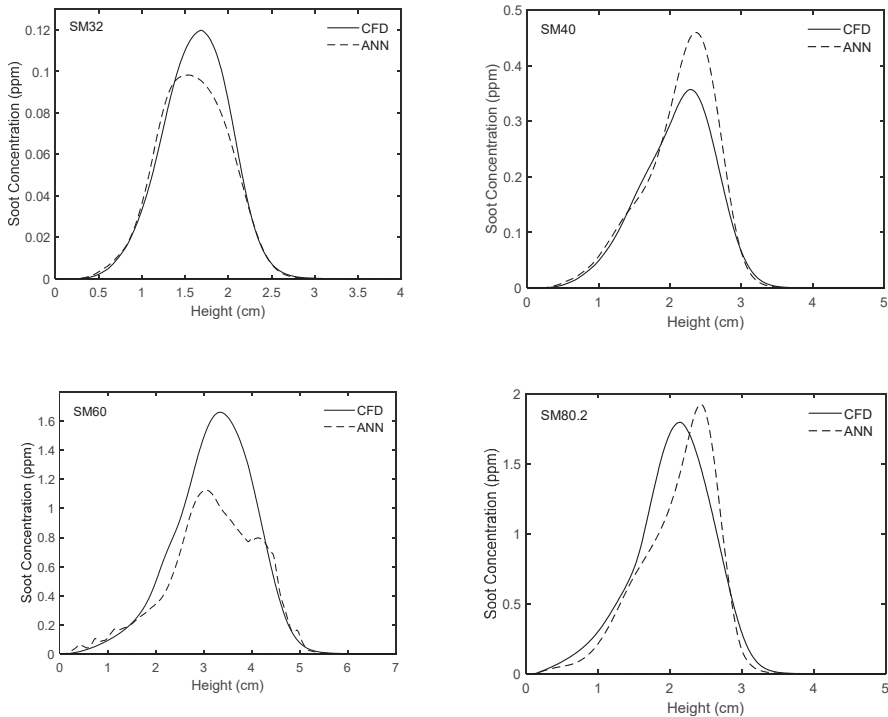


Figure 11. Comparison of experimentally-validated CFD results and those obtained from the ANN for different flames along the streamline of maximum soot.

Figures 12–15 reveal the results of a more rigorous test, wherein the network was used to predict the soot concentration for SA and CE flames mentioned in Table 2. As can be seen, the network predicts the overall soot field for the SA flame very well. However, as stated above, the error is higher for the CE flame. In Figure 12, it is shown that for the SA flame, by using the proposed network, f_v reaches a peak of 12.85 ppm and the high-soot zone becomes shorter than the same respective area in the 2D plot obtained from the numerical solution of the flame. It should be noted that in the CFD results, the maximum f_v for SA flame is equal to 10.74 ppm. In addition, as shown in Figures 14 and 15, the network predicts the soot concentration for the SA flame along the centerline and the streamline of maximum soot with only a slight discrepancy.

Figure 13 shows that although our network is able to predict the soot zone size and shape for the CE flame accurately, the values of f_v are underestimated. As shown, based on the network results, the f_v peaks at 2.9 ppm. However, the maximum value of f_v according to our CFD results is 6.13 ppm. Figures 14 and 15 also demonstrate that the network underestimates the soot concentration for the CE flame along the centerline and the streamline of maximum soot (the values of relative errors are reported in Table 4). As mentioned above, this degradation in performance happens if the modelled compositions deviate significantly from the network’s working range.

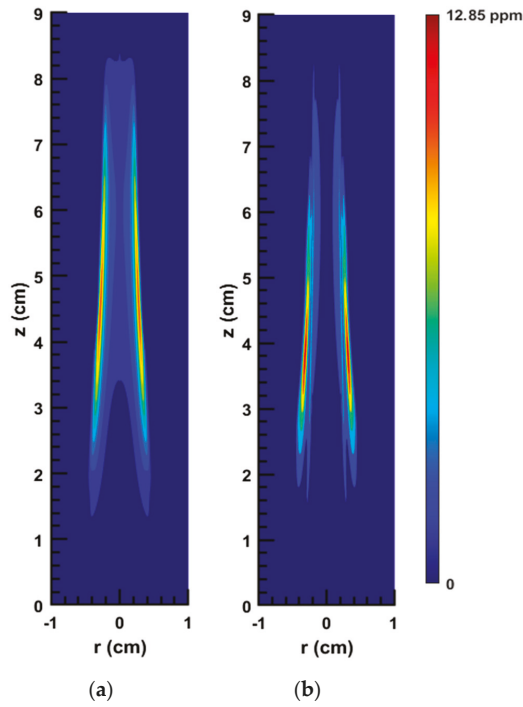


Figure 12. 2D soot concentration field of the SA flame: (a) original numerical solution; (b) ANN prediction.

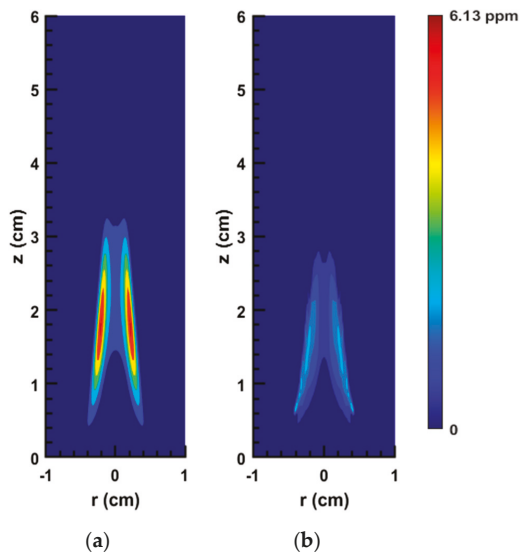


Figure 13. 2D soot concentration field of the CE flame: (a) original numerical solution; (b) ANN prediction.

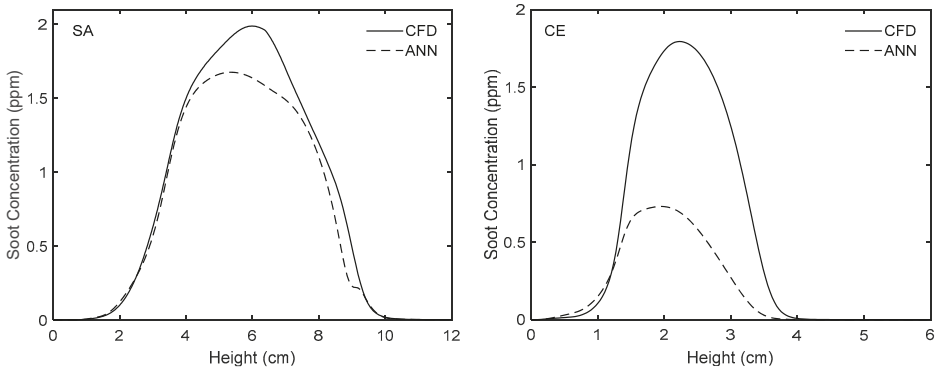


Figure 14. Comparison of experimentally-validated CFD results and those obtained from the ANN along the centerline for the flames used to test the network.

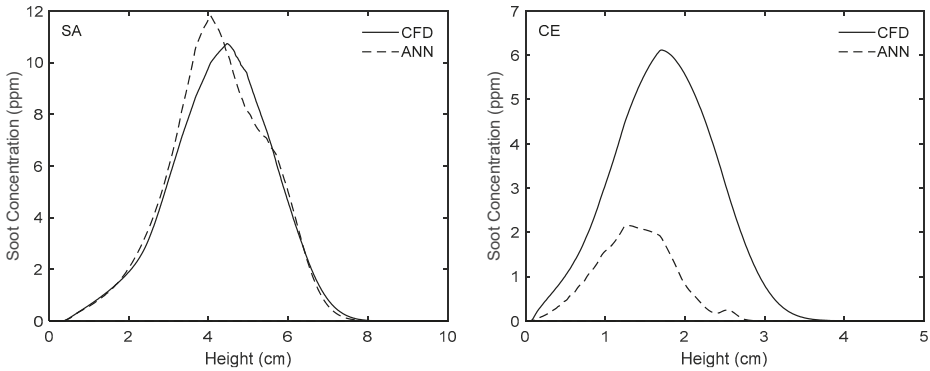


Figure 15. Comparison of experimentally-validated CFD results and those obtained from the ANN along the streamline of maximum soot for the flames used to test the network.

All the errors mentioned above are relative because the range of f_v in this study is wide, from around 0.1 to 20 ppm. In general, for the flames with low f_v the absolute error was also very low (for example around 10^{-4}). Conversely, the flames with high f_v had absolute errors in the order of magnitude of 1. To display the graphs of absolute error in an easy-to-read way, the following equation was developed firstly:

$$e = \frac{\left| \int_0^1 2\pi r f_v(r, z) dr - \int_0^1 2\pi r f_{v,ANN}(r, z) dr \right|}{\int_0^1 2\pi r dr} \tag{10}$$

In the above equation, the error e is a function of z (height) only, due to averaging in the radial direction. It is worth mentioning that taking the average of soot volume fraction over one direction (here r direction) reduces the error fluctuations significantly and makes the error behavior more obvious without obfuscating it. The domain $r \in [0, 1]$ was chosen since it covers all the soot regions in all the ten flames discussed above. Figure 16a shows the results obtained from the above equation for the flames SM32, SY48, SA, and CE. As can be seen, for the flame SM32, the error reaches a peak of around 10^{-4} while for the other three flames the maximum error is slightly less than 1 (noting that the scale of the vertical axis is logarithmic). However, as shown in Tables 1 and 2, the peak f_v for these flames are 0.12,

16.39, 10.74, and 6.13, respectively. By normalizing the error graphs with the peak f_v , the percentage of error can be obtained:

$$e_N = \frac{e}{f_{v,peak}}, \quad (11)$$

Figure 16b shows the variations of e_N versus height. As demonstrated, when z is less than 4 cm, the CE flame has the highest error among these flames (this was shown in Figure 13 and was discussed above comprehensively). For the SA and SY48 flames, e_N fluctuates more but is less than 2%. For the SM32 flame, the normalized error is clearly less than 0.5%. It should be pointed out that, to analyse the soot estimator concept, different types of errors, especially relative errors (similar to the errors defined in this study), must be used because the problem is challenging, and the range of the soot concentration and the number of the flames are vast.

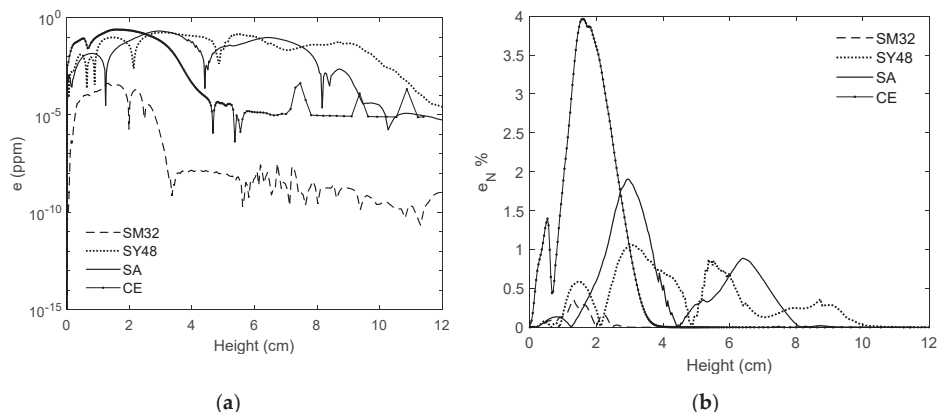


Figure 16. The variations of average error versus height: (a) absolute error; (b) absolute error normalized with the peak soot volume fraction.

4. Conclusions and Future Works

In this study, a supervised Artificial Neural Network (ANN) technique was used to accurately estimate the soot concentration fields in laminar diffusion flames. Eight different ethylene/air flames at various operating conditions were modeled using the CoFlame code. Then, the Lagrangian histories of soot-containing fluid parcels were considered as the input dataset. The effects of data pre-processing, number of input parameters, random splitting, and training method on the network performance and results were discussed. A grid search procedure was used to study the effects of the number of hidden layers, number of neurons, and the activation functions. In conclusion, the {10,10,10,10} network architecture together with eight input parameters, the Levenberg-Marquardt training method, and the hyperbolic tangent activation function were identified as the most effective framework.

The resulting network was tested in two different ways: (1) it was applied to predict the soot volume fraction for all eight flames that were used in the training phase; (2) two new flames were then introduced to the network and its predictions were analyzed. In general, the network predicts the overall soot field accurately and efficiently. However, some degradation in the accuracy becomes noticeable once the datasets deviate significantly from the network's dynamic range. It is also shown in this study that the ANN approach scales extremely well to added dimensions, which is an important step for exploring more complex cases such as transient and turbulent sooting flames (where timescales of the data are much larger). Overall, this study demonstrates the potential of the soot estimator to be implemented through the use of neural networks.

In machine learning, the accuracy of the predictions is related to how close the target properties are to the training datasets. To improve the estimator's predictions and test the network at

different conditions, more flames should be simulated using the CoFlame code and validated against experimental measurements. In this case, the training and testing datasets are expanded so that the issue of the lack of data can be resolved and the network's dynamic range can be developed. In addition, it is intended for the next step to use the estimator tool for predicting soot characteristics in transient and turbulent flames. In the next step, similar to the concept presented in the present study, machine-learning and deep-learning programs will be used as post-processing tools to estimate the soot characteristics based on the soot-related gas-phase quantities obtained from Reynolds-averaged Navier-Stokes (RANS), large eddy simulation (LES), and direct numerical simulation (DNS) solutions. Afterwards, this approach can be applied to estimate the soot characteristics in complicated industrial cases such as an actual engine. In this case, the industrial sector would have an accurate and computationally inexpensive tool in which only the gas-phase conservation equations (which are typically solved in any combustion simulation) need to be solved. In short, the tool would take advantage of detailed soot formation models with no need to solve the soot partial differential equations as well as different soot-related terms such as soot particle nucleation, coagulation, PAH condensation, HACA surface growth, oxidation, and fragmentation, since all of them are replaced with an ANN.

Author Contributions: Conceptualization, S.B.D. and L.Z.; methodology, M.J., S.K. and L.Z.; software, M.J., S.K. and L.Z.; writing—original draft preparation, M.J. and S.K.; writing—review and editing, S.B.D.; supervision, S.B.D. All authors have read and agreed to the published version of the manuscript.

Funding: This research received no external funding.

Acknowledgments: The authors acknowledge funding from the Canadian Research Chairs Program and the Natural Sciences and Engineering Research Council (NSERC).

Conflicts of Interest: The authors declare no conflict of interest.

References

- Center for American Progress. Soot Pollution. Available online: <https://www.americanprogress.org/issues/green/news/2012/08/10/12007/soot-pollution-101/> (accessed on 7 September 2020).
- Environmental Protection Agency. Particulate Matter (PM) Basics. Available online: <https://www.epa.gov/pm-pollution> (accessed on 7 September 2020).
- Lighty, J.A.S.; Veranth, J.M.; Sarofim, A.F. Combustion aerosols: Factors governing their size and composition and implications to human health. *J. Air Waste Manag. Assoc.* **2000**, *50*, 1565–1618. [[CrossRef](#)] [[PubMed](#)]
- Jacobson, M.Z. Strong radiative heating due to the mixing state of black carbon in atmospheric aerosols. *Nature* **2001**, *409*, 695–697. [[CrossRef](#)] [[PubMed](#)]
- Williams, M.; Minjares, R. A Technical Summary of Euro 6/VI Vehicle Emission Standards. *Int. Counc. Clean Transp. Brief. Pap.* **2016**. Available online: <https://theicct.org/publications/technical-summary-euro-6-vehicle-emission-standards> (accessed on 7 September 2020).
- Alexander, R.; Bozorgzadeh, S.; Khosousi, A.; Dworkin, S.B. Development and testing of a soot particle concentration estimator using lagrangian post-processing. *Eng. Appl. Comput. Fluid Mech.* **2018**, *12*, 236–249. [[CrossRef](#)]
- Mueller, M.E.; Pitsch, H. LES model for sooting turbulent nonpremixed flames. *Combust. Flame* **2012**, *159*, 2166–2180. [[CrossRef](#)]
- Han, W.; Raman, V.; Mueller, M.E.; Chen, Z. Effects of combustion models on soot formation and evolution in turbulent nonpremixed flames. *Proc. Combust. Inst.* **2019**, *37*, 985–992. [[CrossRef](#)]
- Brocklehurst, H.T.; Priddin, C.H.; Moss, J.B. Soot predictions within an aero gas turbine combustion chamber. In Proceedings of the ASME Turbo Expo, Orlando, FL, USA, 2–5 June 1997. [[CrossRef](#)]
- Tolpadi, A.K.; Danis, A.M.; Mongia, H.C.; Lindstedt, R.P. Soot Modeling in Gas Turbine Combustors. In Proceedings of the ASME Turbo Expo, Orlando, FL, USA, 2–5 June 1997. [[CrossRef](#)]
- Mueller, M.E.; Pitsch, H. Large eddy simulation of soot evolution in an aircraft combustor. *Phys. Fluids* **2013**, *25*, 110812. [[CrossRef](#)]
- Eaves, N.A.; Zhang, Q.; Liu, F.; Guo, H.; Dworkin, S.B.; Thomson, M.J. CoFlame: A refined and validated numerical algorithm for modeling sooting laminar coflow diffusion flames. *Comput. Phys. Commun.* **2016**, *207*, 464–477. [[CrossRef](#)]

13. Mueller, M.E.; Blanquart, G.; Pitsch, H. Hybrid Method of Moments for modeling soot formation and growth. *Combust. Flame* **2009**, *156*, 1143–1155. [CrossRef]
14. Bisetti, F.; Blanquart, G.; Mueller, M.E.; Pitsch, H. On the formation and early evolution of soot in turbulent nonpremixed flames. *Combust. Flame* **2012**, *159*, 317–335. [CrossRef]
15. Attili, A.; Bisetti, F.; Mueller, M.E.; Pitsch, H. Formation, growth, and transport of soot in a three-dimensional turbulent non-premixed jet flame. *Combust. Flame* **2014**, *161*, 1849–1865. [CrossRef]
16. Wick, A.; Attili, A.; Bisetti, F.; Pitsch, H. DNS-driven analysis of the Flamelet/Progress Variable model assumptions on soot inception, growth, and oxidation in turbulent flames. *Combust. Flame* **2020**, *214*, 437–449. [CrossRef]
17. Zimmer, L.; Dworkin, S.B.; Attili, A.; Pitsch, H.; Bisetti, F. A soot particle concentration estimator applied to a transient turbulent non-premixed jet flame. In Proceedings of the Combustion Institute—Canadian Section Spring Technical Meeting, Kelowna, BC, Canada, 13–16 May 2019.
18. Zimmer, L.; Kostic, S.; Dworkin, S.B. A novel soot concentration field estimator applied to sooting ethylene/air laminar flames. *Eng. Appl. Comput. Fluid Mech.* **2019**, *13*, 470–481. [CrossRef]
19. Bozorgzadeh, S. Development of a Soot Concentration Estimator for Industrial Combustion Applications. Master’s Thesis, Ryerson University, Toronto, ON, Canada, 2014.
20. Veshkini, A.; Dworkin, S.B.; Thomson, M.J. A soot particle surface reactivity model applied to a wide range of laminar ethylene/air flames. *Combust. Flame* **2014**, *161*, 3191–3200. [CrossRef]
21. Kholghy, M.R.; Veshkini, A.; Thomson, M.J. The core-shell internal nanostructure of soot—A criterion to model soot maturity. *Carbon* **2016**, *100*, 508–536. [CrossRef]
22. Nielsen, M. Neural Networks and Deep Learning. Available online: <http://neuralnetworksanddeeplearning.com/> (accessed on 7 September 2020).
23. Wang, Y.; Li, Y.; Song, Y.; Rong, X. The influence of the activation function in a convolution neural network model of facial expression recognition. *Appl. Sci.* **2020**, *10*, 1897. [CrossRef]
24. Liu, Q.; Wu, Y. Supervised Learning. In *Encyclopedia of the Sciences of Learning*; Springer: Boston, MA, USA, 2012; pp. 3243–3245.
25. The Mathworks Inc. Levenberg-Marquardt Backpropagation. Available online: <https://www.mathworks.com/help/deeplearning/ref/trainlm.html> (accessed on 7 September 2020).
26. Yu, H.; Wilamowski, B.M. Levenberg-marquardt training. In *Intelligent Systems*; CRC Press: Boca Raton, FL, USA, 2011; pp. 1–16.
27. Christo, F.C.; Masri, A.R.; Nebot, E.M.; Turanyi, T. Utilizing artificial neural network and repro-modelling in turbulent combustion. In Proceedings of the ICNN’95—IEEE International Conference on Neural Networks, Perth, WA, Australia, 27 November–1 December 1995; pp. 911–916. [CrossRef]
28. Christo, F.C.; Masri, A.R.; Nebot, E.M.; Pope, S.B. An integrated PDF/neural network approach for simulating turbulent reacting systems. *Symp. Int. Combust.* **1996**, *26*, 43–48. [CrossRef]
29. Li, S.; Yang, B.; Qi, F. Accelerate global sensitivity analysis using artificial neural network algorithm: Case studies for combustion kinetic model. *Combust. Flame* **2016**, *168*, 53–64. [CrossRef]
30. Christo, F.C.; Masri, A.R.; Nebot, E.M. Artificial neural network implementation of chemistry with pdf simulation of H₂/CO₂ flames. *Combust. Flame* **1996**, *106*, 406–427. [CrossRef]
31. Blasco, J.A.; Fueyo, N.; Dopazo, C.; Ballester, J. Modelling the temporal evolution of a reduced combustion chemical system with an artificial neural network. *Combust. Flame* **1998**, *113*, 38–52. [CrossRef]
32. Blasco, J.A.; Fueyo, N.; Larroya, J.C.; Dopazo, C.; Chen, Y.J. A single-step time-integrator of a methane-air chemical system using artificial neural networks. *Comput. Chem. Eng.* **1999**, *23*, 1127–1133. [CrossRef]
33. Ihme, M.; Schmitt, C.; Pitsch, H. Optimal artificial neural networks and tabulation methods for chemistry representation in les of a bluff-body swirl-stabilized flame. *Proc. Combust. Inst.* **2009**, *32*, 1527–1535. [CrossRef]
34. Pulga, L.; Bianchi, G.M.; Falfari, S.; Forte, C. A machine learning methodology for improving the accuracy of laminar flame simulations with reduced chemical kinetics mechanisms. *Combust. Flame* **2020**, *216*, 72–81. [CrossRef]
35. Ranade, R.; Li, G.; Li, S.; Echehki, T. An Efficient Machine-Learning Approach for PDF Tabulation in Turbulent Combustion Closure. *Combust. Sci. Technol.* **2019**. [CrossRef]
36. Ranade, R.; Alqahtani, S.; Farooq, A.; Echehki, T. An ANN based hybrid chemistry framework for complex fuels. *Fuel* **2019**, *241*, 625–636. [CrossRef]

37. Emami, M.D.; Eshghinejad Fard, A. Laminar flamelet modeling of a turbulent CH₄/H₂/N₂ jet diffusion flame using artificial neural networks. *Appl. Math. Model.* **2012**, *36*, 2082–2093. [CrossRef]
38. Inal, F.; Tayfur, G.; Melton, T.R.; Senkan, S.M. Experimental and artificial neural network modeling study on soot formation in premixed hydrocarbon flames. *Fuel* **2003**, *82*, 1477–1490. [CrossRef]
39. Inal, F. Artificial neural network predictions of polycyclic aromatic hydrocarbon formation in premixed n-heptane flames. *Fuel Process. Technol.* **2006**, *87*, 1031–1036. [CrossRef]
40. Eaves, N.A.; Thomson, M.J.; Dworkin, S.B. The Effect of Conjugate Heat Transfer on Soot Formation Modeling at Elevated Pressures. *Combust. Sci. Technol.* **2013**, *185*, 1799–1819. [CrossRef]
41. Veshkini, A.; Dworkin, S.B. A computational study of soot formation and flame structure of coflow laminar methane/air diffusion flames under microgravity and normal gravity. *Combust. Theory Model.* **2017**, *21*, 864–878. [CrossRef]
42. Mansouri, A.; Eaves, N.A.; Thomson, M.J.; Dworkin, S.B. Influence of pressure on near nozzle flow field and soot formation in laminar co-flow diffusion flames. *Combust. Theory Model.* **2019**, *23*, 536–548. [CrossRef]
43. Smooke, M.D.; Long, M.B.; Connelly, B.C.; Colket, M.B.; Hall, R.J. Soot formation in laminar diffusion flames. *Combust. Flame* **2005**, *143*, 613–628. [CrossRef]
44. Shaddix, C.R.; Smyth, K.C. Laser-induced incandescence measurements of soot production in steady and flickering methane, propane, and ethylene diffusion flames. *Combust. Flame* **1996**, *107*, 418–452. [CrossRef]
45. Farrar, D.E.; Glauber, R.R. Multicollinearity in Regression Analysis: The Problem Revisited. *Rev. Econ. Stat.* **1967**, *49*, 92–107. [CrossRef]
46. Allen, M.P. *Understanding Regression Analysis*; Springer: Boston, MA, USA, 2007; pp. 176–180.
47. RYAN, T.P. *Modern Regression Methods*; John Wiley & Sons, Inc.: Hoboken, NJ, USA, 2008.
48. Chatterjee, S.; Hadi, A.S. *Regression Analysis by Example*; John Wiley & Sons, Inc.: Hoboken, NJ, USA, 2006.
49. Aceves, S.M.; Flowers, D.L.; Chen, J.Y.; Babajimopoulos, A. *Fast Prediction of HCCI Combustion with an Artificial Neural Network Linked to a Fluid Mechanics Code*; SAE: Warrendale, PA, USA, 2006. [CrossRef]
50. Berger, L.; Kleinheinz, K.; Attili, A.; Bisetti, F.; Pitsch, H.; Mueller, M.E. Numerically accurate computational techniques for optimal estimator analyses of multi-parameter models. *Combust. Theory Model.* **2018**, *22*, 480–504. [CrossRef]
51. The Mathworks Inc. MATLAB R2018a. Available online: www.mathworks.com/products/matlab (accessed on 7 September 2020).
52. Hagan, M.T.; Menhaj, M.B. Training Feedforward Networks with the Marquardt Algorithm. *IEEE Trans. Neural Netw.* **1994**, *5*, 989–993. [CrossRef] [PubMed]
53. Möller, M.F. A scaled conjugate gradient algorithm for fast supervised learning. *Neural Netw.* **1993**, *6*, 525–533. [CrossRef]
54. Andrei, N. Conjugate gradient algorithms for molecular formation under pairwise potential minimization. In Proceedings of the Fifth Workshop on Mathematical Modelling of Environmental and Life Sciences Problems, Constanta, Romania, 10–13 September 2006; pp. 7–26.
55. The Mathworks Inc. Scaled Conjugate Gradient Backpropagation. Available online: <https://www.mathworks.com/help/deeplearning/ref/trainscg.html> (accessed on 4 September 2020).
56. Memon, Z.A.; Samad, F.; Awan, Z.R.; Aziz, A.; Siddiqi, S.S. CPU-GPU processing. *Int. J. Comput. Sci. Netw. Secur.* **2017**, *17*, 188–193.
57. Lind, E.; Pantigoso, A. A Performance Comparison between CPU and GPU in TensorFlow. Bachelor's Thesis, KTH Royal Institute of Technology, Stockholm, Sweden, 2019.
58. Schlegel, D. *Deep Machine Learning on GPUs*; Seminar Talk, Computer Engineering Group; University of Heidelberg: Heidelberg, Germany, 2015.
59. Hsu, W.; Chang, C.C.; Lin, C.J. *A Practical Guide to Support Vector Classification*; Technical Report; Department of Computer Science, National Taiwan University: Taipei, Taiwan, 2003.
60. Chicco, D. Ten quick tips for machine learning in computational biology. *BioData Min.* **2017**, *10*, 35. [CrossRef]
61. Bergstra, J.; Bengio, Y. Random search for hyper-parameter optimization. *J. Mach. Learn. Res.* **2012**, *13*, 281–305.
62. Feng, C.; Wang, H.; Lu, N.; Chen, T.; He, H.; Lu, Y.; Tu, X.M. Log-transformation and its implications for data analysis. *Shanghai Arch. Psychiatry* **2014**, *26*, 105–109. [CrossRef]
63. Feng, C.; Wang, H.; Lu, N.; Tu, X.M. Log transformation: Application and interpretation in biomedical research. *Stat. Med.* **2013**, *32*, 230–239. [CrossRef] [PubMed]

64. de Villiers, J.; Barnard, E. Backpropagation Neural Nets with One and Two Hidden Layers. *IEEE Trans. Neural Netw.* **1993**, *4*, 136–141. [[CrossRef](#)] [[PubMed](#)]
65. Santoro, R.J.; Semerjian, H.G.; Dobbins, R.A. Soot particle measurements in diffusion flames. *Combust. Flame* **1983**, *51*, 203–218. [[CrossRef](#)]
66. Cepeda, F.; Jerez, A.; Demarco, R.; Liu, F.; Fuentes, A. Influence of water-vapor in oxidizer stream on the sooting behavior for laminar coflow ethylene diffusion flames. *Combust. Flame* **2019**, *210*, 114–125. [[CrossRef](#)]
67. Heinlein, J.; Schulte, G.; Fritsching, U.; Guardani, R. Mapping the structure of a liquid spray by means of neural networks. *Chem. Eng. Process. Process Intensif.* **2007**, *46*, 1357–1364. [[CrossRef](#)]
68. Machine Learning. Available online: https://en.wikipedia.org/wiki/Machine_Learning (accessed on 7 September 2020).



© 2020 by the authors. Licensee MDPI, Basel, Switzerland. This article is an open access article distributed under the terms and conditions of the Creative Commons Attribution (CC BY) license (<http://creativecommons.org/licenses/by/4.0/>).

Article

Acceleration of Premixed Flames in Obstructed Pipes with Both Extremes Open

Abdulafeez Adebisi, Olatunde Abidakun and Vyacheslav Akkerman *

Center for Innovation in Gas Research and Utilization (CIGRU), Department of Mechanical and Aerospace Engineering, West Virginia University, 1306 Evansdale Drive, Morgantown, WV 26506-6106, USA; abadebisi@mix.wvu.edu (A.A.); oaabidakun@mix.wvu.edu (O.A.)

* Correspondence: vyacheslav.akkerman@mail.wvu.edu

Received: 19 June 2020; Accepted: 1 August 2020; Published: 7 August 2020

Abstract: Premixed flame propagation in obstructed channels with both extremes open is studied by means of computational simulations of the reacting flow equations with a fully-compressible hydrodynamics, transport properties (heat conduction, diffusion and viscosity) and an Arrhenius chemical kinetics. The aim of this paper is to distinguish and scrutinize various regimes of flame propagation in this configuration depending on the geometrical and thermal-chemical parameters. The parametric study includes various channel widths, blockage ratios, and thermal expansion ratios. It is found that the interplay of these three critical parameters determines a regime of flame propagation. Specifically, either a flame propagates quasi-steady, without acceleration, or it experiences three consecutive distinctive phases (quasi-steady propagation, acceleration and saturation). This study is mainly focused on the flame acceleration regime. The accelerating phase is exponential in nature, which correlates well with the theoretical prediction from the literature. The accelerating trend also qualitatively resembles that from semi-open channels, but acceleration is substantially weaker when both extremes are open. Likewise, the identified regime of quasi-steady propagation fits the regime of flame oscillations, found for the low Reynolds number flames. In addition, the machine learning logistic regression algorithm is employed to characterize and differentiate the parametric domains of accelerating and non-accelerating flames.

Keywords: premixed combustion; obstructed channels; flame acceleration; thermal expansion; computational simulations; machine learning

1. Introduction

Semi-open channels and tubes (where one end of the pipe is closed while another end is open; a flame is ignited at the closed end and propagates towards the open extreme), with evenly arranged and closely packed obstacles along the sidewalls, have been reported to experience ultrafast premixed flame acceleration (FA) and eventually an event of deflagration-to-detonation transition (DDT) [1–5]. This acceleration mechanism is conceptually laminar, being devoted to a powerful jet flow along the pipe centerline [1]. The cause of such acceleration is attributed to the cumulative effects of delayed burning in the pockets between the obstacles, with turbulence playing only a supplementary role [2]. On the contrary, industrial and laboratory conduits oftentimes have both extremes open, which attracted the interest for decades, starting with the classical experimental works on choked flames [6] and quasi-detonations [7] in open obstructed pipes; see also [8,9] and references therein for details. In such a situation of both open extremes of an obstructed pipe, a new gas volume, generated by expansion of the burning matter in the combustion process, flows from the side pockets into two distributed streams moving towards the two open ends, as illustrated in Figure 1. Non-restriction of the flow in axial direction results in a mechanism of flame propagation different from that previously observed in semi-open channels. For narrow channels, oscillations of the flame shape and velocity

dominate in the flame dynamics [10,11]. Occurrence of these oscillations is due to regularly repeated acceleration-deceleration sequences causing the flame to have varying instantaneous shape, area and velocity [10].

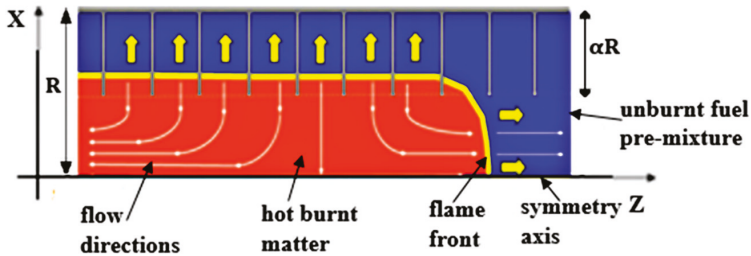


Figure 1. A schematic of an obstructed channel with both extremes open (upper half is shown).

A significant difference in flame propagation observed in these pipe configurations, coupled to potential improvements of practical applications [12] and associated with deeper understanding of flame propagation in such applications, have stirred up a significant interest. In a bid to satisfy the prevailing concerns and gain further insight into the morphology and propagation of premixed flames in obstructed conduits, a number of studies of burning in semi-open obstructed channels have been performed [13–15]. The analytical, numerical and experimental investigations of FA in fully-open channels suggested that hydraulic resistance of the fluid in a pipe is responsible for sudden acceleration and the initial stage of DDT [16,17]. However, a subsequent analytical investigation [18] showed that the hydraulic resistance is not necessary to drive obstacles-based acceleration in an open channel; in fact, it hinders FA at the initial stage of the combustion process. In particular, flame propagation in narrow obstructed channels with open ends has been computationally studied [10], where regular fluctuations of the burning rates around the quasi-steady solutions have been found for the majority of the simulation runs performed. Other geometrical and thermochemical parameters such as the obstacles blockage ratio, the spacing between the obstacles and the thermal expansion ratio have been observed to influence the flame oscillatory behavior in terms of the oscillation periods and amplitudes. However, some pilot studies reported in [10] showed the possibility of FA after the initial oscillations or steady flame propagation.

In this light, exploring the flame behavior and characterizing various propagation regimes that the flame undergoes constitute the basis of the present work. Specifically, we aim to elucidate and quantify the morphology and dynamics of a premixed flame propagating through a comb-shaped array of obstacles in open channels of various blockage ratios, considering fuel mixtures of various thermal expansion ratios. The analysis is conducted by means of computational simulations of the reacting flow equations involving transport properties, a fully-compressible hydrodynamics and an Arrhenius chemical kinetics. A special attention is paid to relatively wide channels, in which the possibility of flame portraying more than one propagation regimes has been indicated. In the present work, it is also of our interest to validate the theoretical formulation [18] by comparing it with the simulation results obtained. Subsequently, we have identified three main stages of flame propagation in a fully-open obstructed pipe, namely: (i) quasi-steady propagation, (ii) exponential FA, and (iii) saturation of the burning velocity. Comparison of the exponential acceleration stage with a respective prediction from [18] shows a good correlation, especially at a later stage of exponential acceleration.

2. Research Methodology

The research methodology employed here is based on scrutinizing reacting flows in fully-open, obstructed channels by means of computational simulations of the governing partial differential equations (PDE) for a conservation/balance of mass, momentum, energy and species, including a

fully-compressible hydrodynamics, transport properties (heat conduction, diffusion and viscosity), and an Arrhenius chemical kinetics represented by a one-step irreversible reaction of the first order.

2.1. Governing Equations

In a two-dimensional (2D) geometry, considered in the present work, the governing PDEs read:

$$\frac{\partial \rho}{\partial t} + \frac{\partial}{\partial x_i}(\rho u_i) = 0, \quad \frac{\partial}{\partial t}(\rho u_i) + \frac{\partial}{\partial x_j}(\rho u_i u_j + \delta_{ij} P + \gamma_{i,j}) = 0, \tag{1}$$

$$\frac{\partial}{\partial t}(\rho e + \frac{1}{2} \rho u_i u_i) + \frac{\partial}{\partial x_j}(\rho u_i h + \frac{1}{2} \rho u_i u_j u_j + q_i - u_j \gamma_{i,j}) = 0, \tag{2}$$

$$\frac{\partial}{\partial t}(\rho Y_F) + \frac{\partial}{\partial x_i}(\rho u_i Y_F - \frac{\eta}{Sc} \frac{\partial Y_F}{\partial x_i}) = -\frac{\rho Y_F}{\tau_R} \exp\left(-\frac{E_a}{R_u T}\right), \tag{3}$$

where Y_F is a progress variable representing the mass fraction of the fuel mixture; $e = QY_F + C_v T$ and $h = QY_F + C_p T$ are the specific internal energy and enthalpy, respectively, with the specific heats at constant volume, C_v , and pressure, C_p , and the energy release from the reaction $Q = (\Theta - 1)C_p T_f$. Here T_f is the initial temperature of the fuel mixture and $\Theta \equiv \rho_f / \rho_b$ is the thermal expansion ratio. Equation (3) describes a single, first-order Arrhenius reaction, with the activation energy E_a and the constant of time dimension τ_R . In our code, the cumulative choice (interplay) of the three parameters Q , E_a and τ_R constitutes an eigenvalue problem, solution to which yields the unstretched laminar burning velocity $S_L = S_L(Q, E_a, \tau_R)$, which is also a unity of velocity dimension in the present work. Here we took $S_L = 3.47$ m/s resembling typical hydrogen-air flames as well as oxy-methane or oxy-propane combustion. The speed of sound in this fuel mixture is 100 times larger, $c_s = 347$ m/s such that the hydrodynamics is almost incompressible at the initial stage of burning, with the initial Mach number associated with flame propagation being as small as $M_0 \equiv S_L / c_s = 10^{-2}$. However, for a corrugated flame front, the real (total) burning velocity U_w exceeds S_L , and it is calculated as [19]:

$$U_w = \frac{1}{2R\rho_f} \int \frac{\rho Y}{\tau_R} \exp\left(-\frac{E_A}{R_u T}\right) dx dz. \tag{4}$$

Both the fuel mixture and burnt matter are assumed to be ideal gases obeying the equation of state:

$$P = \rho R_u T / m, \tag{5}$$

with the same molecular weight of $m = 2.9 \times 10^{-2}$ kg/mol and the specific heats of $C_v = 5R_p/2m$ and $C_p = 7R_p/2m$, where $R_u = 8.314$ kJ/(kmol·K) is the universal gas constant. The stress tensor $\gamma_{i,j}$ and the energy diffusion vector q_i are given by

$$\gamma_{i,j} = \zeta \left(\frac{\partial u_i}{\partial x_j} + \frac{\partial u_j}{\partial x_i} - \frac{2}{3} \frac{\partial u_k}{\partial x_k} \delta_{i,j} \right), \quad q_i = -\zeta \left(\frac{C_p}{Pr} \frac{\partial T}{\partial x_i} + \frac{Q}{Sc} \frac{\partial Y_F}{\partial x_i} \right), \tag{6}$$

with the dynamic viscosity $\zeta = \rho \nu$, the Prandtl, Pr , and Schmidt, Sc , numbers. To avoid any impact of the diffusional-thermal instability, here we consider equidiffusive burning, so the Lewis number (defined as the thermal-to-mass diffusivities ratio) is unity, $Le = 1$. In the simulations, this condition is imposed by taking the Prandtl and Schmidt numbers $Pr = Sc = 1$ such that $Le \equiv Sc/Pr = 1$. Then the thermal flame thickness can be defined, conventionally, as:

$$L_f = \zeta / Pr \rho S_L = \nu / Pr S_L = \nu / S_L. \tag{7}$$

It is however noted that the quantity (7) is only a thermal-chemical parameter of length dimension, while the real size of the internal flame structure can be an order of magnitude larger [20]. Indeed, according to [20], a real width of the burning zone, determined by the characteristic length scale of the temperature profile gradient, is about $(4 \sim 5)L_f$, while it is the thickness of the *active reaction zone*, which is actually of the order of L_f [20]. Nevertheless, L_f is one of the key parameters in our studies, for the following reasons. First, it controls the choice of the computational mesh size making sure that the grid is sufficiently fine to resolve the flame front, having several grid point inside it; see a discussion below. Second, L_f is a characteristic flame length scale. Along with a characteristic flame velocity scale S_L , they determine the characteristic flame time scale $t_f \equiv L_f/S_L$. Moreover, in addition to L_f , another important length scale in this work is the radius (half-width) of the channel R , but it will also be measured in terms of L_f , because their ratio constitutes the Reynolds number associated with flame propagation, $Re = RS_L/\nu = R/PrL_f = R/L_f$. The ratio of R and S_L allows introducing a convenient dimensionless time $\tau \equiv tS_L/R$. Consequently, in our investigations, we are monitoring the instantaneous scaled burning velocity, $U_w(\tau)/S_L$, as well as the instantaneous scaled flame tip positions and velocities, $Z_{tip}(\tau)/R$ and $U_{tip}(\tau)/S_L$, versus the scaled time τ , for the given values of $Re = R/L_f$.

Finally, the quantity of L_f may be needed to impose appropriate ignition conditions. We usually imitate the initial flame structure by the classical Zeldovich-Frank-Kamenetskii (ZFK) solution for the profiles of the temperature, fuel mass fraction, pressure and velocities in the domain before and after a planar flame front, which reads [21]:

$$T = T_f + T_f(\Theta - 1)\exp(z/L_f) \text{ if } z > 0 \text{ (fuel)}, \quad (8)$$

$$T = \Theta T_f \text{ if } z < 0 \text{ (burnt)}, \quad (9)$$

$$Y_F = (\Theta - T/T_f)/(\Theta - 1), \quad P = P_f, \quad u_x = 0, \quad u_z = 0, \quad (10)$$

such that $Y_F = 0$, and $T = T_b = \Theta T_f$ in the burnt matter ($z < 0$), while $Y_F \rightarrow 1$, and $T \rightarrow T_f$ in the fresh fuel mixture ($z \gg L_f > 0$). The original pressure P throughout the domain equals the initial pressure of the fuel mixture, P_f , and both velocity components are set to zero at the very beginning.

2.2. Computational Platform

We use an in-house computational fluid dynamics (CFD) fully-compressible, finite-volume Navier–Stokes code, which solves, in particular, the reacting flow Equations (1)–(6). The embryo of this code was originally developed in the middle of 1990s by Eriksson at Volvo Aero. In the following decades, this computational platform has been comprehensively updated and tested by numerous research groups worldwide, including (but not limited to) researchers from Chalmers University of Technology, Royal Institute of Technology, Uppsala and Umeå Universities in Sweden, Tsinghua University in China, Princeton and West Virginia Universities in the U.S. The current version of the solver is adapted for parallel computations and is available in 2D versions (Cartesian and cylindrical axisymmetric ones) as well as in a fully three-dimensional (3D) Cartesian version (though solely a 2D Cartesian set of Equations (1)–(6) is modelled in the present work). In order to save the computational time while resolve the regions of particular interest (leading pressure and shock waves, detonation or flame fronts), a self-adaptive structured computational grid is employed, as will be detailed below. This adaptive grid makes the computational package perfect, in particular, for fundamental studies of reacting and non-reacting flows in conduits of high aspect ratios such as used in the present work.

The code is robust and accurate, having been successfully utilized in numerous aero-acoustic [22–24] and combustion [1–5,10,19,20,25–35] applications, including combustion instabilities [25–29], flame-acoustic coupling [19], FA [30–33] and DDT in unobstructed [34,35] and obstructed [2] conduits. Specifically, in [25], the solver was validated by being able to reproduce a classical physical solution for pressure, temperature, burning velocity and other significant parameters of a planar flame front. Subsequently, the solver

successfully reproduced an onset and development of the intrinsic Darrieus-Landau flame instability: in a planar, 2D channel [25]; in a cylindrical tube (narrow [26], moderate [27] or wide [28]); and in an open space [29]. Such intriguing nonlinear phenomena as flame-acoustic resonance [19] and flame oscillations in channels [20] were also modeled by means of this solver. The code has been widely used and shown to be particularly successful in modelling various mechanisms of FA in pipes such as FA due to wall friction in 2D channels [30] and cylindrical tubes [31,32] as well as FA due to a finger-like flame shape [33]. The code was able to reproduce how both the mechanisms can potentially drive through all the stages of the DDT scenario, including the latest one—detonation triggering. We have successfully modelled such a DDT for FA due to wall friction [34] and for finger FA [35]. It is emphasized that all numerical works overviewed here [25–35] employed unobstructed geometry. Subsequently, we incorporated obstacles into the computational platform and successfully modelled FA [3–5] and DDT [2] in semi-open obstructed channels.

Finally, it should be mentioned in passing that modelling of DDT often faces difficulties. In particular, no real mechanism of detonation triggering is available for a simplified Arrhenius chemical kinetics employed here, while detailed chemistry would affect the results, in particular, the timing of the detonation onset. However, in the present work, we do not actually focus on DDT and detonation but consider mostly FA at the early (subsonic) stage of the combustion process. Moreover, we analyze the scaled values U_{tip}/S_L , Z_{tip}/R , τ , Re , Θ etc.—rather than the dimensional quantities of velocities, lengths, time and energies. This makes our consideration rather qualitative than quantitative. In other words, it is conventionally adopted that the chemistry is “immersed” in the chosen parameters such as E_a , τ_R , Q and, thereby, S_L , while the evolution of the scaled variables should not change much. In fact, in this work we scrutinize FA in fully-open obstructed channels as compared with the situations considered in our previous works [1–5,10]. Since all these works employed the same computational platform, with the same one-step Arrhenius kinetics, there is no background to use anything else in the present work, which justifies the usage of this computational platform for this particular problem.

2.3. Computational Approach, Parameters and Domain

The numerical approach is based on a cell-centered, finite-volume numerical scheme, which is of the second-order accuracy in time and the fourth-order in space for the convective terms, and of the second-order in space for the diffusive terms. The code employs the balance Equations (1)–(3) in a unified form [25]

$$\frac{\partial G}{\partial t} + \frac{\partial E_G}{\partial z} + \frac{\partial F_G}{\partial x} = H_G, \quad (11)$$

where G stands for any of the variables ρ , ρu_x , ρu_z , ρY_F and e , while E_G and F_G designate the related axial and radial fluxes, respectively, and H_G is the source term. The spatial discretization is obtained by integrating any of the conservation laws (1)–(3) in the form (11) over a given grid cell. More details about the numerical method are available, for instance, in [2,5,10,25].

In the present work, a premixed flame propagates in a long 2D channel of width $2R$, with both extremes open, where the fraction of width $2R\alpha$, near the walls, is blocked by the obstacles with the spacing (the distance between two neighboring obstacles) ΔZ . In this light, the major dimensionless parameters of this study are the thermal expansion ratio Θ , the blockage ratio α , the scaled spacing $\Delta Z/R$, and the Reynolds number associated with flame propagation $Re = R/L_f$. To be specific, the following thermal-chemical and configurational parameters have been taken: various $\Theta = 5, 6, 8, 10$; $\alpha = 1/3, 1/2, 2/3$; $R/L_f = 24, 36, 48$; and fixed $\Delta Z/R = 1/4$. The initial temperature, pressure and density of the fuel mixture are $T_f = 300$ K, $P_f = 100$ kPa, and $\rho_f = 1.16$ kg/m³, respectively.

In order to save the computational cost, similar to [5,10], we are looking for a symmetric solution such that only half of the channel is actually modeled by employing the symmetry condition at the bottom as illustrated in Figure 1. To keep the flame segments as planar as possible, we employ the walls of the channels and the obstacles to be adiabatic, $\mathbf{n} \cdot \mathbf{VT} = 0$, and free-slip, $\mathbf{n} \cdot \mathbf{u} = 0$, where \mathbf{n} is a

normal vector at the surface of the wall/obstacle. The absorbing (non-reflecting) characteristic boundary conditions are set at both open extremes to prevent the reflection of the sound waves and weak shocks from these outlets. Such non-reflecting boundary conditions have been widely tested in our previous works [19,20,25]. Initially, the parameters at the right (unburnt) end are $\rho = \rho_f$, $T = T_f$ and $u_z = -S_L$, while those at the left (burnt) extreme are $\rho = \rho_f/\Theta$, $T = \Theta T_f$, and $u_z = -\Theta S_L$. The initial flame structure was imitated by the ZFK solution for a planar flame front, Equations (8)–(10). Such a planar ZFK flame was initiated at a distance $50 L_f$ from the left (burnt) end of the channel.

The computational domain is being reconstructed depending on an instantaneous location of a flame front and the leading pressure wave, so the length of the domain grows with time. Such a reconstruction of the grid is achieved by using the third-order splines to interpolate the flow variables during the grid reconstruction and preserves the second-order accuracy of the numerical scheme. The dynamic grid consists of a structured rectangular grid, with the walls of the grid parallel to each direction. This adaptive mesh has the minimal cell size of $0.2 L_f$, which has been justified in the previous works employing this solver; see, for instance, [10,20] (and references therein). Indeed, it is recalled that L_f correlates with the width of the active reaction zone, while the thermal (temperature-based) flame thickness is about $(4 \sim 5)L_f$ [20]. Consequently, taking the grid size of $0.2 L_f$, we obtain about five grid points inside the active reaction zone and 20–25 grid points inside the flame front. Therefore, the grid used in the present work has a sufficiently fine resolution as the thickness of the reaction zone appears distributed over several computational cells.

3. Results and Discussion

The morphology and propagation of premixed flames in obstructed channels with both ends open demonstrate unique and distinct characteristics as compared to semi-open channels. Initially, an oscillating trend has been observed for $R/L_f = 12$ [10], with the oscillation characteristics being dependent on the thermal expansion ratio Θ , the blockage ratio α , and the obstacle spacing ΔZ . The series of snapshots in Figure 2 shows the flame development and the flow distributions for burning with $\Theta = 8$ in a channel having $R/L_f = 48$ and $\alpha = 1/2$. An initially planar flame front undergoes folding as it propagates due to the influence of thermal expansion across the flame front, while the entire flow is directed towards the left extreme as seen in Figure 2a. Eventually, after propagating through circa two channel widths, Figure 2b, the flow is distributed between the two extremes and the flame has gradually attained a tulip-like shape. The momentum released from the left extreme, along with the accompanied heat losses, moderate flame propagation significantly. As seen in Figure 2, the pockets of the unburnt fuel mixture are generated as the flame moves further, thereby creating the effect of delayed burning (thermal expansion) from each of these pockets. As the unburnt gas in these pockets starts burning, the expanding gases flow into the core of the channel and are distributed between the two flows moving towards two extremes. With further propagation away from the left extreme, the unburned pockets are further away from the left outlet, Figure 2c,d, and the new gas volume, generated by thermal expansion in the burning process, flows in the direction causing least resistance, i.e., in the direction of the flame. In this regime, the flame starts undergoing significant acceleration, which is sustained as the flame front travels further. This is accompanied by continuous formation and isolation of the new pockets from the left extreme, thereby propelling the flame further through formation of a jet flow in the core path of the channel. This regime of burning is observed in Figure 2e–g. As burning progresses further, the flame velocity grows, and the flame shape develops into a highly corrugated structure as seen in Figure 2g. With increasing Mach number, the influence of gas compressibility becomes significant, subsequently causing moderation of FA and saturation of the burning velocity to a near-constant value. Interestingly, at the saturated velocity state, the flame front appears more stable such that the small-scale wrinkles disappear as seen in Figure 2h.

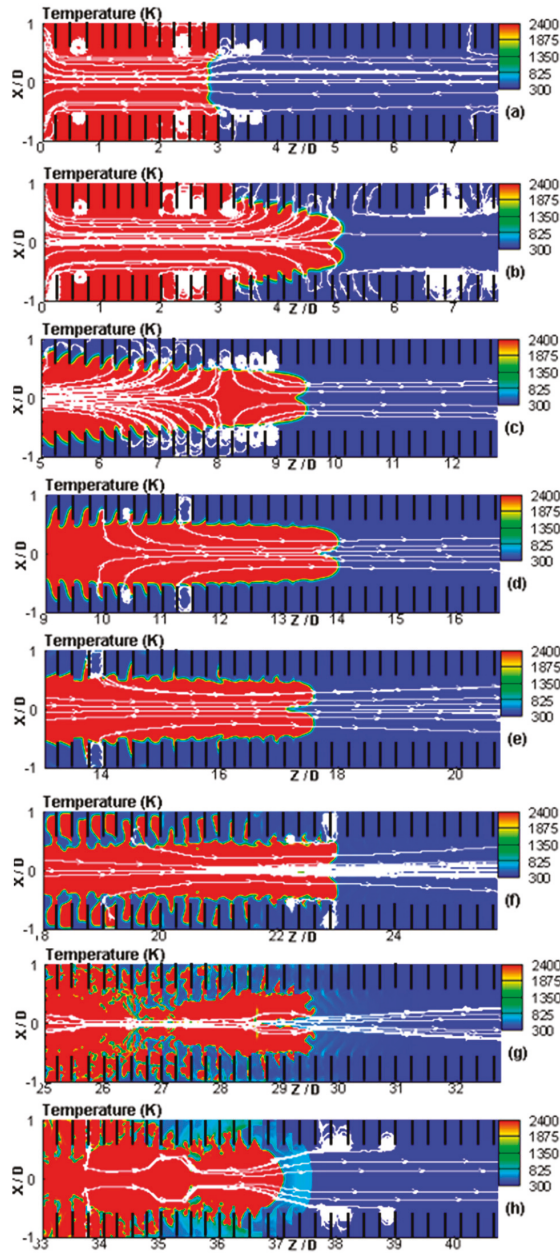


Figure 2. Consecutive color temperature snapshots for the evolution of a flame with the thermal expansion ratio $\Theta = 8$ propagating in a channel with the blockage ratio $\alpha = 1/2$: initial (concave) flame folding (a); transition to a convex flame (b); isolation of new pockets between the obstacles (c); fast flame acceleration (d,e); jet-flow formation along the channel centerline (f); development of a highly-corrugated flame structure (g); and disappearance of small-scale wrinkles (h).

These observations provide the insights into the physics of premixed flames in obstructed channels with both ends open. Namely, a flame undergoes initial quasi-steady propagation, which dominates in the region of the simultaneous (near equal) flows of the expanding gases towards both extremes of the channels. Subsequently, the onset of FA occurs, which is then supplanted by the state of saturated propagation velocity. Figure 3a shows the evolution of the flame tip position scaled by the channel half-width R . To visualize these regimes clearly, it is important to analyze the derivative of the flame tip position (i.e., the flame tip velocity). This quantity, scaled by the laminar flame speed S_L , is presented in Figure 3b, indicating the regimes of quasi-steady propagation, exponential acceleration and the saturated flame velocity. The flame tip variations with time are qualitatively similar to the experimental results of Middha and Hansen [36] as well as that of Yanez et al. [37]. The exponential acceleration regime mimics the trend seen in the semi-open channel with closely packed obstacles [37], namely, exponential FA without initial quasi-steady propagation. However, such initial quasi-steady propagation is quite similar to the oscillatory regime identified in narrower channels [10]. Apparently, the oscillations can correlate with prolonged quasi-steady propagation as the flame tries to balance the complex flow dynamics and gas expansion in such a highly confined space. Figures 4 and 5 compare the structures of the flame and the flow at the accelerating phase (Figure 4) to that at the saturated phase (Figure 5). To be specific, the characteristic instantaneous temperature snapshots as well as those for vorticity and shock waves are shown. It is seen that the leading vortices, inherent during the accelerating phases, are absent at the saturated phase, with strong vortices confined behind the flame front. Likewise, the leading shock waves in the accelerating phase are not apparent when the flame velocity saturates to a steady one.

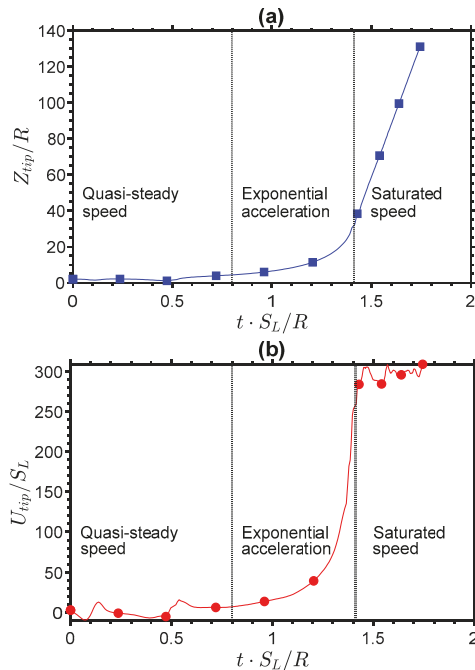


Figure 3. The scaled flame tip position Z_{tip}/R (a) and velocity U_{tip}/S_L (b) versus the scaled time $\tau = tS_L/R$ for a flame with the expansion ratio $\Theta = 8$ in a channel with the blockage ratio $\alpha = 1/2$.

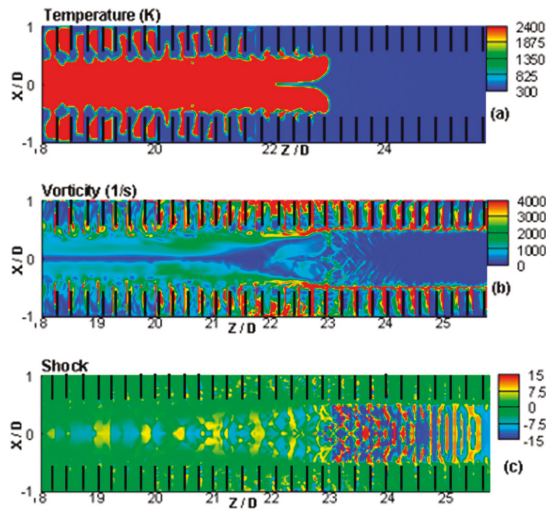


Figure 4. The characteristic instantaneous snapshots of the temperature (a), vorticity (b) and shock waves (c) taken at the acceleration phase of the evolution of a flame with the thermal expansion ratio $\Theta = 8$ propagating in a channel with the blockage ratio $\alpha = 1/2$.

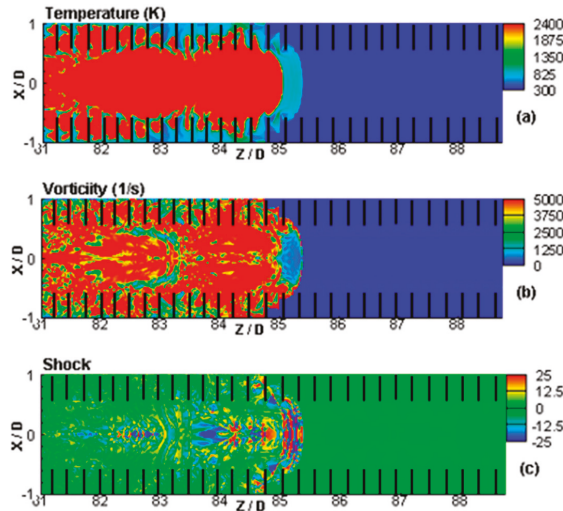


Figure 5. The characteristic instantaneous snapshots of the temperature (a), vorticity (b) and shock waves (c) taken at the saturation phase of the evolution of a flame with the thermal expansion ratio $\Theta = 8$ propagating in a channel with the blockage ratio $\alpha = 1/2$.

We next study the impacts of the blockage ratio α , the channel half-width R and the thermal expansion ratio Θ on the flame dynamics. Specifically, Figures 6–8 show the scaled flame tip position Z_{tip}/R and the scaled burning velocity U_w/S_L versus the scaled time $\tau = tS_L/R$. The flame propagation trend is strongly influenced by the blockage ratios. Namely, as α grows, the duration of quasi-steady propagation also increases. For the lowest blockage ratio considered, $\alpha = 1/3$, a flame propagates quasi-steadily without acceleration. For low α , the core (unobstructed) flow area is increased as such the volume of the gas flowing out increases accordingly, while the new gas volume, generated in the

pockets, is reduced. Consequently, the contribution of delayed burning to propelling the flame front decreases, thereby moderating the flame velocity tremendously.

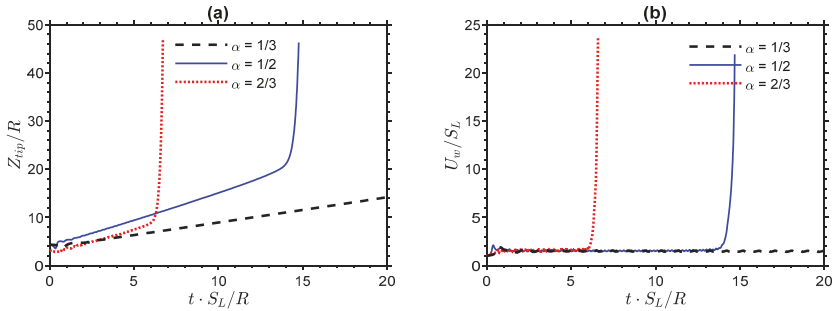


Figure 6. The scaled flame tip position Z_{tip}/R (a) and the scaled burning velocity U_w/S_L (b) versus the scaled time $\tau = tS_L/R$ for the $\Theta = 8$ flame in the channels of half-width $R = 24 L_f$ with various blockage ratios $\alpha = 1/3, 1/2, 2/3$.

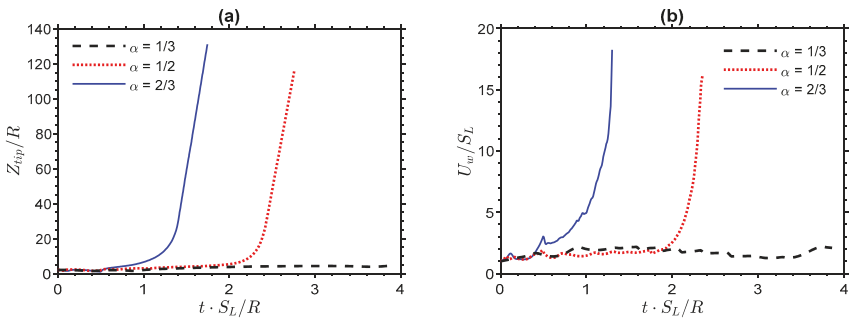


Figure 7. The scaled flame tip position Z_{tip}/R (a) and the scaled burning velocity U_w/S_L (b) versus the scaled time $\tau = tS_L/R$ for the $\Theta = 8$ flame in the channels of half-width $R = 36 L_f$ with various blockage ratios $\alpha = 1/3, 1/2, 2/3$.

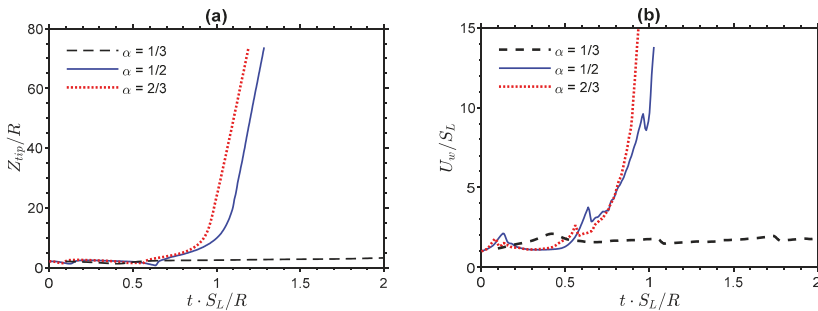


Figure 8. The scaled flame tip position Z_{tip}/R (a) and the scaled burning velocity U_w/S_L (b) versus the scaled time $\tau = tS_L/R$ for the $\Theta = 8$ flame in the channels of half-width $R = 48 L_f$ with various blockage ratios $\alpha = 1/3, 1/2, 2/3$.

Moreover, increasing the channel half-width reduces the duration of quasi-steady propagation for $\alpha = 1/2$ and $2/3$. This effect is observed more apparently in Figure 9a. Here, as the channel half-width grows from $24 L_f$ to $48 L_f$, the scaled time τ , taken before acceleration starts, decreases by a factor of 10, from 6 to 0.6. Consequently, this initial time delay (prior to acceleration) diminishes as the channel widens. Therefore, a growth of the channel width provides an impact similar to that of growing α . For a wider channel, $R = 48 L_f$, the large blockage ratios, $\alpha = 1/2$ and $2/3$, provide the similar effects on flame propagation and the difference in the durations of the stages of quasi-steady propagation is minor, see Figure 8, while no acceleration is seen for $\alpha = 1/3$ in this case.

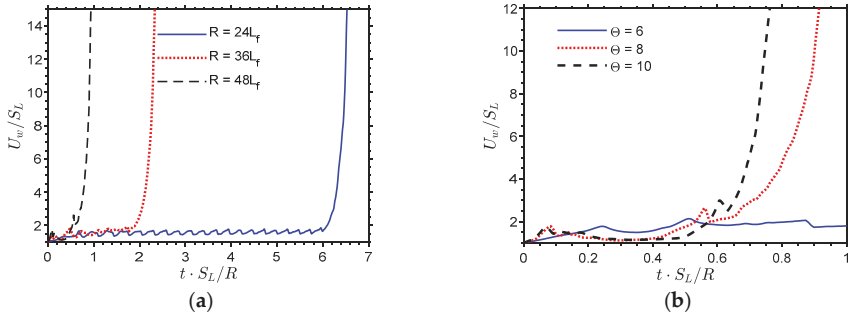


Figure 9. The scaled burning velocity U_w/S_L versus the scaled time $\tau = tS_L/R$ for burning in the obstructed channels of $\alpha = 2/3$ for: $\Theta = 8$ with various $R/L_f = 24, 36, 48$ (a) and $R/L_f = 48$ with various $\Theta = 6, 8, 10$ (b).

Similar to the effect of the blockage ratio, an increase in the thermal expansion ratio Θ shortens the stage of quasi-steady propagation, and at the subsequent stage of acceleration, the acceleration rate is increased as shown in Figure 9b. For the fuel mixtures of large Θ , the expansion produced across the flame is obviously enhanced, and the flame surface area will grow accordingly, leading to faster transition to the accelerating phase and faster FA. In contrast, the flames of lower thermal expansion propagates quasi-steadily without undergoing any significant acceleration.

In order to scrutinize the exponential regime of FA, which follows the quasi-steady phase observed in this scenario, we next recall a theory of FA in fully-open obstructed channels [18]. While [18] considered both inviscid and viscous formulations, here we chose the inviscid theory only in order to avoid considering the length on the conduit. Then, within the inviscid formulation, the flame tip velocity U_{tip} obeys the evolution equation [18]:

$$U_{tip} = \frac{dZ_{tip}}{dt} = \frac{(\Theta - 1)}{(1 - \alpha)} \frac{Z_{tip}}{\sqrt{\Theta + 1}} + \Theta S_L, \tag{12}$$

with the solution:

$$Z_f = \frac{\Theta R}{\sigma_0} \exp(\sigma_0 S_L/R) - 1, \tag{13}$$

where the scaled exponential acceleration rate for the fully open channel, σ_o , is given by [18]:

$$\sigma_o = \frac{1}{(\sqrt{\Theta + 1})} \frac{(\Theta - 1)}{(1 - \alpha)} = \frac{\sigma_s}{\sqrt{\Theta + 1}}. \tag{14}$$

The indexes o and s in Equation (14) are devoted to the fully-open and semi-open channels, respectively. It is seen from Equation (14) that the exponential acceleration rate in fully-open channels is much less than that in semi-open channels, for the same fuel. Obviously, this is because the flow is split in two parts when both ends of a pipe are open. To validate this theory by our simulation results

and to understand the exponential acceleration regimes clearly, we plot Equation (13) and compare it with the simulation results. For this purpose, a quasi-steady stage of flame propagation is extracted from the simulation by shifting the flame tip position Z_{tip} , accordingly, such that the instant $t = 0$ indicates that exponential FA starts. This comparison is shown in Figures 10–12 for the accelerating flame regime only. Figure 10 presents the trend in the $R = 24 L_f$ channel; in Figure 10a, the theory predicts the later stage of exponential acceleration quite well, while in Figure 10b, $\alpha = 2/3$, the theory diverges from the simulation later in time but shows better prediction at an early propagation stage.

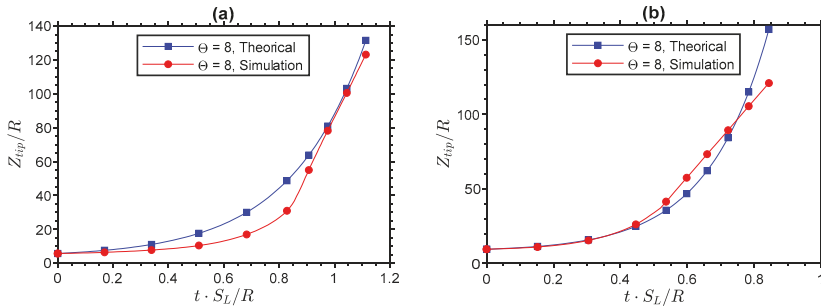


Figure 10. The scaled flame tip position Z_{tip}/R versus the scaled time $\tau = tS_L/R$ for burning in the channels of half-width $R = 24 L_f$ with the blockage ratios $\alpha = 1/2$ (a) and $\alpha = 2/3$ (b).

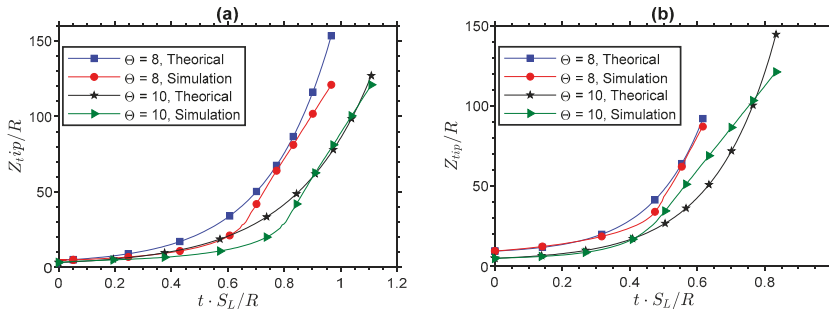


Figure 11. The scaled flame tip position Z_{tip}/R versus the scaled time $\tau = tS_L/R$ for burning in the channels of half-width $R = 36 L_f$ with the blockage ratios $\alpha = 1/2$ (a) and $\alpha = 2/3$ (b).

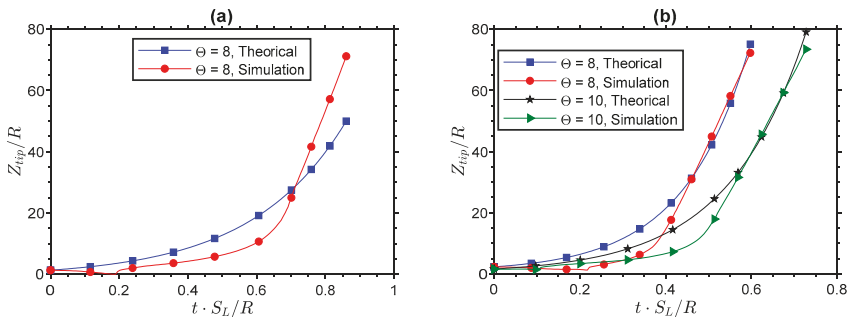


Figure 12. The scaled flame tip position Z_{tip}/R versus the scaled time $\tau = tS_L/R$ for burning in the channels of half-width $R = 48 L_f$ with the blockage ratios $\alpha = 1/2$ (a) and $\alpha = 2/3$ (b).

In Figure 11a, representing the channel of half-width $36 L_f$ and $\alpha = 1/2$, the theory captures the later trend better for $\Theta = 10$. However, for the $\alpha = 2/3$ case, Figure 11b, the later acceleration trend is better captured when $\Theta = 8$. The trends for $\alpha = 1/2, 2/3$ and $\Theta = 8, 10$ in the channel of half-width $48 L_f$ are shown in Figure 12. Here, the later trend of exponential acceleration is better captured for $\alpha = 2/3$ and $\Theta = 8, 10$, see Figure 12b. Although the theory yields a good approximation of exponential acceleration, it narrowly captures the trend in the earlier acceleration phase. In fact, theoretically, the exponential acceleration rates have definite value even for the low blockage and thermal expansion ratios. For instance, for $\alpha = 1/3$ with $\Theta = 6$, we have $\sigma_0 = 2.17$. However, no acceleration has actually been observed with such a set of parameters. The simulation results for the combination of such a low α and Θ do not show FA. In fact, acceleration is only noticeable when both α and Θ are large. Specifically, at $\alpha = 1/2$ with $\Theta = 8$, FA becomes noticeable when $\sigma_0 = 3.66$. Therefore, initiation of actual exponential acceleration will happen when $2.17 \leq \sigma_0 \leq 3.66$, which corresponds to $1/3 \leq \alpha \leq 1/2$ and $6 \leq \Theta \leq 8$.

The resulting saturated velocity occurring due to gas compression is expected to be lower than the Chapman-Jouget (CJ) deflagration velocity, which is defined as [38]:

$$\frac{U_{CJ}}{c_s} = \left[1 + \frac{\gamma(\gamma - 1)}{2(\gamma + 1)} \right] \sqrt{2 \left(\frac{\Theta - 1}{\gamma + 1} \right)}. \tag{15}$$

Figure 13 presents the scaled flame tip velocity versus the scaled flame tip position (such a phase diagram), for $\Theta = 8$ and $\Theta = 10$ in Figure 13a,b, respectively. The solid horizontal lines show the scaled CJ deflagration velocity, Equation (15), which is thereby compared to the saturated flame tip velocity. It is seen that Equation (15) exceeds the computational saturated flame velocity for all the cases considered in Figure 13. In the case of $\Theta = 8$, Figure 13a, weak R -dependence is observed: the saturated flame velocity is slightly higher for $R = 24 L_f$ than that for $R = 36 L_f$. However, in the case of $\Theta = 10$, Figure 13b, the saturated velocity curves collapse to the same value for all widths for each blockage ratios $\alpha = 1/2$ and $\alpha = 2/3$. We can therefore conclude from Figure 13 that the saturated flame tip velocity for $\alpha = 1/2$ exceeds that for $\alpha = 2/3$, and this value is almost independent of the channel width, particularly for $\Theta = 10$.

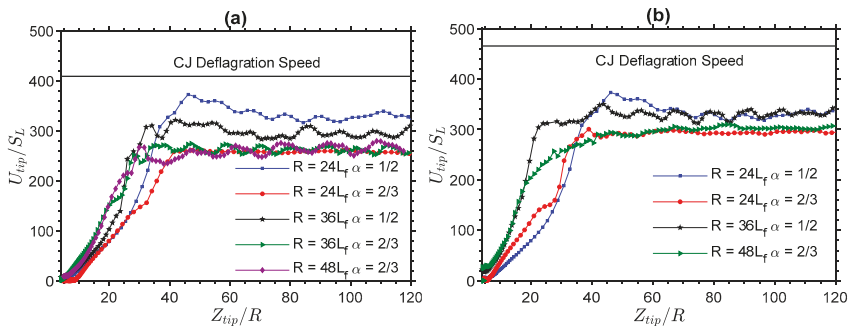


Figure 13. The scaled flame tip velocity U_{tip}/S_L versus the scaled flame position Z_{tip}/R for the $\Theta = 8$ (a) and $\Theta = 10$ (b) flames propagating in channels of various widths and blockage ratios.

While the present simulations are limited to a 2D Cartesian geometry, it is of interest to discuss how the computational results might change in a 3D geometry, either cylindrical axisymmetric or 3D Cartesian, as both situations are closer to the practical reality than the 2D planar channel studied here. We start the discussion with the analogies observed in unobstructed conduits with both ends open, where computational simulations demonstrated regular flame oscillations in the 2D channels [20] but flame acceleration in the cylindrical pipes [32]. We expect the same qualitative trend in the obstructed

conduits because a 3D geometry is generally associated with higher increment in the flame surface area and, thereby, faster flame propagation. The exponential acceleration rate grows more than twice.

Quantitatively, the cylindrical counterpart of the evolution Equation (12) will take the form:

$$U_{tip} = \frac{dZ_{tip}}{dt} = 2 \frac{(\Theta - 1)}{(1 - \alpha)} \left[1 + \frac{1}{2(\Theta - 1)} \right] \frac{Z_{tip}}{\sqrt{\Theta + 1}} + \Theta S_L, \tag{16}$$

with the solution:

$$Z_f = \frac{\Theta R}{\sigma_{0,cyl}} \exp(\sigma_{0,cyl} S_L / R) - 1, \quad \sigma_{o,cyl} = \frac{\sigma_{s,cyl}}{\sqrt{\Theta + 1}} = \frac{2}{(\sqrt{\Theta + 1})} \frac{(\Theta - 1)}{(1 - \alpha)} \left[1 + \frac{1}{2(\Theta - 1)} \right] \tag{17}$$

(see [2,18] to understand the origin of these equations). According to Equation (17), the exponential acceleration rate in the cylindrical geometry exceeds its 2D counterpart more than twice indeed. The same trend has been seen in semi-open conduits, obstructed as well as unobstructed, when switching from the 2D planar to the cylindrical-axisymmetric geometries.

In addition, turbulence is an essentially 3D phenomenon, so it will provide an extra effect in the 3D geometry. In all these respects, we expect much stronger flame acceleration in the 3D case, with a little (if any) chance of non-accelerative trends of flame propagation.

We next develop a predictive model for the propagation trends observed in obstructed channels with both ends open by employing a *machine learning* (ML)-based technology. The goodness of fit of the model has been calculated using the confusion matrix method for logistic regression method [39]. It is presented as the prediction accuracy for the models and it represents how well the model predicts the observed accelerating/non-accelerating flame trends. Specifically, a logistic regression algorithm is adopted to train these data sets in order to classify the accelerating versus non-accelerating flame trends considering Θ , α and $Re = R/L_f$ as the parameters. Logistic regression has been chosen to be employed because this is one of the most widely used ML algorithms for the classification problems, which nevertheless is relatively simple to implement. To justify such a choice, it is noted that logistic regression has already been employed in a similar complex problem of flame propagation, which involved fast flame detection to address accidental fire scenarios [40].

Figure 14 is a schematic of the ML model. The procedure involves feeding the learning algorithm with the training sets: Θ , α and/or Re and the “classification” variable. Here, the classification variable indicates accelerating or not accelerating event. So, the algorithm uses this data set to learn a hypothesis function, h , that maps input x to the predicted output y .

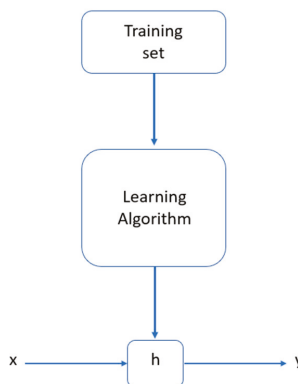


Figure 14. Schematic representaiton of the machine learning model.

Specifically, we consider a hypothesis function in logistic regression in the form:

$$h_{\theta}(x) = g(\theta^T x), \quad 0 \leq h_{\theta}(x) \leq 1, \tag{18}$$

where g is the sigmoid function, which is depicted in Figure 15 and is defined as:

$$g(z) = \frac{1}{1 + e^{-z}}, \quad z = \theta^T x. \tag{19}$$

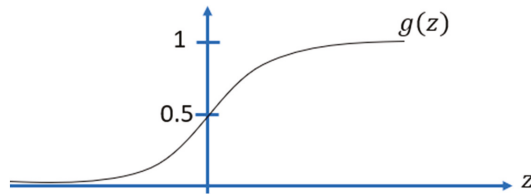


Figure 15. The sigmoid function $g(z)$ of Equation (19).

As a result, the function $h_{\theta}(x)$ describes the probability of $y = 1$ for a given x value. As such, if $h_{\theta}(x) \geq 0.5$ then $y = 1$, and $y = 0$ for $h_{\theta}(x) < 0.5$. From the simulation results, the cases undergoing acceleration are classified as 1, and the cases with only quasi-steady propagation are 0. The training sets consist of the input variable $x(\Theta, \alpha, Re)$ and y . The results obtained for the hypothesis function have been subsequently used to classify and develop the regime diagrams depicted in Figures 16 and 17.

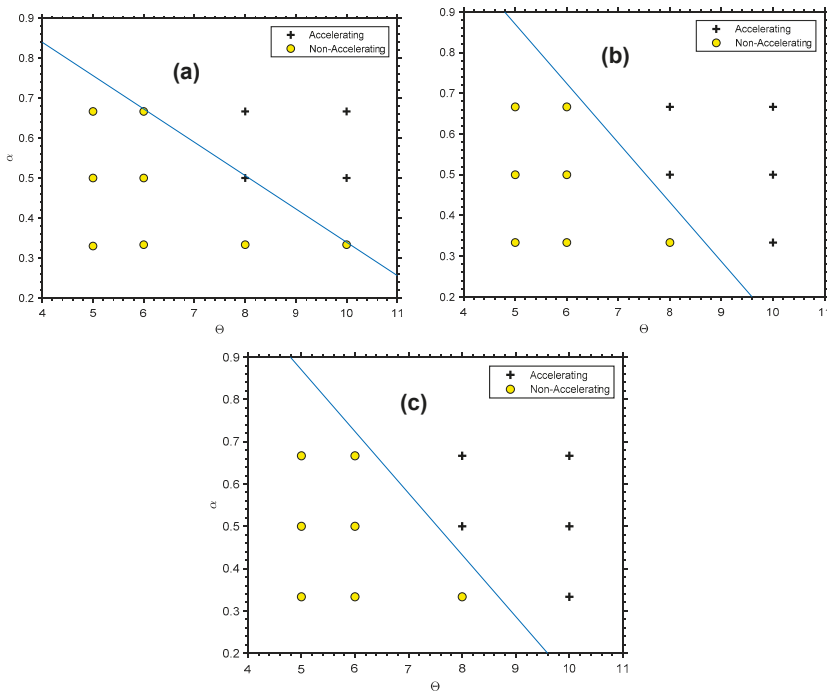


Figure 16. The $\alpha - \Theta$ burning regime diagram—for $Re = 24$ (a) $Re = 36$ (b) and $Re = 48$ (c).

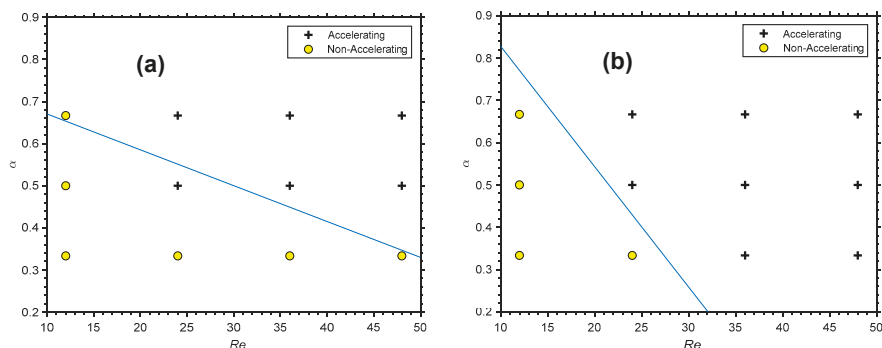


Figure 17. The $\alpha - Re$ burning regime diagram for $\Theta = 8$ (a) and $\Theta = 10$ (b).

Specifically, Figure 16a shows the classification results obtained for $Re = 24$, with the solid line indicating the decision boundary represented by the variable z . Essentially, the equation satisfying the accelerating phase is $-131.69 + 9.36\Theta + 112.29\alpha \geq 0$, with a training accuracy of 91.67%. For $Re = 36$ and 48 in Figure 16b,c, the predicted hypothesis is the same, and the decision boundary is represented by $-111.73 + 10.19\Theta + 69.85\alpha \geq 0$, with the training accuracy of 100%.

Finally, the data are classified based on the flame propagation Reynolds number Re , and the developed model predicts if a flame accelerates or not based on Re . Figure 17 shows this result, for $\Theta = 8$ and $\Theta = 10$ in Figure 17a,b, respectively. The model prediction is therefore $-17.01 + 0.19\Theta + 22.62\alpha \geq 0$, with 83.3% prediction accuracy for $\Theta = 8$, and $-14.4 + 1.14\Theta + 39.9\alpha \geq 0$, with a 100% prediction accuracy for $\Theta = 10$.

It should be noted that the prediction accuracies reported here are solely based on the training data set. However, in the future works, our research plan is to generate more data to improve and test the present model more extensively.

4. Conclusions

While apparent flame oscillations are found to dominate in the relatively narrow fully-open obstructed channels with $Re = R/L_f = 12$, for the wider channels such as having $Re = 24, 36, 48$, the propagation trends are observed to be quite distinctive. To be specific, when the parameters Re , α and Θ are beyond their respective critical values, we have identified the three distinctive phases/regimes of burning such as (i) initial quasi-steady flame propagation, followed by (ii) exponential FA and (iii) the final saturation of the flame velocity. Typically, all three regimes occur when $\Theta = 8, 10$, $\alpha = 1/2, 2/3$ and $Re = 24, 36, 48$. It is noticed that all three parameters (Re , α and Θ) significantly impact the duration of quasi-steady propagation. Specifically, while in the $Re = 24$ channel, quasi-steady propagation lasts as long as $\sim 6 R/S_L$, this time reduces to $0.6 R/S_L$ when $Re = 48$. The regime of quasi-steady propagation is also influenced by the blockage ratio α and the thermal expansion ratio Θ . Namely, as α decreases, the volume of the pockets of unburned gas, left behind the leading flame segment, also reduces, causing drastic moderation of the effect of delayed burning, which is the major factor for the Bychkov mechanism of ultrafast FA [1]. Likewise, thermal expansion plays a similar role: a lower gas expansion, Θ , means reduced propulsion forces and, as a result, moderated propagation of the flame front.

The nature of exponential acceleration has been explored by comparing the simulation results with the theory [18] developed for FA in obstructed channels with closely packed obstacles and both extremes open. According to the plots of this comparison, the theory [18] predicts the later stage of exponential acceleration better than it predicts the earlier stage. The simulation results helped to understand the applicability domain of this theory to realistic flames. This domain is identified to be somewhere between $\{\alpha = 1/3; \Theta = 6\}$ and $\{\alpha = 1/2; \Theta = 8\}$.

Furthermore, the regime of the saturated burning velocity has been scrutinized in the present instigation. Specifically, the growing flame velocity saturates when it starts approaching the speed of sound. It has been identified that the main parameter influencing the final saturated flame tip velocity is the blockage ratio α . In particular, with $\alpha = 1/2$, the flame velocity saturates to a higher value than that in the case of $\alpha = 2/3$. It is also noted that all the saturated flame velocities obtained in the present simulations appeared lower than the respective CJ deflagration velocity.

Finally, a logistic regression ML algorithm was utilized to learn about the hypothesis functions that predict when a flame undergoes acceleration and when it continuously propagates in a quasi-steady state without FA. As a result, the models, identifying when the flames would experience all three regimes (quasi-steady propagation, acceleration, and saturation) and when it only propagates with near-constant velocity, are developed. Such an identification is based on the interplay between the Reynolds number associated with flame propagation Re , the blockage ratio α , and the thermal expansion ratio Θ , as demonstrated by the diagrams of Figures 16 and 17.

Author Contributions: Conceptualization, A.A. and V.A.; funding acquisition, V.A.; investigation, A.A., O.A. and V.A.; methodology, A.A. and V.A.; project administration, V.A.; resources, V.A.; supervision, V.A.; writing, A.A., O.A. and V.A. All authors have read and agreed to the published version of the manuscript.

Funding: This research was funded by the U.S. National Science Foundation (NSF), through the CAREER Award No. 1554254 (V.A.), as well as by the West Virginia Higher Education Policy Commission, through the grant #HEPC.dsr.18.7 (V.A.).

Acknowledgments: The authors thank Damir Valiev of Tsinghua University, China, for numerous useful discussions as well as for providing significant help with the computational platform and numerical approaches.

Conflicts of Interest: The authors declare no conflict of interest.

References

- Bychkov, V.; Valiev, D.; Eriksson, L.-E. Physical Mechanism of Ultrafast Flame Acceleration. *Phys. Rev. Lett.* **2008**, *101*, 164501. [[CrossRef](#)] [[PubMed](#)]
- Valiev, D.; Bychkov, V.; Akkerman, V.; Law, C.K.; Eriksson, L.-E. Flame acceleration in channels with obstacles in the deflagration-to-detonation transition. *Combust. Flame* **2010**, *157*, 1012–1021. [[CrossRef](#)]
- Adebiyi, A.; Abidakun, O.; Idowu, G.; Valiev, D.; Akkerman, V.; Akkerman, V. Analysis of nonequidiffusive premixed flames in obstructed channels. *Phys. Rev. Fluids* **2019**, *4*, 063201. [[CrossRef](#)]
- Adebiyi, A.; Alkandari, R.; Valiev, D.; Akkerman, V. Effect of surface friction on ultrafast flame acceleration in obstructed cylindrical pipes. *AIP Adv.* **2019**, *9*, 035249. [[CrossRef](#)]
- Ugarte, O.J.; Akkerman, V.; Sadek, J.; Valiev, D.; Akkerman, V. Critical role of blockage ratio for flame acceleration in channels with tightly spaced obstacles. *Phys. Fluids* **2016**, *28*, 093602. [[CrossRef](#)]
- Lee, J.; Knystautas, R.; Chan, C. Turbulent flame propagation in obstacle-filled tubes. *Symp. (Int.) Combust.* **1985**, *20*, 1663–1672. [[CrossRef](#)]
- Teodorczyk, A.; Lee, J.; Knystautas, R. Propagation mechanism of quasi-detonations. *Symp. (Int.) Combust.* **1989**, *22*, 1723–1731. [[CrossRef](#)]
- Zhu, Y.; Chao, J.; Lee, J. An experimental investigation of the propagation mechanism of critical deflagration waves that lead to the onset of detonation. *Proc. Combust. Inst.* **2007**, *31*, 2455–2462. [[CrossRef](#)]
- Gronidin, J.-S.; Lee, J.H.S. Experimental observation of the onset of detonation downstream of a perforated plate. *Shock. Waves* **2010**, *20*, 381–386. [[CrossRef](#)]
- Adebiyi, A.; Ridgeway, E.; Alkandari, R.; Cathreno, A.; Valiev, D.; Akkerman, V. Premixed flame oscillations in obstructed channels with both ends open. *Proc. Combust. Inst.* **2019**, *37*, 1919–1926. [[CrossRef](#)]
- Di Stazio, A.; Chauveau, C.; Dayma, G.; Dagaut, P. Oscillating flames in micro-combustion. *Combust. Flame* **2016**, *167*, 392–394. [[CrossRef](#)]
- Ciccarelli, G.; Dorofeev, S. Flame acceleration and transition to detonation in ducts. *Prog. Energy Combust. Sci.* **2008**, *34*, 499–550. [[CrossRef](#)]
- Heidari, A.; Wen, J. Numerical simulation of flame acceleration and deflagration to detonation transition in hydrogen-air mixture. *Int. J. Hydrogen Energy* **2014**, *39*, 21317–21327. [[CrossRef](#)]

14. Bychkov, V.; Akkerman, V.; Valiev, D.; Law, C.K. Influence of gas compression on flame acceleration in channels with obstacles. *Combust. Flame* **2010**, *157*, 2008–2011. [[CrossRef](#)]
15. Ciccarelli, G.; Johansen, C.; Parravani, M. The role of shock–flame interactions on flame acceleration in an obstacle laden channel. *Combust. Flame* **2010**, *157*, 2125–2136. [[CrossRef](#)]
16. Johansen, C.; Ciccarelli, G. Visualization of the unburned gas flow field ahead of an accelerating flame in an obstructed square channel. *Combust. Flame* **2009**, *156*, 405–416. [[CrossRef](#)]
17. Ciccarelli, G.; Fowler, C.J.; Bardon, M. Effect of obstacle size and spacing on the initial stage of flame acceleration in a rough tube. *Shock. Waves* **2005**, *14*, 161–166. [[CrossRef](#)]
18. Bychkov, V.; Sadek, J.; Akkerman, V. Analysis of flame acceleration in open or vented obstructed pipes. *Phys. Rev. E* **2017**, *95*, 013111. [[CrossRef](#)]
19. Petchenko, A.; Bychkov, V.; Akkerman, V.; Eriksson, L.-E. Flame-sound interaction in tubes with non-slip walls. *Combust. Flame* **2007**, *149*, 418–434. [[CrossRef](#)]
20. Akkerman, V.; Bychkov, V.; Petchenko, A.; Eriksson, L.-E. Flame oscillations in tubes with non-slip at the walls. *Combust. Flame* **2006**, *145*, 675–687. [[CrossRef](#)]
21. Zeldovich, Y.B.; Barenblatt, G.I.; Librovich, V.B.; Makhviladze, G.M. *The Mathematical Theory of Combustion and Explosions*; Springer Science and Business Media LLC: Berlin/Heidelberg, Germany, 1985.
22. Andersson, N.; Eriksson, L.-E.; Davidson, L. Investigation of an isothermal Mach 0.75 jet and its radiated sound using large-eddy simulation and Kirchhoff surface integration. *Int. J. Heat Fluid Flow* **2005**, *26*, 393–410. [[CrossRef](#)]
23. Andersson, N.; Eriksson, L.-E.; Davidson, L. Large-Eddy Simulation of Subsonic Turbulent Jets and Their Radiated Sound. *AIAA J.* **2005**, *43*, 1899–1912. [[CrossRef](#)]
24. Wollblad, C.; Davidson, L.; Eriksson, L.-E. Large Eddy Simulation of Transonic Flow with Shock Wave/Turbulent Boundary Layer Interaction. *AIAA J.* **2006**, *44*, 2340–2353. [[CrossRef](#)]
25. Bychkov, V.; Golberg, S.M.; Liberman, M.; Eriksson, L.E. Propagation of curved stationary flames in tubes. *Phys. Rev. E* **1996**, *54*, 3713–3724. [[CrossRef](#)] [[PubMed](#)]
26. Bychkov, V.V.; Golberg, M.; Liberman, M.; Kleev, A.I.; Eriksson, L.-E. Numerical Simulation of Curved Flames in Cylindrical Tubes. *Combust. Sci. Technol.* **1997**, *129*, 217–242. [[CrossRef](#)]
27. Travnikov, O.Y.; Bychkov, V.V.; Liberman, M. Numerical studies of flames in wide tubes: Stability limits of curved stationary flames. *Phys. Rev. E* **2000**, *61*, 468–474. [[CrossRef](#)]
28. Liberman, M.A.; Ivanov, M.F.; Peil, O.E.; Valiev, D.M.; Eriksson, L.-E. Numerical studies of curved stationary flames in wide tubes. *Combust. Theory Model.* **2003**, *7*, 653–676. [[CrossRef](#)]
29. Liberman, M.; Ivanov, M.F.; Peil, O.; Valiev, D.; Eriksson, L.-E. Self-acceleration and fractal structure of outward freely propagating flames. *Phys. Fluids* **2004**, *16*, 2476–2482. [[CrossRef](#)]
30. Bychkov, V.; Petchenko, A.; Akkerman, V.; Eriksson, L.-E. Theory and modeling of accelerating flames in tubes. *Phys. Rev. E* **2005**, *72*, 046307. [[CrossRef](#)] [[PubMed](#)]
31. Akkerman, V.; Bychkov, V.; Petchenko, A.; Eriksson, L.-E. Accelerating flames in cylindrical tubes with non-slip at the walls. *Combust. Flame* **2006**, *145*, 206–219. [[CrossRef](#)]
32. Akkerman, V.; Law, C.K.; Bychkov, V.; Eriksson, L.-E. Analysis of flame acceleration induced by wall friction in open tubes. *Phys. Fluids* **2010**, *22*, 053606. [[CrossRef](#)]
33. Bychkov, V.; Akkerman, V.; Fru, G.; Petchenko, A.; Eriksson, L.-E. Flame acceleration in the early stages of burning in tubes. *Combust. Flame* **2007**, *150*, 263–276. [[CrossRef](#)]
34. Valiev, D.; Bychkov, V.; Akkerman, V.; Eriksson, L.-E. Different stages of flame acceleration from slow burning to Chapman-Jouguet deflagration. *Phys. Rev. E* **2009**, *80*, 036317. [[CrossRef](#)] [[PubMed](#)]
35. Valiev, D.; Akkerman, V.; Kuznetsov, M.; Eriksson, L.-E.; Law, C.K.; Bychkov, V.; Akkerman, V. Influence of gas compression on flame acceleration in the early stage of burning in tubes. *Combust. Flame* **2013**, *160*, 97–111. [[CrossRef](#)]
36. Middha, P.; Hansen, O.R. Predicting deflagration to detonation transition in hydrogen explosions. *Process. Saf. Prog.* **2008**, *27*, 192–204. [[CrossRef](#)]
37. Yáñez, J.; Kuznetsov, M.; Bykov, V. Sudden acceleration of flames in open channels driven by hydraulic resistance. In Proceedings of the 24th International Colloquium on the Dynamics of Explosions and Reactive Systems (ICDERS), Taipei, Taiwan, 28 July–2 August 2013; pp. 1–6.
38. Chue, R.; Clarke, J.; Lee, J.H.S. Chapman-Jouguet deflagration. *Proc. R. Soc. Lond. A* **1993**, *441*, 607–623.

39. Mandal, S.K. Performance analysis of data mining algorithms for breast cancer cell detection using Naïve Bayes, logistic regression and decision tree. *Int. J. Eng. Comput. Sci.* **2017**, *6*, 20388–20391.
40. Kong, S.G.; Jin, D.; Li, S.; Kim, H. Fast fire flame detection in surveillance video using logistic regression and temporal smoothing. *Fire Saf. J.* **2016**, *79*, 37–43. [[CrossRef](#)]



© 2020 by the authors. Licensee MDPI, Basel, Switzerland. This article is an open access article distributed under the terms and conditions of the Creative Commons Attribution (CC BY) license (<http://creativecommons.org/licenses/by/4.0/>).

Article

Numerical Investigation of the Required Quantity of Inert Gas Agents in Fire Suppression Systems

Xiaoqin Hu ^{1,*}, Arjen Kraaijeveld ¹ and Torgrim Log ^{1,2}

¹ Fire Disaster Research Group, Department of Safety, Chemical and Bioengineering, Faculty of Engineering and Natural Sciences, Western Norway University of Applied Science, 5528 Haugesund, Norway;

Arjen.Kraaijeveld@hvl.no (A.K.); Torgrim.Log@hvl.no (T.L.)

² Kårstø Gas Processing Plant, Equinor, 5565 Kårstø, Norway

* Correspondence: Xiaoqin.Hu@hvl.no; Tel.: +47-4663-1923

Received: 13 April 2020; Accepted: 14 May 2020; Published: 16 May 2020

Abstract: Inert gas agents have the potential to be widely used in fire suppression systems due to health and safety concerns associated with active chemicals. To suppress fire while minimizing hypoxic effects in an occupied area, the discharge quantity of inert gas agents should be carefully designed to dilute the oxygen concentration to a specific threshold level. In this study, the general expressions between oxygen concentration, the discharge rate of inert gas agents, and the ventilation rate of the air-agent mixture are derived first. Then, explicit formulas to calculate the discharge/ventilation rate and the required quantity of inert gas agents are given if the discharge rate and ventilation rate both are constants. To investigate the dilution and fire extinguishing efficiencies of inert gas agents, two scenarios with a discharge of inert gas agents into an enclosure are modeled using the Fire Dynamic Simulator (FDS). The simulation results show that the average oxygen mass fraction approximately reaches the design level at the end of the discharge period. Variation in oxygen concentration along the enclosure height is analyzed. For the scenario with a fire source, oxygen mass fraction decreases fast as oxygen is consumed by the combustion process. Thus, the fire is extinguished a little earlier than the end of the discharge period.

Keywords: gas fire suppression; inert gas agents; agent quantity; discharge rate; ventilation rate

1. Introduction

The production of halons for fire protection was banned in most countries due to the stratospheric ozone layer depletion issue [1]. Over the last three decades, the agents used in gas fire suppression systems have therefore undergone a transition from halon agents to clean agents. The most commercialized clean agents are summarized in [2] and can be categorized into two groups, i.e., halocarbon compounds and inert gases. Halocarbon clean agents extinguish fires by a combination of chemical and physical mechanisms [3,4]. In fires, all halocarbon agents produce decomposition products which may represent a threat to the health and safety of the occupants. Inert gas agents suppress fires by diluting the oxygen concentration to a specific threshold level below which the fire flames are suppressed [5–7]. Research shows that lowering the oxygen concentration in air to below approximately 12% by volume will extinguish flaming fires [2,8]. Compared with halocarbon agents, the inert gas agents are less efficient as fire extinguishing agents in terms of required storage volume and agent weight but produce no hazardous decomposition products. Therefore, there is a potential for inert gas agents to be applied as a means of fire protection in some specific cases where health and safety related to toxicity is highly focused. Some research [9] has been carried out to investigate the application of inert gas agents in some typical buildings for disabled persons, elderly in nursing homes, and other citizens with reduced cognitive function, etc. Inert gas agents also have great potential as inhibitors of gas explosions by reducing or possibly eliminating the risk of explosions [10–12].

The commercial inert gas agents available for fire suppression systems are Argon (IG-01), Nitrogen (IG-100), Nitrogen+Argon (IG-55), and Nitrogen + Argon + CO₂ (IG-541) [2,13,14]. The inert gas agents are stored as compressed gases and the storage volumes are much larger than that of halocarbon clean agents [2,15]. Fire suppression systems are supposed to discharge a specific amount of inert gas agents into an enclosure to achieve the desired oxygen concentration within a specified time period. If the oxygen concentration is diluted much lower than the desired level, it is called over-discharge in the present study. Over-discharge of inert gas agents results in increasing requirements in storage capacity. Over-discharge of inert agents also leads to an oxygen level that is too low, which in occupied areas, can cause severe hypoxic effects [16]. Due to health concerns, the National Fire Protection Association (NFPA) [17] limits the exposure time for clean agents to 5 min. For inert gas agents, the maximum exposure time has been intensively investigated. Research of Lambertsen and Gelfand [18] shows that cognitive performance does not drop until the inhaled oxygen level is below 14%. It does, however, decrease significantly if the oxygen level is reduced to 10%. Some tests on humans during moderate exercise (walking at a 3 mile per hour pace) were conducted by Ansul [19]. The results show that the cognitive performance returns to high scores when breathing is shifted from a 10% oxygen atmosphere to the INERGEN atmosphere (10% oxygen with 4% CO₂). The presence of CO₂ in the INERGEN agent can favorably affect the respiration, arterial blood oxygenation, and brain blood flow, which is called the “CO₂ Effect”. The benefit of the “CO₂ Effect” continues for at least 10 min and undoubtedly well beyond. Laursen [9] suggests the maximum exposure time can be up to 30 min for people with COPD (chronic obstructive pulmonary disease) if they are exposed to an INERGEN atmosphere (10–12.5% O₂ with 3.5–4% CO₂). The desired oxygen concentration after discharge is expected to be no less than 10% in practice. The agent IG-541 with an 8% fraction of CO₂, therefore, has the potential to be widely applied for fire suppression in occupied areas.

Over-discharge of inert agent leads to hypoxia effects for occupants while under-discharge fails to dilute oxygen concentration to suppress the fire. Therefore, the quantity of inert agents released should be carefully planned to obtain a design oxygen level at which fire can be suppressed and severe hypoxic effects can be avoided. The required quantity of inert gas agents can easily be calculated for an enclosure without ventilation [2]. However, the gas discharge usually generates an overpressure effect in a closed compartment which might lead to destructive events [2,14]. The BETTATI design manual [14] recommends a resistance value of 500 Pa as a conservative value. Therefore, it is necessary to run ventilation systems to eliminate overpressure effects in an enclosure. The operation of a ventilation system during the discharge of inert gas agents results in exhausting the discharged agent-air mixture. It then becomes difficult to estimate the oxygen level in the enclosure and also to evaluate the required quantity of inert gas agents to obtain and sustain the required oxygen level.

The present paper first derives expressions to calculate oxygen concentration as a function of ventilation mass/volume rate, oxygen level, and discharge period. Then, explicit formulas are presented to calculate the discharge rate of inert gas agents to obtain a design oxygen level when the discharge rate and ventilation rate are constant. The required quantity of inert gas agents is integral to the discharge rate over the entire discharge time period. The dilution efficiency and fire extinguishing efficiency of inert gas agents are investigated through a series of numerical simulations using computational fluid dynamics (CFD) fire dynamic simulator (FDS) software v.6.5.3 [20], which is developed by the National Institute of Standards and Technology (NIST) of the United States Department of Commerce. FDS has been widely used in numerical fire safety validations [21,22].

2. Required Quantity of Inert Gas Agents

Before discussing the discharge of inert gas agents, the limiting oxygen mass fraction, which is defined as the minimum oxygen level to support flaming combustion, is introduced first. Then the discharge mass/volume rate to obtain a design oxygen level is discussed and finally, the calculation of the required quantity of inert gas agents is analyzed.

2.1. Limiting Oxygen Mass Fraction

Frederick [23] assumed that a combustion reaction is suppressed if the energy released from the combustion is not sufficient to raise the fuel-air-product mixture above a critical flame temperature (T_{CFT}) [24]. The amount of energy released by the combustion processes can be approximately estimated by the mass of oxygen consumed through oxygen consumption calorimetry [25]. The basis of the method is that the amount of energy (ΔH_{O_2}) released per unit mass of oxygen consumed is approximately constant. The constant is found to be around 13,100 kJ per kilogram oxygen consumed [25,26].

Under constant pressure and adiabatic conditions, the energy required to raise the bulk temperature of a unit mass at ambient temperature (T_m) to the critical flame temperature (T_{CFT}) may be expressed by:

$$Q = \bar{c}_p(T_{CFT} - T_m), \quad (1)$$

where \bar{c}_p is the average specific heat, which can be calculated based on the composition of the reacting fuel and any inert gases.

To reach the critical flame temperature (T_{CFT}), the combustion energy should be no less than the energy calculated from Equation (1). Based on the method of oxygen consumption calorimetry, the oxygen mass fraction in this volume should be no less than the limiting mass fraction:

$$\hat{Y}_{O_2,lim} = \frac{\bar{c}_p(T_{CFT} - T_m)}{\Delta H_{O_2}} \quad (2)$$

If the oxygen mass fraction Y_{m,O_2} is lower than $\hat{Y}_{O_2,lim}$, the energy released from the combustion is less than $\hat{Y}_{O_2,lim}\Delta H_{O_2}$, which is no more than the energy shown in Equation (1). Thus, the amount of energy is not sufficient to raise the fuel-air-product mixture above T_{CFT} and the combustion process will self-terminate.

Assuming an average specific heat \bar{c}_p of 1.2 kJ/(kg · K), critical flame temperature (T_{CFT}) 1700 K for hydrocarbon diffusion flames [23,24] and ambient temperature 300 K, the limiting oxygen fraction $\hat{Y}_{O_2,lim}$ is estimated to be 12.8%. This value is in good agreement with the experiments giving volume concentrations in the range of 10.3 % to 13.9 % [24,27]. Note that these results are expressed as volume fractions.

2.2. Discharge Mass Rate of Inert Gas Agents

Inert gas agents may be discharged into an enclosure to dilute the oxygen concentration to below the design level, which results in the combustion process self-terminating. Oxygen concentration is the key factor in determining the suppression of flaming combustion. The mass fraction of oxygen in ambient air is approximately 0.23. Thus, the mass fraction of oxygen (Y_{m,O_2}) can easily be derived from the mass fraction of air ($Y_{m,air}$), i.e., $Y_{m,O_2} = 0.23Y_{m,air}$. In the following discussion, the air mass fraction in an enclosure is estimated first to derive the oxygen mass fraction. The ventilation system in the later discussion only refers to mechanical ventilation, i.e., exhaust fans. To simplify the discussion, it is assumed that air and inert gas agents are mixed instantaneously and inert gas agents and air at any time are uniformly distributed in an enclosure. Thus, the exhausted mixture from ventilation vents has the same air/agents mass fraction distribution as that remaining in the enclosure.

The mass fraction of air in an enclosure at time t is assumed to be $Y_{m,air}(t)$. At the start, i.e., at $t = 0$, $Y_{m,air}(0) = 1$. After a small time interval Δt , the air mass fraction decreases due to the introduction of inert gas agents at $t > 0$. The air mass fraction at time $t + \Delta t$ is approximately given by:

$$Y_{m,air}(t + \Delta t) \approx Y_{m,air}(t) \frac{m(t)}{m(t) + R_m(t)\Delta t} \quad (3)$$

where $R_m(t)$ is the discharge mass rate of the inert gas agent (kg/s). $R_m(t)$ may be constant or a function of time. $m(t)$ (kg) is the total mass of the mixture in the enclosure at time t and can be expressed as:

$$m(t) = m_0 + \int_0^t (R_m(\xi) - E_m(\xi)) d\xi, \tag{4}$$

where m_0 is the total mass initially present at time 0. The second term on the right represents the net increase of mass over time range $[0, t]$ and ξ is the time variable. $E_m(t)$ is the ventilation mass rate of the mixture (kg/s). If $E_m > R_m$, the total mass of mixture in the enclosure would decrease with time. To ensure that the total mass $m(t)$ is positive, the second term on the right of Equation (4) should be smaller than m_0 .

To deduce an explicit expression to calculate $Y_{m,air}$ at any time t , an iterative procedure is applied to Equation (3). A small time interval Δt is chosen to discretize the time, this is $t = n\Delta t$ and $t_i = i\Delta t$ ($0 \leq i \leq n$). Repeating the iterative procedure by the use of Equation (3) and applying the initial condition $Y_{m,air}(0) = 1$, the mass fraction of air at time t is:

$$Y_{m,air}(t) = \lim_{n \rightarrow \infty} \prod_{i=0}^{n-1} \frac{m(t_i)}{m(t_i) + R_m(t_i)\Delta t} \tag{5}$$

By taking the natural logarithm of both sides of the above the equation and rearranging it, Equation (5) becomes:

$$\ln\left(\frac{1}{Y_{m,air}(t)}\right) = \lim_{n \rightarrow \infty} \sum_{i=0}^{n-1} \ln\left(1 + \frac{R_m(t_i)}{m(t_i)} \Delta t\right). \tag{6}$$

If the time interval Δt is extremely small, the right term in Equation (6) may be approximated by:

$$\ln\left(1 + \frac{R_m(t_i)}{m(t_i)} \Delta t\right) \approx \frac{R_m(t_i)}{m(t_i)} \Delta t. \tag{7}$$

If $\Delta t \rightarrow 0$, that is $n \rightarrow \infty$, Equation (7) may then be written as:

$$\lim_{n \rightarrow \infty} \sum_{i=0}^{n-1} \frac{R_m(t_i)}{m(t_i)} \Delta t = \int_0^t \frac{R_m(\xi)}{m(\xi)} d\xi. \tag{8}$$

Substituting Equation (7) and Equation (8) into Equation (6) and rearranging it, the mass fraction of air may be expressed as:

$$Y_{m,air}(t) = e^{-\int_0^t \frac{R_m(\xi)}{m(\xi)} d\xi}. \tag{9}$$

If $Y_{m,O_2} = 0.23Y_{m,air}$ is applied, the mass fraction of oxygen in an enclosure at time t is given by:

$$Y_{m,O_2}(t) = 0.23e^{-\int_0^t \frac{R_m(\xi)}{m(\xi)} d\xi}. \tag{10}$$

Equation (10) gives an expression to calculate oxygen mass fraction as a function of ventilation mass rate, discharge mass rate, and discharge time.

To estimate the discharge quantity of inert gas agents, an explicit formula is required to calculate the discharge rate. It is easy to explicitly calculate the discharge mass rate from Equation (10) if the discharge mass rate R_m and ventilation mass rate E_m are constants. Assuming that V_0 represents the volume of the enclosure and ρ_{air} denotes the density of the ambient air, $m(t)$ can be simplified as:

$$m(t) = V_0\rho_{air} + (R_m - E_m)t, \tag{11}$$

If R_m and E_m are both constants and not equal to each other, it can be assumed that $E_m = kR_m$ ($k \neq 1$). By substituting Equation (11) into Equation (10), the required agent discharge mass rate to obtain a design oxygen fraction Y_{m,O_2}^* is given by

$$R_m = \frac{V_0 \rho_{air}}{t(1-k)} \left(\frac{Y_{m,O_2}^*}{0.23} \right)^{k-1} - 1, \tag{12}$$

If the ventilation mass rate equals the discharge mass rate, that is $E_m = R_m$ ($k = 1$), the discharge mass rate of agents to obtain the design oxygen fraction Y_{m,O_2}^* is:

$$R_m = \frac{V_0 \rho_{air}}{t} \ln \frac{0.23}{Y_{m,O_2}^*}, \tag{13}$$

2.3. Discharge Volume Rate of Inert Gas Agents

In practice, the discharge of inert gas agents and exhaust of agent-air mixture is usually measured as volume rates. The ventilation mass rate (E_m) can not be directly converted into the volume rate (E_V) as the density of the agent-air mixture varies during the discharge period. Therefore, the discharge volume rate (R_V) can not be derived from Equation (10), Equation (12), and Equation (13) directly.

To derive the discharge volume rate, a concept called standard volume (V^*) is defined as the volume at atmospheric pressure and ambient temperature. At the start, the standard volume $V^*(0)$ equals the enclosure volume V_0 . After a discharge time t , the specific volume is:

$$V^*(t) = V_0 + \int_0^t (R_V(\xi) - E_V(\xi)) d\xi, \tag{14}$$

The volume fraction of air in an enclosure at time $t + \Delta t$ can then be approximately estimated from Equation (14) at time t :

$$Y_{V,air}(t + \Delta t) \approx Y_{V,air}(t) \frac{V^*(t)}{V^*(t) + R_V(t)\Delta t}, \tag{15}$$

Applying the same procedure as Equation (5) to Equation (9) to the above equation, the volume percentage of oxygen is expressed as a function of discharge volume rate, ventilation volume rate, and discharge time:

$$Y_{V,O_2}(t) = 0.21 e^{-\int_0^t \frac{R_V(\xi)}{V^*(\xi)} d\xi}, \tag{16}$$

If the discharge volume rate R_V and ventilation volume rate E_V are constants and $E_V = k R_V$ ($k \neq 1$), the required discharge volume rate of the agent to obtain a design oxygen volume fraction Y_{V,O_2}^* could be derived from Equation (16) as:

$$R_V = \frac{V_0}{t(1-k)} \left(\frac{Y_{V,O_2}^*}{0.21} \right)^{k-1} - 1, \tag{17}$$

If $E_V = R_V$ ($k = 1$), the discharge volume rate of the inert gas agent to obtain the design oxygen fraction Y_{V,O_2}^* is given by:

$$R_V = \frac{V_0}{t} \ln \frac{0.21}{Y_{V,O_2}^*}, \tag{18}$$

Equation (17) with $k = 0$ and Equation (18) match the expressions shown in [2,14], which calculate the discharge rate from a design volume fraction of inert gas agents, not a design volume fraction of oxygen.

Equations (14) through to Equation (18) are derived by assuming that the inert gas agents are discharged at the same temperature as the air in the enclosure. The inert gas agent is, however, stored in cylinders at high pressures, i.e., 200–300 bar. When released, it expands. The energy required for this expansion results in a loss of internal energy, i.e., a temperature depletion. Therefore, inert gas agents are discharged at a lower temperature than the ambient air. When inert gas agents enter into an enclosure, the inert gas agents expand and meanwhile cool down the surrounding air. The temperature of the air-agents mixture in the enclosure is dynamic during a discharge period. The ideal gas law shows that the thermal expansion of gas agents is proportional to temperature change if the agents' mass and pressure are fixed. The ambient air is cooled down during the discharge period, which mitigates the effects of thermal expansion of inert gas agents. The effects of the thermal expansion of inert gas agents and the thermal contraction of air are very difficult to estimate and could be analyzed in future studies. In this study, the combined effect of thermal expansion of inert gas agents and thermal contraction of air is assumed to be proportional to the square root of temperature change. The discharge volume rate calculated from Equation (17) and Equation (18) is the volume rate at air temperature. To get the discharge volume rate at agents temperature, the volume rate at air temperature is simply adjusted by a proportionality coefficient c as:

$$c = \left(\frac{T_{\text{agents}}}{T_{\text{mixture}}} \right)^{0.5}, \quad (19)$$

where T_{agents} is the discharge temperature of inert gas agents and T_{mixture} is the temperature of the air-agents mixture and is calculated as:

$$T_{\text{mixture}} = \frac{c_{p,\text{agents}} Y_{m,\text{agents}} T_{\text{agents}} + c_{p,\text{air}} Y_{m,\text{air}} T_{\text{air}}}{c_{p,\text{agents}} Y_{m,\text{agents}} + c_{p,\text{air}} Y_{m,\text{air}}}, \quad (20)$$

where c_p is the isobaric mass heat capacity. $Y_{m,\text{agents}}$ and $Y_{m,\text{air}}$ are the mass fractions of agents and mass fraction of air respectively when the oxygen level reaches the design level.

2.4. Required Quantity of Inert Gas Agents

If the discharge rate of inert gas agents is given, the discharge quantity of agents to obtain a design oxygen level may be calculated as:

$$m_{\text{agents}} = \int_0^t R_m(x) dx = \int_0^t R_V(\xi) \rho_{\text{agents}} d\xi, \quad (21)$$

If the discharge rate is constant and the density of agents is fixed during the discharge period, the discharged quantity of inert gas agents is the product of discharge mass rate and discharge period:

$$m_{\text{agents}} = R_m t = R_V \rho_{\text{agents}} t, \quad (22)$$

Substituting Equation (12) and Equation (13) into Equation (22) and assuming $V_0 = 1 \text{ m}^3$, $\rho_{\text{air}} = 1.2 \text{ kg/m}^3$ and $Y_{m,\text{O}_2}^* = 12.8\%$, the quantity of inert gas agents per unit volume becomes a function of k ($k = E_m/R_m$). Here k should satisfy $k < \frac{V_0 \rho_{\text{air}}}{m_{\text{agents}}} + 1$ according to Equation (11). Figure 1 shows the quantity of inert gas agents as a function of k . The required inert gas quantity to obtain a design oxygen level per unit enclosure volume decreases with increasing values of k . Therefore, venting out the air-agent mixture not only removes the overpressure effect in an enclosure, it also lowers the mass requirement of inert gas agents. The explanation is that oxygen is also vented out when the mixture is vented out of an enclosure, which can accelerate the decrease of oxygen concentration and further reduce the required quantity of inert gas agents.

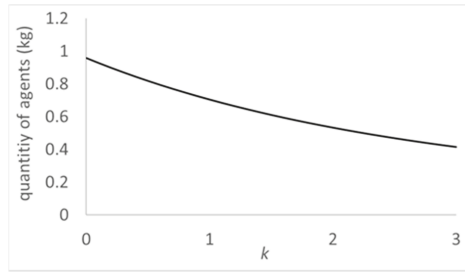


Figure 1. Required quantity of inert gas agents per unit volume vs. k ($k = E_m/R_m$).

3. Numerical Investigation

In the previous section, the expressions needed for estimating oxygen fraction were derived based on the assumption that inert gas agents and air at any time are uniformly distributed within the enclosure. However, the assumption is not correct as it takes time to mix agents and air. Moreover, agents and air have different densities, which might result in an uneven distribution of oxygen along the enclosure height. The fire extinguishing efficiency of inert gas agents also needs investigation due to possible uneven distribution of oxygen and other combustion conditions. Therefore, several issues should be considered:

- Is the design oxygen level obtained at the end of the discharge period?
- What is the variation of oxygen fraction along the enclosure height?
- Would the pressure in an enclosure exceed the resistance value of 500 Pa during the discharge period?
- What about the extinguishing efficiency of the inert gas agents?

To investigate these issues, scenarios with the discharge of inert gas agents into an enclosure were numerically modeled using FDS 6.5.3. The enclosure is a studio with a bathroom, an entrance, and a main room. The size of the enclosure is the same as that of the test room built by Kraaijeveld [28] for fire suppression tests. It is 2.4 m high and its layout is shown in Figure 2. The door between the main room and the bathroom was open while the other two doors in the entrance were closed. The vent to discharge inert gas agents and the vent to exhaust the agent-air mixture were mounted at the right bottom corner of the ceiling (red square in Figure 2b) and the left bottom corner of the ceiling (green square in Figure 2b), respectively. The discharge of inert gas agents and exhaust of air-agents mixture were run in parallel. When the discharge and ventilation were not in operation, the two vents were closed.

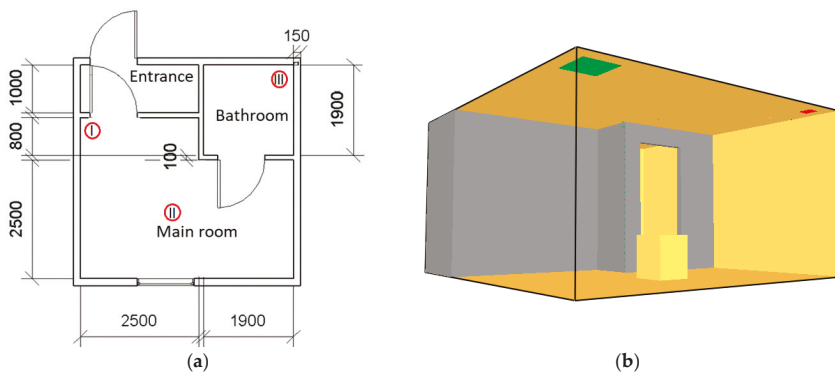


Figure 2. (a) Test room layout (unit: mm) and (b) the corresponding simulation model.

Two kinds of inter gas agents, IG-100 and IG-541, were applied in the model separately. The necessary chemical and physical properties of the two agents are shown in Table 1. In this scenario, the temperature of inert gas agents discharged from the vent was assumed to be -5°C [29]. The agents were discharged into the enclosure for a 60 s period. The design oxygen volume fraction was set to be 11.51% for IG-100 and 12.55% for IG-54, which equals 12.8% in mass fraction for both agents. The discharge and ventilation rates were calculated from Equations (17) to (19) in volume rate since the volume flow rate is for practical reasons normally recorded. The discharge rates are listed in Table 2. The ratio of ventilation rate to discharge rate (k) varies between 0.8–1.2.

Table 1. Chemical and physical properties of inert gas agents at 1 atm and $T = 293\text{ K}$ [2,14]. The fraction represents volume%.

Agent	Chemical Formula	Density (kg/m^3)	Isobaric Mass Heat Capacity ($\text{kJ}/\text{kg K}$)
IG-100	N_2	1.16	1.04
IG-541	52% N_2 , 40% Ar, 8% CO_2	1.42	0.78

Table 2. Summary of simulation cases. $\alpha = 0.0264\text{ s}^{-2}$ and “-” represents no parameters are required to set up.

HRR (kW)	$Y_{\text{m},\text{O}_2}^*$	Discharge Period	Inert Gas Agent	$k (=E_v/R_v)$	$R_v(\text{m}^3/\text{s})$	Case Index
HRR = 0	12.8%	0–60 s	IG-100	0.8	0.4220	C0_100_0.8
HRR = 0	12.8%	0–60 s	IG-100	0.9	0.4095	C0_100_0.9
HRR = 0	12.8%	0–60 s	IG-100	1.0	0.3973	C0_100_1.0
HRR = 0	12.8%	0–60 s	IG-100	1.1	0.3855	C0_100_1.1
HRR = 0	12.8%	0–60 s	IG-100	1.2	0.3473	C0_100_1.2
HRR = 0	12.8%	0–60 s	IG-541	0.8	0.3559	C0_541_0.8
HRR = 0	12.8%	0–60 s	IG-541	0.9	0.3467	C0_541_0.9
HRR = 0	12.8%	0–60 s	IG-541	1.0	0.3380	C0_541_1.0
HRR = 0	12.8%	0–60 s	IG-541	1.1	0.3294	C0_541_1.1
HRR = 0	12.8%	0–60 s	IG-541	1.2	0.3211	C0_541_1.2
HRR = $\alpha \cdot t^2$	-	-	-	-	-	C1_0
HRR = $\alpha \cdot t^2$	12.8%	30–90 s	IG-541	1.0	0.3380	C1_1.0

A new scenario with a chair fire in the room was arranged to investigate the extinguishing efficiency of inert agents. The scenario was designed similarly to the experiments conducted by Kraaijeveld [28]. A $0.5 \times 0.5 \times 0.6\text{ m}^3$ chair was placed 2.0 m from the left wall and 1.1 m from the back wall, as indicated in Figure 2b. The combustion property of fabric was applied to the chair [20] and the auto-ignition temperature (T_{AIT}) was set to be 210°C [30]. The chair was ignited by hot particles which were placed above the chair to heat the chair to above the auto-ignition temperature. The heat release rate (HRR) for the chair was set to be a t -squared fire with a $0.0264\text{ kW}/\text{s}^2$ growth rate for the first 90 s and reached the fully developed phase in the remaining simulation time period [26]. The discharge of agents IG-541 started at $t = 30\text{ s}$, i.e., when the fire was well established, and ended at 90 s, i.e., a 60 s discharge period. As the oxygen level under different ratio (k) has been investigated in the first scenario, it only focused on the extinguishing efficiency of inert gas agents in this scenario. The ventilation volume rate was set to be the same as the discharge rate. In the simulation, the simple flame extinction model in FDS was applied to gauge whether or not combustion was viable based on the local oxygen concentration. The simple flame extinction model assumes that combustion does not take place if the temperature is below the auto-ignition temperature (T_{AIT}) for fuel or if the heat released from the combustion process is not sufficient to raise the fuel-air-product mixture temperature above the empirically determined critical flame temperature (T_{CFT}). The heat released from the combustion process is limited by the availability of oxygen as shown in Section 2.1, thus the suppression of flaming combustion is based on the oxygen concentration. To observe the extinguishing efficiency of the inert gas agents, a case without a discharge of agents was also simulated. The simulation cases are summarized in Table 2.

To analyze the mesh sensitivity, four different Cartesian mesh solutions were applied to discretize the computational domain. The four solutions used cubic cells with sizes of 0.18 m, 0.15 m, 0.10 m, and 0.075 m, respectively, for the whole computational domain. The mesh sensitivity of the simulations was analyzed by comparing the temperature and oxygen mass fraction below the ceiling at the room center from the simulation case C1_1.0. Figure 3 shows the predictions of temperatures and oxygen mass fractions versus time. It is obvious that the convergence of temperature is obtained for the three finer meshes. The discrepancy of predicted temperatures from the two finest mesh solutions is no more than 9.6%. The same trend is also observed for the predicted oxygen mass fraction. Therefore, it is reasonable to assume that the mesh solution of 0.1 m is adequate to produce mesh independent simulation results. The following discussion is therefore based on the results from simulations with this mesh solution.

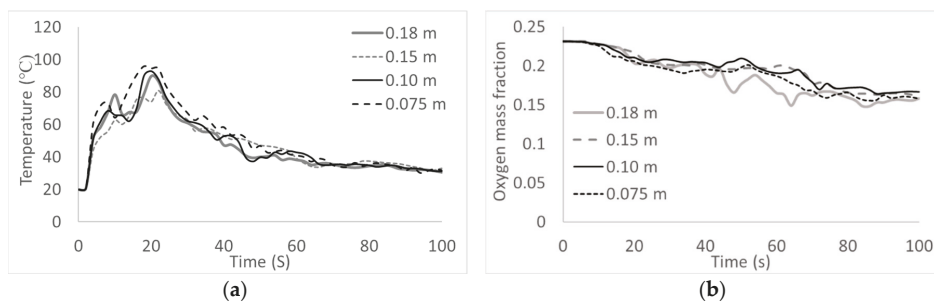


Figure 3. Predicted temperatures (a) and mass fraction versus time below the ceiling at the main room center from four mesh solutions (b).

4. Simulation Results and Discussion

The simulation results from scenario C0 (HRR = 0) are used to investigate the average oxygen mass fraction, oxygen distribution, and pressure within the enclosure. In a later results discussion, the predicted oxygen mass fraction, instead of the volume fraction, is given as the oxygen mass fraction used in determining the fire extinguishing efficiency in the FDS simulation models.

Figure 4 shows the average oxygen mass fraction against time for the case C0_100_1.0. The average oxygen concentration was reduced during the discharge period (first 60 s) and stayed constant for the next 40 s. The horizontal dashed line is the design oxygen mass fraction (12.8%), which corresponds to the inert gas agents' mass fraction of 44.35%. The oxygen mass fraction of the other cases displayed a similar trend as shown in Figure 4. As seen in Table 3, the average oxygen mass fraction at the end of the discharge period (60 s) did, however, vary slightly compared to case C0_100_1.0. The discrepancy between the obtained level and the design level was no more than 0.9% for case series C0_100 and 1.7% for case series C0_541. The discrepancy for the case series C0_541 is larger than that for the case series C0_100. The reason is that the density of IG-100 is close to the air density while the density of IG-541 is higher than the air density. The agent IG-541 descended to the floor during the discharge period and the air-agents mixture below the ceiling contained more oxygen than the average level. Thus, more oxygen was exhausted from the ceiling vent than expected, which resulted in the oxygen mass fraction being a little lower than the designed level. This indicates that the obtained oxygen level in an enclosure can be slightly influenced by the density of inert gas agents.

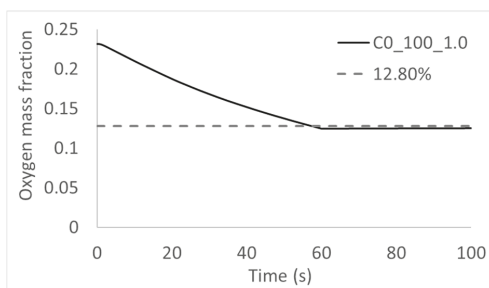


Figure 4. Oxygen mass fraction vs. time for the case C0_100_1.0.

Table 3. Predicted average oxygen mass fraction and pressure difference for case series C0.

Case Index	Y _{O₂}	Pressure Difference (Pa)
C0_100_0.8	11.9%	1.79×10^4
C0_100_0.9	12.1%	8.30×10^3
C0_100_1.0	12.5%	23.3
C0_100_1.1	12.8%	-7.14×10^3
C0_100_1.2	13.0%	-1.33×10^4
C0_541_0.8	11.1%	1.50×10^4
C0_541_0.9	11.3%	7.11×10^4
C0_541_1.0	11.4%	25.1
C0_541_1.1	11.6%	-6.7×10^3
C0_541_1.2	11.8%	-1.17×10^4

Table 3 also gives the pressure difference from standard atmospheric pressure within the enclosure. There is a very small pressure difference if the ventilation rate equals the discharge rate. However, if the ventilation rate varies from 10% to 20% up or down of the discharge rate, the pressure difference varies from about 10^3 to 10^4 Pa. This means that the enclosure structure may be exposed to damaging pressures if the ventilation rate is smaller than the discharge rate.

To investigate the oxygen distribution within the enclosure, the modeled oxygen mass fraction was analyzed at floor level (height 0.1 m), at 1.2 m height and at ceiling level (height 2.3 m) at three locations (see Figure 2). Figures 5 and 6 show the oxygen mass fraction at these heights and at the three locations (I, II, and III) for the case C0_100_1.0 and C0_541_1.0 respectively. At each height or location, the lowest, median, and highest values are shown as short horizontal dashes. The horizontal line is the average oxygen mass fraction in the enclosure. Figure 5 shows that the obtained oxygen level varied slightly around the average level at three heights and three locations for the case C0_100_1.0. The oxygen mass fraction varied between 11.6 and 14.4 % within the enclosure. The slight variation is partly a result of the similar density between IG-100 and air and thermal expansion of inert gas agents. Figure 6 shows the oxygen level for case C0_541_1.0. At the floor level, the oxygen mass fraction was always lower than the average level at the three other locations. At height 1.2 m above the floor, the oxygen mass fraction was slightly lower than the average level at three locations. At ceiling height, the oxygen mass fraction was always higher than the design level and varied between 16.7 and 20.4%. Therefore, it can be concluded that the oxygen mass fraction decreased with decreasing enclosure height and the value was normally no more than the design level at the middle height of the enclosure for IG-541. This is partly a result of the density difference between the IG-541 at -5 °C and the ambient air.

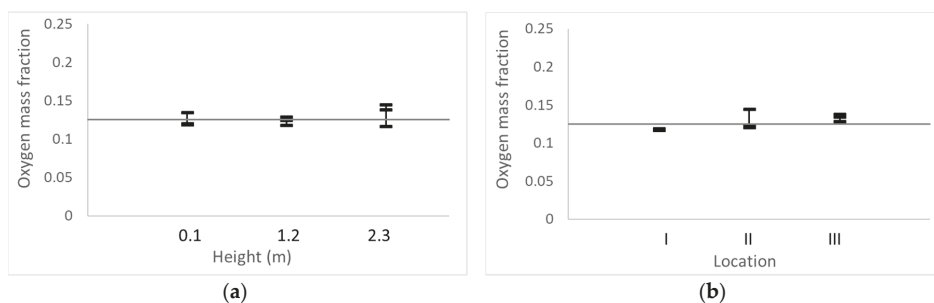


Figure 5. The lowest, median, and highest oxygen mass fraction at height 0.1, 1.2, and 2.3 m above the floor (a), and at locations I, II, and III at 100 s for case C0_100_1.0 (b).

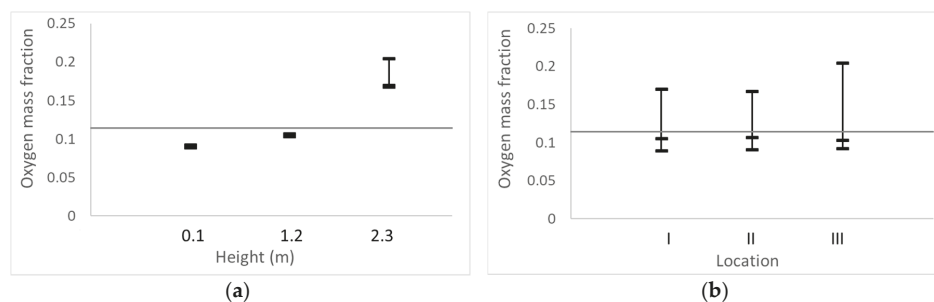


Figure 6. The lowest, median, and highest oxygen mass fraction at height 0.1, 1.2, and 2.3 m above the floor (a), and at locations I, II, and III at 100 s for case series C0_541_1.0 (b).

The extinguishing efficiency of inert gas agents was investigated through the case series C1, which set HRR as a t-square fire. In the case C1_0, no inert gas agents were discharged into the enclosure and the HRR grows approximately as the square of time (Figure 7). The oxygen was consumed by the combustion processes and its mass fraction dropped from 23.1% to 21.6% at the end of the 100 s simulation period. For the case C1_1.0, inert gas agent IG-541 was released into the enclosure between 30 s and 90 s. The HRR of case C1_1.0 increased during the first 70 s and then dropped to 0 at 76 s. The simple flame extinction model adopted in FDS models terminates combustion due to oxygen starvation. It might not match the reality as smoldering combustion may continue at a very low rate even at oxygen concentrations insufficient to sustain flaming combustion. The oxygen mass fraction around the fire source decreased from 12.8% to 11.4% between 72 s and 76 s. Two phenomena were observed from the case C1_1.0. The oxygen mass fraction dropped faster than the case C0_541_1.0, which runs without a fire source. The reason for this is that oxygen was consumed during the combustion, which accelerated the decrease in oxygen concentration. The second phenomenon is that HRR reached 0 at an oxygen level of 11.4%, which is lower than the design level. The design oxygen mass fraction 12.8% is derived from Equation (2) with an ambient temperature of 300 K, air specific heat c_p of 1.2 kJ/(kg·K), and critical flame temperature (T_{CFI}) of 1700 K. However, the real ambient temperature around the chair reached 340 K. The specific heat of IG-541 is 0.82 kJ/(kg·K) at this temperature, which means the specific heat of air-agents mixture is lower than 1.2 kJ/(kg·K). The critical flame temperature (T_{CFI}) adopted in FDS is 1600 K [23], which is lower than the value suggested in Section 2.1. The limiting oxygen concentration estimates are based on the heat required to heat the combustion products from the ambient temperature to the critical flame temperature (T_{CFI}). When experiencing a locally increased “ambient temperature”, less heat is required to reach the critical flame temperature, i.e., more inert gases are needed to prevent combustion taking place. Therefore, the real oxygen limit level should be lower than 12.8% according to Equation (2) in the case C1_1.0. After the fire was extinguished at 80 s, the IG-541 was discharged

continuously until 90 s and the oxygen mass fraction reached 10.2%. The oxygen level of 10.2 % is an acceptable value in an occupied area considering the benefit of the “CO₂ Effect”.

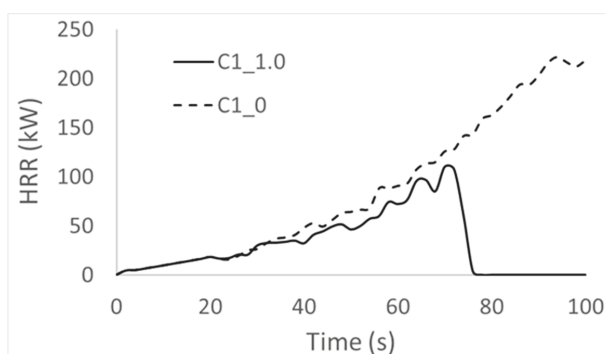


Figure 7. Heat release rates (HRRs) versus time for series case C1.

5. Conclusions and Suggestions for Future Studies

This paper proposes general expressions between oxygen level, discharge rate, and ventilation rate. Explicit equations are given to calculate the discharge rate and the required quantity of inert gas agents to obtain a design oxygen level when the discharge rate and ventilation rate are both constants.

The proposed expressions in the present study are derived based on the assumption that inert gas agents and air at any time are uniformly distributed in an enclosure. The assumption simplifies the gas discharge phenomenon. To investigate the discharge efficiency and extinguishing efficiency of inert gas agents, several simulation scenarios with and without a fire source were run using the CFD simulation tool—FDS. The simulation results show that:

- The design oxygen level could be approximately obtained at the end of the discharge period if the discharge rate and ventilation rate are calculated from the suggested equations. The obtained oxygen level in an enclosure can be slightly influenced by the density of inert gas agents.
- Oxygen fraction varies with height as a result of density differences between air and inert gas agents. The oxygen mass fraction was normally below the design level at the lower half of the enclosure.
- To avoid enclosure over-pressure effects, the discharge volume rate should be close to the ventilation volume rate.
- For the case with a chair fire, the HRR dropped to zero before the end of the discharge period partly due to the oxygen consumed in combustion.

This study demonstrates that ventilation systems not only play an important role in mitigating the possible released inert gas agent overpressure effect but also reduce the required quantity of inert gas agents to obtain a design oxygen level. The oxygen mass fraction increased with the height of the enclosure if the density of an inert gas agent is higher than the density of the air. This ensures that inert gas fire suppression systems perform better in the low elevation in an enclosure as most inert gas agents have a higher density than that of air. In the case with a fire, the oxygen consumed in combustion during discharge time accelerated the fire extinguishing. In future work, the inert gas agents extinguishing efficiency for different fire sizes, and the thermal pressure caused by fires in an enclosure should be investigated. In addition to the mechanical ventilation system, the natural ventilation system, e.g., open doors, windows, and leaks [31,32] in reality also alters the ventilation flow rate and should be taken into consideration in future studies. Moreover, experimental validations are needed for the practical applications of this study as variation in the agents' discharge rate may be expected.

Author Contributions: Conceptualization, X.H.; methodology, X.H. and T.L.; software, X.H.; validation, X.H.; formal analysis, X.H.; investigation, X.H.; resources, X.H. and A.K.; data curation, X.H. and A.K.; writing—original draft preparation, X.H.; writing—review and editing, T.L. and A.K.; visualization, X.H. and T.L.; supervision, T.L.; project administration, X.H. All authors have read and agreed to the published version of the manuscript.

Funding: This research received no external funding.

Conflicts of Interest: The authors declare no conflict of interest.

Nomenclature

\bar{c}_p	average specific heat (kJ/(kg·K))
E_m	ventilation mass rate of mixture (kg/s)
E_V	ventilation volume rate of mixture (m ³ /s)
ΔH_{O_2}	energy released per unit mass of oxygen consumed (kJ/kg)
HRR	heat release rate (kW)
k	ratio of ventilation rate to discharge rate
m	total mass of gases in the enclosure (kg)
m_0	total mass in the enclosure at start (kg)
m_{agents}	discharge quantity of agents (kg)
Q	energy (kJ)
R_m	discharge mass rate of agents (kg/s)
R_V	discharge volume rate of agents (m ³ /s)
t	time (s)
T_{CFT}	critical flame temperature (K)
T_m	ambient temperature (K)
V_0	volume of an enclosure (m ³)
V^*	standard volume (m ³)
Y_m	mass fraction
$Y_{m,air}$	air mass fraction in mixture
Y_{m,O_2}	oxygen mass fraction in mixture
Y_{m,O_2}^*	design oxygen mass fraction
$Y_{V,air}$	air volume fraction in mixture
Y_{V,O_2}	oxygen volume fraction in mixture
Y_{V,O_2}^*	design oxygen fraction
Y_V	volume fraction
$\hat{Y}_{O_2,lim}$	limiting oxygen fraction to sustain a flame
ρ	density (kg/m ³)

References

- Grant, C.C. Halon design calculations. In *SFPE Handbook of Fire Protection Engineering*, 5th ed.; Hurley, M.J., Gottuk, D.T., Hall, J.R., Jr., Harada, K., Kuligowski, E.D., Puchovsky, M., Torero, J.L., Watts, J.M., Jr., Wieczorek, C.J., Eds.; Springer: New York, NY, USA, 2016; Chapter 43; pp. 1450–1482. [[CrossRef](#)]
- DiNunno, P.J.; Forssell, E.W. Clean agent total flooding fire extinguishing systems. In *SFPE Handbook of Fire Protection Engineering*, 5th ed.; Hurley, M.J., Gottuk, D.T., Hall, J.R., Jr., Harada, K., Kuligowski, E.D., Puchovsky, M., Torero, J.L., Watts, J.M., Jr., Wieczorek, C.J., Eds.; Springer: New York, NY, USA, 2016; Chapter 44; pp. 1483–1530. [[CrossRef](#)]
- Forsell, E.W.; Back, G.G.; Beyler, C.L.; DiNunno, P.J.; Hansen, R.; Beene, D. An evaluation of the international maritime organization's gaseous agents test protocol. *Fire Technol.* **2001**, *37*, 37–67. [[CrossRef](#)]
- Zou, Y.; Vahdat, N.; Collins, M. Fire protection with bromoalkene/nitrogen gaseous mixtures. *Ind. Eng. Chem. Res.* **2001**, *40*, 4649–4653. [[CrossRef](#)]
- Senecal, J.A. Flame extinguishing in the cup-burner by inert gases. *Fire Saf. J.* **2005**, *40*, 579–591. [[CrossRef](#)]
- Yu, H.Z.; Kasiski, R.; Daelhousen, M. Characterization of Twin-Fluid (Water Mist and Inert Gas) Fire Extinguishing Systems by Testing and Modeling. *Fire Technol.* **2015**, *51*, 923–950. [[CrossRef](#)]
- Khattri, S.K.; Log, T.; Kraaijeveld, A. Tunnel Fire Dynamics as a Function of Longitudinal Ventilation Air Oxygen Content. *Sustainability* **2019**, *11*, 203. [[CrossRef](#)]

8. De Rosa, M.I.; Litton, C.D. Effectiveness of various concentrations of an inert gas mixture for preventing and suppressing mining equipment cab fires: Development of a dual cab fire inerting system. *Fire Technol.* **2007**, *43*, 29–44. [[CrossRef](#)]
9. Laursen, T. Fire protection for weak citizens. In Proceedings of the Nordic Fire and Safety Days, Copenhagen, Denmark, 20–21 August 2019. [[CrossRef](#)]
10. Wang, Y.; Meng, X.; Ji, W.; Pei, B.; Lin, C.; Feng, H.; Zheng, L. The Inhibition Effect of Gas–Solid Two-Phase Inhibitors on Methane Explosion. *Energies* **2019**, *12*, 398. [[CrossRef](#)]
11. Li, M.H.; Xu, J.C.; Wang, C.J.; Wang, B.Z. Thermal and kinetics mechanism of explosion mitigation of methane-air mixture by N₂/CO₂ in a closed compartment. *Fuel* **2019**, 255. [[CrossRef](#)]
12. Bakka, M.S.; Handal, E.K.; Log, T. Analysis of a High-Voltage Room Quasi-Smoke Gas Explosion. *Energies* **2020**, *13*, 601. [[CrossRef](#)]
13. Kraaijeveld, A. *Rapport Vedrørende Anvendelse av IG-541 Som Alternative til Sprinkleranlegg*; Western Norway University of Applied Sciences: Bergen, Norway, 2018.
14. Bettati. *Design Manual for Inert Gas System IG 100-IG01-IG55-IG541*; Bettati Antincendio: Reggio Emilia, Italy, 2010.
15. Wickham, R.T. Review of the Use of Carbon Dioxide Total Flooding Fire Extinguishing Systems. 2003. Available online: www.epa.gov/snap/review-use-carbon-dioxide-total-flooding-fire-extinguishing-systems (accessed on 6 January 2020).
16. Akyuz, E. Quantification of human error probability towards the gas inerting process on-board crude oil tankers. *Saf. Sci.* **2015**, *80*, 77–86. [[CrossRef](#)]
17. National Fire Protection Association. *Standard on Clean Agent Fire Extinguishing Systems*; National Fire Protection Association: Quincy, MA, USA, 2001.
18. Lambertsen, C.J.; Gelfand, R. *Comparison of CO₂-Induced Improvements in Arterial SaO₂ during Abrupt Exposures of Human Subjects to 12 and 10 ATA Inspired O₂ in N₂, in Rest and Exercise*; Undersea and Hyperbaric Medical Society: North Palm Beach, FL, USA, 1996.
19. Ansul. *Clean Fire Extinguishing Agents Human Safety Testing*; Tyco Fire & Security, Ansul Incorporated: Marinette, WI, USA, 2004.
20. McGrattan, K.; Hostikka, S.; McDermott, R.; Floyd, J.; Weinschenk, C.; Overholt, K. *Fire Dynamics Simulator User's Guide*, 6th ed.; NIST Special Publication: Gaithersburg, MD, USA, 2017. [[CrossRef](#)]
21. Zimny, M.; Antosiewicz, P.; Krajewski, G.; Burdzy, T.; Krasuski, A.; Wegrzyński, W. Several Problems with Froude-Number Based Scale Modeling of Fires in Small Compartments. *Energies* **2019**, *12*, 3625. [[CrossRef](#)]
22. Brzezińska, D. Ventilation System Influence on Hydrogen Explosion Hazards in Industrial Lead-Acid Battery Rooms. *Energies* **2018**, *11*, 2086. [[CrossRef](#)]
23. McGrattan, K.; Hostikka, S.; McDermott, R.; Floyd, J.; Weinschenk, C.; Overholt, K. *Fire Dynamics Simulator Technical Reference Guide Volume 1: Mathematical Model*, 6th ed.; NIST Special Publication No. 1018; NIST: Gaithersburg, MD, USA, 2013.
24. Beyler, C. Flammability limits of premixed and diffusion flames. In *SFPE Handbook of Fire Protection Engineering*, 5th ed.; Hurlley, M.J., Gottuk, D.T., Hall, J.R., Jr., Harada, K., Kuligowski, E.D., Puchovsky, M., Torero, J.L., Watts, J.M., Jr., Wieczorek, C.J., Eds.; SFPE: Gaithersburg, MD, USA, 2016; Chapter 17; pp. 529–553. [[CrossRef](#)]
25. Huggett, C. Estimation of rate of heat release by means of oxygen consumption measurements. *Fire Mater.* **1980**, *4*, 61–65. [[CrossRef](#)]
26. Karlsson, B.; Quintiere, J.G. *Enclosure Fire Dynamics*; CRC Press LLC: London, UK, 1999; pp. 38–59, ISBN 0-8493-1300-7.
27. Simmons, R.F.; Wolfhard, H.G. Some Limiting Oxygen Concentrations for Diffusion Flames in Air Diluted with Nitrogen. *Combust. Flame* **1957**, *1*, 155–161. [[CrossRef](#)]
28. Kraaijeveld, A. Fire protection of at risk groups by IG-541 and water based sprinklers: Full scale tests. In Proceedings of the Nordic Fire and Safety Days, Copenhagen, Denmark, 20–21 August 2019. [[CrossRef](#)]
29. O'Rourke, S.T. Analysis of Hold Times for Gaseous Fire Suppression Agents in Total Flooding Applications. Master's Thesis, University of Maryland, College Park, MD, USA, 2005.
30. Graf, S.H. *Ignition Temperatures of Various Papers, Woods, and Fabrics*; Oregon State College, Engineering Experiment Station: Corvallis, OR, USA, 1949.

31. Boron, S.; Wegrzynski, W.; Kubica, P.; Czarnecki, L. Numerical Modelling of the Fire Extinguishing Gas Retention in Small Compartments. *Appl. Sci.* **2019**, *9*, 663. [[CrossRef](#)]
32. Kubica, P.; Czarnecki, L.; Boron, S.; Wegrzynski, W. Maximizing the retention time of inert gases used in fixed gaseous extinguishing systems. *Fire Saf. J.* **2016**, *80*, 1–8. [[CrossRef](#)]



© 2020 by the authors. Licensee MDPI, Basel, Switzerland. This article is an open access article distributed under the terms and conditions of the Creative Commons Attribution (CC BY) license (<http://creativecommons.org/licenses/by/4.0/>).

MDPI
St. Alban-Anlage 66
4052 Basel
Switzerland
Tel. +41 61 683 77 34
Fax +41 61 302 89 18
www.mdpi.com

Energies Editorial Office
E-mail: energies@mdpi.com
www.mdpi.com/journal/energies



MDPI
St. Alban-Anlage 66
4052 Basel
Switzerland
Tel: +41 61 683 77 34
www.mdpi.com



ISBN 978-3-0365-4684-1